

CONDUCTIVITY, DIELECTRIC AND PIEZOELECTRIC PROPERTIES OF $\text{SrBi}_4\text{Ti}_4\text{O}_{15}$

THÈSE N° 2227 (2000)

PRÉSENTÉE AU DÉPARTEMENT DES MATÉRIAUX

ÉCOLE POLYTECHNIQUE FÉDÉRALE DE LAUSANNE

POUR L'OBTENTION DU GRADE DE DOCTEUR ÈS SCIENCES TECHNIQUES

PAR

Cyril VOISARD

Ingénieur en science des matériaux diplômé EPF
de nationalité suisse et originaire de Fontenais (JU)

acceptée sur proposition du jury:

Prof. N. Setter, directrice de thèse
Dr C. Cavalloni, rapporteur
Dr D. Damjanovic, rapporteur
Dr P. Duran Martin, rapporteur
Prof. H. Mathieu, rapporteur

Lausanne, EPFL
2000

ABSTRACT

Strontium Bismuth Titanate is a very promising material for high temperature piezoelectric applications. Its elevated ferroelectric phase transition (530°C), linear piezoelectric properties under low field and relatively low room temperature conductivity (compared to others Bismuth Titanates) make it very attractive for precision sensors. However, under severe conditions (low frequency, high field, high temperature or low oxygen partial pressure) some of those advantages disappear. Piezoelectric response is dominated by charge drift in general becomes unstable. Above all, at high temperature and low oxygen partial pressure, a large conductivity increase reduces the piezoelectric efficiency of the material. In this work, electrical conductivity, piezoelectric properties and dielectric permittivity of SrBIT ceramic have been investigated in conditions of high temperature, low oxygen partial pressure, low to moderate driving field and frequency. As a result of this research, a better understanding of SrBIT properties was achieved. Thanks to a careful study of SrBIT processing as a bulk ceramic, a reproducible route was established. Many basic mechanisms leading to both SrBIT crystallization and sintering have been identified. It was demonstrated that a detailed knowledge of the exact processing conditions is required in order to achieve high quality material.

DC conductivity measurements were carried out as a function of temperature, oxygen partial pressure and dopant concentration. It was found that the apparent activation energy for conduction for undoped SrBIT was 1 eV between 140 and 220°C and 1.5 eV between 450 and 700°C. Decrease of the activation energy in the lower temperature range has been discussed considering grain boundary conductivity, as a transition from electronic to ionic conduction or as consequence of small polarons conduction. It was shown that lower activation energy resulted from Manganese doping (0.5 eV), this was interpreted as either growing influence of grain boundary conductivity as dopant concentration increases or as shallow hole trap formation. DC conductivity measurements and acceptor/donor doping experiments demonstrated p-type conductivity in the low temperature range (up to 220°C) as donor doping decreases conductivity, while oxygen partial pressure controlled measurements indicated n-type conductivity at higher temperature (above 700°C).

An electrical impedance analysis was performed with several equivalent circuits. The aim of these models was to simulate the impedance of SrBIT. The best approximation was found with a distributed element of Havriliak-Negami type. However, as the physical justification for this circuit was not clear, the investigation of the grain, grain boundary and electrode impedances was performed with multiple discrete parallel RC elements. With temperature, grain size and oxygen activity variations, the identification of three separate contributions as grain, grain boundary and electrode was realized.

The anisotropy of conductivity and permittivity was demonstrated with textured material and both DC and AC analysis. With the master curves built for the electrical modulus, it was found that the impedance probably related to Bismuth oxide layers produces an additional high

frequency arc. From this finding and by comparing characteristic relaxation frequencies of undoped, 2 mol.% Mn and 4 mol.% Nb SrBIT, it was determined that conductivity is higher in the ab plane direction than in the c direction within both perovskite units and Bismuth oxide layers.

With conductivity measurements under controlled oxygen partial pressure, it was found that an acceptor-based (intrinsic or extrinsic) model could be used to describe the electrical conductivity under controlled oxygen partial pressure of both undoped and 2 mol.% Mn doped SrBIT. However, as neither a $pO_2^{-1/6}$ region (intrinsic oxygen vacancies compensated by electrons) for undoped SrBIT nor a $pO_2^{-1/4}$ region (oxygen vacancies compensated by singly ionized acceptors) for Mn doped SrBIT were seen, it was concluded that the acceptor-controlled model is not sufficient for a complete description of SrBIT. For this reason and in order to include the low oxygen partial pressure behavior of undoped SrBIT, a donor-based (intrinsic) model was also considered. The source of intrinsic donors would be in that case Bi^{3+} cations sitting on Sr^{2+} sites in the perovskite sublattice. Considering Bismuth vacancies as the negative compensating species, both $pO_2^{-1/4}$ and pO_2 -independent regions could be predicted with the model. However, even if the donor-controlled model seems to better match conductivity measurements in the full pO_2 range, rejecting the acceptor-based model would be an error. It is actually not demonstrated that in SrBIT the concentration of exchanged Bismuth cations is always (all temperature, pressure) larger than the natural acceptor impurity concentration. It is very likely that the cation exchange is dependent of the oxygen partial pressure. It is also not proved as suggested in the literature that direct compensation between exchanged Strontium and Bismuth exists, reducing the net donor-excess. With the acceptor-controlled model, the mass-action constants for reduction and for ionization of intrinsic carriers across the band gap were determined. The band gap of SrBIT was estimated to be 3.5 eV. The ionic conductivity of SrBIT was determined at high temperature with measurements under controlled oxygen partial pressure. It was found that the electrical conductivity of SrBIT is probably mixed (electronic and ionic) as the estimation of the transference number provided quite large values ($t=0.8$ at $800^\circ C$). From electronic and ionic conductivity data, mixed conduction can actually be predicted in a large temperature range (above room temperature).

The piezoelectric measurements using direct effect demonstrated that it is actually possible to unlock piezoelectrically active ferroelectric domain walls and create non-linear piezoelectric properties in undoped SrBIT. This occurs above a threshold elastic field, which is thermally activated. With a piezoelectric composite, it was demonstrated that the electromechanical coupling between two different phases creates a piezoelectric relaxation. This one could be positive or negative depending on the respective properties of each composite's component. It was shown experimentally that a small temperature change is sufficient to transform a positive relaxation into a negative one. While these experiments did not provide a detailed microstructural explanation for the piezoelectric relaxation observed in 2 mol.% Mn doped SrBIT, they gave a first insight into an original phenomenological approach. Microstructure and piezoelectric properties were related with the calculation of a piezoelectric relaxation composite made of two textured samples. This demonstrated that a piezoelectric relaxation may occur just because of anisotropy. Microstructural reproduction of this coupling is actually an important feature of Aurivillius phases.

RÉSUMÉ

Le Titanate de Strontium Bismuth (abrégé SrBIT) est un matériau très prometteur pour des applications piézo-électriques à haute température. Grâce à une température de transition de phase ferro-électrique élevée (530°C), à des propriétés piézo-électriques très stables sous faible champ et à une conductivité électrique relativement basse à température ambiante (comparée à d'autres Titanates de Bismuth), ce matériau est très intéressant pour réaliser des capteurs de précision. Cependant, sous conditions extrêmes (basse fréquence, champ élevé, haute température ou basse pression d'oxygène), ces avantages disparaissent et la réponse piézo-électrique, dominée par les dérives de charge, devient instable. Mais avant tout, à haute température et basse pression d'oxygène, l'accroissement très fort de la conductivité réduit considérablement l'effet piézo-électrique de SrBIT. Dans ce travail, la conductivité électrique, les propriétés piézo-électriques et la permittivité diélectrique de SrBIT ont été étudiées à haute température, basse pression partielle d'oxygène, faible champ et fréquence. Cette recherche a permis une meilleure compréhension des propriétés de SrBIT.

Par une étude détaillée de la préparation de SrBIT sous forme de céramique massive, une méthode de préparation reproductible a été établie. Différents mécanismes élémentaires qui interviennent lors de la cristallisation ou du frittage ont été identifiés. Mais, il a été démontré également qu'une connaissance pointue des paramètres du procédé est requise pour garantir la préparation de matériaux de bonne qualité.

Des mesures de conductivité électrique de type DC ont été effectuées en variant la température, la pression partielle d'oxygène et la teneur en dopant. L'énergie d'activation pour la conductivité déterminée lors de ce travail de thèse est de 1 eV entre 140 et 220°C et de 1.5 eV entre 450 et 700°C. La diminution de l'énergie d'activation dans la gamme inférieure de température a été interprétée comme la conséquence d'une conductivité aux joints de grain prépondérante à basse température. Les hypothèses de la transition d'un régime électronique à un régime ionique ou la conduction par polarons ont également été considérées. La diminution de l'énergie d'activation (0.5 eV) par le dopage de type accepteur de SrBIT a été interprétée comme soit l'influence grandissante de la conductivité des joints de grains soit le piégeage des trous dans des niveaux peu profonds. Les mesures de conductivité DC et les dopages de type donneur et accepteur ont démontré une conductivité de type p dans la gamme inférieure de température (jusqu'à 220°C), car l'ajout d'une certaine quantité de Niobium (donneur) diminue la conductivité de SrBIT. Par contre, les mesures effectuées à plus haute température sous pression partielle d'oxygène contrôlée indiquent une conductivité de type n.

L'analyse de l'impédance électrique de SrBIT a été réalisée à l'aide de différents circuits équivalents. A l'aide de ces modèles, l'impédance de SrBIT a pu être simulée. La meilleure approximation a été trouvée avec un élément distribué de type Havriliak-Negami. Cependant, comme la justification physique de ce circuit n'est pas claire l'étude de l'impédance des grains, des joints de grains et de l'interface céramique-électrode a été effectuée avec plusieurs circuits

équivalents de type discret. À l'aide de l'influence de la température, de la taille de grain et de la pression partielle d'oxygène, l'identification de l'impédance des grains, des joints de grains et de l'électrode a pu être établie.

L'anisotropie de la conductivité et de la permittivité a été démontrée par l'analyse AC et DC de matériau texturé. Grâce à des courbes maîtresses construites pour le module électrique, l'impédance probablement liée aux couches d'oxyde de Bismuth a été observée à haute fréquence. Avec ce résultat et en comparant les fréquences de relaxation de SrBIT non-dopé, dopé accepteur (2 % mol Mn) et dopé donneur (4 % mol.), il a pu être démontré que la conductivité est plus grande dans la direction dite "plan ab" que dans la direction "c" pour les unités de structure pérovskite et pour les couches d'oxyde de Bismuth.

Avec des mesures de conductivité DC à haute température ($>700^{\circ}\text{C}$) sous pression partielle d'oxygène contrôlée, il a pu être démontré qu'un modèle basé sur un excès d'accepteurs pouvait être avantageusement utilisé pour décrire la conductivité de SrBIT non-dopé et dopé accepteur. Cependant, comme aucune région en $p\text{O}_2^{-1/6}$ (compensation des lacunes d'oxygènes intrinsèques par des électrons) pour SrBIT non-dopé ou en $p\text{O}_2^{-1/4}$ (compensation des lacunes d'oxygènes par des accepteurs simplement ionisés) pour SrBIT dopé Mn n'ont été observées, il a été conclu qu'un modèle basé uniquement sur un excès d'accepteurs était insuffisant. C'est pourquoi, afin aussi d'inclure le comportement de SrBIT à très basse pression d'oxygène, un autre modèle, basé sur un excès intrinsèque de donneurs a également été considéré. Dans ce modèle, la source intrinsèque de donneur proviendrait d'un échange de site entre Bi^{3+} des couches d'oxydes de Bismuth et Sr^{2+} des unités pérovskite. En assumant la compensation des défauts positifs par des lacunes de Bismuth, une région de conductivité en $p\text{O}_2^{-1/4}$ et une autre indépendante de la pression peuvent être prédites. Cependant, même si ce modèle semble mieux correspondre aux mesures de conductivité, rejeter le modèle accepteur serait une erreur. En effet, il n'est pas prouvé que la concentration de donneurs intrinsèque soit toujours supérieure (à n'importe quelle température ou pression) que la concentration d'impuretés. Il est par exemple très probable que l'échange de cations soit dépendant de la pression partielle d'oxygène. De plus, la compensation directe des deux cations échangés ne peut pas être exclue, ce qui réduirait l'excès net de donneur. Avec le modèle accepteur, les constantes d'équilibre pour la création de lacunes d'oxygène et pour l'ionisation de porteurs au travers de la bande interdite ont été déterminées. L'énergie de la bande interdite de SrBIT a été estimée à 3.5 eV. Avec les mesures de conductivité sous pression partielle d'oxygène contrôlée, la conductivité ionique de SrBIT a été estimée à haute température. Ainsi, il est proposé que la conductivité de SrBIT est de type mixte (électronique et ionique), par exemple le nombre de transférence à 800°C est de 0.8. À partir des mesures de conductivité ionique et électronique, une conduction mixte sur une large gamme de température peut être prédite.

Des mesures piézo-électriques ont démontré que le désancrage de parois de domaines ferro-électriques actives pour la piézo-électricité de SrBIT était possible, ce qui induit des propriétés piézo-électriques non linéaires. Ceci se produit au-dessus d'un seuil de champ élastique qui est activé thermiquement. Avec un composite piézo-électrique, la création d'une relaxation piézo-électrique par le couplage électro-mécanique de deux différentes phases a été démontré. Cette relaxation peut être positive ou négative selon les propriétés des matériaux constituant le composite. Par exemple, un petit écart de température transforme une relaxation positive en relaxation négative. Bien que ces expériences ne permettent pas d'expliquer les relaxations piézo-

électriques observées pour SrBIT dopé Manganèse, elles donnent un premier aperçu d'une approche phénoménologique originale. Le lien entre la microstructure et la relaxation piézo-électrique a été établi par le calcul du coefficient piézo-électrique d'un composite constitué de deux échantillons texturés. Il a ainsi été démontré que les différences de propriétés dues à l'anisotropie de SrBIT suffisent à créer une relaxation. La reproduction interne à la microstructure de ce couplage est certainement une caractéristique importante des phases d'Aurivillius.

TABLE OF CONTENT

Abstract	1
Résumé	3
Table of content	7

INTRODUCTION

1.1	General Introduction.....	13
1.2	Materials Review.....	14
1.3	Selected Materials Properties.....	16
1.3.1	Crystallographic structure	16
1.3.2	DC and AC Conductivity	17
1.3.3	Conductivity at Low Oxygen Partial Pressure	18
1.3.4	Piezoelectricity	18
1.3.5	Objective of the Thesis	19

MATERIAL PROCESSING

2.1	Foreword	23
2.2	Introduction	24
2.3	Experimental methods	25
2.4	Processing route	27
2.5	Phase Formation	31
2.5.1	Single oxides	31
2.5.2	Binary Oxides.....	31
2.5.3	Ternary Oxides	33
2.5.4	Identification of SrBIT Phase Formation.....	34
2.6	Sintering.....	37
2.6.1	General Process Description	37
2.6.2	Dilatometry Experiments	37
2.6.3	Fracture Surface by Scanning Electron Microscope.....	40
2.6.4	Porosity Quantification	41
2.6.5	Microstructure of undoped SrBIT	42
2.7	Doping	45
2.7.1	Acceptor doping with MnCO ₃	45
2.7.2	Donor Doping with Nb ₂ O ₅	47
2.8	Preparation of Textured Material using Hot forging.....	49
2.9	Summary and Conclusion	52

DC AND AC CONDUCTIVITY	55
3.1 Foreword.....	57
3.2 Electrical DC Conductivity.....	58
3.2.1 Introduction.....	58
3.2.2 Charging Current Expression.....	58
3.3 Experimental Considerations.....	60
3.3.1 DC Conductivity Measurement.....	60
3.3.2 Determination of Grain Boundary Conductivity.....	61
3.3.2.1 Motivation.....	61
3.3.2.2 Application to SrBIT.....	64
3.4 Electrical DC Conductivity of Undoped SrBIT.....	69
3.4.1 Conductivity of random oriented ceramic.....	69
3.4.2 Charging current of SrBIT.....	70
3.4.3 Calculation of grain and grain boundary conductivities.....	71
3.4.4 Conductivity of Hot Forged Ceramics.....	74
3.4.5 Acceptor Doping of SrBIT Random Oriented Ceramics.....	77
3.4.6 Donor Doping of SrBIT Random Oriented Ceramics.....	80
3.5 Impedance Analysis.....	83
3.5.1 Introduction.....	83
3.5.2 Definitions of basic functions.....	84
3.5.3 Description of Equivalent Circuits.....	86
3.6 Results of the Impedance Analysis.....	94
3.6.1 Equivalent Circuit Determination.....	94
3.6.2 Detailed Evaluation of the Havriliak-Negami Model.....	96
3.6.3 Undoped SrBIT Ceramics-Model with Three RC Components.....	99
3.6.4 Modulus analysis in the lower AC temperature range.....	103
3.6.5 Master Curve Drawing.....	105
3.6.6 Mn doping effect on impedance.....	114
3.6.7 Grain size effect.....	116
3.6.8 Impedance transient under changing pO_2	118
3.7 Summary and Conclusion.....	123

CONDUCTIVITY UNDER CONTROLLED OXYGEN PARTIAL PRESSURE.....125

4.1 Foreword.....	127
4.2 Basics of Defect Chemistry.....	129
4.2.1 Point Defects Considerations.....	129
4.2.2 Interpretation of Conductivity Measurements.....	131
4.2.2.1 Electron and hole traps.....	132
4.3 Experimental Conditions.....	135
4.3.1 General Presentation.....	135
4.3.2 Oxygen Partial Pressure Regulation.....	135
4.3.3 Conductivity Measurement.....	140
4.3.4 Data Processing.....	140
4.3.4.1 Conductivity transients.....	140

4.3.4.2	Ionic Conductivity Calculation.....	142
4.4	Electrical Conductivity of SrBIT under Controlled Oxygen Partial Pressure	143
4.4.1	BaTiO ₃ used as a reference material.....	143
4.4.2	DC Electrical conductivity of SrBIT in Ar-O ₂	145
4.4.2.1	Undoped SrBIT.....	145
4.4.2.2	Manganese doping outcome	148
4.4.2.3	Donor doping effect	153
4.4.3	DC Electrical conductivity of SrBIT in full pO ₂ range	155
4.4.3.1	Evaluation of “intrinsic” donor-excess	157
4.4.4	Ionic conductivity calculation	159
4.5	Summary and Conclusion.....	164
 PIEZOELECTRIC PROPERTIES		167
5.1	Foreword.....	169
5.2	Piezoelectricity basics.....	170
5.3	Experimental	172
5.3.1	Poling Procedure.....	172
5.3.2	Measurement Set-up	172
5.4	Piezoelectric Properties of SrBIT.....	175
5.4.1	General Behavior.....	175
5.4.2	Piezoelectric Properties at Higher Temperature.....	178
5.4.3	Piezoelectric Relaxation.....	180
5.4.4	Modelization of the Piezoelectric Relaxation	184
5.4.5	Experimental Verification of the Model	185
5.4.6	Numeric Simulation of Equation 5-7.....	189
5.5	Summary and Conclusion.....	196
 CONCLUSION		197
6.1	Summary and Conclusion.....	199
6.1.1	Material Processing.....	199
6.1.2	DC and AC Conductivity	199
6.1.3	Conductivity under Controlled Oxygen Partial Pressure.....	201
6.1.4	Piezoelectric Properties.....	202
6.2	Future work and Outlook	204
 Bibliography.....		11
Figure caption.....		213
Acknowledgements.....		221
Curriculum Vitae		223

1

INTRODUCTION

1.1 GENERAL INTRODUCTION

A typical feature of modern technology is probably the ability of systems to sense the surroundings, e.g. temperature, pressure with a good accuracy in order to optimize the operation (self-regulation). This is commonly achieved with the so called «smart materials» used as functional elements. Under any stimulus, «smart materials» can be set into an «informed state» more or less quickly, exhibiting thus a smart behavior [1]. Many of smart materials are ceramics, but there are also metallic one (Ni-Ti shape memory alloys) or organic ones such as PVDF (monomer is $\text{CH}_2\text{-CF}_2$) which β phase is pyroelectric [2]. With simple polymer processing, it allows building of large area detectors.

Functional ceramics are used as electrical conductors, e.g. for humidity sensors (MgCr_2O_4 [3]) or fuel cells (ZrO_2), as semiconductors for energy conversion (TiO_2), as insulators for piezoelectric applications ($\text{Pb}(\text{Zr},\text{Ti})\text{O}_3$). They can be used as single crystals (quartz), polycrystals (high temperature Bismuth Titanates-based pressure sensor), thin or thick films ($\text{Pb}(\text{Zr},\text{Ti})\text{O}_3$) or as coatings on glass fibers (ZnO). Piezoelectrics are met in computers application (disk drive shock sensor, touch-input panels), medicine (invasive catheters, pacemakers) or in security (motion detection, step switch). Transportation is another important large domain for consumer and industrial application of piezoelectric devices. For example, in-cylinder combustion [4] can be regulated thanks to ceramic pressure sensors, developed after the invention of the charge amplifier in 1950 by Kistler [5]. Cylinder pressure feedback is used to control spark timing, fuel injector pulse width and timing or exhaust gas recirculation rate. Low cost sensor designs consist of bulk piezoelectric transducers in bar shape ([6]), ring ([7]) or tube ([8]) made of PZT as proposed by Randall [7]. However depolarization near ferroelectric phase transition (365°C for PZT-5a) implies strong temperature limitations and requires the choice of non-standard materials with high transition temperature, such as Bismuth Titanates like $\text{SrBi}_4\text{Ti}_4\text{O}_{15}$ (written SrBIT). Among piezoelectric materials, $\text{SrBi}_4\text{Ti}_4\text{O}_{15}$ has the additional advantages to avoid any complex signal treatment imposed by non-linear piezoelectric properties of PZT.

Beside a strong industrial interest for SrBIT in regulation systems, there is also a scientific interest in this material, since most of its properties are presently poorly understood. Conductivity and piezoelectricity, for example, of SrBIT were hardly investigated, since discovery of the material by Aurivillius in 1949 [14]. Therefore, there are two driving forces for investigation of SrBIT: an academic one, with goal of better understanding of its properties and an industrial one with aim of its integration into new smart systems.

1.2 MATERIALS REVIEW

Large costs and relatively low sensitivity associated with single crystals use have driven extensive work towards equivalent low cost ceramic materials (e.g. $\text{Pb}(\text{Zr},\text{Ti})\text{O}_3$ to replace quartz for pressure sensors). In this frame Bismuth Titanates ceramics of the Aurivillius family (formula $\text{A}_{m-n-1}\text{Bi}_n\text{B}_m\text{O}_{3m+3}$) are good candidates for piezoelectric sensors at elevated temperatures (up to 400°C or more). Some basic properties are listed in Table 1-1 for selected Bismuth Titanate compounds. The Curie temperature ranges from 310°C up to 940°C and many of them are ferroelectric above 500°C , which allows their use up to 400°C before losing too much polarization. The piezoelectric coefficients are quite small (around 15 pC/N) compared to other materials (e.g. 200 pC/N for $\text{PbZr}_{0.52}\text{Ti}_{0.48}\text{O}_3$ [9]). Thus, Bismuth Titanate are not suitable for simple actuators, they would require amplification systems such as RAINBOW or CYMBAL design. The dielectric constants are small (around 200 at room temperature). It was shown by Reznichenko [10] that the Curie temperature (T_c) for the Aurivillius compounds $\text{A}_{m-n-1}\text{Bi}_n\text{B}_m\text{O}_{3m+3}$ for a given B cation increases in the order Ba, Sr, Pb, Ca, Bi, but it decreases with the ionic radius of the A cation (general trend) and the number of layers (m).

Table 1-1: properties of some Bismuth Titanates at room temperature.

Compound	Ionic radius of A [Å]	Curie Temperature [°C]	Piezoelectric Coefficient [pC/N]	Dielectric Constant (100 kHz)
$\text{Bi}_3\text{TiNbO}_9$	1.37	940	5	100 (500kHz)
$\text{SrBi}_2\text{Nb}_2\text{O}_9$	1.44	440	10	190
$\text{Bi}_4\text{Ti}_3\text{O}_{12}\text{c}$	1.37	675	20	180
$\text{Na}_{0.5}\text{Bi}_{4.5}\text{Ti}_4\text{O}_{15}$	1.38	655	10	200
$\text{K}_{0.5}\text{Bi}_{4.5}\text{Ti}_4\text{O}_{15}$	1.42	550	10	140
$\text{BaBi}_4\text{Ti}_4\text{O}_{15}$	1.45	395	12	150
$\text{SrBi}_4\text{Ti}_4\text{O}_{15}$	1.39	530	15	190
$\text{PbBi}_4\text{Ti}_4\text{O}_{15}$	1.48	570	23	220
$\text{CaBi}_4\text{Ti}_4\text{O}_{15}$	1.37	787	14	170 (10 kHz)
$\text{Sr}_2\text{Bi}_4\text{Ti}_5\text{O}_{18}$	1.39	310	25	230

According to Table 1-1, $\text{Bi}_3\text{TiNbO}_9$ would be suitable for very high temperature piezoelectric applications, however its sensitivity is quite low. $\text{Bi}_4\text{Ti}_3\text{O}_{12}$ has also a quite elevated ferroelectric phase transition with a higher sensitivity, but due to elevated electrical conductivity [11], it should be doped in order to be used. $\text{SrBi}_4\text{Ti}_4\text{O}_{15}$ is ferroelectric only up to 530°C and its piezoelectric sensitivity is slightly smaller compared to $\text{Bi}_4\text{Ti}_3\text{O}_{12}$. However, its room temperature piezoelectric properties are very interesting, since as reported by Damjanovic [12] this material exhibits a linear piezoelectric behavior under low field conditions. In addition, its electrical conductivity is smaller than $\text{Bi}_4\text{Ti}_3\text{O}_{12}$'s value, what facilitates its initial poling and use under dynamic field conditions. Therefore, $\text{SrBi}_4\text{Ti}_4\text{O}_{15}$, written as SrBIT in this work, was

selected for a detailed analysis of its conductivity and piezoelectricity under severe conditions (low frequency, high temperature, low oxygen partial pressure).

1.3 SELECTED MATERIALS PROPERTIES

1.3.1 Crystallographic structure

In the early work of Aurivillius [13-15], the crystallographic structure of the mixed Bismuth oxide have been described. Their formula can be written: $\text{Me}_2\text{O}_2(\text{Me}'_{m-1}\text{R}_m\text{O}_{3m+1})$ with the metallic cations Me and Me' (Bi, Ca, Sr, Ba) and R (Ti, Nb, Ta). It consists of m perovskite units $(\text{Me}'_{m-1}\text{R}_m\text{O}_{3m+1})^{2-}$ separated by an oxide layer $(\text{Bi}_2\text{O}_2)^{2+}$. Subbarao [16] proposed that only Bi^{3+} can enter the oxide layer. Thus the formula should be written as: $\text{Bi}_2\text{O}_2(\text{Me}_{m-1}\text{R}_m\text{O}_{3m+1})$. In the perovskite unit the coordination number of the Me cations is 12 (cubo-octahedral site) and 6 in the case of the R cations (octahedral sites). The coordination of the Bi^{3+} cations in the Bi oxide layer is only 4. Newnham [17] concluded that only Bi^{3+} or Pb^{2+} ions can enter the asymmetrical (pyramidal coordination) oxide layer site due to their lone-pair of electrons (inducing covalent oriented bond). Actually even Pb^{2+} does not enter the Bismuth oxide layer [17]. The tolerance factor for the perovskite units $(\text{Me}_{m-1}\text{R}_m\text{O}_{3m+1})$ as determined by Subbarao [16] in the case of $m=4$ should be comprised between 0.85 and 0.89, which corresponds to cationic radius for R site of 0.63 to 0.72 in the case of $\text{Me}=\text{Bi}^{3+}$. Armstrong [18] indicated for $\text{Bi}_4\text{Ti}_3\text{O}_{12}$ radius limits for cation substitutions in the perovskite units: 1.02 Å to 1.3 Å for Bi^{3+} and 0.58 Å to 0.65 Å for Ti^{4+} .

SrBIT consists of four pseudo-perovskite units $(\text{SrBi}_2\text{Ti}_4\text{O}_{13})^{2-}$ separated by Bismuth oxide layers $(\text{Bi}_2\text{O}_2)^{2+}$. As the exact structure of $\text{SrBi}_4\text{Ti}_4\text{O}_{15}$ (positions of ions) is unknown, the paraelectric structure of $\text{BaBi}_4\text{Ti}_4\text{O}_{15}$ (written as BaBIT) is presented in Figure 1-1. In Figure 1-1 a, b, and c axis are defined as used throughout this work. The largest crystallographic axis is called c axis, while it is not the polar direction [19]. In Figure 1-1, the “ab plane” direction, which represents all directions contained within the (001) plane is easily identified.

The high temperature space group of SrBIT, BaBIT and other Aurivillius phases called prototype phase is $I4/mmm$ (tetragonal system), while the room temperature space group of Aurivillius phases with even number of perovskite units is $A2_1am$ (orthorhombic system) [19,20]. According to Reaney, Newnham, Rae and Dorrian [17,21-23] there are two kinds of octahedra tilts in Aurivillius phases with more than one perovskite layer. The first one around c-axis is anti-phase and leads to cell doubling in the ab plane and the second one is in-phase and occurs around the polar axis, denoted as the a axis. There is also a polar distortion dominated by displacement of cations. The polarization vector lies in the ab plane.

Reaney [21,24] observed the persistence of the diffraction pattern associated with the anti-phase tilt around the c-axis above the ferroelectric phase transition. The author interpreted this as a non-ferroelectric transition between a paraelectric orthorhombic phase and the tetragonal prototype one. This implies that on cooling, ferroelastic domains are created prior to ferroelectric ones. Thus, 180° ferroelectric domains are formed within pre-existing ferroelastic domains [24].

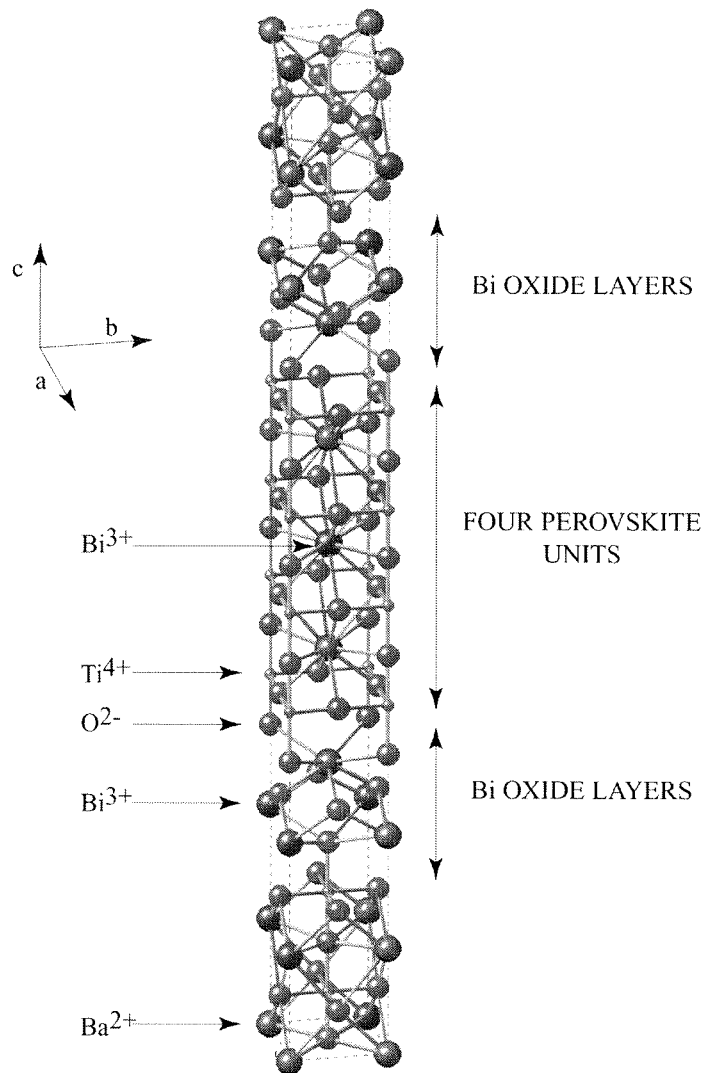


Figure 1-1: crystal structure of $\text{BaBi}_4\text{Ti}_4\text{O}_{15}$ high temperature tetragonal phase.

As shown in Chapter 2, the microstructure of SrBIT is made of plate-like grains (1-5 μm large and 200 nm thick), for these crystallites the smallest dimension corresponds to the crystallographic c -axis. Using hot forging (see chapter 2), it was possible to align respective c -axis of most of the grains within the microstructure. This technique produced c and ab textured ceramics, whose different properties reflect the anisotropy of the crystallographic cell.

1.3.2 DC and AC Conductivity

The AC and DC electrical conductivity of Bismuth Titanates have been studied in Shulman's thesis [Shulman, 1995 #182] for $\text{Bi}_4\text{Ti}_3\text{O}_{12}$, by James' group for $\text{SrBi}_2\text{Ta}_2\text{O}_9$, $\text{SrBi}_4\text{Ti}_4\text{O}_{15}$ and $\text{SrBi}_5\text{FeTi}_4\text{O}_{18}$ [25-29] and several other authors as Huanosta for $\text{Bi}_4\text{Ti}_3\text{O}_{12}$ [30], Kim for

BaBi₄Ti₄O₁₅ [31] and Chen for SrBi₂Ta₂O₉ and SrBi₂Nb₂O₉ [32], Yi for PbBi₄Ti₄O₁₅ [33] and Rama Sastry for (Na_{0.5}Bi_{0.5})_{1-x}Ca_xBi₄Ti₄O₁₅ [34].

All authors reported Arrhenius behavior for the electrical conductivity and very often only a single impedance arc was observed in the complex plane. An interesting results of Shulman's thesis was that p-type conductivity of Bi₄Ti₃O₁₂ (written BIT) could be completely compensated by donor doping to create n-type BIT and that piezoelectric loss was completely reduced by such doping. AC and DC conductivity measurements by James [25] on SrBIT were only used as a comparison basis for both our DC and AC measurements results. The most interesting work was produced by Chen [32] with SrBi₂Ta₂O₉ ceramics, the author observed three different, well-defined impedance arcs above 575°C. This experimental result was actually a basis for the three components equivalent circuit proposed in Chapter 3 to simulate the electrical impedance of SrBIT.

However, according to our knowledge, no publications related to the influence of grain size or oxygen partial pressure on the impedance of Aurivillius phases are known. In addition, none of the above given papers report separate temperature dependence of grain and grain boundary conductivities.

1.3.3 Conductivity at Low Oxygen Partial Pressure

In order to investigate point defects influence on the properties (dielectric or piezoelectric) of a ceramic, the dependence of the conductivity towards the oxygen partial pressure was investigated. Extensive work was made on BaTiO₃ [35-39] in the early 80's which was used as reference in the present work. Measurement of Bismuth Titanate conductivity as a function of partial pressure was recently published in the case of SrBi₂Nb₂O₉ [40]. In that case, there is a large pO₂ independent region under 10⁻⁵ atm a large and fast raise of conductivity around 10⁻¹⁰ atm.

1.3.4 Piezoelectricity

Piezoelectric properties of SrBIT have been already investigated by Damjanovic [12] as a function of applied elastic AC field and frequency. The author reported a perfectly linear piezoelectric behavior. According to Damjanovic, the piezoelectric coefficient of SrBIT has no dependence towards frequency and AC field up to 200°C and below 12 MPa AC field; piezoelectric loss (phase angle between force and charge) is negligible. Thus there is no charge's hysteresis during field cycling.

However our results demonstrate that there exists for undoped SrBIT a non-linear piezoelectric behavior that is temperature and field-triggered. At 150°C under 50 MPa AC stress at 1 Hz, a strong field dependence of the piezoelectric coefficient has been observed.

1.3.5 Objective of the Thesis

Bismuth Titanates are good candidates for piezoelectric applications as described above. However a detailed understanding of its conductivity is still lacking. For this reason, AC and DC electrical conductivity measurements versus temperature, frequency and oxygen partial pressure were performed. Such investigations should in addition help to understand the behavior of SrBIT in severe conditions such as required for high temperature sensor applications.

Oxygen partial pressure dependence of Bismuth Titanate has never been studied in a systematic way (except for recent publication by Palenduz [40]). In this work, the electrical conductivity of one Bismuth Titanate at low oxygen partial pressure will be discussed in details.

Deep analysis of the dielectric properties requires well-defined experimental measurement systems in unusual or severe conditions (low oxygen partial pressure, high temperature, low frequency). Development of such experimental tools was also part of this thesis.

Finally, a better understanding of the stability of the piezoelectric properties of SrBIT was a major objective of this thesis too. For this purpose, field, frequency and temperature dependencies of the longitudinal piezoelectric coefficient of random oriented and textured SrBIT were investigated.

2

MATERIAL PROCESSING

2.1 FOREWORD

Subjects of this thesis are properties of polycrystalline $\text{SrBi}_4\text{Ti}_4\text{O}_{15}$ (written as SrBIT). Properties of other forms as SrBIT single crystal [41], glass [42] and thin films [43,44] have been reported in the literature. All samples measured during this work have been processed in the EPFL Ceramics Laboratory, starting from commercial raw powders. Most of them were random oriented ceramics, i.e. without any global preferential orientation of grains. Due to intrinsic limitations, it was actually never possible to process fully dense ceramics with natural sintering, the usual relative density was about 90%. The anisotropy of SrBIT was investigated with textured samples, having certain degree of preferential orientation. These samples were prepared using hot forging (sintering under uniaxial pressure). SrBIT was doped using two different materials: MnCO_3 for acceptor doping and Nb_2O_5 for donor doping. The procedure used for SrBIT doping was precise enough to resolve 0.5 mol.% of Mn concentration.

The preparation procedure of SrBIT bulk ceramics was investigated in details in order to improve the reproducibility of the material. At first, synthesis of SrBIT powder was studied qualitatively by X-ray diffraction. These investigations demonstrated the formation of the solid solution between SrO and Bi_2O_3 and of three intermediate compounds $\text{Bi}_{12}\text{TiO}_{20}$, SrTiO_3 and $\text{Bi}_4\text{Ti}_3\text{O}_{12}$. The calcination temperatures used for SrBIT preparation were significantly higher than reported in the literature by Gelfuso [45] for example. However, no loss of reactivity during sintering was noticed. Powders processed with our method were always single phase. Thus, sintering was not reactive, since the desired crystalline phase was already formed after the calcination step. Finding the right sintering conditions in the desired furnace was always needed, due to unusual sintering mechanism. This required a deep analysis of the densification process, using dilatometry, scanning electron microscope and X-ray diffraction. It was found that both agglomerate re-arrangement and liquid phase-assisted sintering occurred during SrBIT densification.

2.2 INTRODUCTION

This chapter describes the results obtained during the optimization of the processing route of SrBIT, realized to improve its reproducibility. The descriptions of the different mechanisms are only qualitative, no data concerning for example kinetic, diffusion or surface energy will be provided. SrBIT is actually not suitable for a conventional study of sintering, since for example most of the firing models were developed for spherical grains while SrBIT grains are plate-like. As shown in Figure 2-11, there is almost no densification up to 1200°C. As a consequence, the interesting region for any study concerning sintering is located within a very narrow temperature (about 10°C) just below the decomposition temperature.

Basic SrBIT piezoelectric properties have been known for many years, however no commercial material is available yet. Therefore a complete processing route for SrBIT had to be developed. It is based on conventional mixed oxide techniques, starting from raw powders of SrCO₃, Bi₂O₃ and TiO₂, with solid-state reactions. This procedure and the involved chemical reactions will be described in sections 2.4 and 2.5.

Cold uniaxial pressing was used to produce cylindrical samples; no polymer binder was ever added although green bodies were quite fragile, end capping was often noticed above 60 MPa. Natural sintering at elevated temperature for material consolidation followed pressing. In section 2.6, scanning electron microscopy and dilatometry will demonstrate that a first step of SrBIT densification is the re-arrangement of agglomerates. This step is followed by liquid phase-assisted final densification about 10°C below decomposition temperature. The presence of some liquid phase will be demonstrated with dilatometry experiments in cycling mode. Finally, using scanning electron microscopy observations, grain coarsening of undoped SrBIT will be presented.

Grain oriented ceramics have been prepared by hot forging (uniaxial without die). The degree of texture was quantitatively characterized using indexes calculated from X-ray diffraction.

2.3 EXPERIMENTAL METHODS

X-ray powder diffraction was used to identify the crystalline phases, measure the cell parameters and characterize the texture quality. The diffractometer used was a *SIEMENS KRISTALLOFLEX 805* in the θ - 2θ mode with a CuK_α beam. Standard measurements were performed between $2\theta=5^\circ$ and 65° , with an angular step of 0.04° and an integration time of 4 seconds. Because of the low symmetry of the room temperature crystal lattice (orthorhombic) of SrBIT and the large size of the c axis (41 \AA), there are many diffraction peaks in the observed range. There are also many reflection superpositions due to the insufficient resolution of the system (especially due to the wavelength of the beam); it was extremely difficult or impossible to index the full spectrum. Only the first 17 diffraction peaks could be clearly indexed, thus for lattice parameter determination, the X-ray diffraction spectrum was restricted to those 17 peaks. The cell parameters were calculated with a least square fitting of the measured d_{hkl} with the appropriate spectrum indexing. X-ray diffraction was used also to identify crystalline phases with the aid of the International Crystallographic Tables [46]. SrBIT powder was briefly characterized using two methods: particle size distribution of the powders was measured with a *HORIBA Particle Size Analyzer*. The densification mechanisms were studied with a *SETARAM* dilatometer in a vertical configuration. All dilatometer measurements were done in air with cylindrical samples (about 8 mm in diameter and 5-10 mm in height). In order to avoid reaction between SrBIT and Alumina measurement parts, a stack of "insulating" dense material was used. It was made of two insulating SrTiO_3 discs and two buffering SrBIT discs, Figure 2-1. SrTiO_3 does not react with Alumina but reacts little with SrBIT, however the buffer SrBIT disc was thick enough to avoid any reaction with the sample.

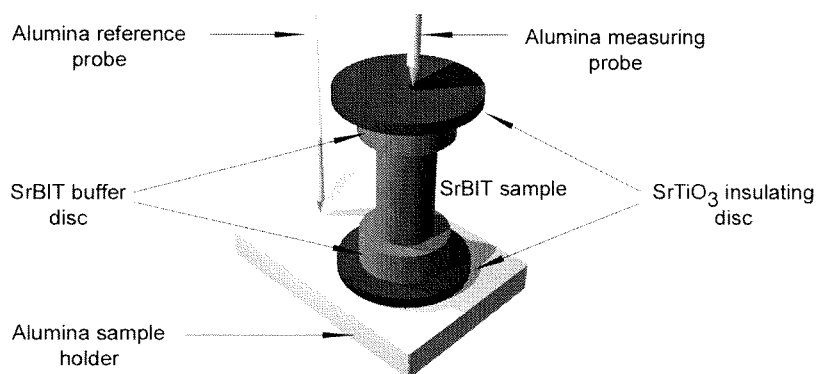


Figure 2-1: schematic view of the ceramic stack used for dilatometry. The SrBIT sample is placed between two buffering sintered SrBIT discs and two insulating SrTiO_3 discs. The measuring and reference Alumina probes are also shown.

Powders and microstructures were observed with a scanning electron microscope (SEM): *PHILIP XL-30* with a field emission gun. All the samples were gold metallized prior to SEM observations using a sputtering machine. Thermal etching revealed the microstructure of $0.25 \mu\text{m}$ diamond

polished SrBIT surface. This etching was made at 1100°C for 5 minutes in air. Over-etching was often observed in case of too elevated annealing time or temperature.

2.4 PROCESSING ROUTE

Chemical reagent grade of Bi_2O_3 , TiO_2 and SrCO_3 , Table 2-1, Figure 2-2, Figure 2-3, Figure 2-4, were mixed together in proper amount in isopropanol with ZrO_2 balls in PVC bottles in a rotary mill for 24 hours. After fast drying the slurry (to avoid segregation), the powder mixture was calcined at elevated temperature (up to 1050°C) using temperature profile of Figure 2-5 in covered Alumina crucibles. The temperature profile was determined to ensure complete SrBIT formation and complete removal of any intermediate phase (see below for a more detailed explanation of the calcination mechanisms). Up to 950°C the heating rate was $2^\circ\text{C}/\text{min}$ and then only $1^\circ\text{C}/\text{min}$. up to 1050°C with 4 hours dwelling at 950°C , 1000°C and 1050°C , Figure 2-5. It was recently proposed by Gelfuso [45] to crystallize SrBIT at 850°C for 24 hours. With a lower calcination temperature, the reactivity of the final powder should be higher and the sintering temperature decreased as proposed by the same author: 1160°C for 3 hours. However our results for these calcination and sintering profiles indicate both intermediate phases and poor densification (those results are not presented here). However, low temperature calcination could be justified if Gelfuso has used much more reactive raw powders than ours. Nevertheless, purity of the final product was not clearly demonstrated in Gelfuso's work.

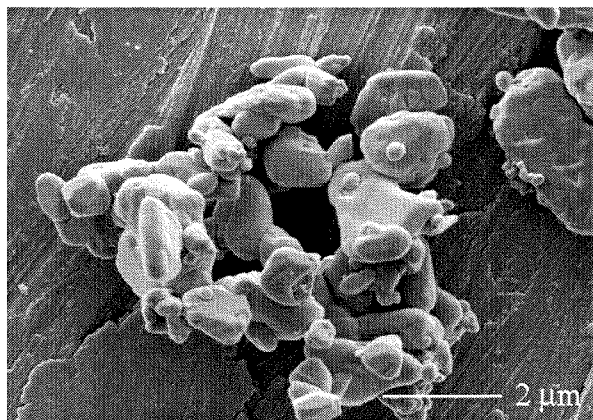


Figure 2-2: Bismuth oxide used for SrBIT preparation.

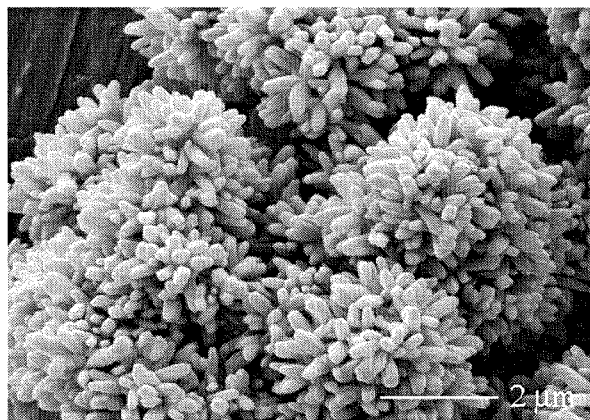


Figure 2-3: Titanium oxide used for SrBIT preparation.

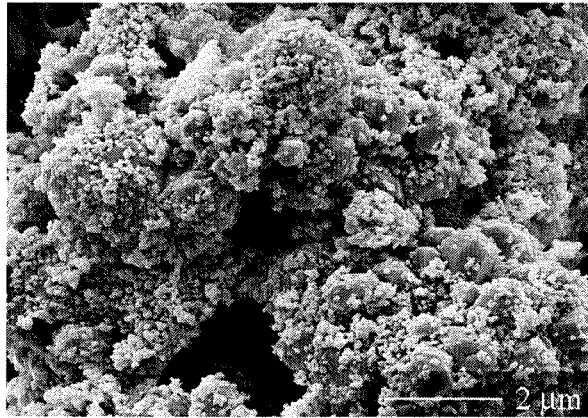


Figure 2-4: Strontium carbonate used for SrBIT preparation.

After calcination the powder was milled using monosized ZrO_2 balls in isopropanol in PVC bottles for 72 hours. Milling was actually efficient enough to break strong agglomerates, but did not modified significantly particles mean size. The milled powder was de-agglomerated by sieving. SEM observations of sintered SrBIT clearly show that SrBIT particles produced by this technique are platelets, Figure 2-7. A typical particle size distribution of SrBIT powder is shown in Figure 2-6. This distribution is quite wide, since median diameter is $2.4 \mu m$ with a standard deviation of $0.9 \mu m$. Wide distribution is usually required for better particle stacking, while narrow one ensures more uniform sintering. However, in the case of SrBIT, particles are plate-like, this means that thickness (about 100 nm) is much smaller than width (a few microns). Thus, the distribution given in Figure 2-6 is an average over thickness and width distributions. Therefore, the information given by this measurement is only indicative.

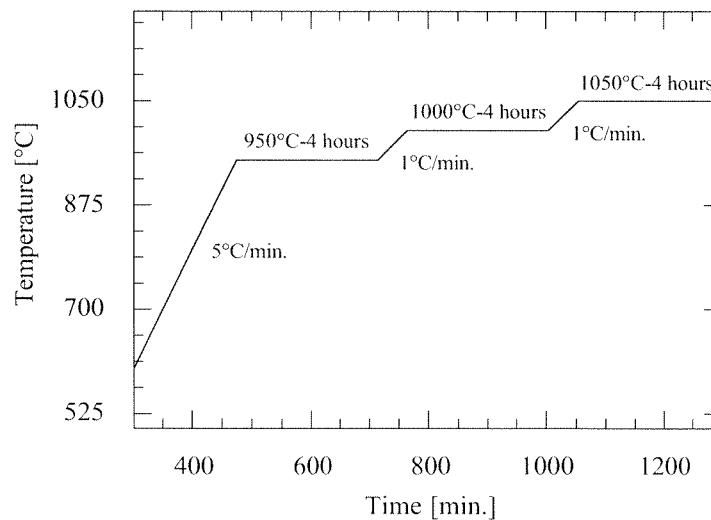


Figure 2-5: Temperature profile used for a "one step" SrBIT synthesis from Bi_2O_3 , TiO_2 and $SrCO_3$ raw powders.

Table 2-1: references of chemicals used for SrBIT preparation.

Compound	Bi ₂ O ₃	TiO ₂	SrCO ₃
Supply	Ferro 320-A	Tioxide High purity HPT-3	Johnson Matthey Specpure grade I
Known impurities	CaO 30 ppm	Cl 200 ppm	P, W 100 ppm
		S 100 ppm	Te, Zr, As 50 ppm
		Sb, Sn, Si 50 ppm	Zn, Cs, Hg 30 ppm
Crystalline phase	α -monoclinic	Rutile tetragonal	Orthorhombic
	Platelets	Agglomerates 2mm	Equiaxed
Morphology	D=2 μ m	Particles 200 nm	D=200 μ m

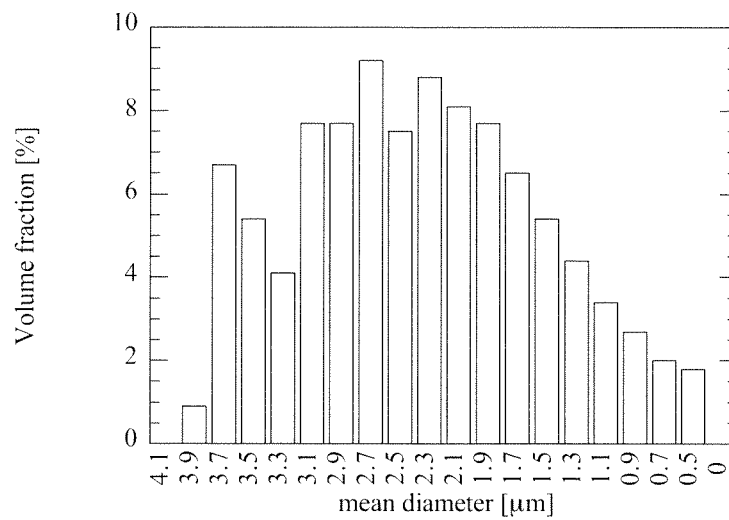


Figure 2-6: Particle size distribution for undoped SrBIT calcined in three steps (950, 1000, 1050°C, 4 hours each) and ball milled for 72 hours in isopropanol.

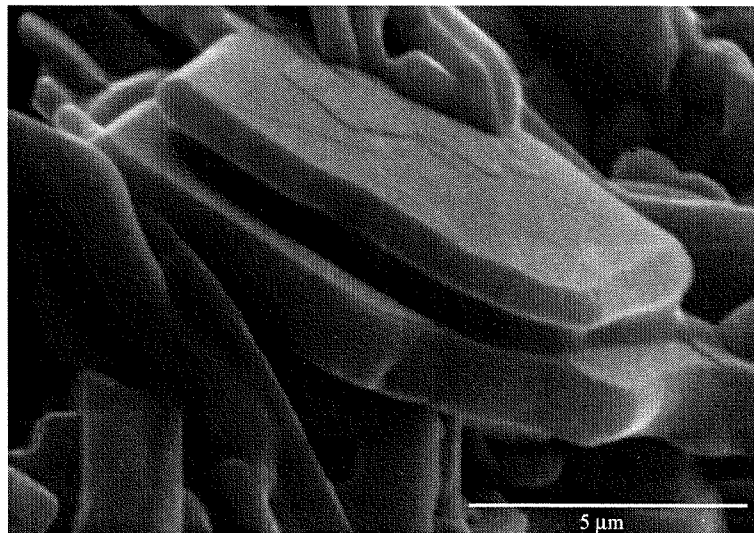


Figure 2-7: example of a typical fired microstructure for undoped SrBIT, indicating the possibility of a liquid phase.

As the general route for SrBIT preparation was given in this section, the next one will be dedicated to a more detailed investigation of phase formation during solid-state calcination. As ternary phase diagram of SrO-TiO₂-Bi₂O₃ is unknown (only properties of ternary compounds have been determined); the following analysis will be based on the three binary phase diagrams [47]. Each crystalline phase of the system was identified with X-ray diffraction.

2.5 PHASE FORMATION

In order to produce an homogeneous single phase material starting from three different raw powders, two routes can be used: either a single step calcination of the three oxides or a two steps method with a precursor powder made of a reacted mixture of SrO and Bi₂O₃. Analysis of crystalline phases in both methods indicated however formation of the same intermediate phases. Therefore only the single step method (used for all samples preparation) will be described here. In the next sections, chemical formula, crystallographic references and temperature range (stability range if available) of all possible phases in the ternary SrO-Bi₂O₃-TiO₂ systems will be given. Such long description is however required to understand the identification of the intermediate phases produced during calcination.

2.5.1 Single oxides

In the following description of encountered crystalline phases, for each of them the reference number of the associated standard X-ray diffraction file [Data, 1998 #412] will be given in parenthesis. Raw materials were Bismuth oxide in the monoclinic α -phase, Titanium oxide in the tetragonal Rutile phase and Strontium carbonate. Bismuth oxide α phase (14-6991), which is yellow transforms into the β phase (18-244) at 730°C (tetragonal) and into δ phase (16-654) at 750°C (cubic). Finally Bi₂O₃ melts at 840°C, such low melting point comes with a high volatility of Bismuth oxide at high temperature. Titanium oxide has many polymorphs: Rutile (tetragonal, 21-1276), Anatase (tetragonal) and the Brookite phase (orthorhombic). The Anatase phase is converted into Rutile above 700°C. Strontium carbonate decomposes into SrO (cubic, 6-520) and CO₂ above 800°C. At 920°C, SrO becomes hexagonal during the decomposition. However, as demonstrated in section 2.5.4, SrCO₃ reacts with Bi₂O₃ and TiO₂ prior to its decomposition into SrO.

2.5.2 Binary Oxides

In the Bi₂O₃-TiO₂ binary phase diagram, there are four different intermediate phases: Bi₂Ti₄O₁₁, Bi₄Ti₃O₁₂ (α and β phase) and Bi₈TiO₁₄. The crystallographic tables indicate additional phases: Bi₂₀TiO₃₂, Bi₁₂TiO₂₀, and Bi₂Ti₂O₇. It is interesting to note that the composition of the powder mixture for SrBIT preparation is SrO+2Bi₂O₃+4TiO₂, that is a 33 mol.% Bi₂O₃ and 66 mol.% TiO₂, which is also the composition of Bi₂Ti₂O₇.

Table 2-2: binary compounds in the $\text{Bi}_2\text{O}_3\text{-TiO}_2$ system. The compositions are given in mol.%.

Phase	Composition $\text{Bi}_2\text{O}_3\text{-TiO}_2$	Stability range	JCPDS File Number [Data, 1998 #412]
Bi_2O_3	100-0	<840°C	14-6991
$\text{Bi}_{20}\text{TiO}_{32}$	90-10		42-202
$\text{Bi}_{12}\text{TiO}_{20}$	86-14		34-97
$\text{Bi}_8\text{TiO}_{14}$	80-20	<865°C	
$\text{Bi}_4\text{Ti}_3\text{O}_{12}$	40-60	<1210°C	35-795
$\text{Bi}_2\text{Ti}_2\text{O}_7$	33-66		32-118
$\text{Bi}_2\text{Ti}_4\text{O}_{11}$	20-80	<1275°C	15-325
TiO_2	0-100	<1830°C	21-1276

The phase diagram [47] of SrO-TiO_2 system indicates four intermediate phases: Sr_2TiO_4 (α and β phases), $\text{Sr}_3\text{Ti}_2\text{O}_7$, SrTiO_3 . But the crystallographic database gives three additional compounds: $\text{Sr}_4\text{Ti}_3\text{O}_{10}$, $\text{SrTi}_{12}\text{O}_{19}$, $\text{SrTi}_{21}\text{O}_{38}$. The initial SrO+TiO_2 mixture for SrBIT preparation is 20% SrO and 80% TiO_2 , but there exists no compound with this composition.

Table 2-3: binary compounds in the SrO-TiO_2 system. The compositions are given in mol.%.

Phase	Composition SrO-TiO_2	Stability range	JCPDS File Number [46]
SrO	100-0		6-520
Sr_2TiO_4	66-33	<1860°C (β phase)	39-1471
$\text{Sr}_3\text{Ti}_2\text{O}_7$	60-40	<1640°C	11-663
$\text{Sr}_4\text{Ti}_3\text{O}_{10}$	57-43		22-1444
SrTiO_3	50-50	<2040°C	40-1500
$\text{SrTi}_{12}\text{O}_{19}$	7-93		22-1443
$\text{SrTi}_{21}\text{O}_{38}$	5-95		22-1121
TiO_2	0-100	<1830°C	21-1276

The most interesting feature in the $\text{SrO-Bi}_2\text{O}_3$ binary phase diagram is its solid solution which extends up to 50%. The intermediate phases as given by the phase diagram are: $\text{Sr}_3\text{Bi}_2\text{O}_6$, $\text{Sr}_2\text{Bi}_2\text{O}_5$, SrBi_2O_4 and two solid solutions (α and β). The crystallographic tables indicate an additional compound: $\text{Sr}_3\text{Bi}_4\text{O}_9$. There are also examples of the solid solutions: $\text{Sr}_{0.90}\text{Bi}_{1.10}\text{O}_{2.55}$, $\text{Sr}_{2.25}\text{Bi}_{6.75}\text{O}_{12.38}$, $\text{Sr}_{0.16}\text{Bi}_{3.84}\text{O}_{5.92}$. For the equivalent binary $\text{SrO-Bi}_2\text{O}_3$ mixture, the composition is 33 mol.% SrO and 66 mol.% Bi_2O_3 .

Table 2-4: binary compounds in the SrO-Bi₂O₃ system. The compositions are given in mol.%.

Phase	Composition	Stability range	JCPDS File Number
	SrO-Bi ₂ O ₃		[46]
SrO	100-0		6-520
Sr ₃ Bi ₂ O ₆	75-25	<1000°C	46-497
Sr ₂ Bi ₂ O ₅	66-33	<940°C	39-1472
SrBi ₂ O ₄	50-50	<800°C	39-1424
Sr _{0.90} Bi _{1.10} O _{2.55}	62-38		31-1341
Sr ₃ Bi ₄ O ₉	60-40		42-1458
Sr _{2.25} Bi _{6.75} O _{12.38}	40-60		45-609
Sr _{0.16} Bi _{3.84} O _{5.92}	7-93		45-608
Bi ₂ O ₃	0-100	<840°C	14-6991

To sum up, from the binary phase diagrams, one can expect the formation of the following phases: Bi₂Ti₂O₇ and its neighbors Bi₂Ti₄O₁₁ and Bi₄Ti₃O₁₂, SrTiO₃ and some solid solution between SrO and Bi₂O₃. If any SrO-Bi₂O₃ solid solution of unknown composition is created first, then it shifts Bi₂O₃-TiO₂ and SrO-TiO₂ binary compounds to TiO₂ richer phases such as Bi₂Ti₄O₁₁, Sr₃Ti₂O₇ and SrTiO₃.

2.5.3 Ternary Oxides

Ternary compounds of SrO-Bi₂O₃-TiO₂ system are SrBi₄Ti₄O₁₅, Sr₂Bi₄Ti₅O₁₈, SrBi₈Ti₇O₂₇ (mixture of SrBi₄Ti₄O₁₅ and Bi₄Ti₃O₁₂).

Table 2-5: ternary compounds in the SrO-Bi₂O₃-TiO₂ system. The compositions are given in mol.%.

Phase	Composition	Stability range	JCPDS File Number
	SrO-Bi ₂ O ₃ -TiO ₂		[46]
SrBi ₈ Ti ₇ O ₂₇	8-33-59		31-1342
SrBi ₄ Ti ₄ O ₁₅	14-28-58	<1290°C	43-973
Sr ₂ Bi ₄ Ti ₅ O ₁₈	22-22-56		14-276

All the phases described in the preceding sections were tracked in the X-ray spectrums collected at different calcination temperature, as presented in the next paragraph. Such analysis allowed the determination of the formation path of SrBIT with solid-state reaction.

2.5.4 Identification of SrBIT Phase Formation

Thermal expansion measurement of a stoichiometric $\text{SrCO}_3 + \text{Bi}_2\text{O}_3 + \text{TiO}_2$ powder mixture, Figure 2-8, indicates two major phase transformations. The first one around 715°C and the second one around 830°C . In order to identify these transformations, X-ray diffraction analysis was realized with powder samples calcined at 640°C , 760°C , 950°C and 1050°C without dwelling. Spectrums of this analysis are given in Figure 2-9. From this analysis, four intermediate phases have been identified: $\text{Bi}_4\text{Ti}_3\text{O}_{12}$, $\text{Bi}_{12}\text{TiO}_{20}$, $(\text{SrO})_{0.40}(\text{Bi}_2\text{O}_3)_{0.60}$ and SrTiO_3 .

In the lower temperature range (up to 640°C), SrO and Bi_2O_3 form a solid solution that could be written $(\text{SrO})_{0.40}(\text{Bi}_2\text{O}_3)_{0.60}$. Meanwhile Bi_2O_3 and TiO_2 form $\text{Bi}_{12}\text{TiO}_{20}$, which is a Bi_2O_3 rich phase. In this temperature range, there remains some non-reacted TiO_2 . Above 760°C , the solid solution is reduced, by reaction with TiO_2 as some diffraction peaks of SrTiO_3 and BIT appears. Thus, the first transformation that is observed in Figure 2-8 can be identified with the partial conversion of the solid solution into BIT and SrTiO_3 . The early-formed $\text{Bi}_{12}\text{TiO}_{20}$ incorporates some TiO_2 and is transformed into BIT. Above 950°C , SrTiO_3 and BIT are converted into SrBIT. The same way, the remaining solid solution reacts with BIT to form SrBIT.

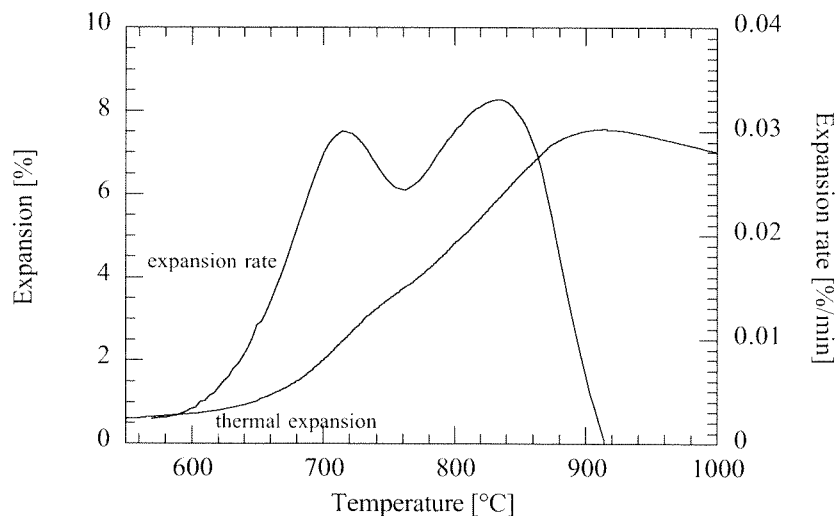


Figure 2-8: expansion and expansion rate versus temperature for $\text{SrCO}_3 + 2\text{Bi}_2\text{O}_3 + 4\text{TiO}_2$ powder mixture.

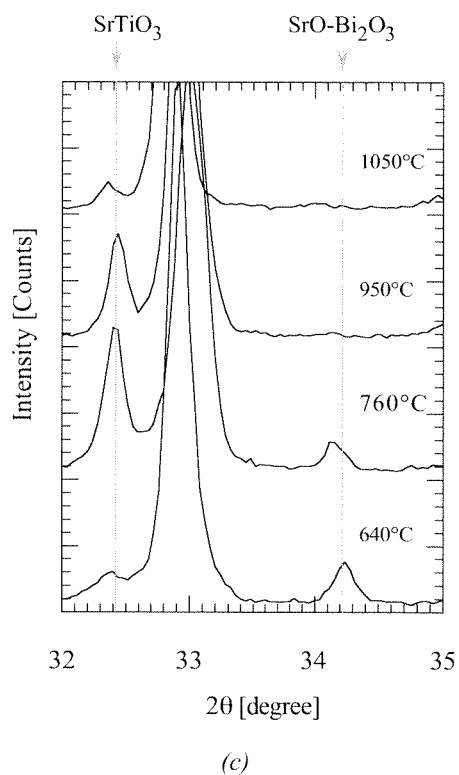
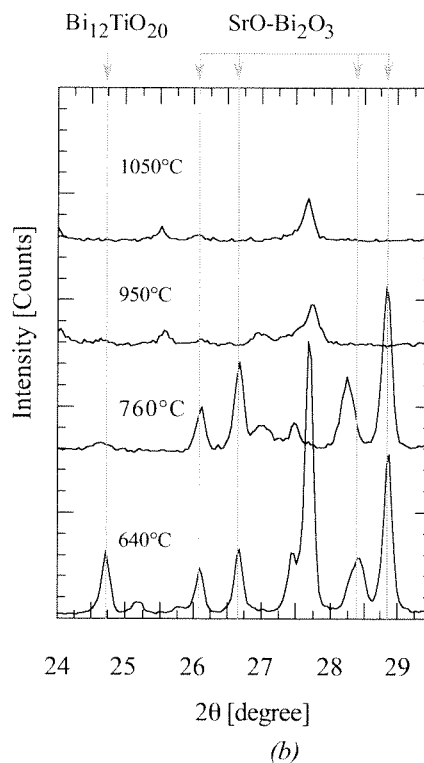
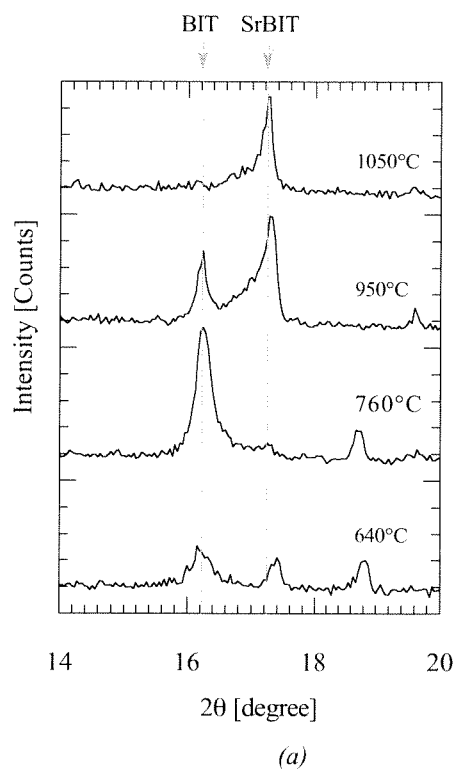


Figure 2-9: x-ray diffraction spectrums after calcination of raw materials at elevated temperature: (a) 14-20° region showing an intermediate $\text{Bi}_4\text{Ti}_3\text{O}_{12}$ (BIT phase ((060) line) replaced by the final $\text{SrBi}_4\text{Ti}_4\text{O}_{15}$ (SrBIT) composition ((008) line). (b) 24-29.5° region indicating some solid solution between SrO and Bi_2O_3 ((101), (012) and (104) lines for a $(\text{SrO})_{0.40}$ - $(\text{Bi}_2\text{O}_3)_{0.60}$ solution) that disappears above 800°C and some cubic $\text{Bi}_{12}\text{TiO}_{20}$ intermediate phase ((220) line as indicated and also (310) at 27.7° as for (117) SrBIT line). (c) 33-35° region showing the intermediate cubic SrTiO_3 phase ((110) line) and the solid solution between SrO and Bi_2O_3 ((107) line). Large diffraction peaks close to 33° are not identified for clarity.

Since the standard calcination of SrBIT was realized at 1050°C with a slow temperature profile, Figure 2-5, all intermediate phases were converted into SrBIT. It follows that sintering was non-reactive.

Sintering of SrBIT is described in the next section. Using dilatometry and electronic microscopy, it will be demonstrated that there are two steps during densification: agglomerate re-arrangement and liquid phase-assisted sintering. It was actually not demonstrated whether the latter is actually pure viscous sintering process or if it includes significant mass transport by diffusion.

2.6 SINTERING

2.6.1 General Process Description

Uniaxial pressing was used to shape the material into green bodies of 10 mm diameter and about 2 mm thick discs of about 55% relative density. No binders were used to improve mechanical strength of the green body so the applied force was only 3kN. Above this value end capping or cracks were systematically present. The green bodies were fired at 1250°C in a tube furnace in air (not flowing) for 12 minutes, Figure 2-10. No compensating powder was used to saturate the atmosphere. However, 1 wt.% Bi_2O_3 excess was added to the powder mixture before calcination to compensate Bi_2O_3 loss during the whole process.

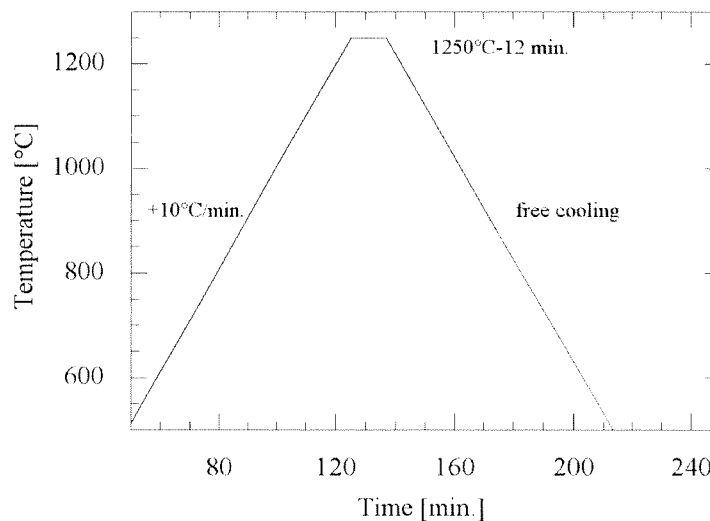


Figure 2-10: Temperature profile used for green bodies sintering. The cooling part of the profile was not controlled (free cooling).

In order to understand the densification mechanisms of SrBIT, a detailed analysis by dilatometry was necessary.

2.6.2 Dilatometry Experiments

Typical densification of SrBIT during heating (shrinkage and shrinkage rate) is presented in Figure 2-11. From the expansion rate, two densification stages can clearly be separated: the first one around 1258°C and the other one near 1275°C.

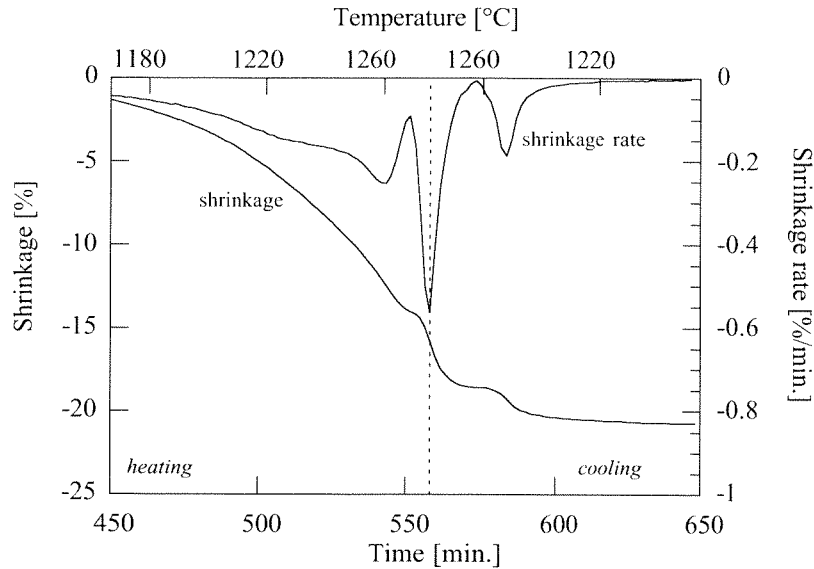


Figure 2-11: shrinkage and shrinkage rate for undoped SrBIT at 5°C/min.

Since the densification rate measured near 1275°C was quite elevated, formation of a liquid phase was suspected. In order to demonstrate it, a second heating/cooling cycle was applied to a sintered sample. The result of this cycling is presented in Figure 2-12. According to this figure, there is a large expansion of about 2% at 1263°C, which is eliminated on cooling. No solid-state transformation would produce such large strain without breaking the sample; it is very likely caused by the formation of a liquid phase. Such liquid phase could originate from congruent or incongruent melting of SrBIT. The presence of a significant amount of $\text{Sr}_2\text{Bi}_4\text{Ti}_5\text{O}_{18}$ in some over-sintered samples as shown in Figure 2-13 would indicate an incongruent melting of SrBIT. In the case of incongruent melting, a solid phase is actually converted isothermally into another solid phase and into liquid. On cooling, the new solid phase is not converted back into the original solid. The shoulder seen on the left of the diffraction peak of SrBIT in Figure 2-13 is a good indication of the actual formation of $\text{Sr}_2\text{Bi}_4\text{Ti}_5\text{O}_{18}$ and may be a proof for the incongruent melting of SrBIT.

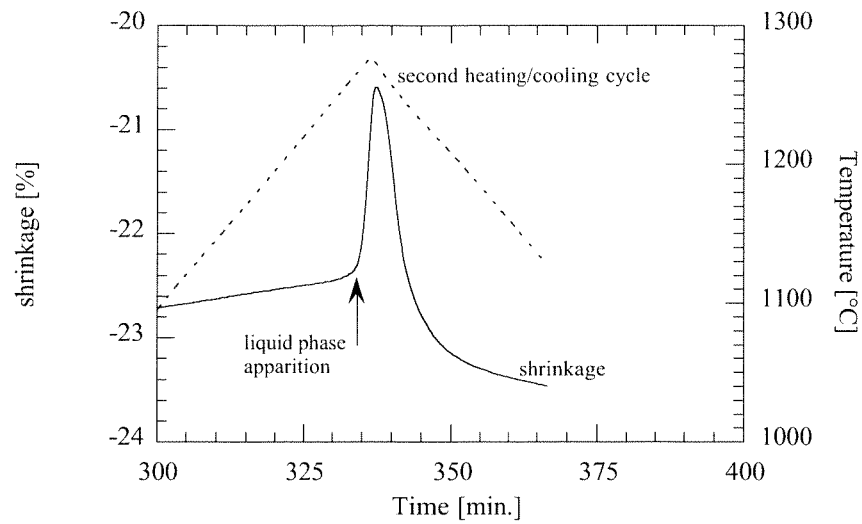


Figure 2-12: shrinkage and temperature versus time during the second heating/cooling cycle of dilatometer experiment.

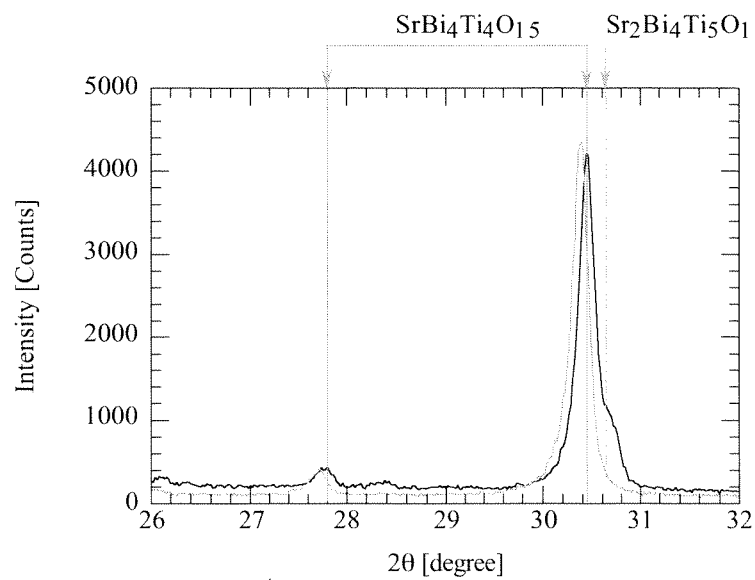


Figure 2-13: X-ray diffraction spectrum of SrBIT sintered at the optimized temperature (gray line) and 10°C above (black line). The shoulder on the left of $\text{SrBi}_4\text{Ti}_4\text{O}_{15}$ diffraction peak is a good indication of $\text{Sr}_2\text{Bi}_4\text{Ti}_5\text{O}_{18}$ formation and incongruent melting of $\text{SrBi}_4\text{Ti}_4\text{O}_{15}$.

2.6.3 Fracture Surface by Scanning Electron Microscope

The densification mechanisms given by Figure 2-11 were studied by fracture surface observation using scanning electron microscope. For this purpose, SrBIT was sintered at three different temperatures: 1230°C (below the first stage), 1270°C (at the beginning of the second stage) and 1285°C (near the final densification stage). The results are presented in Figure 2-14, Figure 2-15 and Figure 2-16.

The microstructure of Figure 2-14, indicates no densification of SrBIT up to 1230°C, the structure remains completely open. Particles are obviously not randomly distributed and form agglomerates, as indicated by an arrow in Figure 2-14. These agglomerates are a few microns large. Such agglomerates are very significant for sintering, since they could induce inhomogeneous densification of SrBIT. According to Figure 2-14 prior to any diffusion-controlled sintering, residual porosity would be reduced by agglomerate re-arrangement.

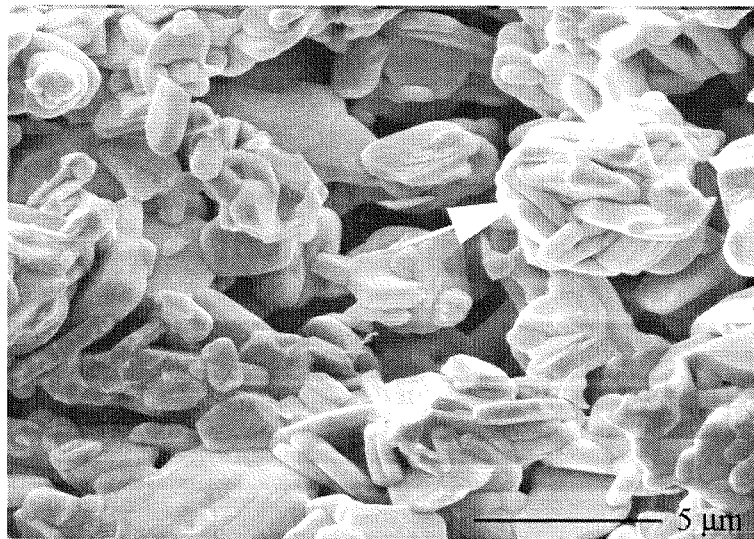


Figure 2-14: fracture surface by SEM for SrBIT sintered at 1230°C, 4 minutes with a heating rate of 5°C/min.

Agglomerates re-arrangement is seen in Figure 2-15 for SrBIT sintered at 1270°C; it is above the first densification peak of Figure 2-11. This fracture surface shows only inter-grain fracture, revealing still weak grain boundaries. At this stage, re-arrangement strongly reduces the content of open porosity, albeit the mean size of the residual pores is still quite large. Such pores are due to the geometry of the particles as indicated by an arrow in Figure 2-15. Stacking of plate-like grains creates necessarily large void in-between.

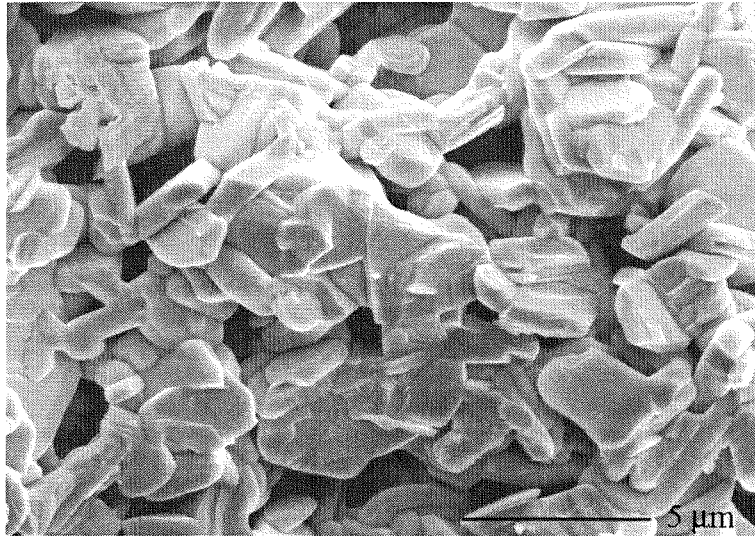


Figure 2-15: fracture surface by SEM for SrBIT sintered at 1270°C, 4 minutes with a heating rate of 5°C/min.

Final stage of sintering, which is liquid phase-assisted modifies the microstructure much more than the previous step, as seen in Figure 2-16. Thus above 1285°C, fracture is intra-grain, as grains become much more bounded together. Nevertheless, even at this stage there remain large pores.

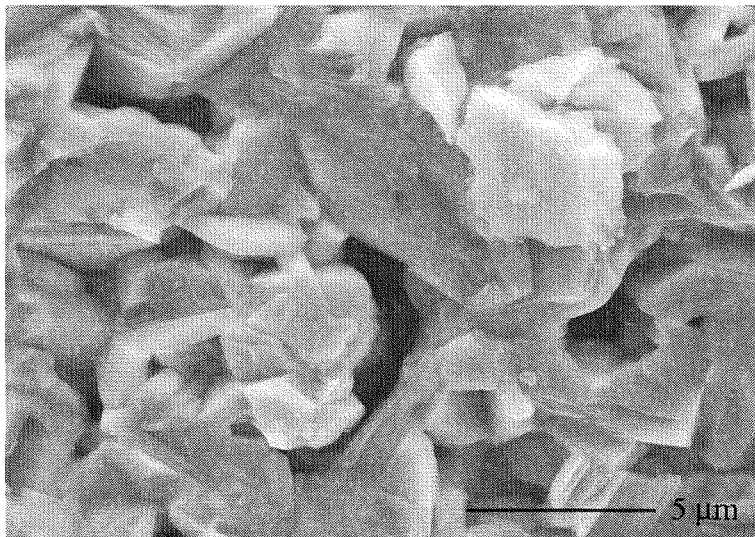


Figure 2-16: fracture surface by SEM for SrBIT sintered at 1285°C, 4 minutes with a heating rate of 5°C/min.

2.6.4 Porosity Quantification

Using the conventional Archimedes method for open and closed porosity measurements, SrBIT sintering was optimized in the tube furnace dedicated to sample preparation. Temperatures given in this section are much lower than sintering temperatures found by dilatometer measurements. This could be explained by a difference in temperature measurement proximity in both furnaces. But, differences in sintering temperatures could be caused by different degrees of atmosphere

saturation in the furnaces too. Compared to dilatometer experiments of section 2.6.2, temperatures given in Figure 2-17 are probably 30°C lower.

According to Figure 2-17, open porosity is strongly reduced at early stages. Meanwhile, closed porosity increases as open porosity collapses. The optimum for the best relative density is probably at 1250°C. At 1260°C, closed porosity increases again, which could be explained by a large amount of liquid phase formation and freezing.

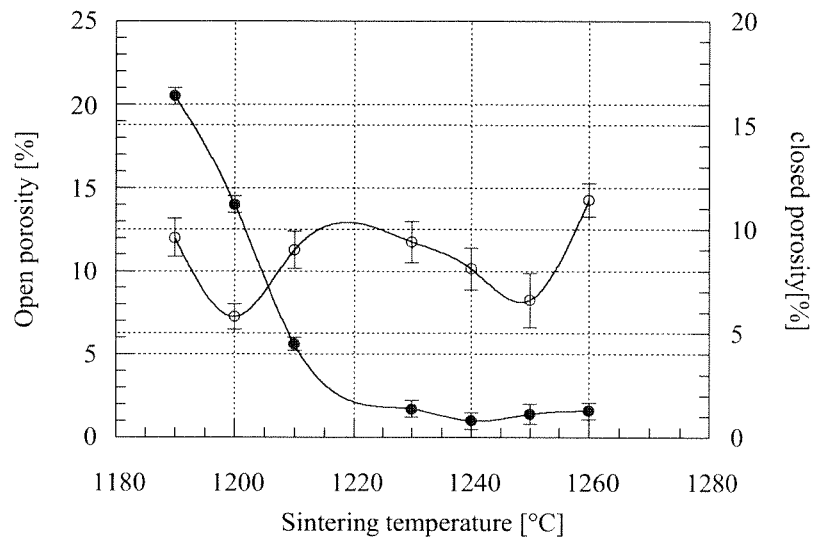


Figure 2-17: open (filled circles) and closed (open circles) porosities versus sintering temperature for one sintering in air of undoped SrBIT.

Complete removal of porosity by natural sintering seems not possible, mainly because of the particle shape. The highest relative density achieved with external pressure was 92%. As described below, hot forging was the only way to get a higher relative density. However, this method creates an anisotropic material, which is not always desired.

2.6.5 Microstructure of undoped SrBIT

Revealing SrBIT microstructure requires a careful preparation of the surface. Samples should be diamond polished down to 0.25 μm and the prepared surface has to be cleaned in an ultra-sonic bath. Thermal etching should actually be optimized for every composition and powder batch, as SrBIT is extremely sensitive to over-etching. Undoped SrBIT fired at 1250°C as presented in Figure 2-18, was etched at 1100°C for 5 minutes. The sample was put in the pre-heated furnace and quenched in air. Quenching produced some intragrain cracks but did not break the whole material.

Microstructures were observed using scanning electron microscope (Philips XL-30 with Field Emission Gun), typically at a magnification of five thousands. Prepared surfaces were gold metallized using a sputtering machine to reduce electrostatic charging. A typical microstructure for undoped SrBIT in the optimized sintering conditions is given in Figure 2-18.

It is clear from Figure 2-18 that SrBIT grains are not isotropic, but rather plate-like. Thus, it is not possible to give a single grain size for such microstructure. Grains should be described with their width and thickness. A typical width would be 1-5 μm and a typical thickness would be 200 nm. As already mentioned, plate-like grains create hard-to-remove porosity.

Looking at Figure 2-18, it is also clear that grains are not really randomly distributed. There are actually some grains colonies, oriented along a common direction. Arrows in Figure 2-18 give some of the preferential orientations that define colonies. These three directions are actually closed to each other. It would however be quite risky to conclude that this common direction corresponds to the pressing direction. No relation between the uniaxial force used for green body's preparation and the internal texture was studied. However, in order to reduce this texture, uniaxial pressing could be replaced by isostatic pressing.

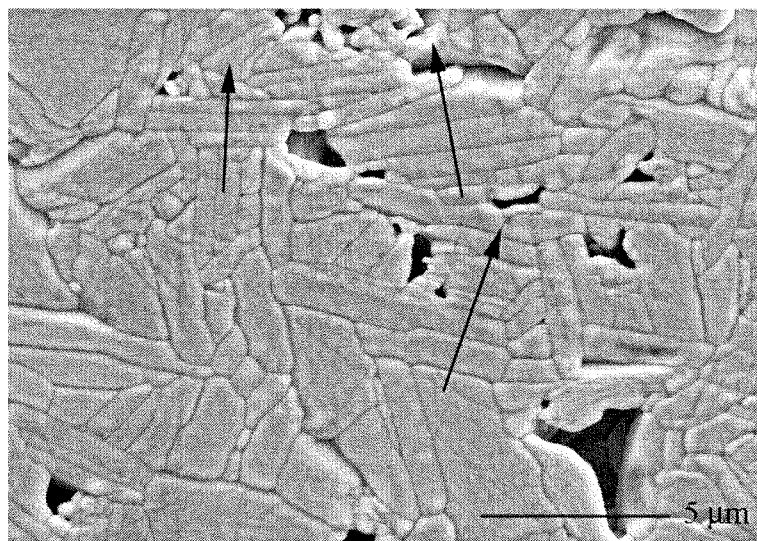


Figure 2-18: microstructure of undoped SrBIT fired at 1250°C for 12 minutes. Arrows indicate localized preferential orientations defining grains colonies.

Long time sintering (24 hours) does not instigate any grain coarsening as long as sintering temperature is kept well below a critical value. Microstructure corresponding to long time sintering is not presented here, as it is identical to the one given in Figure 2-18. If sintering temperature is too high, but below ceramic decomposition temperature, pronounced grain coarsening occurs and leads to microstructure such as shown in Figure 2-19.

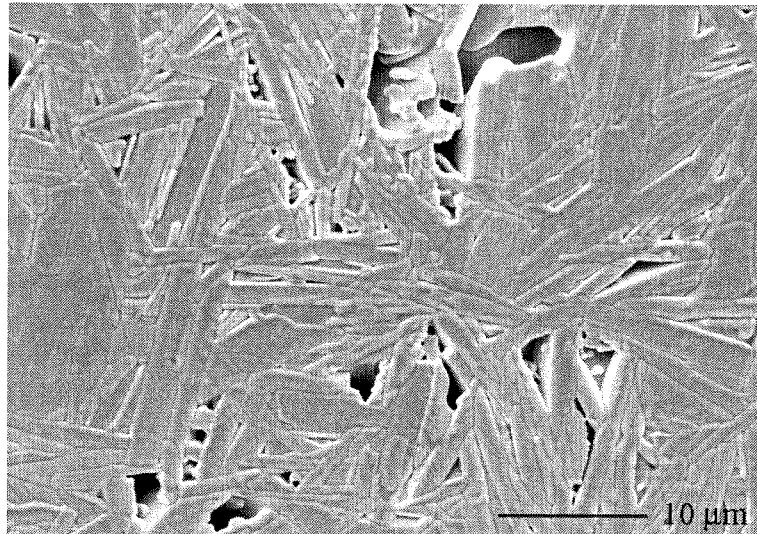


Figure 2-19: microstructure of SrBIT sintered 11°C above the usual firing temperature, but still below decomposition temperature, showing grain coarsening.

According to Figure 2-19, grains as large as 10 microns are grown if the sintering temperature is too high. Meanwhile, no change in thickness is observed. The ceramic of Figure 2-19 was sintered 11°C above the usual sintering temperature. This is a small deviation, but it has dramatic consequences. X-ray diffraction indicates no crystalline phase change (not presented here). This microstructure was used in the impedance analysis presented in Chapter 3 to study the influence of grain size. As discussed in Chapter 3, grain coarsening actually decreases the volume fraction of grain boundaries.

Acceptor and donor doping was employed to study the electrical conductivity of SrBIT in air and in oxygen controlled partial pressure. The preparation procedure developed for undoped SrBIT was not modified in the case of either Manganese or Niobium substitution.

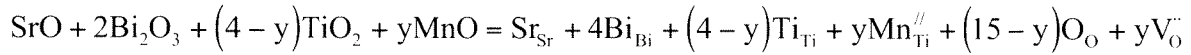
2.7 DOPING

Acceptor and donor doping were used to study electrical conductivity of SrBIT. Dopants were MnCO_3 for acceptor doping and Nb_2O_5 for donor doping. The compositions are given in Table 2-6 and in Table 2-7. Donor doping is described in the next section.

2.7.1 Acceptor doping with MnCO_3

Undoped SrBIT is white, progressive incorporation of Manganese changes its *sintered* color to darker and darker black. On the contrary, Manganese doped SrBIT *powder* is yellow regardless of the composition. The color differentiation occurs after sintering. In the case of Niobium doping, no color change was observed

Manganese doped SrBIT is written as $\text{SrBi}_4\text{Ti}_{4-y}\text{Mn}_y\text{O}_{15-\delta}$ assuming that Manganese is in the divalent oxidation state as MnCO_3 was used as raw powder. The equilibrium equation for Mn incorporation is given by Equation 2-1.



Equation 2-1

It was assumed that in SrBIT Mn^{2+} substitutes Ti^{4+} on the B site of the perovskite, since Kato [48] has shown it in the case of $\text{Bi}_4\text{Ti}_3\text{O}_{12}$. According to Subbarao's work on tolerance factor of $\text{Bi}_2\text{O}_2(\text{Me}_3\text{R}_4\text{O}_{13})$ compounds [16], the ionic radius of cation R should be comprised between 0.63 and 0.72 Å. This requirement is satisfied for Mn^{2+} (0.67 Å), but not in the case of Mn^{4+} (0.53 Å). According to Equation 2-1, divalent Manganese incorporation creates oxygen vacancies to ensure charge conservation. However, divalent state is not the only stable one, trivalent and tetravalent states are more likely in perovskites as demonstrated for BaTiO_3 by Osawa [49]. In addition, the actual oxidation state of Manganese depends on temperature and oxygen partial pressure. At low oxygen partial pressure, the trivalent state is preferred and the tetravalent one at higher oxygen activity.

Table 2-6: Mn doped SrBIT compositions used in this work.

Composition	Composition [mol.%]	Composition [ppm on Ti site]
$\text{SrBi}_4\text{Ti}_{3.995}\text{Mn}_{0.005}\text{O}_{14.995}$	0.5	1250
$\text{SrBi}_4\text{Ti}_{3.990}\text{Mn}_{0.010}\text{O}_{14.990}$	1.0	2500
$\text{SrBi}_4\text{Ti}_{3.985}\text{Mn}_{0.015}\text{O}_{14.985}$	1.5	3750
$\text{SrBi}_4\text{Ti}_{3.980}\text{Mn}_{0.020}\text{O}_{14.980}$	2.0	5000

In order to demonstrate the actual incorporation of Manganese into SrBIT lattice, the three cell parameters of the orthorhombic cell have been calculated from X-ray diffraction measurements, Figure 2-20. Deformation of the cell in the ab plane is easily seen with the orthorhombicity parameter defined as the ratio of a to b, this parameter is presented in Figure 2-21.

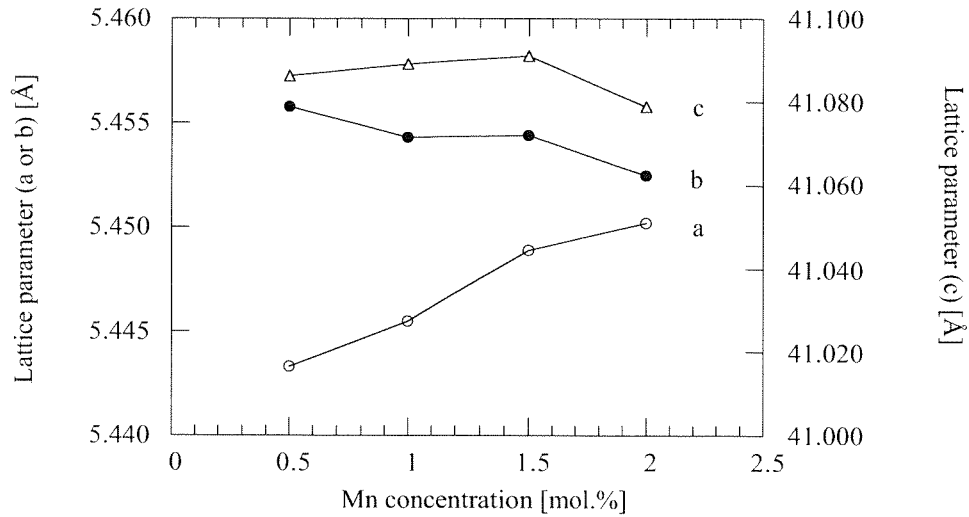


Figure 2-20: cell parameters versus Mn concentration for sintered SrBIT ceramic measured at room temperature.

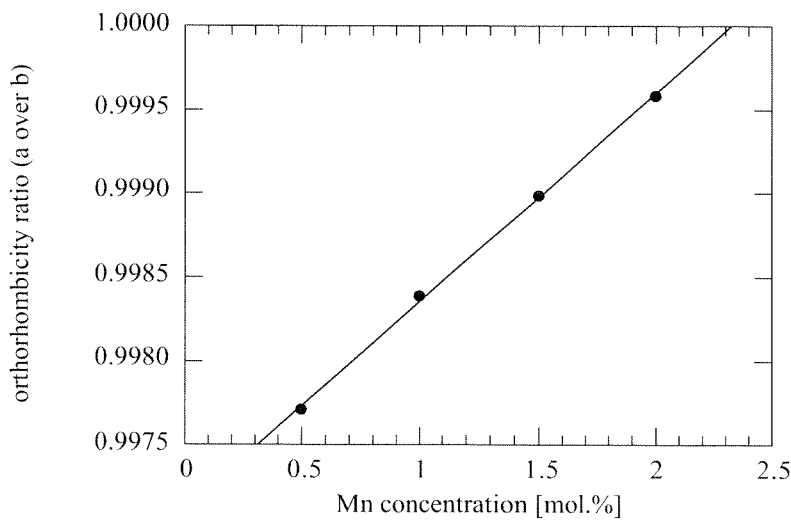


Figure 2-21: a over b orthorhombicity ratio versus Mn concentration.

The microstructure of Manganese doped SrBIT was observed using the same procedure as describe above for undoped material. A typical microstructure of 1.5 mol.% Mn doped SrBIT is presented in Figure 2-22. Compared to undoped SrBIT, Figure 2-18, no marked difference is visible. In addition, the microstructure seems to be single phase, without any second phase in the grain boundaries.

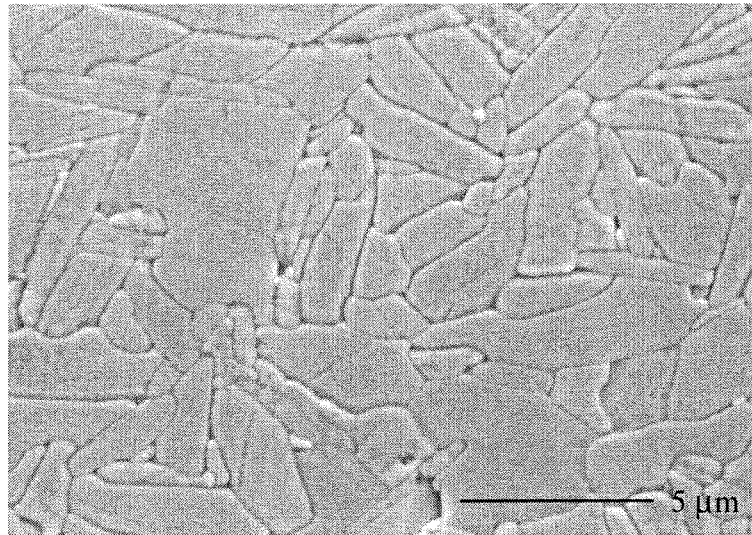
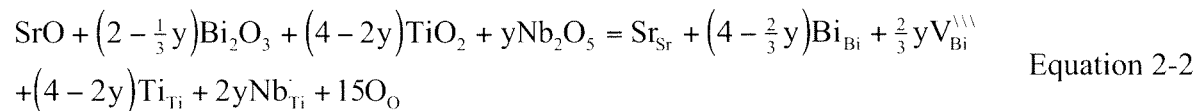


Figure 2-22: microstructure of 1.5 mol.% Mn doped SrBIT fired at 1250°C for 12 minutes.

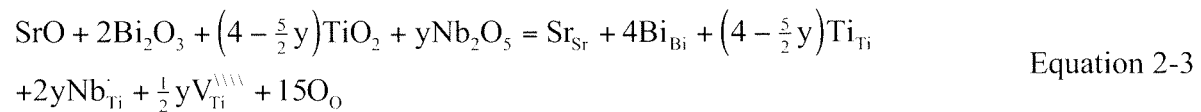
2.7.2 Donor Doping with Nb₂O₅

Donor doping was investigated with Niobium substitution on the Titanium sublattice. Donor doping was realized to reduce conductivity in the p-type regime of SrBIT, its effect has been demonstrated with DC conductivity measurements described in Chapter 3.

Nb doped SrBIT was written as SrBi_{4-2/3y}Nb_{2y}Ti_{4-2y}O₁₅. For pentavalent Niobium substitution on the B site of the perovskite, the equilibrium equation can be written as Equation 2-2, if Niobium is compensated by Bismuth vacancies.



However, if Titanium vacancies compensate Niobium, then the incorporation equation should be written as:



In both compensations, Niobium incorporation was written as a substitution of Titanium, not as an addition. Thus, in principle no TiO₂ second phase should appear, although such expelled TiO₂ was observed in Barium deficient Niobium doped BaTiO₃. Due to elevated Bismuth oxide volatility, the compositions were written with Bismuth vacancies as given in Table 2-7.

Table 2-7: Niobium doped SrBIT compositions used in this work.

Composition	Composition [mol.%]	Composition [ppm on B site]
$\text{SrBi}_{3.9967}\text{Ti}_{3.99}\text{Nb}_{0.010}\text{O}_{15}$	1	2500
$\text{SrBi}_{3.9934}\text{Ti}_{3.98}\text{Nb}_{0.020}\text{O}_{15}$	2	5000
$\text{SrBi}_{3.9950}\text{Ti}_{3.97}\text{Nb}_{0.030}\text{O}_{15}$	3	7500
$\text{SrBi}_{3.9934}\text{Ti}_{3.96}\text{Nb}_{0.040}\text{O}_{15}$	4	10000

The microstructure of 4 mol.% Niobium doped SrBIT is presented in Figure 2-23 for a sintered sample. No strong modification of the microstructure due to Niobium doping can be seen in this picture. Thus, neither Manganese nor Niobium doping affects significantly the microstructure of SrBIT in concentrations used.

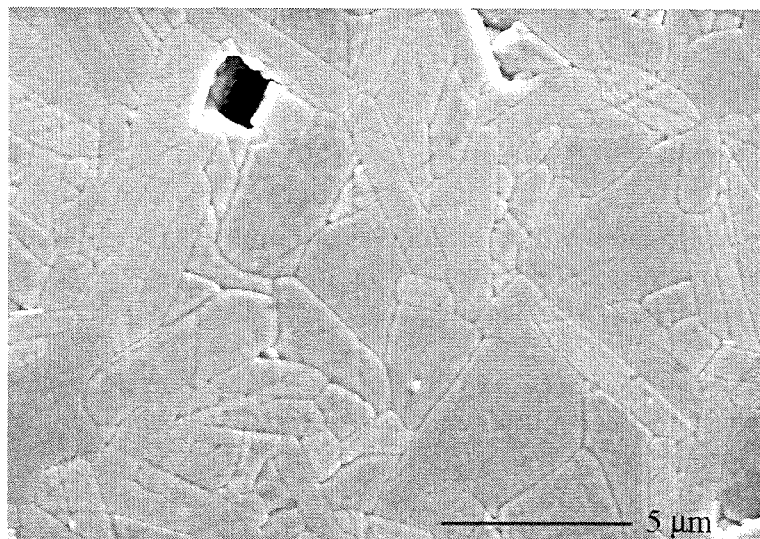


Figure 2-23: microstructure of 4 mol.% Niobium doped SrBIT fired at 1250°C for 12 minutes.

2.8 PREPARATION OF TEXTURED MATERIAL USING HOT FORGING

FORGING

Textured Bismuth Titanate ceramics can be processed using the hot forging technique. It was extensively applied by Takenaka's group to prepare *c* oriented $\text{Bi}_4\text{Ti}_3\text{O}_{12}$ [50] [51-58]. Creating a preferential orientation for Bismuth Titanates is not too difficult; it was already shown in section 2.6.5 and Figure 2-18 that there exist some oriented colonies within naturally sintered ceramic. Because of their high aspect ratio (1-5 μm wide and about 200 nm thick), the random oriented grains of SrBIT are easily re-arranged. Providing that temperature is high enough, grains can slip, tilt and twist to take more favorable orientations compared to the external force. This favored orientation is the *c* axis of the crystallites, thus after hot forging; most of the *c* axes of the grains are collinear with the applied force. Forging is realized without die, the resulting lateral deformation imports for texture degree.

A powder compact (10 mm in diameter and 5 cm in height) was first naturally pre-sintered at 1100°C then it was hot forged at the same temperature under typically 300 N longitudinal force. In order to avoid any contamination from the Silicon Carbide holders, two pieces of sapphire and two sheets of Platinum were placed between sample and holders. Forging was performed under constant stress and monitored with the recorded displacement of the machine. It was typically after 3-5 hours that the ceramic sample was completely forged. The temperature and charge profiles used for SrBIT hot forging are given in Figure 2-24. Using a diamond saw samples were cut in the *ab* plane and *c* directions from the hot forged ceramic.

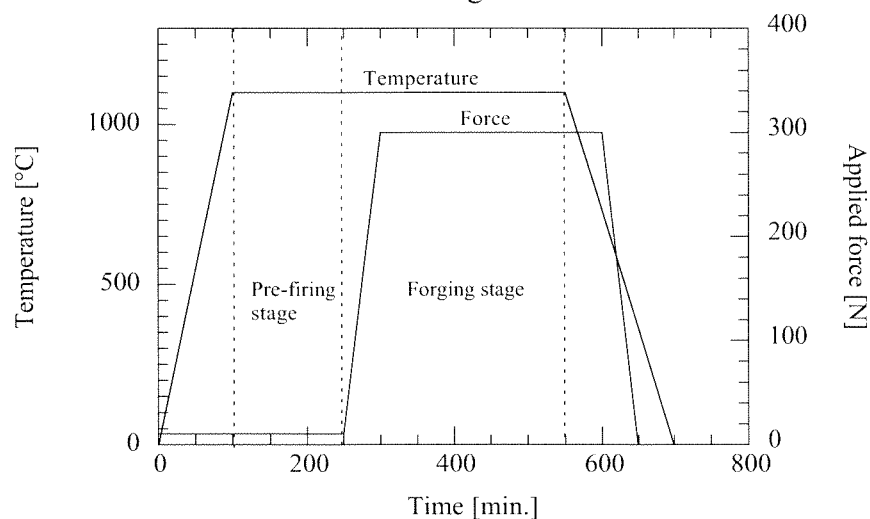


Figure 2-24: temperature and uniaxial force profile used for SrBIT hot forging. The pre-firing process was made at 1100°C for one hour without any applied force and the forging process was done at the same temperature but with a 300 N longitudinal applied force for 5 hours.

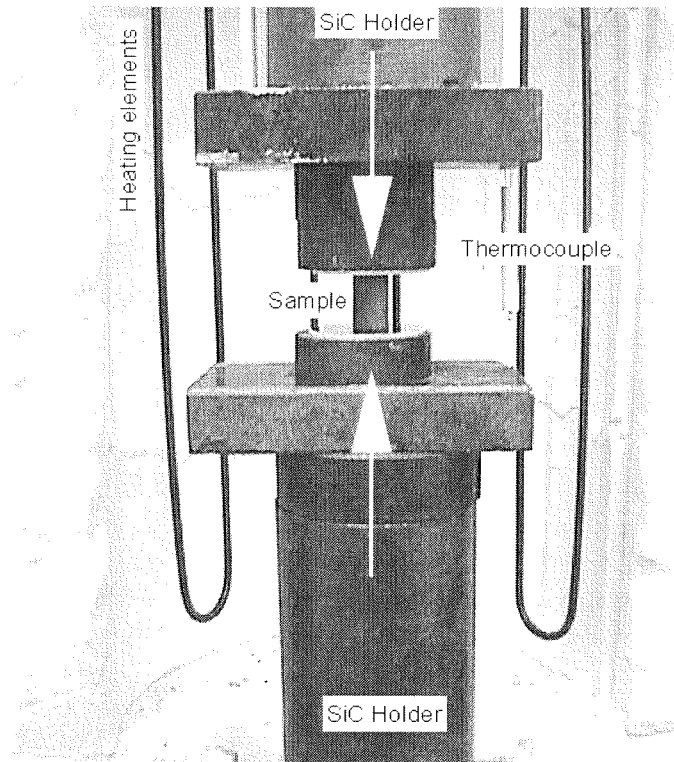


Figure 2-25: hot forging system employed for textured material preparation

The longitudinal and lateral deformations are defined according to Equation 2-4 and Equation 2-5.

$$\gamma = \frac{S_f}{S_i} \quad \text{Equation 2-4}$$

$$\lambda = \frac{h_i - h_f}{h_i} \quad \text{Equation 2-5}$$

Typical values for γ and λ were $\gamma=1.4$ and $\lambda=0.6$.

X-ray diffraction on the ab surface (thus the c direction) of hot forged samples was used to quantify texture. The texture index p_{hkl} is defined as:

$$p_{hkl} = \frac{\frac{I_{hkl}}{I_{hkl}^s}}{\frac{1}{N} \sum_{hkl} \frac{I_{hkl}}{I_{hkl}^s}} \quad \text{Equation 2-6}$$

where I_{hkl} is the intensity in arbitrary units of the texture reference reflection measured for the hot forged ceramic, while I_{hkl}^s is the intensity of the same reflection measured for a random oriented mix of powder. The higher the index, the better the texture, as given in Table 2-8 the texture

index of random SrBIT is one. The indexes given in Table 2-8 have been calculated for the (004) reflection. In Equation 2-6, N is the number of reflections recorded in the X-ray spectrum. The texture indexes for undoped, 2 mol.% Mn doped and 4 mol.% Nb doped SrBIT are given in Table 2-8. Hot forging was much more efficient for Mn doped SrBIT than for other compositions. In some cases, the texture of Mn doped samples was even much more pronounced (5.05 and 6.21). However those samples broke on polishing and were not used for electrical measurements. Texture is slightly lower for undoped and 4 mol.% Nb doped SrBIT, nevertheless as shown in the next chapter, the texture of undoped SrBIT was good enough to highlight its anisotropic properties.

Table 2-8: texture index for undoped, 2 mol.% Mn doped and 4 mol.% Nb doped SrBIT in the “c” direction.

Sample	Undoped SrBIT random	Undoped SrBIT hot forged	2 mol.% Mn doped	4 mol.% Nb doped
P_{hkl}	1	1.75	3.16	1.45

Example of X-ray diffraction spectrums for undoped random and c oriented SrBIT, 2 mol.% Mn doped and 4 mol.% Nb doped SrBIT are given in Figure 2-26. In the case of Mn and Nb doped SrBIT, only (ool) reflections are seen, reflection (111), (113), (115) and (119) are strongly reduced. However, these reflections are detected in the spectrum of undoped SrBIT, indicating a less efficient texturation

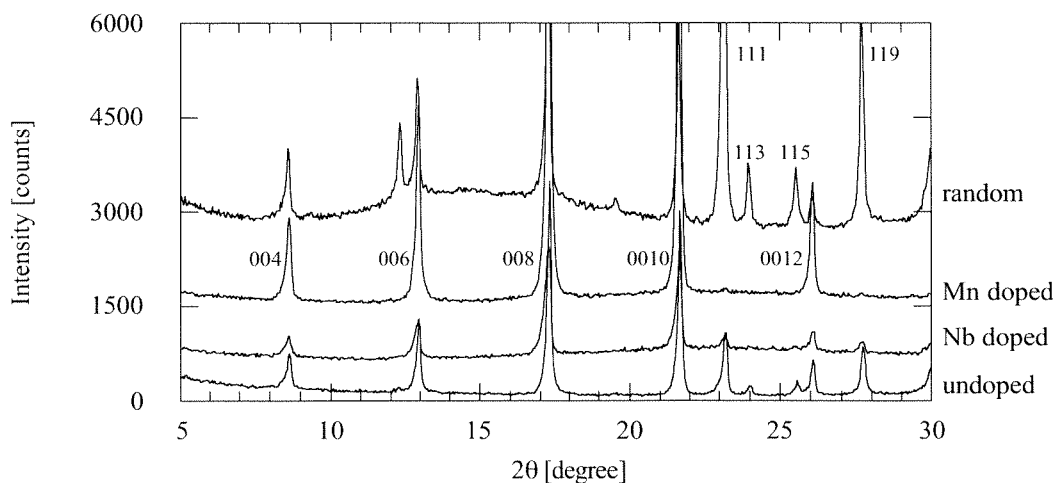


Figure 2-26: comparison between undoped random SrBIT and undoped Mn or Nb doped c oriented hot forged XRD patterns.

2.9 SUMMARY AND CONCLUSION

A standard calcination procedure was established that ensures preparation of a reproducible powder. A long temperature profile at elevated temperature was used to calcine simultaneously the three reagents (SrCO_3 , Bi_2O_3 and TiO_2). This route produces a 1-5 microns large and a hundred nanometers thick plate-like grains.

Intermediate phases formation was investigated by X-ray diffraction. These intermediate phases are SrO- Bi_2O_3 solid solution, $\text{Bi}_{12}\text{TiO}_{20}$, $\text{Bi}_4\text{Ti}_3\text{O}_{12}$ and SrTiO_3 . Although, the exact sequence of phase's formation was not determined, the general mechanism has been elucidated. The first step is the reaction of SrCO_3 with Bi_2O_3 to form the solid solution and of TiO_2 with Bi_2O_3 to form $\text{Bi}_{12}\text{TiO}_{20}$. Above 715°C , the solid solution reacts with $\text{Bi}_{12}\text{TiO}_{20}$ and TiO_2 to form $\text{Bi}_4\text{Ti}_3\text{O}_{12}$ and SrTiO_3 . Thus, the transformation of the solid solution is probably causing the first expansion peak observed at 715°C . Above 830°C , residual SrO- Bi_2O_3 , $\text{Bi}_4\text{Ti}_3\text{O}_{12}$ and SrTiO_3 are converted into $\text{SrBi}_4\text{Ti}_4\text{O}_{15}$.

The sintering process was identified by dilatometry and scanning electron microscopy. It was found that SrBIT is densified through two main mechanisms: agglomerates re-arrangement (around 1258°C) and partial incongruent melting (at 1275°C). The first mechanism was found by observing fracture surfaces at different temperatures and the second one by performing cycled dilatometry experiments. Incongruent melting was demonstrated by the presence of a second solid phase at room temperature ($\text{Sr}_2\text{Bi}_4\text{Ti}_5\text{O}_{18}$).

With careful preparation, the polished surface of thermally etched SrBIT sintered samples was observed with a scanning electron microscope. These observations revealed plate-like grains 1-2 μm width and 200 nm thick. It is proposed that such shape could actually be one reason to account for the residual porosity. SEM observations revealed that SrBIT microstructure contains locally textured regions called colonies.

It was shown that both acceptor and donor doping performed by Manganese and Niobium incorporation respectively into SrBIT lattice does not modify grain size or mean aspect ratio. The actual incorporation of Manganese into SrBIT crystal lattice was demonstrated by progressive lattice deformation as Manganese content increases.

Hot forging was used to prepare (001) textured material. With X-ray diffraction, the degree of texture of undoped Manganese and Niobium doped SrBIT was characterized. This method allowed the definition of two directions within each sample: "c" and "ab plane" parallel and perpendicular respectively to the forging axis.

Low densification rate is mainly related to grain morphology. Producing equiaxed SrBIT grains could be a solution to facilitate sintering. This could in principle be done with a dissolution-precipitation route using surfactants to modify surface energies of SrBIT crystallites. However, in

the case of a ternary oxide, due to kinetics problems, the precipitation stage would probably be difficult to control.

Influence of atmosphere saturation during sintering was not investigated during this work. However, some indications not presented here would indicate that it is actually an important parameter to consider.

Work presented in this chapter was performed to find out a reproducible way to prepare SrBIT bulk ceramic samples. Therefore no search for any quantitative information about either phase's crystallization or sintering kinetics was realized.

3

DC AND AC CONDUCTIVITY

3.1 FOREWORD

This chapter describes both the electrical DC conductivity and AC complex impedance of SrBIT. DC conductivity has been studied in a low temperature range (100-220°C), while the impedance analysis was conducted at higher temperature (400-1000°C). All of the measurements presented in this chapter have been performed in air, except for the transient analysis shown in paragraph 3.6.8.

The anisotropy, the effect of acceptor and donor doping was investigated with DC measurements at low temperature. Results are presented as Arrhenius plots (conductivity in log scales versus reciprocal temperature), with the corresponding activation energies. This technique was also used in an attempt to determine grain and grain boundary conductivities. However, it is shown that due to severe experimental requirements, reliable results are difficult to obtain.

DC measurements bring information on the slow frequency response only. Due to various polarization processes involved in dielectrics, there exists also a response at higher frequency, which should be characterized too. This analysis is presented in the second part of the chapter. It involves selection and test of electrical equivalent circuits and representations of both impedance and modulus in the frequency domain or complex plane. Thanks to this analysis several contributions to the total impedance have been extracted.

3.2 ELECTRICAL DC CONDUCTIVITY

3.2.1 Introduction

The electrical conductivity of piezoelectric ceramics is an important feature that has to be taken into account for a complete understanding of the observed electromechanical properties. For example, efficiency of the poling process is directly related to the electrical conductivity; breakdown strength is actually closely related to conductivity. Measured piezoelectric coefficients of ferroelectrics such as described in Chapter 5 can also be affected by conductivity. Fousek [59] predicted that ferroelectric domain wall mobility could be decreased by conductivity and Tikhomirov [60] actually measured a reduced displacement of walls at low frequency and suggested its interpretation in terms of Fousek's model. Conductivity is a strongly temperature-dependent property; thus for high temperature piezoelectric applications, it is important to consider the electrical conductivity in the desired working temperature range.

Both DC and AC techniques used in this work require the application of an external electrical field to the ceramic. For dielectric materials, such field induces both a resistive current and an electrical polarization. For DC conductivity measurements, the resistive current, called true DC conductivity will be mostly discussed.

3.2.2 Charging Current Expression

For a system consisting of two parallel electrodes with a dielectric material in between under an electric field, the dielectric displacement $D(t)$ is the sum of an instantaneous free space contribution and a delayed material polarization, Equation 3-1. It represents the total charge density induced at the electrodes.

$$D(t) = \epsilon_0 E + P(t) \quad \text{Equation 3-1}$$

According to Jonsher [61], the resulting charging current can be expressed by:

$$i_c(t) = \epsilon_0 E_0 \left\{ \delta(t) + f(t) \right\} + \sigma_0 E_0 \quad \text{Equation 3-2}$$

The delta function is due to the instantaneous response under the step function; this part of the response is however out of the frequency window covered in this work. The time function $f(t)$ expresses the charging current of the dielectric. In the case of Debye-type relaxation, it will take an exponential form. The last term, $\sigma_0 E_0$, represents any direct current conductivity, which would produce a steady current at infinite time. Equation 3-2 clearly shows two different processes: polarization and dc conduction. The polarization current $dP(t)/dt$ characterizes the adjustment of

the polarizing species to a step function field and it must go to zero at infinitely long times, that is no net charges may leave or enter the dielectric system. The steady state current (DC) arises from continuous movement of free charge across the dielectric material from one electrode to the other; this current does not change the charge distribution in the system. Macdonald [62] gave the time-dependent part of Equation 3-2 in another form as Equation 3-3.

$$i(t) = P_{\infty} \delta(t) + \frac{(P_s - P_{\infty})}{\tau} \exp\left(-\frac{t}{\tau}\right) \quad \text{Equation 3-3}$$

where τ is a characteristic relaxation time. This equation holds for a single polarization process of the Debye-type. However, there could exist many different polarization mechanisms acting simultaneously. In this case, there is a charging current associated with every polarization component.

Jonscher [63] gives a generalization for every possible behavior, in terms of a power law:

$$i(t) \propto t^{-s} \quad \text{Equation 3-4}$$

According to Jonscher, this equation could in principle describe the charging current of any dielectric material and Debye-type relaxation would be an exception; therefore the author called Equation 3-4 “universal relaxation law”. It applies to SrBIT where charging current can actually be approximated with a power law, Figure 3-1.

The impedance of SrBIT is quite high; it required the use of high precision measurement systems. For example, under 10 V DC voltage at 120°C, the resulting steady-state current is in the picoampere range. Since electrical conductivity was investigated in the low electrical field regime (far below coercive field), the available maximum DC field was limited (up to 0.1 kV/cm compared to coercive field of 50 kV/cm).

3.3 EXPERIMENTAL CONSIDERATIONS

3.3.1 DC Conductivity Measurement

This section will present the experimental method used for DC conductivity measurements at low temperature (120-220°C) of a ceramic sample. DC electrical conductivity of SrBIT has been measured above 120°C with a voltage step technique. Because of a very large impedance, it was not possible to measure the electrical conductivity of SrBIT below 120°C. Charging currents resulting from voltage step applications were also carefully investigated in order to determine separately grain and grain boundary conductivities, as discussed in section 3.3.2. Unfortunately, it was demonstrated that experimental artifacts could lead to strong misinterpretations of results. This will be extensively demonstrated at the end of this experimental section.

In the voltage step technique, a DC voltage is applied to an electroded sample and the resulting charging current is recorded until a steady state current can be established. Then, the electrical field is removed and the discharging current is recorded the same way. In the ideal situation, the steady state charging current corresponds to pure DC conductivity and the steady-state discharging current is zero. Practically, as the final discharging current is not zero, it is subtracted from the final charging current to get the true DC one. Alternatively, fitting the charging current with a power law allows estimation of the true steady-state current that is equal to the DC current. An example of charging and discharging currents is given in Figure 3-1 in lin-log scale to present the early part of the curve. Time origins of both curves were brought together to allow a direct comparison between them. Both charging and discharging curves of Figure 3-1 can be fitted with power law expressions with exponents close to unity.

The current was measured with a *Keithley 6517A Electrometer/High Resistance Meter*; the electrometer was also used as a voltage source. The lower limit of current detection was about 0.1 pA. As this method involves very small current measurements, it was needed to ensure good shielding of the set up and to use low noise cables. It is clear from Figure 3-1, that it was needed to wait at least 100 seconds to reach steady state. In practice, current was recorded for 20 to 60 minutes.

Temperature was adjusted with DELTA 9023 regulation system from DELTA DESIGN, (San Diego, USA) from 120°C up to 220°C. A thirty minutes or more delay was used prior to any current measurement for temperature stabilization.

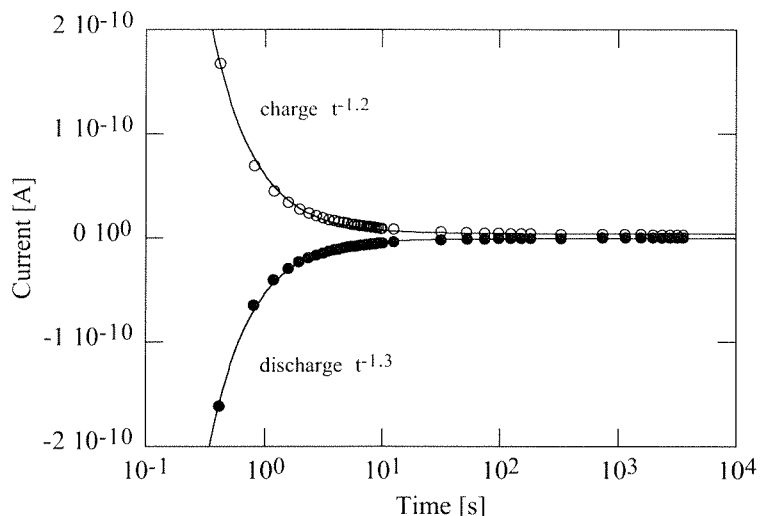


Figure 3-1: Example of a charge-discharge curve used for DC conductivity measurement. Open circles are charging current and filled circles are discharging current. The two curves can be fitted with a power law ($At^n + B$) with $n \approx 1.2$.

3.3.2 Determination of Grain Boundary Conductivity

3.3.2.1 Motivation

In addition to the steady-state DC conductivity, the voltage-step technique can be in principle used to determine separately grain and grain boundary conductivities, it is actually the transposition in the time domain of the frequency response [62,63]. It was extensively used by Waser and Vollmann [64-69] in the case of SrTiO_3 . Evaluation of grain boundary properties of SrBIT with the same technique seems then to be very interesting, because of its special microstructure (plate-like grains, anisotropic properties).

The most commonly used microstructural model is called the bricklayer model. In this model, grains are replaced by monosized and isotropic cubes separated by a boundary phase of thickness d , Figure 3-2. It was successfully applied to SrTiO_3 , which has a suitable microstructure (isotropic properties and regular grains), but its applicability to Bismuth Titanates remains an interesting problem to investigate. Therefore, considerable efforts were made to find out experimental conditions suitable for a microstructural approach to conductivity using a DC technique.

Compared to the impedance analysis that is usually employed for such microstructural characterization, the DC technique allows in principle measurements of much higher impedances (up to gigaohm using a precision electrometer) in a different time window (which is equivalent to another frequency window) from microseconds up to minutes. As shown below, resolution of the complete impedance arc with the AC technique was not possible due to both frequency and

impedance limitations (requiring elevated measurement temperatures). Therefore, detailed DC current analysis was performed to complete the AC analysis.

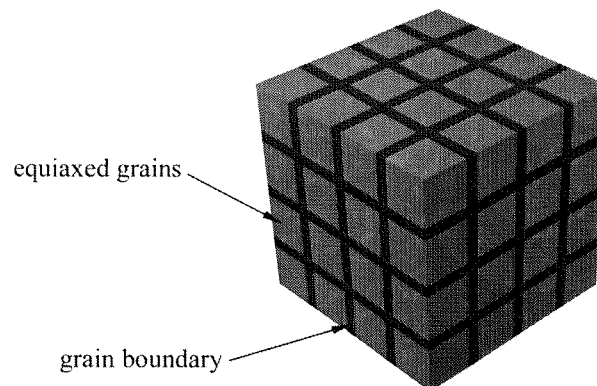


Figure 3-2: idealized bricklayer microstructure. The grains (cubes of size D) are mono-dispersed one separated by the same length in every direction (grain boundary thickness d).

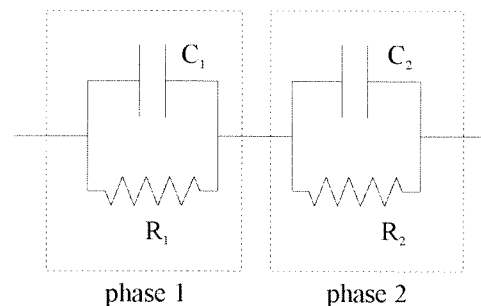


Figure 3-3: electrical equivalent circuit made of two RC elements consisting of one resistor and one capacitor in parallel.

In order to extract any information from the time response curves, an equivalent circuit should modelize the ceramic. The series circuit, Figure 3-3 was used by Vollmann [64-69] to describe the behavior of SrTiO_3 . It is made of two RC components puts in series. The authors assigned the elements to grains ($R_1=R_g$ and $C_1=C_g$) and grain boundaries ($R_2=R_{gb}$ and $C_2=C_{gb}$) respectively. Thus, this very simple model takes into account only grain-to-grain boundary conduction paths, omitting grain boundary-to-grain boundary paths as for example in the model developed by Näfe [70], Equation 3-15, which is presented in section 3.4.3. In addition, it is important to note that the simple RC combination used by Vollmann is the image of ideal Debye-type relaxations each of them with a single discrete relaxation time. As stated by Jonsher, these kinds of relaxation are exceptions among dielectrics.

The transient behavior under DC field of the equivalent circuit of Figure 3-3 can be simplified as follow:

- 1) Providing $C_g \ll C_{gb}$ and $R_g \ll R_{gb}$: initially ($t=0$) the two capacities are not saturated, it is a short-circuit.

- 2) When the polarization inside grains is established, it is equivalent to charging C_g ; its associated resistance (R_g) limits the current. However, as C_g is very small, the current decay associated with this step is very difficult to measure.
- 3) When the interface polarization at the grain boundaries is saturated, equivalent to charging C_{gb} , the measured resistivity is the sum of the two resistances in series (steady state).

Thus, the grain conductivity (σ_g) can be extracted from the first part of the current transient and the total conductivity (σ_T) from the second steady-state current (long time). The grain boundary conductivity (σ_{gb}) is calculated with Equation 3-5 knowing the ratio of the grain boundary thickness (d) to the mean grain size (D).

$$\sigma_{GB} = \frac{d}{D} \frac{\sigma_T \sigma_g}{\sigma_G - \sigma_T} \quad \text{Equation 3-5}$$

This interpretation is represented in Figure 3-4.

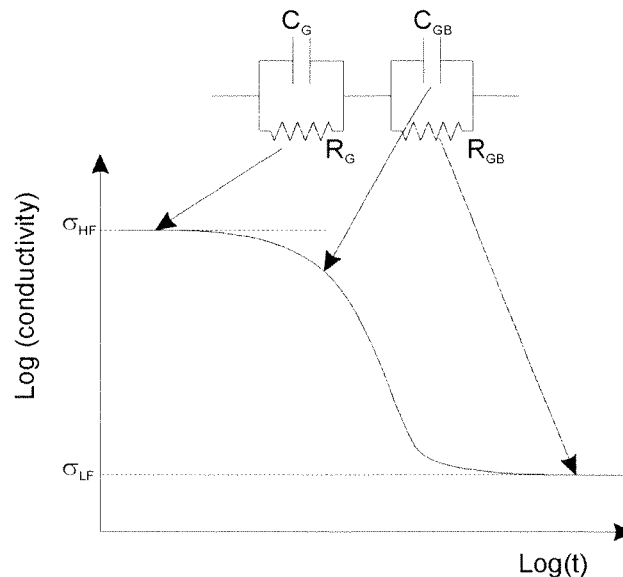


Figure 3-4: Schematic interpretation of the charging current in the frame of the serial model.

In Figure 3-4, the long term current is associated with grain boundary conductivity only, this is however only valid for $\sigma_{gb} \ll \sigma_g$, otherwise the steady-state current is the sum of σ_g and σ_{gb} .

However, it should be mentioned, that this interpretation holds only for $R_g \ll R_{gb}$ and $C_g \ll C_{gb}$. If this is not valid, current transient becomes much more complicated and grain and grain boundary resistances and polarizations cannot be easily resolved any longer.

The relaxation frequency associated with the measured charging current is written ω_r and according to Vollmann it is given by:

$$\omega_R = \frac{1}{R_g C_{gb}}$$

Equation 3-6

Vollmann and Waser [69] successfully applied this DC method to calculate the bulk and the grain boundary conductivities of SrTiO₃, from 120°C up to 360°C. They actually measured a grain conductivity four orders of magnitude larger than the grain boundary conductivity. According to Figure 3-3, it means that in the measured temperature range, charge transport in SrTiO₃ is limited by conduction across grain boundaries.

The very early part of the charging current curve, corresponding to grain polarization in SrTiO₃ was not directly measured with the DC method by Vollmann's group [69]. They had to employ AC methods such as admittance measurements to demonstrate it. Without this proof, the origin of the early steady-state current would still remain unknown.

3.3.2.2 Application to SrBIT

There are four experimental requirements for the charging current analysis of a dielectric: the raise time of the voltage source, the impedance limit of the current measuring device, the cut-off frequency of any operational amplifier and the highest analog to digital conversion rate of the storage system. Thus, the equipment had to be selected according to these conditions. Considering the electrometer, the detection limit was the smallest available and using its analog output data sampling could be performed with an oscilloscope (working in the Megahertz range). However, the built-in preamplifier of the electrometer, which converts input current into voltage has a very slow settling time. Depending on the selected current range, it can be 1ms (mA range) or 2.5 s (pA range). This is not fast enough to study relaxation process down to 10⁻⁶ s. In addition, the raise time of the built-in voltage source is quite large (a hundred of milliseconds). Knowledge of these limitations is very important; otherwise experimental response of SrBIT could be misinterpreted and for example could be identified with Debye-type relaxations.

Charging current of undoped SrBIT at 120°C measured with the electrometer and an oscilloscope is presented in Figure 3-5. According to these results, it seems that there is a steady-state current, before a large current decay. According to the microstructural model, a "grain conductivity" could in principle be calculated from the steady-state value. Unfortunately, even if there really exists such relaxed current below one second, due to speed limitation of the operational amplifier, no conclusions can be drawn from these results. Actually, the "grain conductivity" extracted from this measurement has almost no temperature dependence (E_g "grain"=0.08 eV, this result is not presented here); this is actually a strong indication of an experimental artifact.

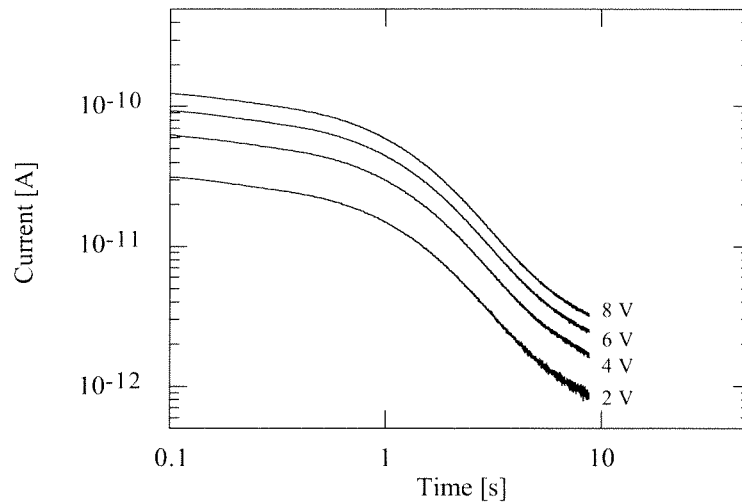


Figure 3-5: charging current measured at 120°C for undoped SrBIT using the electrometer with different electrical fields. In this measurement the A/D conversion was made within the electrometer.

A solution to the electrometer measurement is to use a pulse generator as a voltage source and a grounded resistor as current-to-voltage converter. The pulse generator, model DG535 from Stanford Research System Inc., has a much smaller raise time, so that voltage application could be faster than the expected “grain” relaxation. In this set-up, analog to digital conversion is made with an oscilloscope. Charging current measured with a 1 k Ω grounded resistor (without operational amplifier) is presented in Figure 3-6 for undoped SrBIT at room temperature. Choice of a low resistor was actually imposed by the oscilloscope, since it needs very small load impedance (much smaller than 1 M Ω). For a 1k Ω resistor, above 10⁻⁵ seconds, current converted into voltage is below the resolution of the oscilloscope. It can be solved with an operational amplifier. However, such amplifier has to be fast enough with low pass filter as high as possible.

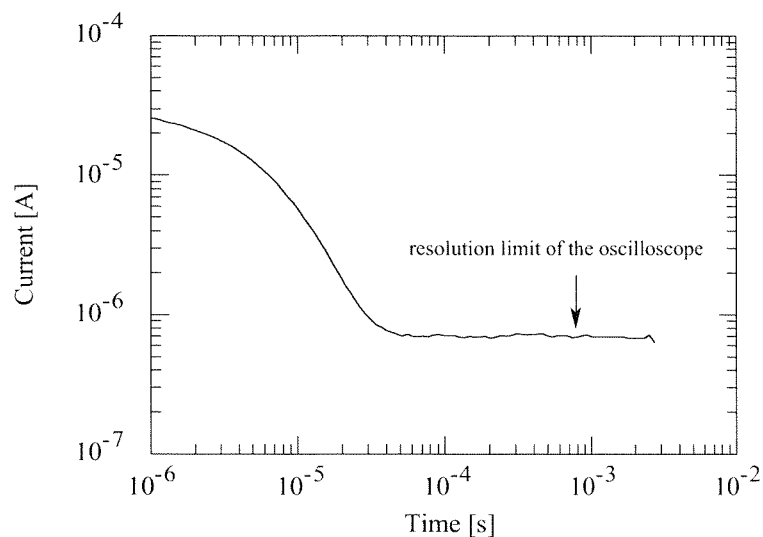


Figure 3-6: charging current versus time for grounded resistor (1 kΩ) measurement for undoped SrBIT at room temperature.

Finally another indirect way to investigate charging current is to measure the electrical charge versus time with a charge amplifier; derivative of charge versus time provides then current. Charge amplifier was type 5011 from Kistler Instrumente (Winterthur, Switzerland). As charge variation is much smaller than current change, evaluation of charging current through charge measurement is in principle much easier. However, taking the derivative of charge brings a quite large noise in log-log scales, therefore interpolation is needed to extract the information. An example of a charge versus time curve is presented in Figure 3-7 for undoped SrBIT at room temperature. Charging current calculated from the derivative of Figure 3-7 is given in Figure 3-8. Jonscher [61] described charging current of many dielectrics with two power laws, one at short time and another one at long time. The short time one has been known as Curie-Von Schweidler law and is expressed by:

$$i(t) \propto t^{-n} \text{ with } 0 < n < 1 \quad \text{Equation 3-7}$$

The form of the second power law depends on the polarizable species. For dipolar systems, Jonscher showed that the long time power law expression is of the form:

$$i(t) \propto t^{-1-m} \text{ with } 0 < m < 1 \quad \text{Equation 3-8}$$

And in the case of carrier-dominated systems, the exponent is very small; therefore the equation was written as:

$$i(t) \propto t^{-1+p} \text{ with } p \approx 1 \quad \text{Equation 3-9}$$

If Figure 3-8 was interpreted according to Jonscher's model, the calculated power law exponents would be equal to -0.76 and -0.3 for the early and late part of the curve respectively. It may indicate that SrBIT charging current obeys a carrier-dominated behavior since the long-time exponent is smaller than the short time one. However, current measured in Figure 3-8 may also be the end of an extremely fast Debye-type relaxation. According to Equation 3-16 and Figure 3-8 for a relaxation time smaller than $1 \mu\text{s}$ and a resistance of $1 \text{ M}\Omega$, the associated capacitance would be lower than 1 pF . It may be larger since the actual value of the associated resistance may be smaller. As this estimation provides realistic values, a fast Debye-type relaxation cannot be excluded from these measurements. However precise extraction of a resistive and a capacitive value from charging current as Vollmann did for SrTiO_3 is not possible, since only part of the curve could be recorded. Interpretation of the charging current with non-Debye relaxation can be realized with a stretched exponential law (Kohlrausch-Williams-Watts relaxation function), Equation 3-14. The interconnection between non-Debye type relaxations observed with AC methods in the complex plane and their time response has been discussed by Alvarez [71]. Non-Debye response was also presented in a phenomenological point of view by Wang and Bates [72]. The stretched exponential function was used by Leon [73] to account for Non-Debye conductivity relaxation in $\text{Li}_{0.5}\text{La}_{0.5}\text{TiO}_3$ fast ionic conductor. Finally a Non-Debye relaxation was for example identified in $(1-x)\text{Pb}(\text{Mg}_{1/3}\text{Nb}_{2/3})\text{O}_3-x\text{PbTiO}_3$ by Fan [74]. Regardless of the way

to interpret charging current the existence of an immediate polarization is shown by charge measurements, Figure 3-7, since early charge level $Q(1 \mu\text{s}) \approx 300 \text{ pC}$ is different from the initial charge level of the charge amplifier $Q(t < 0 \text{ s}) < 1 \text{ pC}$. The increase of collected charge measured above 1 second indicates the setting of the second polarization process. Thus, charge measurements clearly indicate two different polarization processes, one that is so fast that polarization transient cannot be seen and another one, that occurs much more slowly and leads to the observed increase of charge after 1 second, Figure 3-7. Vollmann in the case of SrTiO_3 treated the first one as a Debye-type relaxation. Because the corresponding SrBIT relaxation is either non-Debye or incompletely resolved, similar calculation is unfortunately not possible for SrBIT.

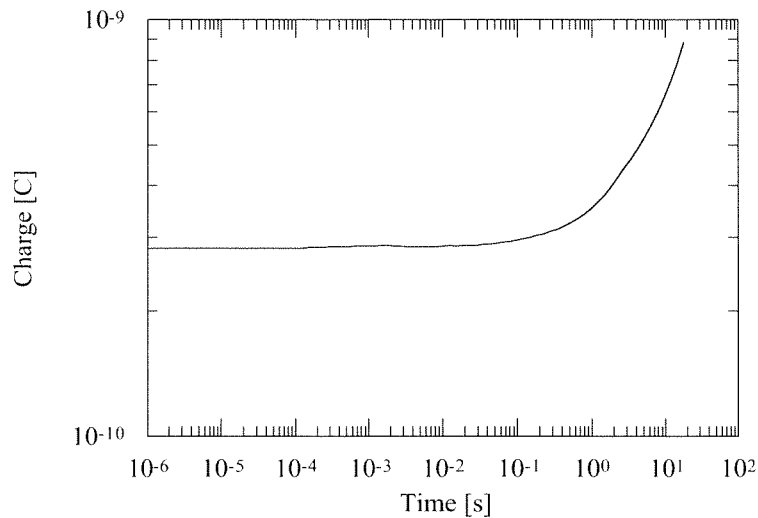


Figure 3-7: charge versus time under 4 V DC voltage for undoped SrBIT at room temperature. Measurement was made in two steps; therefore charge level is different for the measurements.

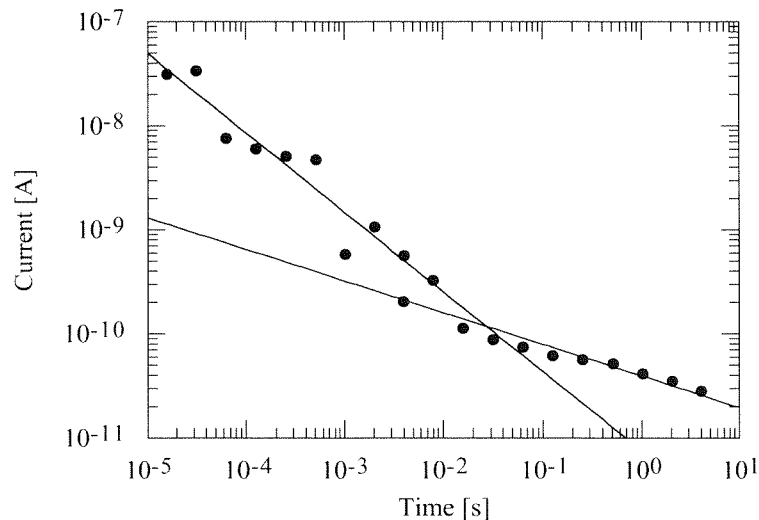


Figure 3-8: current versus time calculated from charge measurement of undoped SrBIT at room temperature.

The same way Vollmann and Waser measured the admittance of SrTiO_3 to demonstrate that their interpretation was correct, admittance measurements of SrBIT can be realized to help interpreting

DC measurements. Measuring the admittance of SrBIT at low frequency is not possible with a LCR bridge at room temperature; the impedance is too large. However, a direct measurement can be made with a function generator (Hewlett-Packard HP33120A) and a current amplifier (Stanford Research System SR570). Such measurement is presented in Figure 3-9. At 560°C, the frequency-independent regime corresponding to true DC conduction is seen, but no evidence of extra polarization is observed.

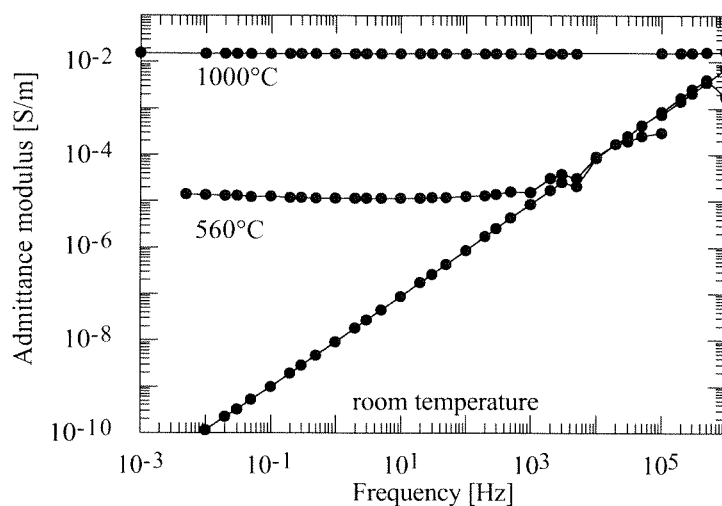


Figure 3-9: admittance versus frequency for undoped SrBIT at room temperature, 560 and 1000°C.

As the phase angle could not be measured with precision with this method, it was unfortunately not possible to extend the complex impedance analysis performed at elevated temperature.

In conclusion, investigation of the early part of charging current of SrBIT could not be performed with the same model as used for SrTiO₃. This is due to the fact that the observed relaxations are either non-Debye or incompletely resolved. Nevertheless, the actual existence of two separate polarization processes is demonstrated by charge measurements, Figure 3-7.

The next section is dedicated to the global behavior of SrBIT ceramic samples that is without any considerations about separate grain and grain boundary contributions. Results presented below, down to section 3.4.6, are global DC conductivities calculated from long time steady-state current measurements. The activation energy for conduction, anisotropy and doping effect will be discussed in details.

3.4 ELECTRICAL DC CONDUCTIVITY OF UNDOPED SRBIT

3.4.1 Conductivity of random oriented ceramic

The electrical DC conductivity of undoped SrBIT is presented from 180°C up to 220°C in Figure 3-10. At 220°C, the electrical conductivity of SrBIT is typically $3 \cdot 10^{-10}$ S/m; the activation energy for conduction, written E_σ , according to an Arrhénius law Equation 3-10, in this temperature range is 1 eV. James [25] reported DC conductivity measurements of undoped SrBIT of the same order of magnitude. The activation energy given by James in the 200°C to 400°C temperature range is 1.52 eV, which is similar to our measurements above 450°C, see section 3.6.3. As discussed below, limitation of the total conductivity by grain boundary conductivity may explain the observed curve bending or reduction of the apparent activation energy.

$$\sigma = A \exp\left(-\frac{E_\sigma}{k_B T}\right) \quad \text{Equation 3-10}$$

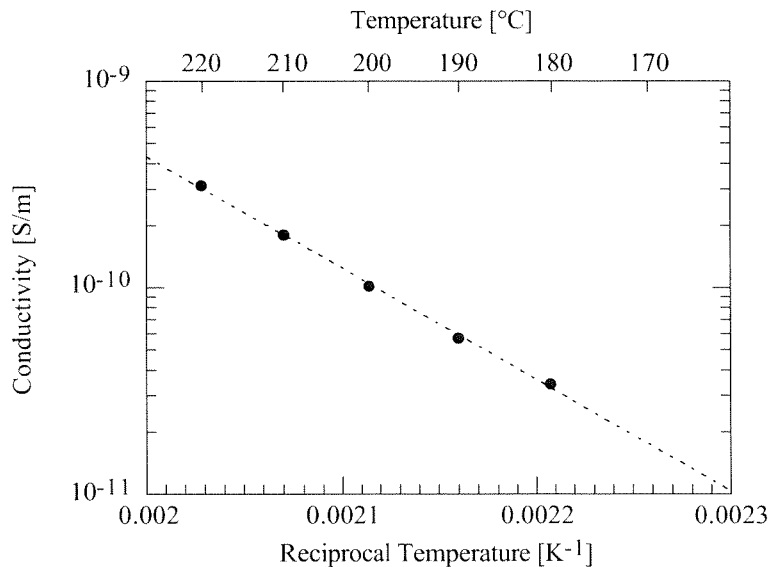


Figure 3-10: Electrical DC conductivity of undoped SrBIT between 180°C and 220°C measured in air after oxygen annealing.

Interpreting the activation energy for conduction requires considerations of the charge carriers concentrations and mobility. It will be demonstrated in Chapter 4, that at high temperatures (above 700°C), the electrical conductivity of undoped SrBIT is n-type and acceptor-controlled (impurities). In addition, acceptor doping, see paragraph 3.4.5 and donor doping, see paragraph 3.4.6, indicate a p-type conduction at low temperature (up to 220°C), that could also be acceptor-

controlled for undoped SrBIT. In the case of p-type conduction, hole concentration (p) should be considered. It is expressed as follow:

$$p \propto \exp\left(-\frac{E_a}{2k_B T}\right) \quad \text{Equation 3-11}$$

where E_a is the energy of the acceptor level and $k_B=1.38 \cdot 10^{-23}$ J/K the Boltzmann Constant. However, conductivity (σ) depends also on the mobility (μ) of the charge carrier, since:

$$\sigma = p\mu e \quad \text{Equation 3-12}$$

where $e=1.602 \cdot 10^{-19}$ C is the elementary charge. If in a first approximation, the temperature dependence of the mobility is neglected, then the activation energy for conduction is half the acceptor level energy according to Equation 3-10 and Equation 3-11. According to Figure 3-10, the activation energy for conduction (E_σ) for undoped SrBIT is 1 eV, thus the corresponding acceptor level would be 2 eV. As calculated in Chapter 4, the band gap energy of SrBIT could be 3.5 eV. Compared to that band gap, an acceptor level (E_a) of 2 eV is quite large. However, adding a mobility component to E_σ decreases E_a . With the mobility contribution, the temperature dependence of conductivity is written:

$$\sigma \propto \frac{1}{T^{-m}} \exp\left(-\frac{2E_\mu + E_a}{2k_B T}\right) \quad \text{Equation 3-13}$$

Adding such exponential dependence towards temperature for the mobility is similar to assuming hopping conduction. The value of the exponent m in Equation 3-13 depends on the assumptions of either back and forth tunneling of electron (adiabatic polaron), in this case $m=1$, or single hopping from one site to the next (non-adiabatic), where $m=-1.5$. With low temperature conductivity measurements (down to 30 K), with donor doped BaTiO₃, Iguchi [75] approximated the conductivity with a similar equation as Equation 3-13 with $m=-1.5$. The author concluded that in the low temperature range, conduction in BaTiO₃ was due to hopping motion of non-adiabatic small polarons. According to Iguchi, the activation energy for this conduction was 0.07 eV, while, Cox [76] reported 0.15 eV. Thus, assuming this energy for SrBIT electron mobility reduces the acceptor level to 1.7 eV. The existence of small polarons in Bi₄Ti₃O₁₂ single crystals was proposed by Myasnikova [77] as the explanation for an optical absorption band.

3.4.2 Charging current of SrBIT

In section 3.5.3, the possibility to simulate the electrical impedance of SrBIT in the frequency domain with distributed systems will be discussed in details. Interconnection between frequency-domain and time-domain relaxation functions was given by Alvarez [71]. According to this author for systems described in the complex plane by distributed relaxation such as Havriliak-Negami, the best description in the time-domain is a stretched exponential known as Kohlrausch-Williams-Watts (KWW) function, Equation 3-14.

$$f(t) = \exp\left[-\left(\frac{t}{\tau}\right)^\beta\right] \quad \text{Equation 3-14}$$

An example of current transient for undoped SrBIT at 120°C is given in Figure 3-11 together with exponential and stretched-exponential approximations. It is clear from this figure that the long time region is better matched with the stretched-exponential compared to the simple exponential. The exponent β of the stretched-exponential of Figure 3-11 was arbitrarily fixed at 0.2. It is found from Figure 3-11 that the calculated relaxation time depends strongly on the choice of the relaxation function. According to the exponential function, the relaxation time is 200, while it is only 20 for the stretched-exponential. This changes a lot the calculated grain boundary permittivity according to Equation 3-19.

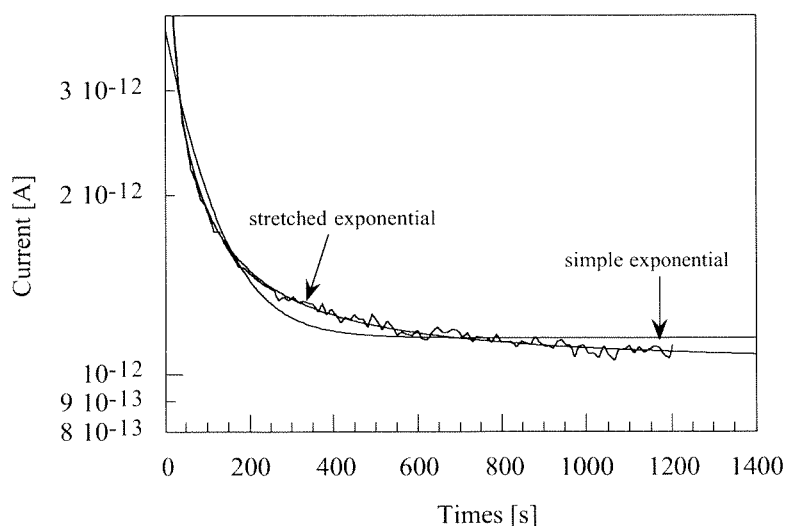


Figure 3-11: charging current for undoped SrBIT at 120°C (solid line) approximated with an exponential (Debye-type relaxation) and stretched exponential.

Thus, the choice of an appropriate model is a strong requirement that has to be investigated in details. The information given by the DC technique is unfortunately not sufficient to define the right equivalent circuit. Impedance analysis described in the second part of this chapter will be used instead.

3.4.3 Calculation of grain and grain boundary conductivities

Calculation of the effect of grain boundary conductivity on the overall behavior of DC conductivity has been realized by Näfe [70] starting from the bricklayer model for ZrO₂. The equation for conductivity proposed by Näfe, Equation 3-15, involves grain size (D), grain boundary thickness (d), enthalpy for grain and grain boundary conduction ΔH_{grain} and ΔH_{gb} respectively and the pre-exponential factors for the Arrhenius expressions of grain and grain boundary conduction, a_g and a_{gb} .

$$\sigma = \frac{2\left(\frac{d}{D}\right)\frac{d}{D}a_{gb}\exp\left(\left(-\frac{\Delta H_{gb}}{RT}\right) + \left(\left(\frac{d}{D}\right)^2\left(2 + \frac{d}{D}\right) + 1 + \frac{d}{D}\right)a_{gb}\exp\left(-\frac{\Delta H_{grain}}{RT}\right)\right)}{T\left(1 + \frac{d}{D}\right)^2\left(1 + \frac{d}{D}a_g\exp\left(\frac{(\Delta H_{gb} - \Delta H_{grain})}{RT}\right)\right)}$$

Equation 3-15

Equation 3-15 describes three different regimes as the temperature increases 1) at low temperature the grain boundary to grain boundary paths limit the conductivity. 2) In an intermediate range the current flows through the grain-to-grain boundary paths. 3) At elevated temperature, the conductivity of the GB is so low that it limits again the total conductivity (in the G-GB paths). The Arrhénius plot for Equation 3-15 is actually bend at both ends.

Equation 3-15 was applied to conductivity measurements of undoped SrBIT, the result is shown in Figure 3-12. The agreement of the approximation with the measurements is quite good. The approximation parameters obtained with this model are given in Table 3-1.

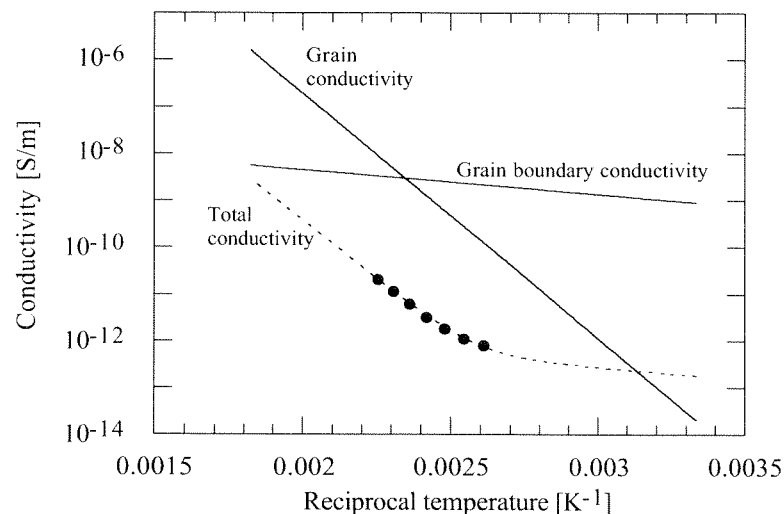


Figure 3-12: electrical conductivity of undoped random oriented SrBIT (filled circles) versus reciprocal temperature together with Näfe model (dashed line). Grain and grain boundary conductivities were calculated with parameters obtained from the approximation.

Due to the complexity of Equation 3-15, it was not attempted to apply any least square fitting to it, therefore parameters given in Table 3-1 are only indicative. The calculated grain boundary thickness to grain size ratio is 10^{-4} , it is a plausible value. For 1 μm large grains, it gives 10 \AA thick boundaries that is within the order of magnitude of cell parameters ($a \approx 5.44 \text{ \AA}$ and $c \approx 41 \text{ \AA}$). Calculation of grain and grain boundary conductivities reveals that conduction would be dominated by grain boundaries in the low temperature range and by grains in the higher range.

This mechanism creates the curve bending observed in Figure 3-12. The calculated activation energy for conduction in grains is about 1 eV as already found in section 3.4.1. In comparison, the activation energy for grain boundary conduction is much smaller, as calculation gives 0.1 eV.

Table 3-1: approximation of conductivity measurement using Näfe model.

Parameter	Approximation value
d/D	10^{-4}
a_g	$5.5 \cdot 10^3$
ΔH_g	1 eV
a_{gb}	$5 \cdot 10^{-8}$
ΔH_{gb}	0.1 eV

In section 3.3.2, it was demonstrated that the measured charging current might be caused by a non-Debye relaxation. It was proposed that a set of two distributed relaxations would better describe the real behavior of SrBIT. However, the Debye-relaxation has the advantage to be simulated with a simple parallel RC, Figure 3-3, circuit that allows calculation of a resistive and a capacitive component from the measured relaxation time. Therefore, in a first attempt to extract the grain and grain boundary permittivity, SrBIT will be simulated with two RC elements, corresponding to two ideal Debye-type relaxations. For one RC equivalent circuit, the relaxation time is simply found with:

$$\tau = RC \quad \text{Equation 3-16}$$

From the ideal bricklayer model it can be shown [62] that the macroscopic capacity used for equivalent circuit simulation, as in Equation 3-16, is related to grain boundary permittivity with:

$$C_{\text{equivalent}} = 3 \frac{\epsilon_{gb} \epsilon_0}{x_{gb}} \frac{t}{A} \quad \text{Equation 3-17}$$

where x_{gb} is the grain boundary volume fraction; t and A are macroscopic thickness and area of the sample. In addition in the bricklayer model the grain boundary volume fraction, x_{gb} , is given by:

$$x_{gb} = \frac{2d}{D} \quad \text{Equation 3-18}$$

Thus, with grain boundary conductivity it is in principle possible to calculate the grain boundary permittivity, with the following expression:

$$\epsilon_{gb} = \frac{2}{3\epsilon_0} \frac{d}{D} \tau \sigma \quad \text{Equation 3-19}$$

At 120°C, the measured relaxation time of undoped SrBIT is 200 seconds and the grain boundary conductivity at this temperature according to Näfe model is $2.3 \cdot 10^{-9}$ S/m, according to Table 3-1. If d/D was 10^{-4} , the calculated grain boundary permittivity would be about 3. The same analysis can be applied to grain permittivity, without $x_{gb}/3$ weighting. Relaxation time for grain is unknown, but should be less than 10^{-6} s as it was not possible to measure it. Thus with a conductivity of $2.8 \cdot 10^{-10}$ S/m, the grain permittivity of undoped SrBIT at 120°C should be less than $3 \cdot 10^{-5}$. This value is quite unrealistic and is another good indication that assuming a Debye-type grain relaxation with a relaxation time smaller than 10^{-6} second is wrong. This analysis shows that separate calculation of grain and grain boundary permittivity of SrBIT is not possible without more detailed knowledge of the relaxation.

It is well known that Aurivillius phases are very anisotropic, therefore the electrical conductivity in the crystallographic (001) direction should be different from the conductivity in the (100) or (010) directions. Since no single crystals were available during this work, conductivity values along crystallographic directions are not available. In replacement, hot forging was used to prepare textured samples. These samples have been described in Chapter 2. For hot forged ceramics, there are two significant directions: the *c* direction and the *ab* plane direction. In the next section, the electrical conductivity measured in both directions will be presented.

3.4.4 Conductivity of Hot Forged Ceramics

DC conductivities of *ab* plane and *c* oriented SrBIT is presented in Figure 3-13. According to this figure, it is clear that conductivity in the *ab* plane direction is much higher than conductivity in the *c* direction, it is actually one order of magnitude greater in the *ab* plane direction than in the *c* direction. The activation energies measured in both directions are identical; it is 1.02 eV in the *ab* plane direction and 1.01 eV in the *c* direction. This supports the assumption of a common charge transport mechanism in both directions. This transport mechanism is restricted in the *c* direction. This indicates that either Bismuth oxide layers or perovskite units carry most of the conductivity. Compared to high temperature impedance measurements, Figure 3-14, the activation energies measured at low temperature with a DC method are smaller. The activation energies measured with the impedance method above 450°C are 1.63 eV in the *c* direction and 1.44 eV in the *ab* plane direction. Increase of the activation energy for conduction is seen as a bending of the conductivity curve as temperature is decreased, Figure 3-15. Such bending could be explained by a grain boundary-controlled conductivity in the low temperature range as discussed in section 3.4.3, while the high temperature region would be grain-controlled, as presented in section 3.4.3 and in Figure 3-12.

Electrical conductivity measurements of SrBIT in *ab* plane and *c* directions are unfortunately not sufficient for a definitive identification of the component, which limits the conductivity, i.e. Bismuth oxide layers or perovskite units. However, as determined in the last chapter of this work, conduction in SrBIT at elevated temperature is partly ionic. The ionic transport should occur in the Bismuth oxide layers, since oxygen vacancies in Aurivillius phases are mostly created in this part of the structure [78]. Regardless of charge carriers, according to Figure 3-14, either Bismuth oxide layers or perovskite units act as conduction inhibitors. If conduction is ionic and oxygen

vacancy concentration is higher in the Bismuth oxide layer, then perovskite units can be seen as limiting conductivity, when measured in the c direction.

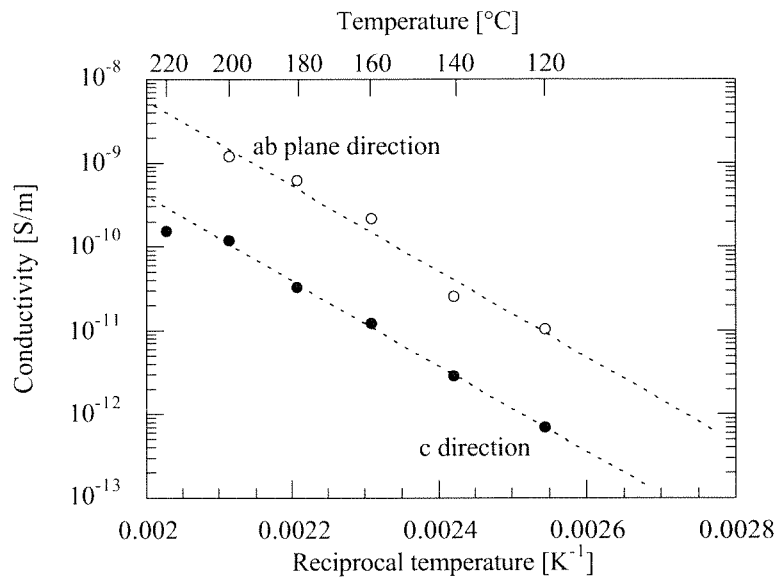


Figure 3-13: electrical conductivity versus temperature of, ab plane and c oriented undoped SrBIT.

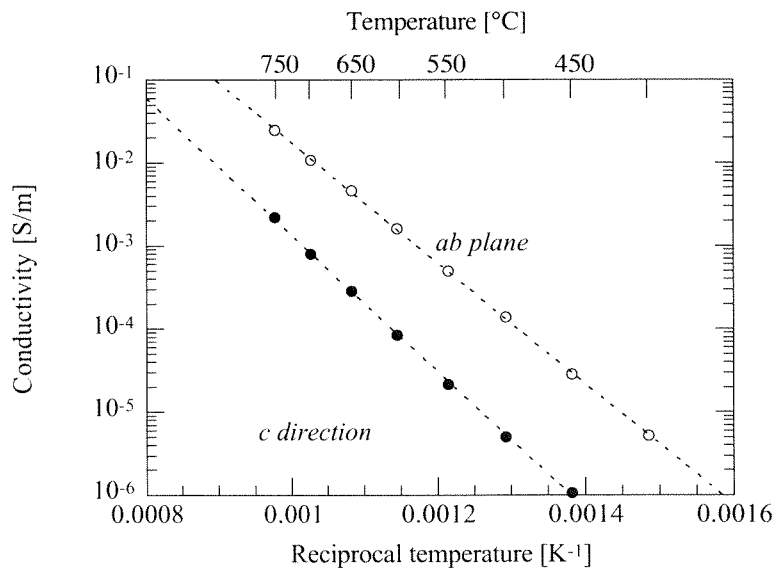


Figure 3-14: conductivity of undoped SrBIT at high temperature measured in the c direction (filled circles) and in the ab direction (open circles) from low frequency extrapolated AC measurements.

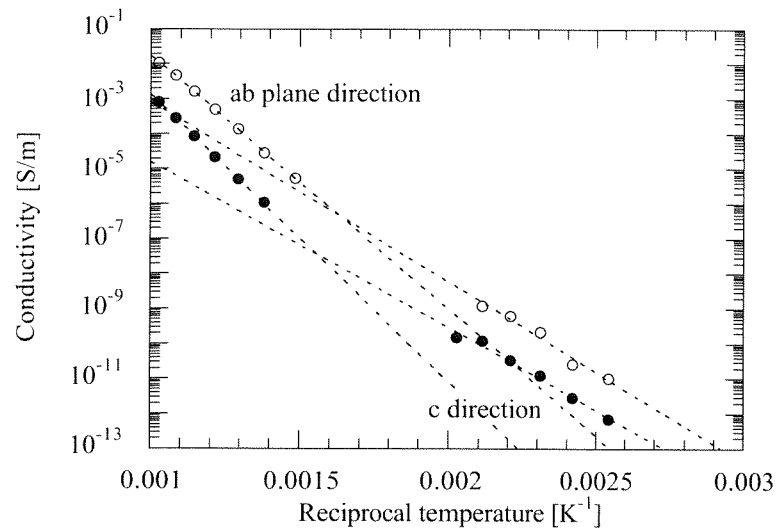


Figure 3-15: electrical conductivity of undoped SrBIT measured in the *ab* plane direction (open circles) and *c* direction (filled circles) with DC method (low temperature range) and low frequency extrapolation of AC method (higher temperature range).

The ferroelectric polarization vector of SrBIT [24] lies in a plane parallel to the Bismuth oxide layers. Thus, around the ferroelectric phase transition (540°C), the dielectric permittivity of SrBIT is higher in the *ab* plane direction than in the *c* direction, Figure 3-16. This may also be due to the effect of the Bismuth oxide layers that break coherence between ferroelectric perovskite units. In addition, difference in polarizability can be seen in the piezoelectric properties, Figure 3-17. Piezoelectric coefficient parallel to the Bismuth oxide layers (*ab* plane direction) is about 21 pC/N and only 8 pC/N in the perpendicular direction. Figure 3-17 is actually presented here to reinforce the illustration of the anisotropy of SrBIT. Piezoelectric properties of SrBIT will be discussed in details in Chapter 5 together with the experimental measurement procedure.

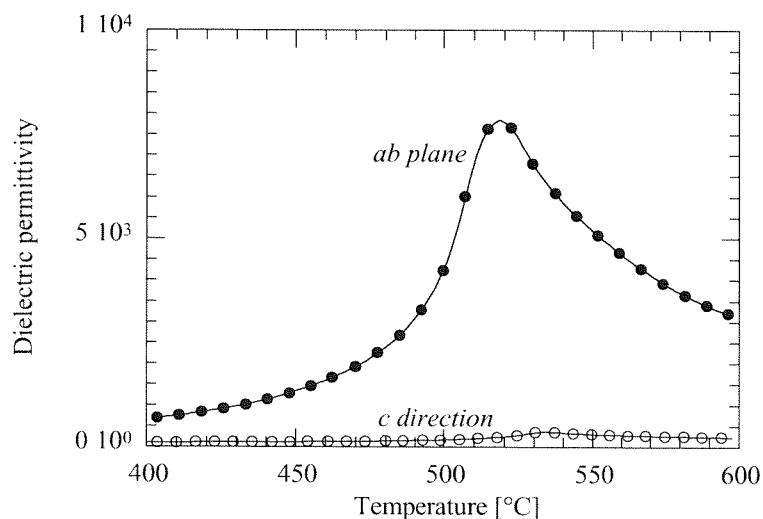


Figure 3-16: dielectric permittivity calculated from C_p measurements for undoped SrBIT measured in the *ab* plane direction (filled circles) and *c* direction (open circles).

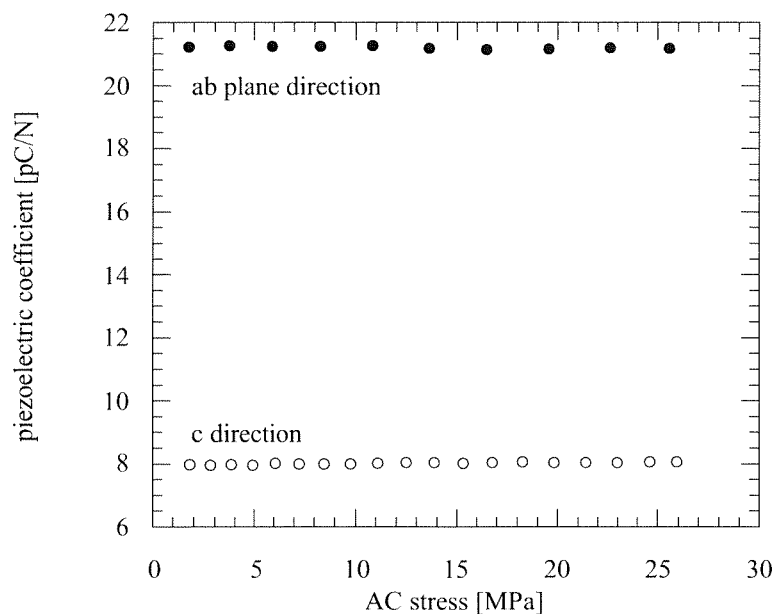


Figure 3-17: longitudinal piezoelectric coefficient versus applied stress (AC field) of undoped SrBIT at room temperature at 1Hz in the *ab* plane and *c* direction. Poling was performed along measured direction.

The anisotropy in electrical conductivity, permittivity and piezoelectricity described in this paragraph will be discussed in Chapter 5 as a basis for the occurrence of a piezoelectric relaxation that has been measured in SrBIT.

Acceptor and donor doping effect on conductivity of SrBIT will be discussed in the next two sections. Doping modifies carrier and point defect concentrations. Conductivity stabilization effect of acceptors and in particular Manganese at low oxygen partial pressure is already known for BaTiO₃, it was necessary to verify it for one Aurivillius phase. However, prior to oxygen controlled conductivity measurements, standard characterization (in air at low temperature) of doping effect is needed, this is shown in sections 3.4.5 and 3.4.6.

3.4.5 Acceptor Doping of SrBIT Random Oriented Ceramics

Manganese has been incorporated in SrBIT in substitution of Titanium on the B site of the perovskite sub-unit. As described in Chapter 2, Manganese was reacted with Titanium deficient SrBIT as MnCO₃. However, it was shown that the more likely oxidation states of Mn in BaTiO₃ were Mn³⁺ and Mn⁴⁺ depending on the oxygen partial pressure [49]. Therefore, the nominal chemical formula of Mn doped SrBIT was written as SrBi₄Ti_{4-y}Mn_yO₁₅. The actual incorporation of Manganese inside SrBIT lattice was demonstrated with the orthorhombicity factor in Chapter 2, Figure 2-21. According to Figure 2-21, Manganese substitution progressively strains the crystallographic cell in the *a-b* plane.

When Manganese is in the Mn^{3+} state on the Ti^{4+} site, it acts as an acceptor, providing holes. Thus, in case of p-type conductivity, the overall conductivity level should increase, if the mobility is not affected. This is actually true, as shown in Figure 3-18 for DC conductivity measured at $220^\circ C$; the electrical conductivity increases as Manganese concentration increases above 0.5 mol.%. If the conductivity of undoped SrBIT in air at room temperature was n-type, it would explain the initial decrease of conductivity seen in Figure 3-18; the second part of the curve would then be explained by a p-type regime. However, according to this idea donor doping should increase conductivity in the same doping range, this is actually not true, Figure 3-21. Another possibility would be that Manganese incorporation into SrBIT lattice would progressively create Mn^{3+} deep hole traps. As a consequence, hole mobility and electrical conductivity would then decrease. Nevertheless, oxygen controlled conductivity measurements presented in Chapter 4, bring another explanation for the occurrence of the conductivity minimum. As explained in Chapter 4, Manganese doping lowers the slope of the conductivity versus pressure curve. Since acceptor doping also shifts the conductivity minimum (of the $\sigma(pO_2)$ curve), the behavior depicted in Figure 3-18 can be easily understood with the aid of Figure 3-19.

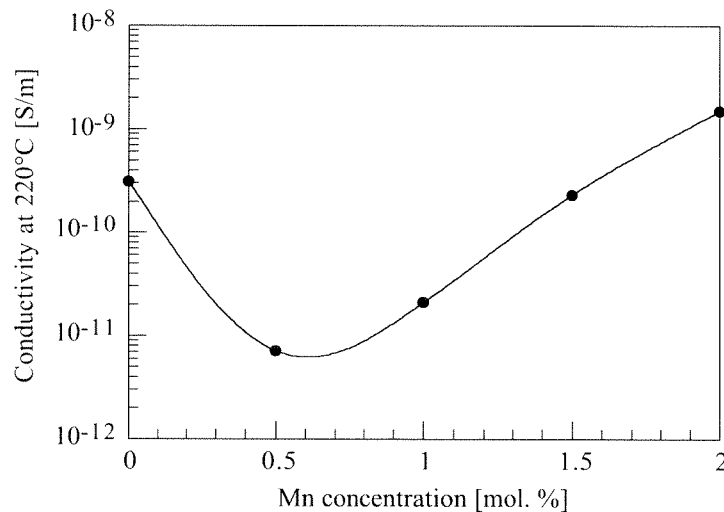


Figure 3-18: DC conductivity measured at $220^\circ C$ versus Mn concentration.

Typical conductivity versus oxygen partial pressure curves for undoped and Mn doped SrBIT are schematically shown in Figure 3-19. In this picture, the two effects of Manganese doping are presented: decrease of the slope and shift of the minimum. Thus, considering conductivity measurement in the p-type region (dashed line), the conductivity of undoped SrBIT is located at point A. For slightly doped SrBIT, the conductivity decreases to point B, due to the slope change and small minimum shift. Finally, for larger Manganese concentrations, conductivity increases to point C, because of a large minimum shift. The shift of the conductivity minimum (pO_2^0) is predicted for acceptor-controlled conductivity (see Chapter 4 for details) with Equation 3-20.

$$p_{O_2}^0 = 4 \left[\frac{\mu_n}{\mu_p} \right]^2 \frac{1}{[A]^2} \frac{K_n}{K_p} \exp\left(-\frac{(\Delta H_n - \Delta H_p)}{k_B T} \right) \quad \text{Equation 3-20}$$

In this equation μ_n and μ_p are electron and hole mobilities, K_n and K_p are mass-action constants for reduction or oxidation reaction and $[A^{\cdot}]$ is the concentration of acceptors. According to Equation 3-20, if $[A^{\cdot}]$ increases, pO_2^0 is decreased.

The simple mechanism proposed to explain the conductivity decrease observed for low Manganese concentrations is schematically presented in Figure 3-18.

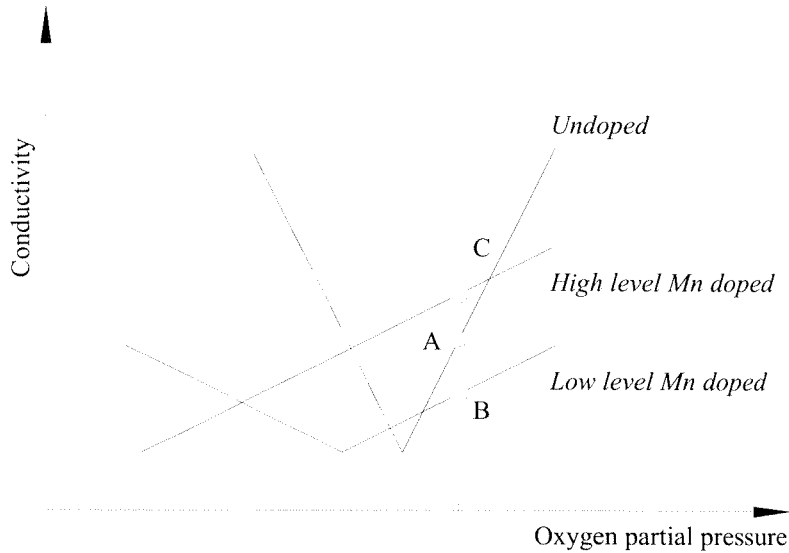


Figure 3-19: schematic of typical conductivity versus oxygen partial pressure curves for undoped, slightly Mn doped and heavily Mn doped SrBIT as determined in Chapter 4.

The hypothesis of lowered hole mobility due to deep hole traps made by acceptor centers is not supported by the measured decrease of activation energy for conduction, Figure 3-20. For 2 mol.% Mn doped SrBIT, the activation energy is only 0.5 eV in the low temperature range. It is about half the value of undoped SrBIT. Thus, Manganese defects would be rather shallow levels.

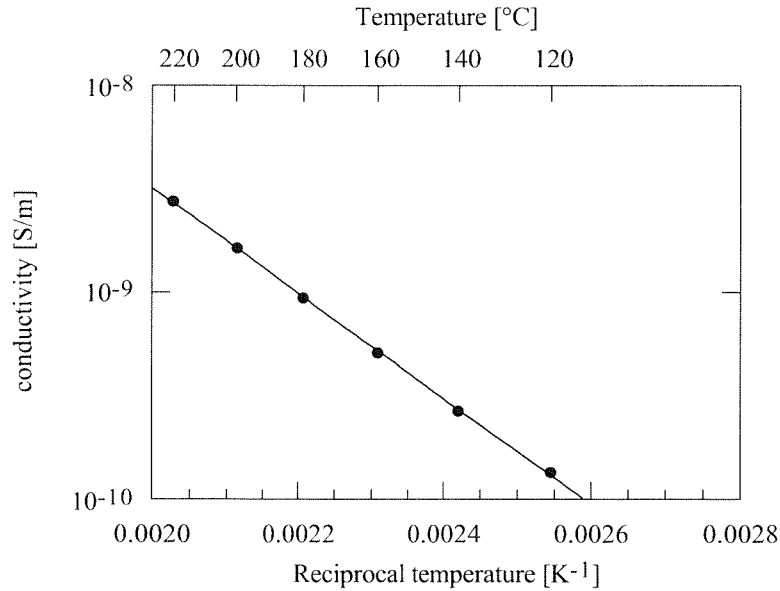


Figure 3-20: DC electrical conductivity versus reciprocal temperature for 2 mol.% Mn doped SrBIT.

Acceptor doping seems to increase DC conductivity, indicating a p-type conductivity, which should come with a conductivity decrease due to donor doping. It will be demonstrated in the next section, that donor doping with Niobium actually decreases the electrical conductivity of SrBIT at low temperature. Apparent complete compensation of the p-type conduction with Niobium is also possible as shown with reduced samples.

3.4.6 Donor Doping of SrBIT Random Oriented Ceramics

Donor doping with Niobium should act in the opposite direction compared to acceptor doping with Manganese. The electrical conductivity of Niobium doped SrBIT at 220°C is presented in Figure 3-21. The effect of Niobium doping on the electrical conductivity of SrBIT is obvious from Figure 3-21; it actually decreases the conductivity of SrBIT. This decay is another proof for p-type conduction at low temperature in air. In the case of donors centers compensated by metallic vacancies (Bismuth vacancies), the concentration of charge carriers is written as Figure 3-20. Description of point defects for donor doped SrBIT is given in more details in Chapter 4. The expected behavior would be a power law.

$$p = (3K_O K_S)^{1/2} [Nb_{Ti}]^{-1/2} p_{O_2}^{+1/4} \quad \text{Equation 3-21}$$

where K_O is the mass-action constant for the oxidation equation, Equation 4-23 and K_S is the mass-action constant for the simultaneous Bismuth and Oxygen vacancy creation. In Equation 3-21, p_{O_2} is the oxygen partial pressure of the surrounding atmosphere and $[Nb_{Ti}]$, the concentration of Niobium. According to Equation 3-21, the concentration of electrons is proportional to $[Nb_{Ti}]^{-1/2}$. This calculated exponent for a power law is actually -1.5, Figure 3-21. This experimental result could affect the electroneutrality equation that was written as the direct

compensation of donors by Bismuth vacancies. However, those low temperature measurements reflect frozen defect states defined at higher temperature on cooling. Thus, these conductivities are not equilibrium values and therefore direct use of Equation 3-21 is not allowed. As an example, low temperature defect chemistry of oxides was treated by Sasaki [79] for ZrO_2 .

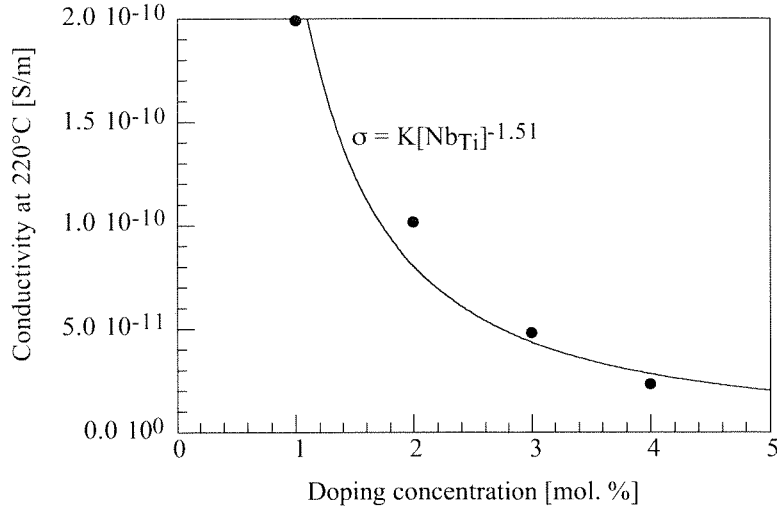


Figure 3-21: DC conductivity measured at 220°C (filled circles) versus doping concentration for Nb doped SrBIT in the as sintered state and power law curve fitting (solid line).

Annealing in flowing Oxygen followed by Argon annealing were performed to demonstrate the complete compensation of the acceptor centers within SrBIT by donors for the highest doping level. According to Figure 3-22, the electrical conductivity after high temperature annealing under reducing conditions is decreased for all Niobium concentrations except for the last one. This means that for these compositions at low temperature, SrBIT is still p-type. For the last composition however, all the acceptors have been compensated and the material is no longer p-type, but n-type. Providing that Niobium solubility is high enough, higher concentrations should show a conductivity increase in the oxidized state, but this was not tested during this work.

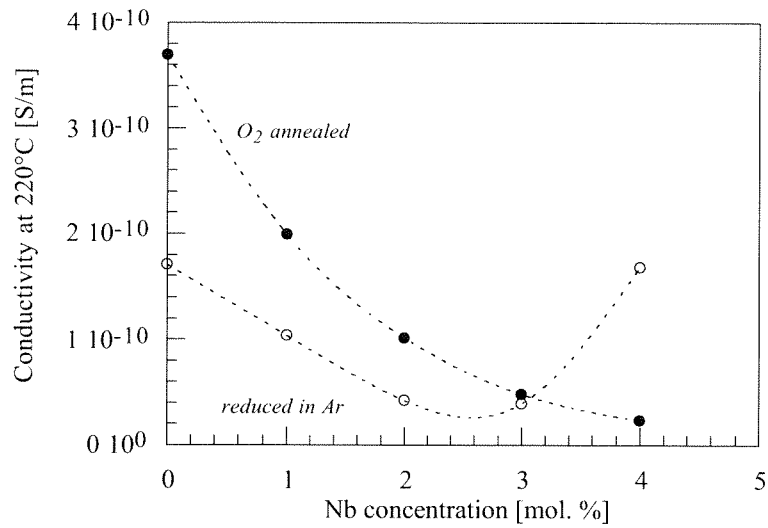


Figure 3-22: DC conductivity for Nb doped SrBIT at 220°C in the as sintered state (filled circles) and after annealing in reducing atmosphere (Ar) for 15 hours at 800°C (open circles).

DC conductivity measurements have been used to investigate the anisotropy and the effect of both acceptor and donor doping. It was also shown that this method was not suitable for a microstructural investigation, in contrast to extensive work made on SrTiO₃ by Vollmann and Waser. However, the second part of this chapter is dedicated to complex impedance analysis that may in principle help to determine grain and grain boundary contribution to the global conductivity.

3.5 IMPEDANCE ANALYSIS

3.5.1 Introduction

In this section, the static DC field is replaced by an oscillating one (called AC field) of amplitude U_0 and frequency f (or pulsation $\omega=2\pi f$). The current passing through the sample is recorded and both impedance absolute value Z and phase angle θ are calculated by the measurement system (we will not use the term impedance modulus to avoid any confusion with the modulus function, see below for its definition). The electrical impedance can be written in a complex form with a real and an imaginary part (Z' and Z'' respectively). The impedance can also be represented in the complex plane (Z'' versus Z'), which gives a semicircle for a single relaxation mechanism.

The interpretation of the measurements can be made using an equivalent electrical circuit. For dielectric characterization (using a conventional four probes LCR meter such as HP4284A), the equivalent circuit considered is usually made of one resistance and one capacitance assembled in parallel; The system calculates automatically what is called the parallel capacitance written C_p and resistance R_p . These two parameters are actually frequency dependent and do not have a simple physical meaning. As ceramics are made of grains and grain boundaries more complicated circuit should be used instead. Actually even in the case of crystals or glasses, if there exist many polarization processes, the equivalent circuit has to be modified. The choice of the right equivalent circuit is in fact the key issue of a good impedance analysis. In addition, since different equivalent circuits can produce the same electrical response, additional criteria, such as the modulus response, have to be involved in the building of the circuit.

There are basically two ways to modify the equivalent circuit: by either adding several discrete elements such as resistances or capacitances, in series or in parallel (we call these models multiple RC circuits) or replacing the perfect RC elements by distributed one. In the latter case, several empirical laws have been proposed: Cole-Cole, Cole-Davidson or Havriliak-Negami laws [62,63,80]. The most important feature of these laws is that the characteristic discrete time constant is replaced by a continuous distribution of time constant around a central value. These laws account for the depression of the semicircle and usually give better fittings than multiple RC models.

In this section, multiple RC equivalent circuit of SrBIT will be evaluated by studying both the temperature and oxygen partial pressure responses, and by checking the influence of the grain size. The observed behavior will be discussed in terms of grain and grain boundary conductivities.

However since only one single impedance semicircle could be clearly measured in SrBIT in the covered temperature (up to 1000°C), impedance (up to 1 M Ω) and frequency ranges (20 Hz to 1 MHz), additional contributions have been tracked with other methods such as modulus

representation, master curve building and use of special microstructures (grain oriented hot forged ceramics).

3.5.2 Definitions of basic functions

Impedance analysis will be conducted with the evaluation of different electrical functions (impedance, admittance, modulus, and permittivity) whose definition is given below. These functions are actually the expression of the same measurement: electrical current versus applied voltage. Analyzing those two signals with several mathematical tools such as complex representation and equivalent circuits will be the basis for the impedance analysis conducted in this chapter.

The convenient plane capacitor configuration was used for all impedance measurements: the opposite faces of a ceramic flat sample (disc or bar) were covered with two metallic layers as electrodes (mainly annealed Pt). An AC electric field ($U(t)$), of frequency ω and amplitude U_0 was applied on the electrodes, which induces a flowing current (I), Equation 3-22, of amplitude I_0 and phase angle δ through the sample. The complex impedance (Z), Equation 3-23, is defined as the ratio of the applied field to the flowing current. Its amplitude, written Z_0 or $|Z|$ and phase angle written δ are both frequency dependent.

$$\begin{aligned} U(\omega t) &= U_0 e^{i\omega t} \\ I(\omega t) &= I_0 e^{i(\omega t + \delta)} \end{aligned} \quad \text{Equation 3-22}$$

$$Z(\omega t) = \frac{U(\omega t)}{I(\omega t)} = Z_0 e^{-i\delta} \quad \text{Equation 3-23}$$

Both real and imaginary parts can be calculated with the modulus and the phase angle.

$$\begin{aligned} Z' &= |Z| \cos(\delta) \\ Z'' &= |Z| \sin(\delta) \\ |Z| &= \sqrt{Z'^2 + Z''^2} \end{aligned} \quad \text{Equation 3-24}$$

Sometimes the real and imaginary parts of the impedance called resistance and reactance respectively are written R (for Z') and X (for Z''). Other related immittance functions are: the admittance (complex reciprocal of impedance) written Y^* , the complex permittivity (ϵ^*) and the electrical modulus (reciprocal of permittivity) known as M^* . The relations between those functions are presented in Table 3-2 with μ and C_0 defined by Equation 3-25 for a plane capacitor of area A and thickness t .

Table 3-2: relations between the four basic immittance functions.

	M	Z	Y	ϵ
M	M	μZ	μY^{-1}	ϵ^{-1}
Z	$\mu^{-1} M$	Z	Y^{-1}	$\mu^{-1} \epsilon^{-1}$
Y	μM^{-1}	Z^{-1}	Y	$\mu \epsilon$
ϵ	M^{-1}	$\mu^{-1} Z^{-1}$	$\mu^{-1} Y$	ϵ

In Table 3-2, the constant μ is defined as:

$$\begin{aligned} \mu &= i\omega C_0 \\ C_0 &= \epsilon_0 \frac{A}{t} \end{aligned} \quad \text{Equation 3-25}$$

According to Table 3-2 the real and imaginary part of the electrical modulus is calculated with:

$$\begin{aligned} M' &= \omega C_0 Z'' \\ M'' &= -\omega C_0 Z' \end{aligned} \quad \text{Equation 3-26}$$

Similarly, the complex permittivity is obtained with:

$$\begin{aligned} \epsilon' &= \frac{1}{\omega C_0} \frac{Z''}{(Z'^2 + Z''^2)} \\ \epsilon'' &= \frac{1}{\omega C_0} \frac{Z'}{(Z'^2 + Z''^2)} \end{aligned} \quad \text{Equation 3-27}$$

As each of these functions are not similarly frequency weighted, for example it is better to use the modulus in the high frequency range and the impedance in the low frequency range. According to Kim's analysis of the impedance of BaBi₄Ti₄O₁₅ single crystals [31] the impedance representation in the complex plane was not sufficient to demonstrate the existence of two separate contributions to the impedance. Use of the modulus representation, however, highlights the high frequency range of the spectrum and revealed in the case of BaBi₄Ti₄O₁₅ the contribution of the Bismuth oxide layers [31], see Figure 3-26.

As a matter of fact, the measured electrical impedance of any system is the global response of this system to the applied field. In order to separate and identify the response in several components, the response has to be evaluated with the aid of an equivalent circuit. Such circuits can be made either of single electrical components as pure resistors or capacitors or have distributed elements (these components are defined with Equation 3-30, Equation 3-31 and Equation 3-32). At the end, both measured and simulated responses are compared and according to their agreement the equivalent circuit is accepted or rejected. In the next two sections, the

calculated response of both single and multiple component equivalent circuits will be presented.

3.5.3 Description of Equivalent Circuits

The first equivalent circuit to be considered is made of one pure resistor (R_0) and one pure capacitor (C_0) put in parallel. This elementary circuit is presented in Figure 3-23. Its electrical complex impedance can be written as Equation 3-27.

$$Z(\omega) = \frac{R_0}{1 + i\omega\tau} \quad \text{Equation 3-28}$$

where τ is a single relaxation time expressed by Equation 3-29. In the complex plane, the plot of the impedance is a perfect semicircle lying on the impedance real axis. This response is also called a Debye-type relaxation.

$$\tau = R_0 C_0 \quad \text{Equation 3-29}$$

The relaxation frequency (ω_R) is simply the reciprocal of the time constant τ . The impedance calculated with Equation 3-27 is represented in Figure 3-23 with arbitrary parameters. The resistor's value is directly given by the intercept of the impedance arc with the real axis in the low frequency range. The relaxation frequency corresponds to the maximum of the imaginary part.

Departure from pure Debye behavior is obtained if the discrete relaxation time is replaced by a continuous distribution of time constants around a central value τ_0 . For a symmetric distribution, the complex permittivity is now written as Equation 3-30.

$$Z(\omega) = \frac{R_0}{1 + (i\omega\tau)^{1-\alpha}} \quad \text{Equation 3-30}$$

This expression is called Cole-Cole function and it still gives a semicircle in the complex plane, though its center is depressed depending on the width of the distribution of time constants. This distribution is characterized by the parameter α .

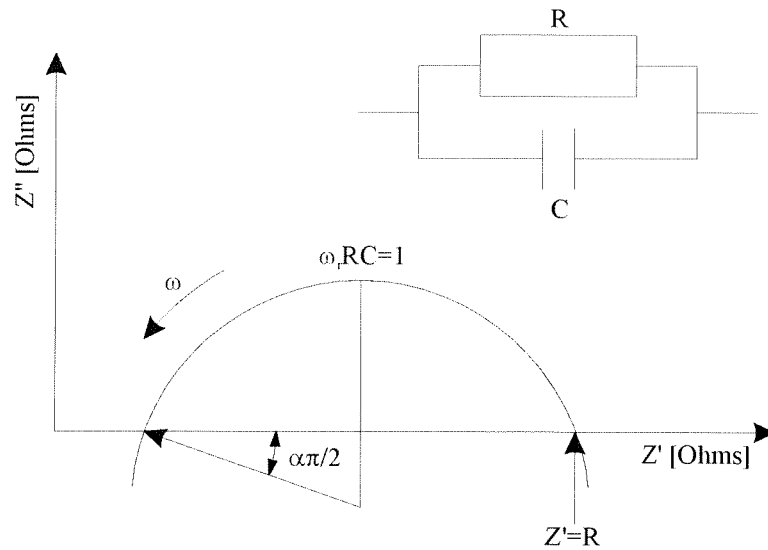


Figure 3-23: impedance in the complex plane in the case of a depressed semicircle corresponding to a simple R-C circuit made of one resistance R_0 and one capacitance C_0 in parallel.

A further step is to take a non-symmetric distribution of time constants as for the Davidson-Cole model; it modifies the complex permittivity with an extra exponent, written β :

$$Z(\omega) = \frac{R_0}{(1 + i\omega\tau)^{1-\beta}} \quad \text{Equation 3-31}$$

It gives a pear-shaped form to the semi-circle. Havriliak and Negami gave the final generalization of the Debye relaxation as a combination of both Cole-Cole and Davidson-Cole expressions [62]:

$$Z(\omega) = \frac{R_0}{(1 + i\omega\tau)^{1-\alpha}} \quad \text{Equation 3-32}$$

Examples of Havriliak-Negami calculated impedance are given Figure 3-24 for arbitrary parameters. In this figure both semi-circle depression and asymmetry of the function are obvious.

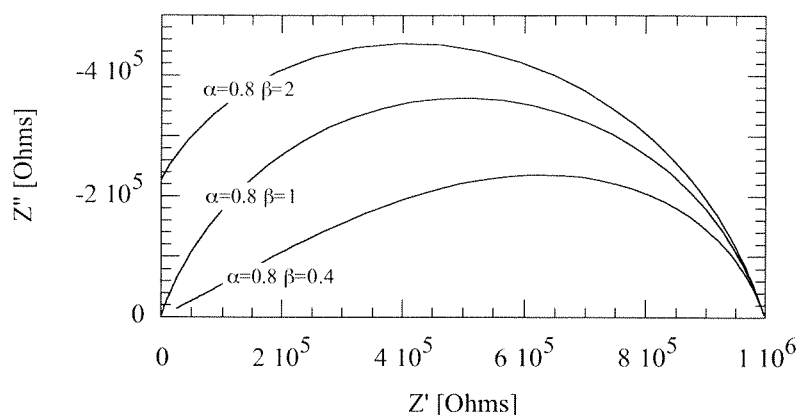


Figure 3-24: illustration of the impedance calculated with the Havriliak-Negami equation with arbitrary parameters.

Actually the Havriliak-Negami expression, Equation 3-32, reduces to Davidson-Cole, Equation 3-31, or Cole-Cole expression Equation 3-30, for $\beta=1$ and $\alpha=1$ respectively. This is the reason why both Cole-Cole and Davidson-Cole laws were not tested as such.

Distributed expressions are usually employed for glasses and polymers, which are continuous and homogeneous media, far from ceramics microstructure. However, since several authors reported distributed expressions for the impedance of Bismuth Titanates, there may exist one common feature that creates this distribution of relaxation processes in Aurivillius structures.

An alternative to distributed circuits that are actually difficult to justify theoretically is the combination of several discrete circuits. A complex circuit can actually be realized with the addition of several elementary circuits such as the one drawn in the top right of Figure 3-23. Such circuits will be called “parallel RC circuit” or “RC circuit” throughout this chapter. Each elementary circuit can then be identified with a microstructural element (e.g. grain, grain boundary, second phase). The influence of the electrode-ceramic interface can be taken into account too by adding its associated equivalent circuit.

Elementary components (resistor, capacitor) or circuit (e.g. parallel RC or distributed Havriliak-Negami) can be assembled in an infinite number of configurations. The simplest one are the series and parallel combinations, they were already described in the preceding section. Building a complex circuit with distributed elements will not be treated. In order to use several distributed circuits, as many isolated impedance arcs as distributed elements in the circuit should actually be measured. Otherwise, it is not possible.

For a system made of several RC elements connected in series, the impedance plot consists of several semicircles. For example in Figure 3-25, the impedance of an equivalent circuit made of two RC elements in series has been calculated with arbitrary parameters. Such circuit will be called “multiple RC circuit” throughout this work. For a ceramic, each one could be in principle attributed to any microstructural element. However semicircles may more or less overlap leading to a difficult interpretation of their origin, Figure 3-27. In some cases, it may be even almost

impossible to decide whether there are one or two contributions to the impedance. For three RC elements in series, the expression used is the summation of Equation 3-28, which gives Equation 3-33 for the real part and Equation 3-34 for the imaginary one.

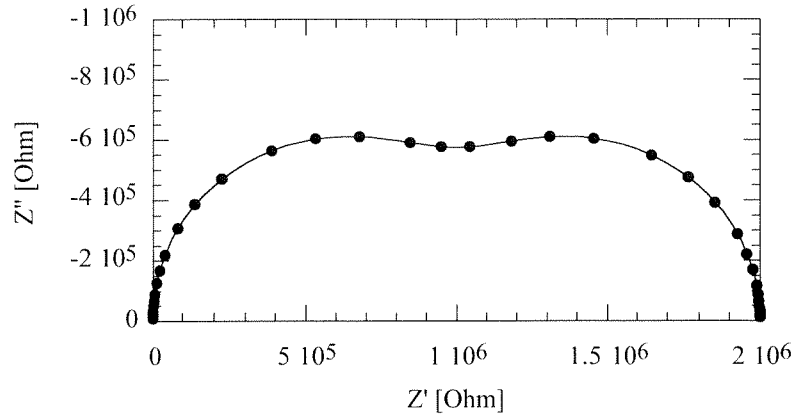


Figure 3-25: impedance in the complex plane of a system consisting of two parallel R-C element in series. This is a simulation calculated with $R_1=R_2=1\text{ M}\Omega$ and $C_1=10\text{ pF}$, $C_2=1\text{ nF}$.

$$Z'(\omega) = \frac{R_1}{(1 + \omega^2\tau_1^2)} + \frac{R_2}{(1 + \omega^2\tau_2^2)} + \frac{R_3}{(1 + \omega^2\tau_3^2)} \quad \text{Equation 3-33}$$

$$Z''(\omega) = \frac{\omega\tau_1 R_1}{(1 + \omega^2\tau_1^2)} + \frac{\omega\tau_2 R_2}{(1 + \omega^2\tau_2^2)} + \frac{\omega\tau_3 R_3}{(1 + \omega^2\tau_3^2)} \quad \text{Equation 3-34}$$

Depending on the values of the resistors and capacitors (R_i and C_i), it could be impossible to resolve distinctly two semicircles in the impedance complex plot but can be in the modulus plot. Such an example is given in Figure 3-26. In this figure, the impedance and modulus of a double RC circuit are calculated (no measurements are presented in Figure 3-26) with input parameters corresponding to the final analysis of Kim for $\text{BaBi}_4\text{Ti}_4\text{O}_{15}$ [31]. In this simulation, the impedance analysis gives only one semi-circle and the modulus representation gives two. In comparison, a single RC circuit would give a single semi-circle in both representations. Thus with the help of the modulus representation, the author chose a double RC circuit for a consistent description of $\text{BaBi}_4\text{Ti}_4\text{O}_{15}$ impedance.

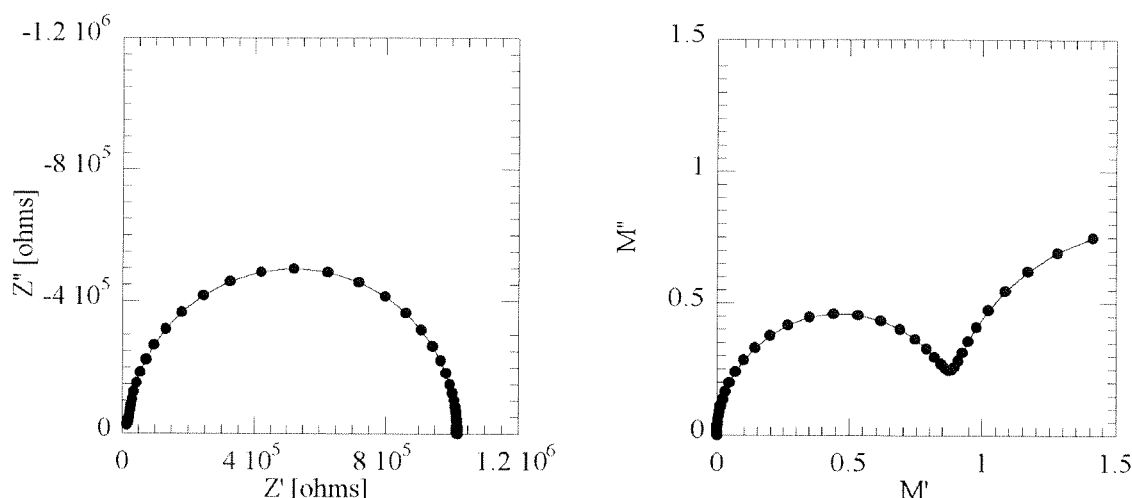


Figure 3-26: simulated impedance (left) and modulus (right) for a double RC circuit with following parameters: $R_1=1\text{ M}\Omega$, $C_1=10\text{ pF}$, $R_2=20\text{ k}\Omega$ and $C_2=5.7\text{ pF}$ according to Kim's analysis of $\text{BaBi}_4\text{Ti}_4\text{O}_{15}$ [31].

More complicated circuits can obviously be built with different configurations, in principle it is also possible to combine discrete elements with distributed one. But the physical significance of the circuit becomes more and more difficult to find as the number of fitting parameters increases. That is the reason why, we tested separately the two kinds of models.

Opposite to the impedance analysis of Zirconia as measured by Kleitz [81] where three contributions identified with grains, grain boundaries and electrodes are easily seen, impedance measurement of Bismuth Titanates ceramics mostly provides only one single semicircle. In these conditions, determination of the appropriate equivalent circuit is quite difficult. In the next section, examples of interpretation of impedance measurements will be given as a starting point for the analysis of SrBIT.

Literature Survey on Aurivillius Phases Impedance Measurements

The literature concerning the impedance analysis of Bismuth Titanates is not so rich. Most of the publications report a single impedance semicircle that is often interpreted with Cole-Cole expressions. There are a very few evidences of additional contributions seen in the complex plot of the impedance. Nevertheless no detailed work has been conducted on the impedance or on the modulus of those material, neither in air nor under controlled oxygen partial pressure. Surprisingly almost no author kept tracking of any second contribution associated with the existing grain boundaries in ceramics.

In the case of $\text{BaBi}_4\text{Ti}_4\text{O}_{15}$ [31] (similar structure to $\text{SrBi}_4\text{Ti}_4\text{O}_{15}$) the impedance measurements give a single contribution both perpendicular and parallel to the Bismuth oxide layers. Nevertheless, according to the authors, in the modulus representation, a second relaxation at higher frequency was identified. The main impedance semicircle was slightly depressed by 5° . The equivalent circuit given for two directions was different: a single RC element parallel to the Bismuth oxide layers and a double one in series perpendicular to them. In order to compare the parameters given by Kim (resistance and capacitance that are aspect ratio dependent), the corresponding conductivities were calculated with the given aspect ratios of the samples (750 m^{-1}

and 84 m^{-1} for the parallel and perpendicular directions respectively) and with the "volume fractions" of both phases equal to 0.2 for Bismuth oxide layers and 0.8 for the pseudo-perovskite units (two layers and eight pseudo perovskite units). The result of this simple calculation is shown in Table 3-3.

Table 3-3: calculation of conductivities from fitted resistances obtained by Kim for $\text{BaBi}_4\text{Ti}_4\text{O}_{15}$.

direction	R_1	σ_1	R_2	σ_2	t/A
parallel	200 k Ω	$3 \cdot 10^{-3} \text{ S/m}$	<u>190 kΩ</u>	$8.4 \cdot 10^{-4} \text{ S/m}$	750
perpendicular	1 M Ω	$6.7 \cdot 10^{-5} \text{ S/m}$	20 k Ω		84

As only one overall resistance is given for the parallel direction (R_1), R_2 (underlined) was calculated with the conductivity measured in the perpendicular direction. Since R_1 and R_2 in the parallel direction are close to each other, it may be an indication that the Bismuth oxide layers control the conduction in the parallel direction. From Table 3-3, one can see that the conductivity of the Bismuth oxide layer would be about ten times greater than the conductivity of the pseudo-perovskite units ($8 \cdot 10^{-4} \text{ S/m}$ and $6.7 \cdot 10^{-5} \text{ S/m}$ respectively).

Another conclusion was made by Yi [33] for $\text{PbBi}_4\text{Ti}_4\text{O}_{15}$ single crystals. From DC conduction measurements, the author concluded that the Bismuth oxide layers act as a barrier against the charge transport, since the measured activation energy was higher (1.0 eV compared to 0.5 eV) and the conductivity lower (one order of magnitude) perpendicular to the layers. But as the electrical polarization of these materials is contained in the pseudo perovskite units [21,24], the highest capacity should be associated with this unit. As a matter of fact, the additional semicircle in the modulus plot as observed by Kim [31] has a much higher radius, which means a smaller permittivity. Since the conductivity of this second element was also greater, one can conclude that the Bismuth oxide layers are conductivity paths and not barriers.

Concerning the impedance of Bismuth Titanates ceramics, Huanosta [30] for $\text{Bi}_4\text{Ti}_3\text{O}_{12}$ observed only one contribution and claimed that the grain boundary conductivity was as high as the grain one, thus preventing the observation of a second relaxation. For single crystals, an additional semicircle was measured in the same work, but it was attributed to "boundaries" between crystalline layers. Several publications by A. R. James [25-29] on the impedance of Bismuth Titanates ceramics report only one semicircle. In $\text{SrBi}_2\text{Ta}_2\text{O}_9$ [28], it was shown that the observed relaxation was not a pure single Debye, since the peak of the imaginary part of both impedance and modulus do not coincide. But the choice of either multiple Debye relaxations or a single distributed relaxation still remains. The calculated depression angle α was 0.23. This angle was only 9° for $\text{SrBi}_5\text{FeTi}_4\text{O}_{18}$. But the apparent poor agreement of the measured curve with the Cole-Cole expression is an indication for additional contributions or for more complicated models such as the Havriliak-Negami expression. The impedance of the mixed ceramic system $(\text{Na}_{0.5}\text{Bi}_{0.5})_{1-x}\text{Ca}_x\text{Bi}_4\text{Ti}_4\text{O}_{15}$ was studied by Rama Sastry [34]. The semicircle for this material was discussed with a Cole-Cole expression. The α parameter varied from 0.7 to 0.95. In another paper by Srinivas and James [29] on $\text{Sr}_2\text{Bi}_4\text{Ti}_5\text{O}_{18}$, the impedance complex plot presents only one semicircle, with a slight deviation at low frequency. Unfortunately the results were not deeply discussed by the authors except the possibility of a grain boundary effect at low frequency.

A clear observation of several contributions in the impedance complex plot was made by T. C. Chen [32] on $\text{SrBi}_2\text{Ta}_2\text{O}_9$ and $\text{SrBi}_2\text{Nb}_2\text{O}_9$ ceramics. Below 400°C , a single semicircle was observed, that could be modeled by a single RC element ($\omega_R=3.25$ kHz) with an additional capacity in series. Above 400°C , a second element could be added and finally at 575°C parts of three semicircles could clearly be measured. In the latter case, the equivalent circuit was made of three RC components at 351 Hz, 10 kHz and 500 kHz respectively. They were attributed to grain, grain boundary and electrode effects. The temperature dependence of the grain and grain boundary conductivities were similar ($E_g=0.9$ eV). An important fact is that the author attributed the measured conductivities entirely to ionic conduction (transference number equal to one).

In summary, there are many reasons to account for the absence of additional (≥ 1) semicircles: the characteristic relaxation frequency may be too low or the corresponding impedance too high for the equipment (for example 20 Hz up to 15 MHz and up to 100 M Ω with HP4194A); if the capacitances are similar but the resistance different, the two curves may not be observed in the impedance plot but can with the modulus representation. This works for two RC in series but not for a parallel layout.

It is also very interesting to note that the impedance complex plot of Bi_2O_3 doped with 17 mole % of ErO_3 do not show any grain boundary arc neither [62]. The absence of grain boundary phase (in the sense of different composition, large concentration of impurities) was proposed by Macdonald to explain it. But, the effect of grain boundaries may also be related to the presence of depleted charge layers or non-ohmic behavior of grain boundaries.

3.6 RESULTS OF THE IMPEDANCE ANALYSIS

3.6.1 Equivalent Circuit Determination

This section deals with the first step of an appropriate equivalent circuit selection. The choice has been limited to series configurations of either discrete (single, multiple) or distributed (Havriliak-Negami) elements. These elements are made of a pure resistor (R) connected in parallel with a pure capacitor (C). The time constant associated with them is unique for discrete RC elements and it is distributed for Havriliak-Negami elements. They can be assembled in series to build multiple RC elements. Representation of the measured impedance of undoped SrBIT show immediately that a single RC circuit is not suitable as its calculated response is very different to the measured one, Figure 3-27. As discussed below, more complex circuits (multiple or distributed) actually provide better simulation

The electrical impedance of SrBIT has been measured at high temperature (450-700°C) from 20 Hz up to 1MHz. In this temperature range, almost a full semicircle could be measured. Below 450°C and above 700°C, the semicircle was incomplete and as the objective was to determine the parameters of the impedance curves, measurements outside this temperature window were not used. As the impedance analysis gives only one clear semi-circle (Figure 3-28), it is difficult to decide how many elements to use to fit the curve. But it is quite obvious from Figure 3-27 that a single element system is not suitable and addition of a second and a third element gradually improves the approximation of Z'' .

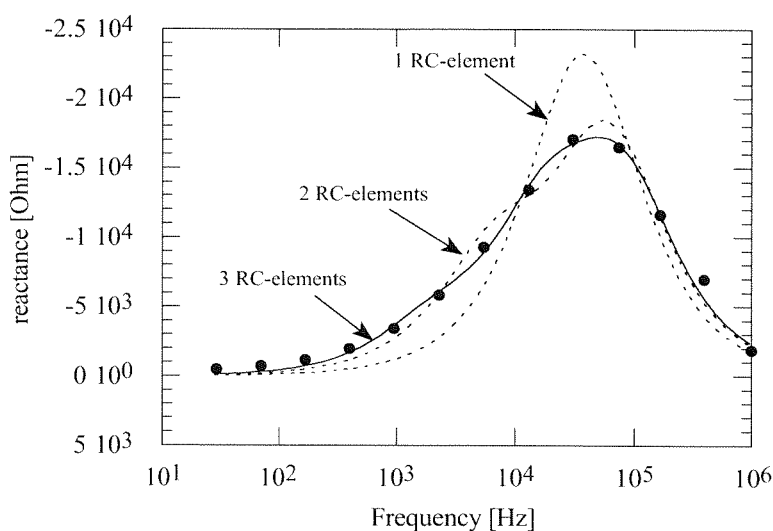


Figure 3-27: measured reactance at 600°C (filled circles) and curve fitting (solid and dashed lines) for undoped SrBIT using one, two or three RC- elements as indicated.

In the complex plane, Figure 3-28, the inadequacy of a single RC element is also clearly seen. Additional elements give the needed widening to the semicircle. But the large dip in the middle of the calculated curve of the 2-RC elements curve was actually not measured. Therefore, the 3-RC-elements fit seems to be the best (in that case the dip is smaller and its absence can be explained by a loss of precision).

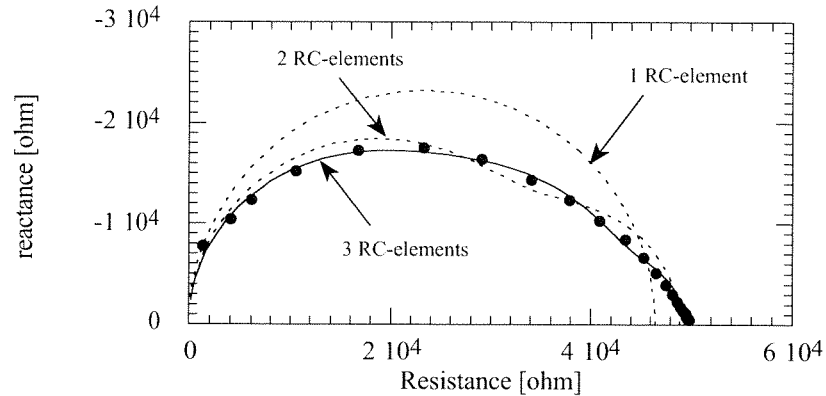


Figure 3-28: curve fitting of the impedance results (filled circles) in the complex plane for undoped SrBIT random at 600°C with one, two or three RC components.

However, the approximations given in Figure 3-28 are all made with discrete relaxations, each of them at its own characteristic frequency. They can be replaced by continuous ones as for the Cole-Cole model, Equation 3-30, (actually its equivalent for impedance) or the Havriliak-Negami model, Equation 3-32. The best fit is obtained with the Havriliak-Negami equation, Equation 3-32, that is non-symmetric and depressed relative to the real axis. The Havriliak-Negami expression is an empirical law that reduces to a pure Debye for $\alpha=\beta=1$.

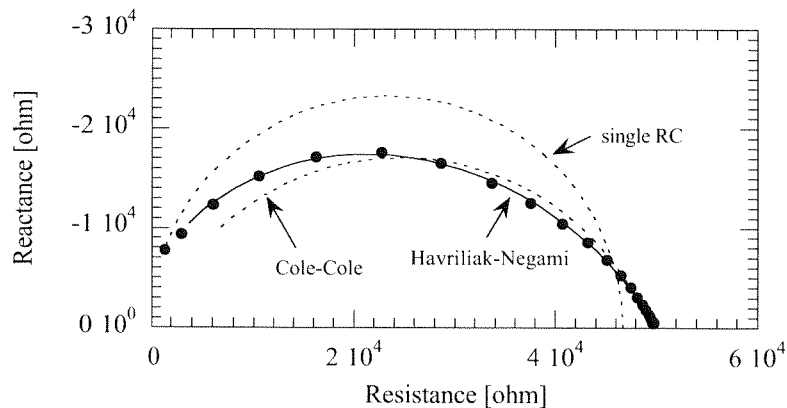


Figure 3-29: curve fitting of the impedance results (filled circles) in the complex plane for undoped SrBIT random at 600°C with distributed elements.

The best-fit parameters are summarized in Table 3-3 for the three basic models. The values are quite close to each other even if the fit is quite poor for the single RC circuit. The main difference in these results is the smallest capacitance value resulting from the Havriliak-Negami expression (26 pF for Havriliak-Negami compared to 91 and 96 pF for single RC and Cole-Cole respectively). As reported above the single RC circuit is not adequate and the single Havriliak-Negami is an especially good approximation of the measurement points. As the Cole-Cole expression can be considered as a special case of Havriliak-Negami, it will not be considered. Finally only the multiple RC circuit and the distributed Havriliak-Negami will be discussed in more details.

Table 3-3: fitted parameters for different relaxation equations corresponding to Figure 3-29.

Model	R	C	ω_R	α	β
Single RC	46 k Ω	91 pF	38 kHz	1	1
Cole-Cole	49 k Ω	96 pF	34 kHz	0.79	1
Havriliak-Negami	50 k Ω	26 pF	123 kHz	0.65	2.05

3.6.2 Detailed Evaluation of the Havriliak-Negami Model

It is obvious from Figure 3-28 and Figure 3-29 that simulation of the impedance response of undoped SrBIT with one distributed element such as Havriliak-Negami expression is very close to actual measurements. Additional agreements were also found between extracted resistance and capacitance with different conductivity measurements (DC conductivity at low temperature, Figure 3-31) and ferroelectric behavior, Figure 3-32. Thus, this paragraph will demonstrate that an equivalent circuit made of one distributed element can simulate two important features of SrBIT: Arrhenius behavior of conductivity and ferroelectric anomaly at 530°C.

The first analysis will be conducted with a single distributed element of the Havriliak-Negami expression (more general law). The parameters that can be extracted from this law are a resistance, a capacitance and two exponents. The exponents describe the width of the distribution of the time constants. As commonly observed, the calculated resistance, Figure 3-30, has an Arrhenius behavior with activation energy of 1.24 eV. No change of slope around the ferroelectric phase transition can be reported with those results because of a coarse temperature step (50°C). Compared to low temperature measurements, the results obtained with this first model are coherent, Figure 3-31.

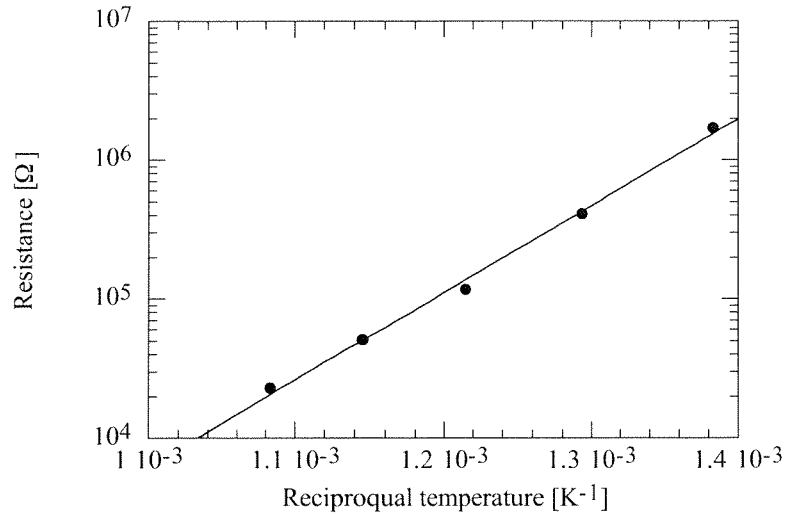


Figure 3-30: associated resistance for single distributed element (Havriliak-Negami) for undoped SrBIT ceramics from 450°C up 650°C.

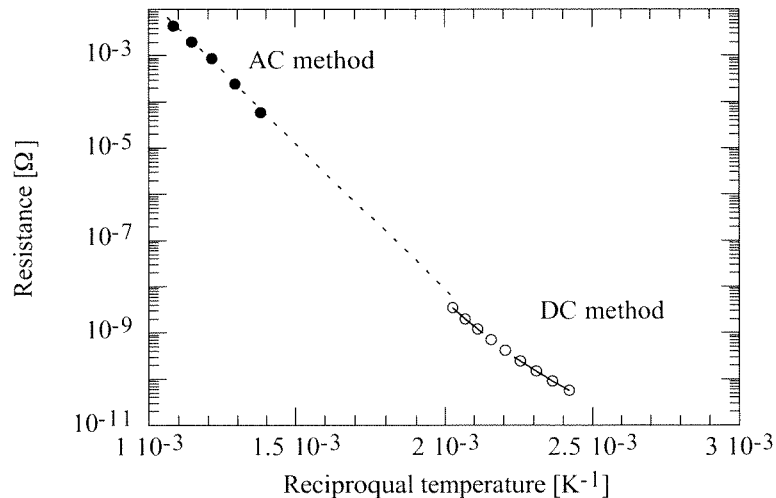


Figure 3-31: comparison between low temperature DC measurements and high temperature AC calculations for undoped SrBIT ceramics.

The capacitance associated with one distributed element at several temperatures is presented in Figure 3-32. Despite a low temperature resolution, a clear capacitance maximum is seen around 530°C, this temperature is identical to the ferroelectric phase transition temperature measured with LCR meters, when selecting “ C_p ” measurement, Figure 3-33. However, a major difference between these two measurements is that the capacitance calculated with Havriliak-Negami equation is frequency independent and can be used to simulate the whole spectrum, while C_p is measured at every frequency using the bridge.

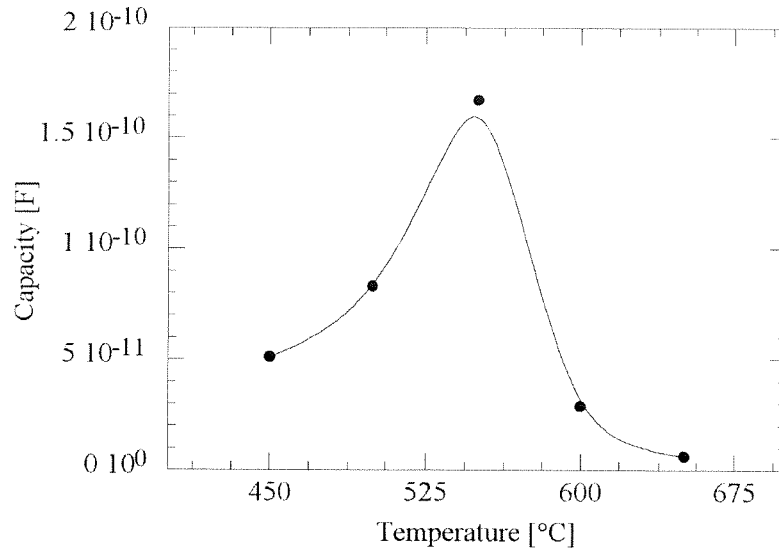


Figure 3-32: associated capacity for single Havriliak-Negami element for undoped SrBIT ceramics from 400°C up to 650°C.

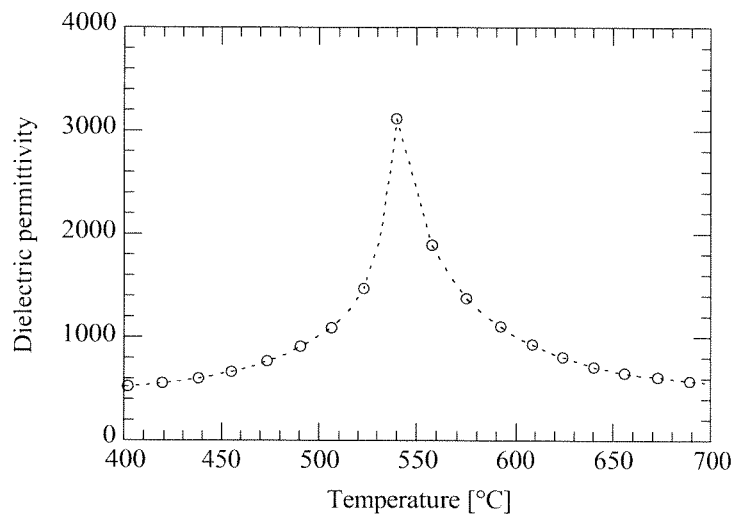


Figure 3-33: dielectric permittivity as a function of temperature for undoped SrBIT at 1 MHz. This figure can be compared with data in Figure 3-32 determined from Havriliak-Negami equations.

As the Havriliak-Negami is an empirical model, the temperature dependence of the exponents cannot be predicted. However those two exponents are modified as the temperature changes, Figure 3-34.

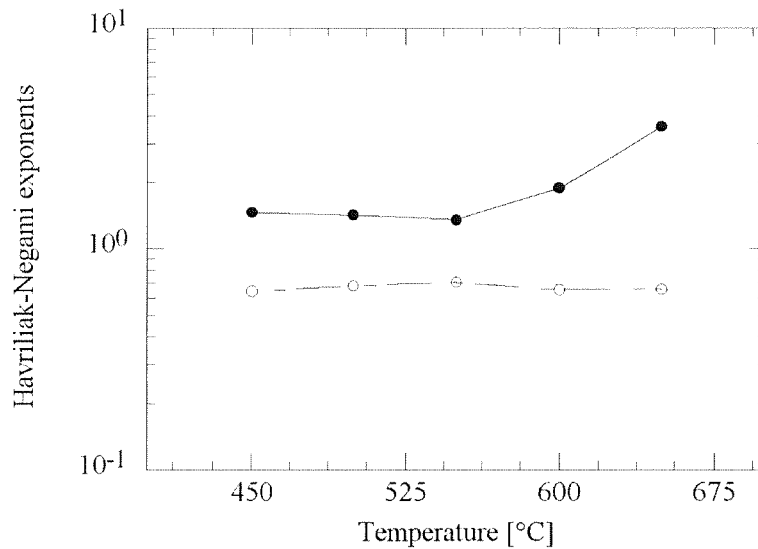


Figure 3-34: Havriliak-Negami exponents α (open circles) and β (filled circles) for a single distributed element model for undoped SrBIT from 450°C up to 650°C.

The very large value of the second exponent (β) is somewhat suspicious, since it is usually between 0 and 1. This could be a strong indication of the failure of this first model. However, the impedance semicircle is not completely resolved at elevated temperature, because the characteristic relaxation frequency leaves the covered frequency window. This may explain the determination of large Havriliak-Negami exponents as shown in Figure 3-34.

3.6.3 Undoped SrBIT Ceramics-Model with Three RC Components

The second way to interpret the impedance semicircle is to use an equivalent circuit made of three non-distributed RC elements in series. Thus, with each of these elements, a characteristic resistance and capacitance can be calculated. The associated relaxation frequency (ω_R) is then simply the inverse of the product $R_i C_i$. The results of this approach for an undoped SrBIT ceramic are given in Figure 3-35 and in Figure 3-36. The fitting results are three pairs R_i and C_i for each temperature; they were associated with three mechanisms (1, 2 and 3) to form coherent temperature dependencies (no cusp if Arrhenius behavior). However, it is still not clear whether the couples of mechanism 1 and 2 should not be exchanged at 600°C, 650°C and 700°C. this would suppress the capacitance anomaly for the first mechanism and increase it for the second.

The activation energies calculated for the three elements are 1.31, 1.36 and 1.59 eV respectively. They are quite close to each other, thus indicating a common physical origin of the associated conduction mechanism. For the first component, the curve can be divided into two regions: below 550°C and above. In the lower temperature region the activation energy is only 0.6 eV and 1.31 eV in the other region.

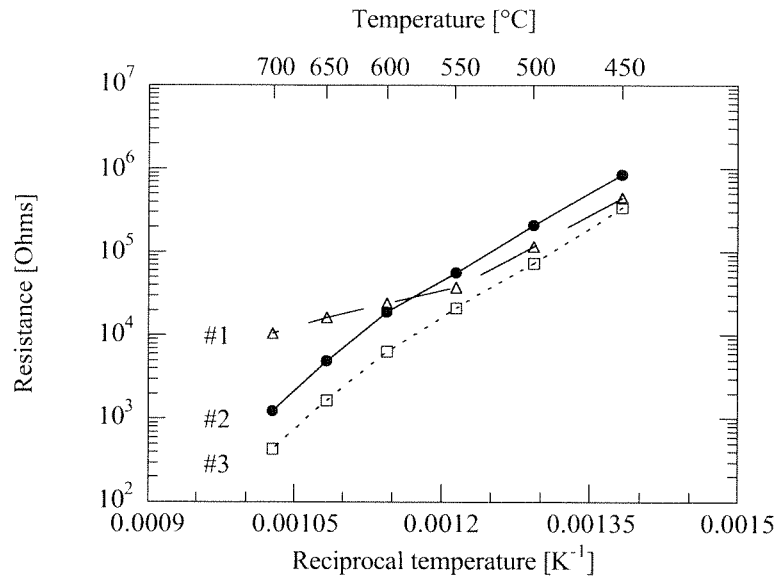


Figure 3-35: calculated resistance associated with each of the three RC components for undoped SrBIT ceramics.

The representation of the capacitance, Figure 3-36, gives additional information on the nature of the different relaxations. The first component exhibits the strongest dielectric anomaly near the ferroelectric phase transition (530°C), compared to the second and to the third. The origin of ferroelectricity is located in the pseudo-perovskite unit and the Bismuth oxide layer is non-ferroelectric in nature. Thus, the first relaxation could be associated with the pseudo-perovskite units and the second or the third relaxation would come from the Bismuth oxide layers. However, since their capacitance is greater (even if one introduces a “volume fraction” correction as above) compared to the first relaxation and that their resistance is of about the same order of magnitude; it seems that this interpretation would be quite presuming. More likely possibility would be to assign the first one to bulk processes (inside the grains) and the second and third one to grain boundaries and electrodes respectively. Chen [32] showed for SrBi₂Ta₂O₉ that the grain and the grain boundary conductivities had a similar activation energy (0.84 and 0.92 eV respectively), but also that the electrode-ferroelectric interface had a much higher activation energy (1.47 eV) compared to the others. This fact is actually verified with our model as two activation energies are close to each other (1.31 and 1.36 for the first and the second) and the third is higher (1.59 eV). This would suggest that the electrode-ceramic interface produces a third relaxation as already expected from the relaxation frequencies (slowest one usually attributed to electrode effects).

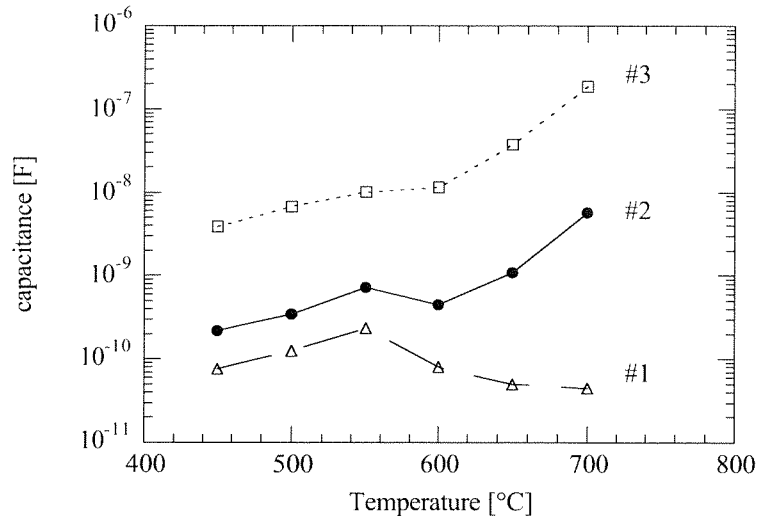


Figure 3-36: calculated capacitance associated with each of the three RC components for undoped SrBIT ceramics.

The relaxation frequencies calculated from the fitted R and C values are consistent with the previous interpretation of the processes, since the grain relaxations are usually related to the highest relaxation frequency [62,81], the grain boundary to the middle one and the interface to the slowest one. Extrapolated to lower temperatures, the relaxation frequency of the first mechanism would be 2.5 mHz (or $\tau=64$ s) at 100°C (usual temperature for DC measurements). Comparing this time constant to Figure 3-7 and Figure 3-11 shows that the relaxation calculated with the impedance analysis corresponds to the long-term steady-state current, not to the “immediate” polarization. Thus, the impedance analysis would not support the hypothesis of grain polarization as the “immediate” response below $1\mu\text{s}$ as discussed with the DC method, Figure 3-7. The high frequency impedance of SrBIT should be related to another microstructural element. As shown below in sections 3.6.4 and 3.6.5, extra impedance arc was actually observed at high frequency. It will be interpreted as a splitting of the grain impedance into Bismuth oxide and perovskite layer impedances. Their respective characteristic relaxation frequencies will be extracted from the modulus master curves. Concerning the low frequency part, it will be assumed that the estimated relaxation frequency corresponds to the grain impedance only, hiding grain boundary and electrode characteristic frequencies (believed to be smaller).

Table 3-4: relaxation frequencies assigned to different microstructural elements for three Bismuth Titanates.

SrBIT	f_R	BaBIT ¹	f_R	SBTaO9 ²	f_R
Grain	82 kHz	Pseudo-perovskite	13 kHz	Grain	500 kHz
Grain Boundary	19 kHz	Bismuth oxide layers	1.4 MHz	Grain Boundary	63 kHz
Electrode	2 kHz			Electrode	350 Hz

According to Table 3-4, grain, grain boundary and electrode relaxation frequencies found for SrBIT with the three RC equivalent circuit agree with reported results on SBTaO9 by Chen. The orders of magnitude for each relaxation are quite similar for the two materials. The largest deviation would be between relaxation frequencies of electrode polarization. However, this one depends also on other parameters (nature of the electrode, deposition process, thickness), so that the fact that they are much lower than the other two is satisfying enough. As indicated in Table 3-4, Kim reported a contribution at very high frequency and identified it with Bismuth oxide layers. Using either modulus modeling at 400°C and master curve building at 200 and 500°C, a similar high frequency relaxation has been measured for ab oriented SrBIT, Figure 3-39 and Figure 3-48.

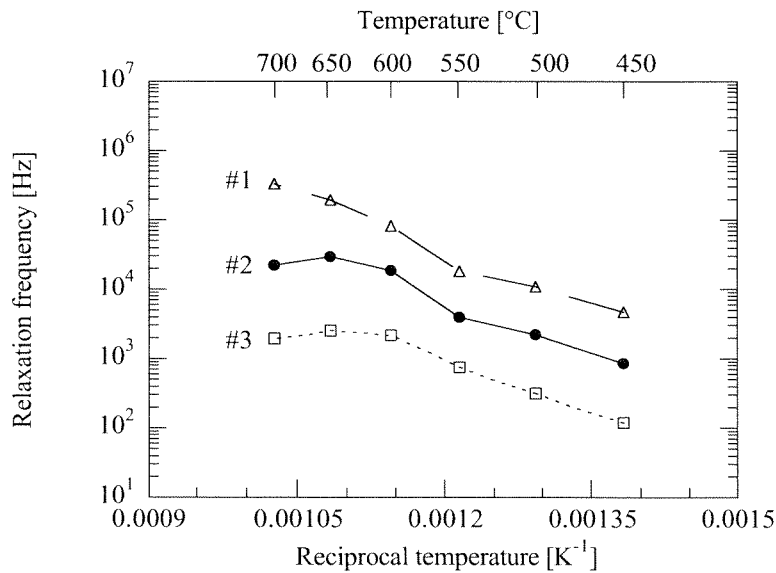


Figure 3-37: relaxation frequencies versus temperature calculated from fitted R and C values for undoped SrBIT random oriented for three RC components.

¹ After Kim [82] S.-K. Kim, M. Miyayama, and H. Yanagida, Electrical Anisotropy of BaBi₄Ti₄O₁₅ single Crystal, *Journal of the Ceramic Society of Japan*, 1994, **102** (8), pp. 719-723..

² After [32] T.-C. Chen, C.-L. Thio, and S. B. Desu, Impedance Spectroscopy of SrBi₂Ta₂O₉ and SrBi₂Nb₂O₉ Ceramics Correlation with Fatigue Behavior, *Journal of Material Research*, 1997, **12** (10), pp. 2628-2635..

3.6.4 Modulus analysis in the lower AC temperature range

Additional contribution in the complex plane could be observed at low temperature (e.g. 100-400°C) and high frequency (1 kHz – 1 MHz) in the modulus representation of an “ab” oriented hot forged sample (undoped), Figure 3-38. At higher temperature, this shoulder to the main semicircle disappears progressively and is no longer visible above 500°C. Precise evaluation of this extra relaxation was made with simulation of the impedance by a double RC circuit made of two discrete RC elements using ZView Software. In order to get a good approximation of the modulus function weighting according to the calculated modulus was also used. The result of this simulation is presented in Figure 3-39 and best-fit parameters are summarized in Table 3-5.

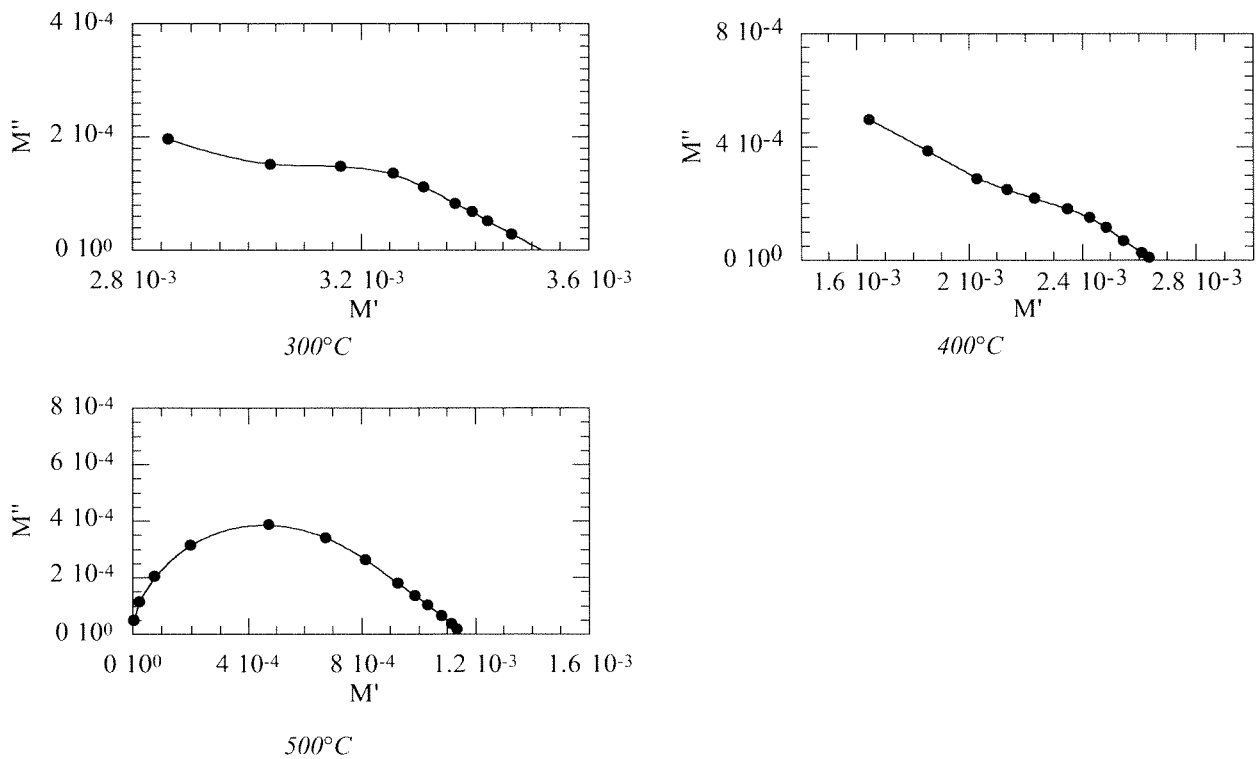


Figure 3-38: electric modulus for hot forged undoped SrBIT measured in the ab direction at 300°C, 400°C and 500°C

As seen in the left plot of Figure 3-39, the impedance semi-circle of undoped SrBIT measured in the ab direction is poorly defined at 400°C, nevertheless the simulation gives satisfying results. The modulus has been calculated with the simulated impedance and the agreement with measurements is worse compared to the impedance representation. However, as the second relaxation is hardly defined in the modulus representation, the approximation quality is good enough for a semi-quantitative analysis.

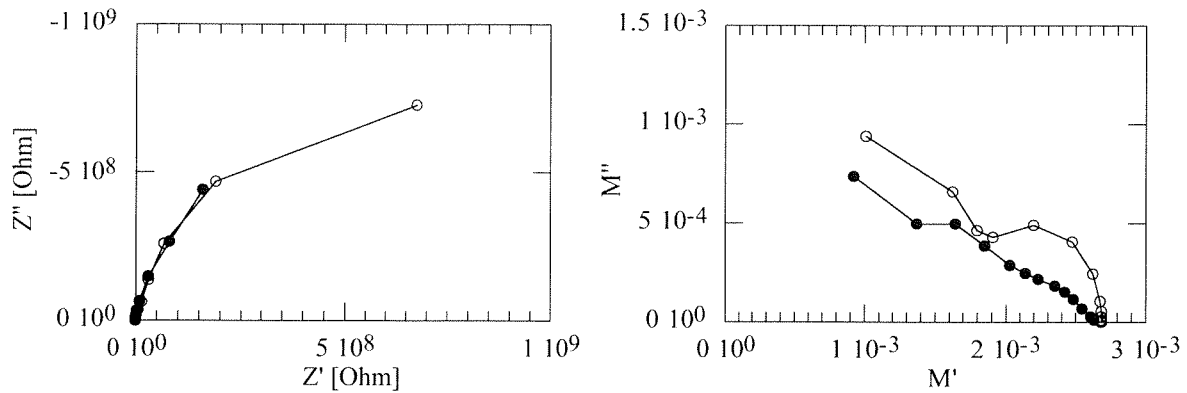


Figure 3-39: measured (filled circles) and simulated (open circles) impedance (left) and modulus (right) functions for undoped SrBIT in the *ab* direction at 400°C.

According to Figure 3-38, the shoulder of modulus at 400°C in the high frequency range would indicate a relaxation below 1 MHz. With the building of a master curve, Figure 3-48, the relaxation frequency can be localized around 10 kHz. An important fact is that this additional relaxation is not visible neither in the *c* direction Figure 3-41 nor for random oriented SrBIT, Figure 3-40, while master curve building provided two relaxations in the two directions, Figure 3-49, Figure 3-50.

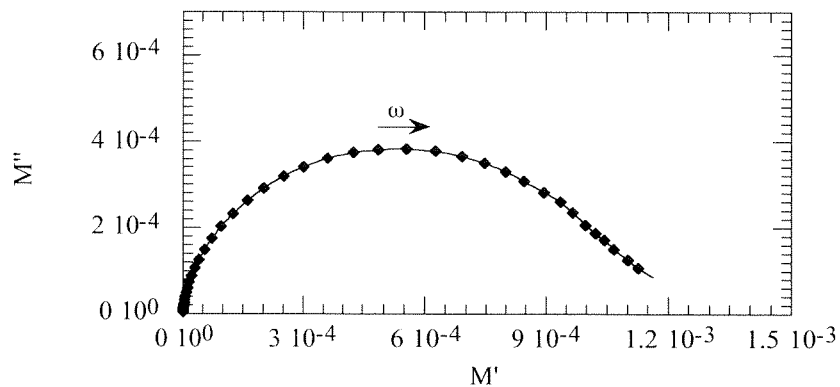


Figure 3-40: electrical modulus in the complex plane for undoped SrBIT at 500°C

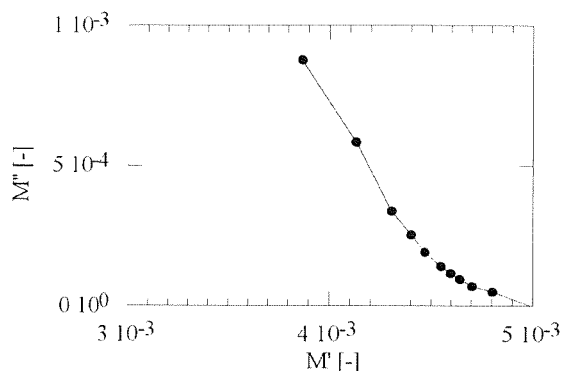


Figure 3-41: measured modulus for undoped SrBIT measured in the c direction at 500°C .

Table 3-5: fitting parameters used to approximate the impedance using modulus weighting.

From Z^*	Low frequency contribution	High frequency contribution
f_R	17 Hz	578 Hz
C	6 pF	12 pF
R	1.5 G Ω	22 M Ω

Because of the special configuration of ab oriented ceramics, an extra high frequency relaxation has been observed in the modulus representation between 300°C and 500°C , Figure 3-38. According to Table 3-5, this second mechanism is much more conductive, but with a similar capacity to the low frequency one. Therefore it occurs at higher frequency. Bismuth oxide layers can be thought to be more conductive than perovskite units in case of ionic conduction, inducing a higher conductivity in the ab plane direction than in the c direction. Thus, the observed additional relaxation can be attributed to Bismuth oxide layers.

Another way to highlight the high frequency spectrum is to draw a master curve from several impedance measurements made at different temperatures. Such master curves provide informations on a large frequency spectrum, larger than the window allowed by measurement equipment. The next section will present the master curves obtained for ab and c oriented textured SrBIT.

3.6.5 Master Curve Drawing

Using the impedance measurements of ab oriented SrBIT at several temperatures in the usual frequency window (20Hz-1 MHz); the modulus master curve at a reference temperature can be calculated. This is realized by shifting along the frequency axis each set of measurement to match some part of the reference curve. Due to the ferroelectric phase transition and the associated change in permittivity, a vertical adjusting coefficient had to be applied too. With the superposition principle, it is theoretically possible to build a master curve at a reference temperature, by shifting curves measured above or below the reference temperature, Figure 3-42. The shift factor a_T was given by William, Landel and Ferry (WLF) [83] written as:

$$\log a_T = \frac{-C_1(T - T_r)}{C_2 + (T - T_r)} \quad \text{Equation 3-35}$$

where C_1 and C_2 are two constants. The shift factor is measured for a chosen M_r'' value with:

$$\log a_T = \log\left(\frac{\omega_r}{\omega}\right) \quad \text{Equation 3-36}$$

where ω_r and ω are the frequencies corresponding to M_r'' . As an example, the shift parameters were determined for undoped SrBIT random oriented, their values are $C_1=4.9$ and $C_2=333.5$; the representation of a_T versus temperature shows good agreement to the WLF law, Figure 3-42.

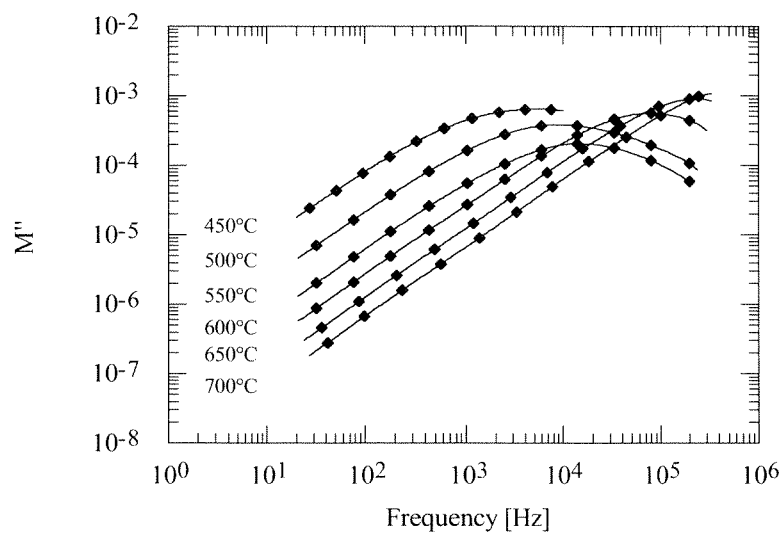


Figure 3-42: imaginary part of the modulus versus frequency at different temperature for undoped SrBIT ceramic.

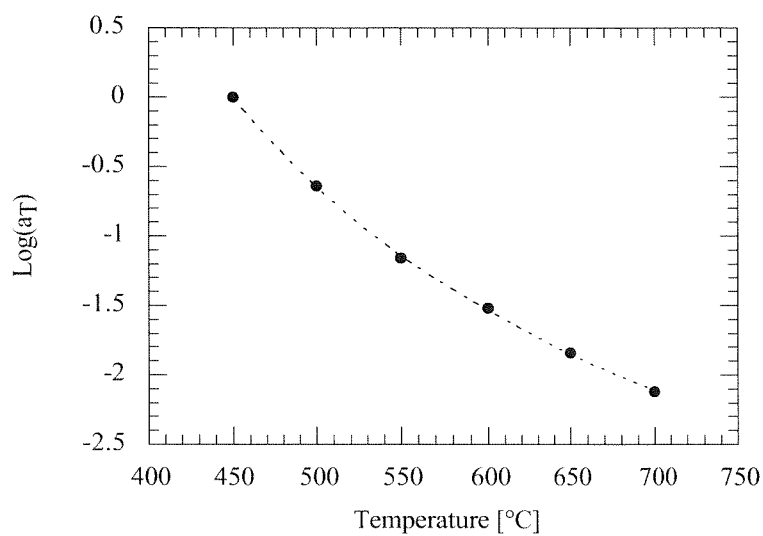


Figure 3-43: Shift factors measured on the imaginary part of the modulus plot of undoped SrBIT and fitting with a WLF expression (dotted line).

Because imaginary parts of impedance and modulus do not coincide, Figure 3-44, for random oriented SrBIT, the single observed relaxation is either non-Debye or multiple in nature. This should be confirmed in a master curve. It is actually not the case since master curve for random oriented ceramic does not clearly indicate any extra relaxation.

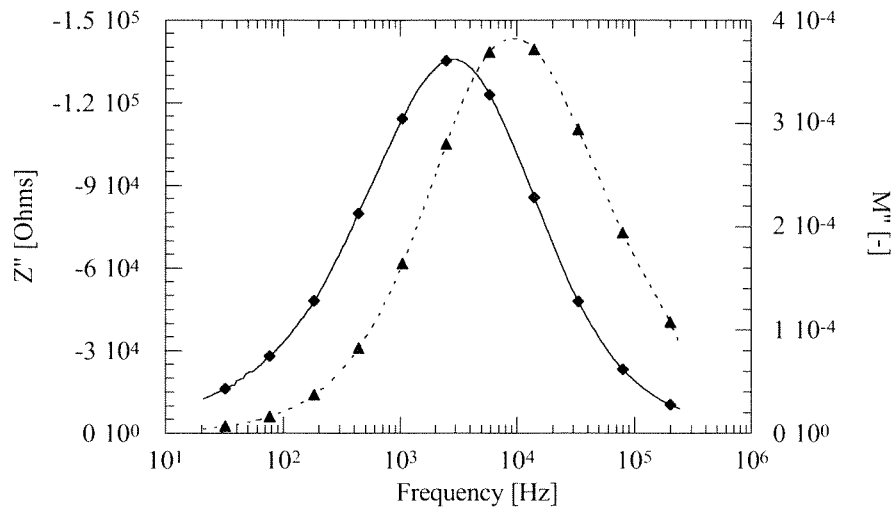


Figure 3-44: imaginary part of the impedance (diamond-shaped) and modulus (triangles) versus frequency for undoped SrBIT at 500°C.

On the contrary, if the same method is used to calculate the master curve of ab oriented SrBIT at 500°C, Figure 3-46, then a second maximum is detected in the M'' spectrum, Figure 3-48. The modulus measurements are presented in Figure 3-46 for several temperatures and the calculated shift factors are given in Figure 3-47. Measurements in the lower temperature range (Figure 3-45) are actually very important for master curve drawing, since the additional relaxation is defined within this temperature range.

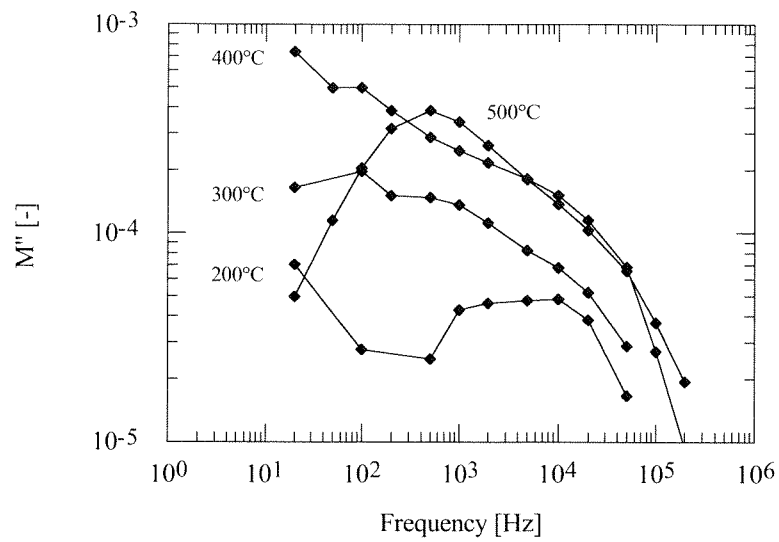


Figure 3-45: imaginary part of the modulus versus frequency at different temperature for undoped ab oriented SrBIT ceramic between 200°C and 500°C.

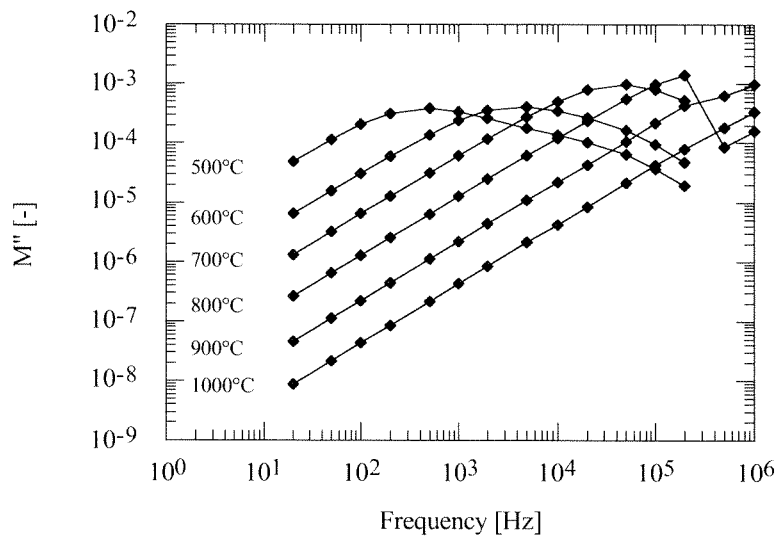


Figure 3-46: imaginary part of the modulus versus frequency at different temperature for undoped ab oriented SrBIT ceramic between 500°C and 1000°C.

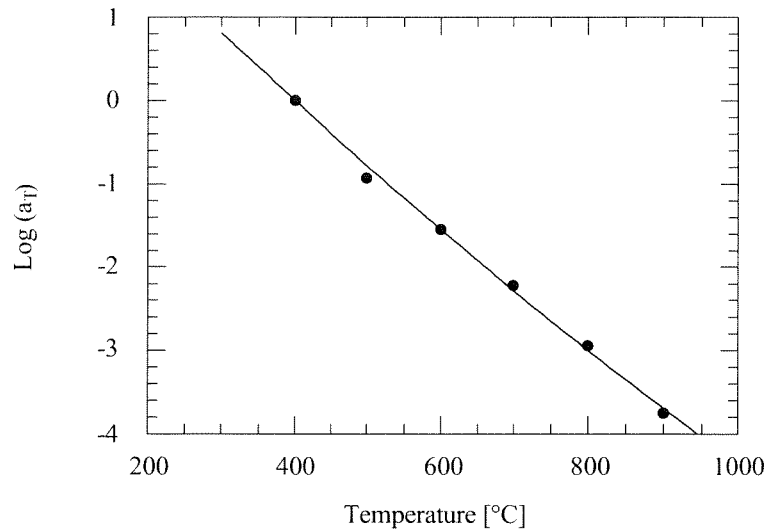


Figure 3-47: Shift factor for the electrical modulus for undoped SrBIT ab oriented.

The major result obtained in the impedance analysis of SrBIT is the master curve for modulus and it is presented in Figure 3-48 at 200°C as a reference temperature and in top left part of Figure 3-49 at 500°C. In these plots, it is clear that the modulus spectrum is made of two separate contributions due to two distinct relaxation mechanisms. They occur just below 1 Hz and in between 1 and 10 kHz at 400°C. The low frequency response has been extensively discussed in the preceding sections as made of several components (grain, grain boundaries and electrodes). As already stated above, the high frequency relaxation seen in Figure 3-48 may come from any kind of relaxation in the Bismuth oxide layers. The role of these layers in one Aurivillius phase was discussed by Shulman [11] for $\text{Bi}_4\text{Ti}_3\text{O}_{12}$. She has shown that oxygen transport in the Bismuth oxide layers creates a dielectric relaxation. Considering that oxygen vacancies are mainly created in these layers [78] and that the electrical conductivity of SrBIT is partly ionic as described in Chapter 4, it is reasonable to assign one relaxation to these layers.

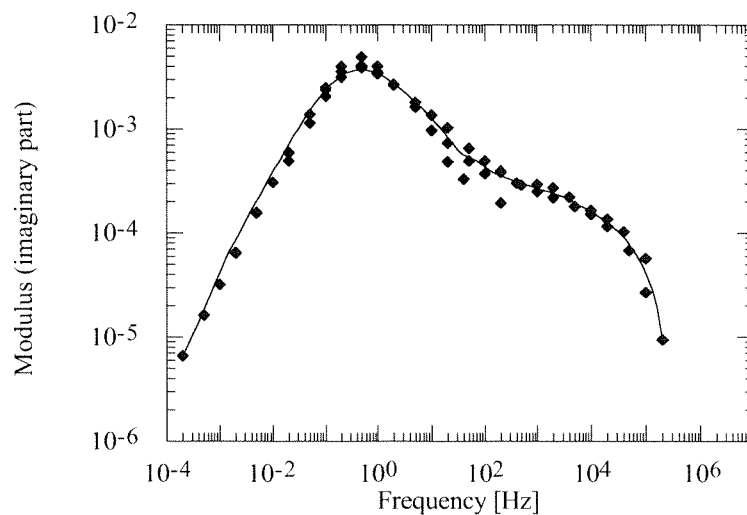


Figure 3-48: calculated master for undoped SrBIT in the ab direction at 200°C.

Master curves were also drawn for acceptor and donor doped SrBIT in the *ab* plane direction at 500°C, they are presented in Figure 3-49. Both undoped and donor doped material exhibit a second relaxation at higher frequency. But in the case of 2 mol.% Mn doped SrBIT only one single relaxation is seen (top right of Figure 3-49). As the characteristic relaxation frequency is the inverse of the product of one resistance and one capacity, an increase of frequency can be induced by a decrease of resistance. Acceptor doping (2 mol.%) causes such a decrease in a p-type conductivity regime, Figure 3-18. Thus, for Mn doped SrBIT the high frequency relaxation is probably not seen because its frequency is too high even in the low temperature range. However, the expected shift to lower frequency range through donor doping is not seen in the bottom part of Figure 3-49. This may be an indication that modification of the total conductivity is not sufficient to explain the observed behavior. Others effects induced by Mn doping such as modification of the oxygen vacancies concentration in the Bismuth oxide layers could be an explanation for the disappearance of the high frequency relaxation. Actually, ionic charge transport plays a role in SrBIT, since calculation of the ionic conductivity in Chapter 4 has shown a large transference number even for undoped SrBIT. Manganese doping was found to increase further the ionic conductivity, Figure 4-20; this is probably achieved by increasing the amount of oxygen vacancies. Thus, it is very likely that Mn doping modifies Bismuth oxide layers more than Nb doping does.

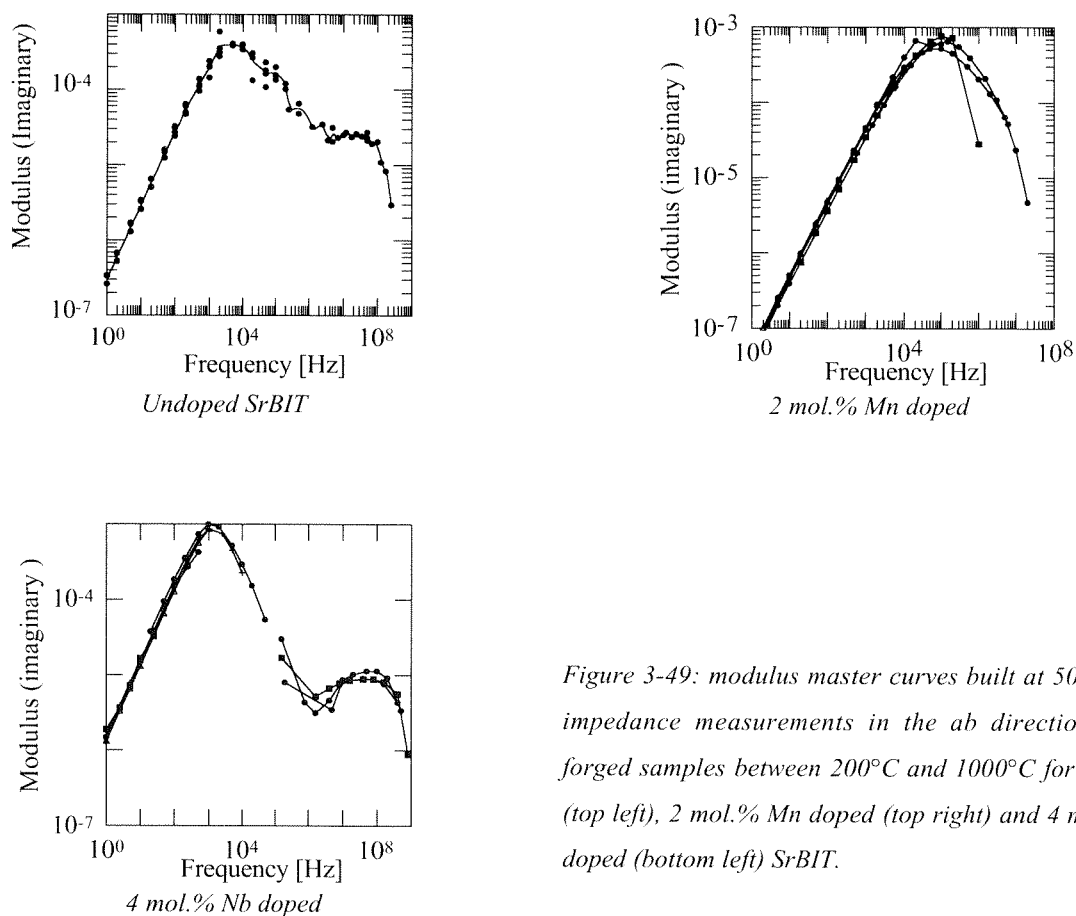


Figure 3-49: modulus master curves built at 500°C with impedance measurements in the *ab* direction of hot forged samples between 200°C and 1000°C for undoped (top left), 2 mol.% Mn doped (top right) and 4 mol.% Nb doped (bottom left) SrBIT.

Impedance measurements were also performed in the c direction of undoped, Mn and Nb doped SrBIT. The corresponding master curves are presented in Figure 3-50. The same general features are seen in these plots compared to the ab plane direction: there are two maximums except for 2 mol.% Mn doped sample, where there is only one. Relaxation frequencies as read on Figure 3-49 and Figure 3-50 are summarized in Table 3-6.

Table 3-6: summary of relaxation frequencies measured in the modulus master curves for undoped, Mn and Nb doped SrBIT at 500°C.

Composition	Direction	f_1	f_2
undoped	ab	6 kHz	25 MHz
	c	350 Hz	4 MHz
2 mol.% Mn doped	ab	3 kHz	none
	c	2 kHz	none
4 mol.% Nb doped	ab	1 kHz	53 MHz
	c	550 Hz	4 MHz

In order to compare frequencies of Table 3-6, it is important to note that these characteristic frequencies are size-independent. Since the relaxation frequency is calculated as the inverse of the product of one resistance and capacitance and because resistance and capacitance can be calculated from conductivity and permittivity with Equation 3-37 and Equation 3-38, it follows that f_R is thickness and area independent, as expressed by Equation 3-39.

$$R = \frac{1}{\sigma} \frac{t}{A} \quad \text{Equation 3-37}$$

$$C = \frac{\epsilon \epsilon_0 A}{t} \quad \text{Equation 3-38}$$

$$f_R = \frac{1}{2\pi \epsilon_0} \frac{\sigma}{\epsilon} \quad \text{Equation 3-39}$$

where t and A are thickness and area of sample and ϵ and σ are permittivity and conductivity. In SrBIT, considering anisotropy of perovskite and Bismuth oxide layers, there are eight parameters to consider, as indicated in Table 3-7. However, they can be reduced to six with the two following assumptions: conductivity in the perovskite unit and permittivity in the Bismuth oxide layer are equal in both ab and c directions. In a first approximation, these assumptions are supported by the low anisotropy of perovskite structure, neglecting the influence of polarization and by the absence of ferroelectric polarization in the Bismuth oxide layers. Thus, the number of independent parameters reduces to six, with the electrical conductivity in the perovskite written σ_P and the dielectric permittivity in the Bismuth oxide layer written ϵ_F . The relaxation frequencies for each element and direction are given in Table 3-6.

Table 3-7: notation of electrical conductivity and dielectric permittivity in the ab plane and c directions for perovskite and Bismuth oxide layer.

	Conductivity	Permittivity
Perovskite	$\sigma_P^c, \sigma_P^{ab}$	$\epsilon_P^c, \epsilon_P^{ab}$
Bismuth oxide layer	$\sigma_F^c, \sigma_F^{ab}$	$\epsilon_F^c, \epsilon_F^{ab}$

Table 3-8: relaxation frequency expressions for ab and c directions in perovskite and Bismuth oxide layer.

	ab plane direction	c direction
Perovskite	$\omega_P^c = \frac{\sigma_P}{\epsilon_P^c}$	$\omega_P^{ab} = \frac{\sigma_P}{\epsilon_P^{ab}}$
Bismuth oxide layer	$\omega_F^c = \frac{\sigma_F^c}{\epsilon_F}$	$\omega_F^{ab} = \frac{\sigma_F^{ab}}{\epsilon_F}$

According to Table 3-6, there are two resulting inequalities concerning relaxation frequencies as given in Table 3-9. The first one implies a larger permittivity in the c direction than in the ab plane direction in the perovskite. This is inconsistent with global dielectric permittivity measurements that show a much larger permittivity in the ab plane direction than in the c direction. Thus, the assumption of isotropic conductivity in the perovskite should be wrong. Actually, because of electrical polarization anisotropy in perovskite sub-units, conductivity should probably be anisotropic too. With the observation of a higher permittivity in the ab plane direction than in the c direction³, especially around ferroelectric phase transition, Figure 3-16, it turns out that conductivity in the ab plane direction should be higher than conductivity in the c direction (for $\omega_{ab} > \omega_c$ and $\epsilon_{ab} > \epsilon_c$ in perovskite). This last result is consistent with low temperature DC measurements, Figure 3-14. The second resulting inequality given in Table 3-9, is a greater conductivity in the ab plane direction than in the c direction, in a same way as for the perovskite. This is not surprising, since it is believed that ionic conduction along these layers is responsible for the ionic contribution to total conductivity. Ionic conductivity across the Bismuth oxide layers is much less likely and provided that transference number is large, total conductivity perpendicular to the layer should be smaller than along them. The assumption of isotropic permittivity is not contradicted.

³ These permittivities correspond to C_p measured at 1 MHz with LCR bridge.

Table 3-9: observed and consecutive inequations for conductivity and permittivity in perovskite and Bismuth oxide layer.

Element	Observation	Consequence
Perovskite	$\omega_P^{ab} > \omega_P^c$	$\epsilon_P^c > \epsilon_P^{ab}$
Bismuth oxide layer	$\omega_F^{ab} > \omega_F^c$	$\sigma_F^{ab} > \sigma_F^c$

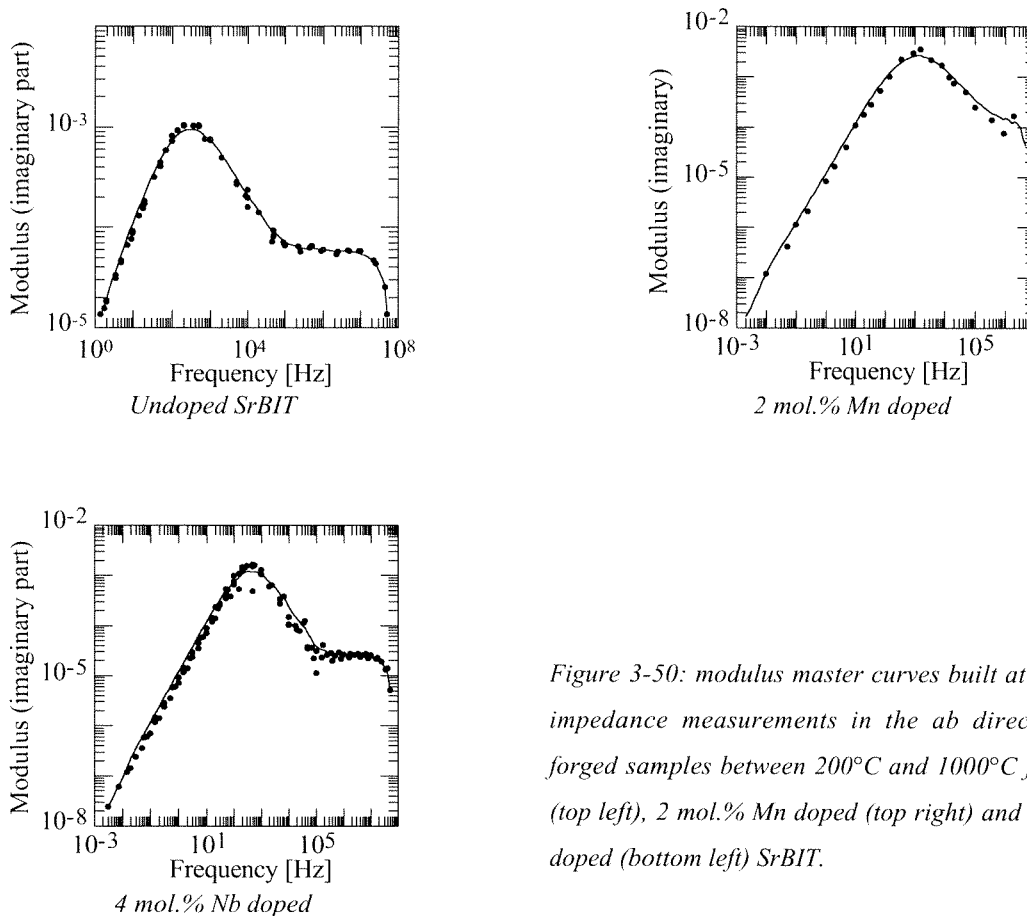


Figure 3-50: modulus master curves built at 500°C with impedance measurements in the *ab* direction of hot forged samples between 200°C and 1000°C for undoped (top left), 2 mol.% Mn doped (top right) and 4 mol.% Nb doped (bottom left) SrBIT.

In summary, it was found by evaluating modulus master curves drawn for undoped, Mn and Nb doped SrBIT that the electrical conductivity in the *ab* plane direction should be higher than in the *c* direction for both perovskite and Bismuth oxide layers. The dielectric permittivity in the perovskite is anisotropic, while it may be isotropic in the Bismuth oxide layers.

In the next section, it will be demonstrated that using Manganese doping, the validity of the multiple RC model is reinforced. In the case of undoped SrBIT, discrimination of the three relaxations was not possible, Figure 3-23, while for Manganese doped SrBIT, Figure 3-51, the existence of the low frequency relaxation is much more clear.

3.6.6 Mn doping effect on impedance

The impedance of 2 mol.% Manganese doped SrBIT was measured between 450°C and 650°C, an example of it is given in Figure 3-51 at 600°C. The most interesting feature of these measurements is that at low frequency (left part of Figure 3-51), there is a clear indication of an additional relaxation. As presented in Figure 3-51, the only way to simulate the measurements points is to use a triple RC circuit, since Havriliak-Negami gives the required flatness of a semi-circle but cannot simulate the observed “tail” in the low frequency range (right part of the figure).

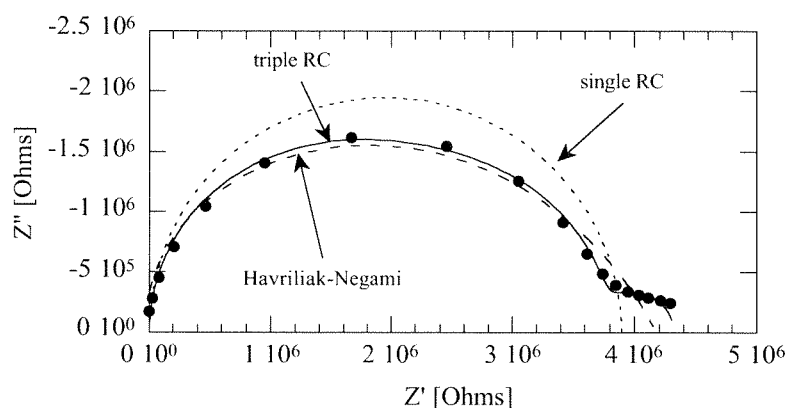


Figure 3-51: electrical impedance in the complex plane (filled circles) of 2 mol.% Mn doped SrBIT at 600°C together with single RC (dotted line), triple RC (solid line) and Havriliak-Negami fittings (dashed line).

Compared to undoped SrBIT, Figure 3-28 and Figure 3-29, the impedance of Manganese doped SrBIT gives a stronger indication for an equivalent circuit made of three different elements, rather than two or of Havriliak-Negami type.

Characteristic parameters extracted from equivalent circuit simulation are presented in Figure 3-52, Figure 3-53 and Figure 3-54. Compared to Figure 3-35, Figure 3-36 and Figure 3-37, the behavior of Manganese doped SrBIT is similar. The relaxation that has the highest relaxation frequency (written #1) according to Figure 3-54 exhibits a slope change near ferroelectric phase transition, Figure 3-52 and there are two relaxations that shows an anomaly near ferroelectric phase transition, Figure 3-53. The difference is that the third relaxation frequency is one order of magnitude lower for Manganese doped SrBIT, Figure 3-54 than for undoped material, Figure 3-37. Thus, it results that the third relaxation is easier to observe in the case of Mn doped SrBIT.

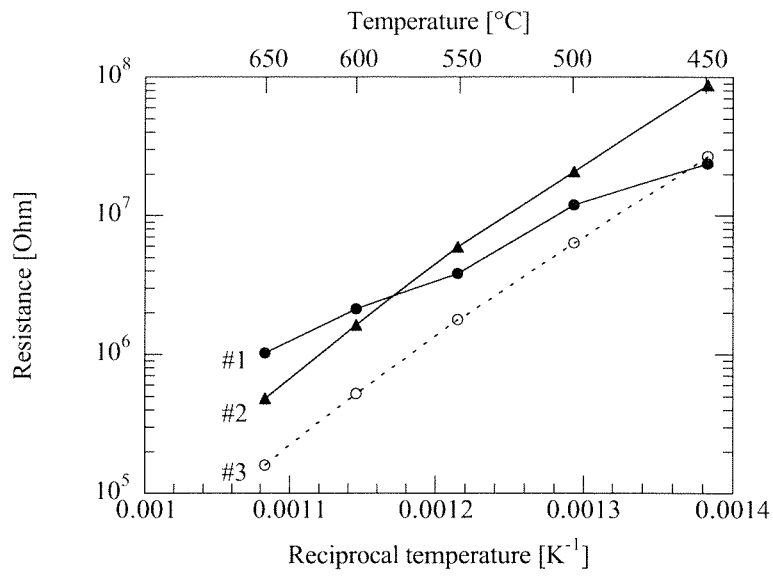


Figure 3-52: resistance versus temperature for three RC model for Mn doped SrBIT

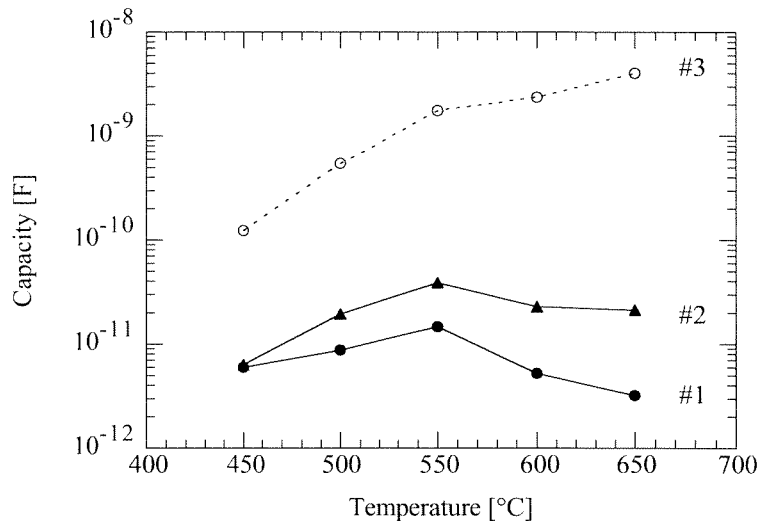


Figure 3-53: capacity versus temperature calculated for three RC model for Mn doped SrBIT.

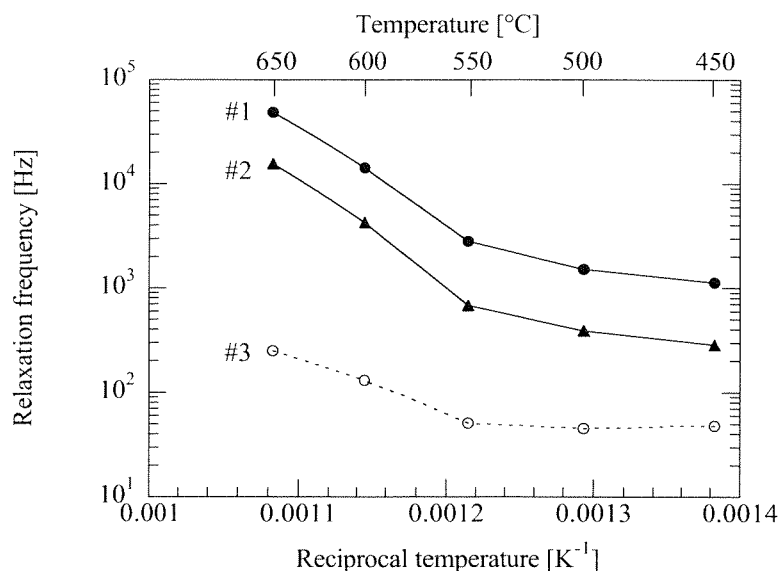


Figure 3-54: relaxation frequency versus temperature calculated for three RC model for Mn doped SrBIT.

Simulation of the impedance response with an equivalent circuit made of three separate RC elements in series was made with the assumption that each of the relaxation mechanism could be identified with grains (actually splitted into perovskite and Bismuth oxide components), grain boundaries and maybe electrodes. If this is true, changing the grain size should provide a way to prove it. This will be realized in the next section, dedicated to grain size effect on the impedance.

3.6.7 Grain size effect

The effect of grain size on the electrical impedance was studied using a standard small grain sample sintered at the optimum temperature and another sample sintered above the optimized temperature. In the latter case, instead of a few microns, grains were 10 to 15 microns large and about 500 nanometers thick, Figure 3-55.

The results of the impedance measurements are presented in Figure 3-56. In this figure, the extracted resistances have been converted into conductivities to allow direct comparison between two samples. All the calculated contributions are smaller in the case of the large grain size sample. But the curves exhibit the same general trends as the small grain size one (same slope). Direct comparison of the conductivity values is not possible, since the powders and the sintering profile temperatures were different. In order to discuss the two sets of results, it is better to draw the ratios of the grain to grain boundary conductivity (first to second relaxation) as shown in Figure 3-57.

As already observed for small grains SrBIT, there is a slope change for grain conductivity around ferroelectric phase transition. On the contrary, grain boundary conductivity does not undergo this transition. This supports the assumption of non-ferroelectric grain boundaries. It follows that at elevated temperature, grain conductivity limits total conductivity of SrBIT, in both small and large grains (assuming no grain boundary-to-grain boundary conductivity paths)

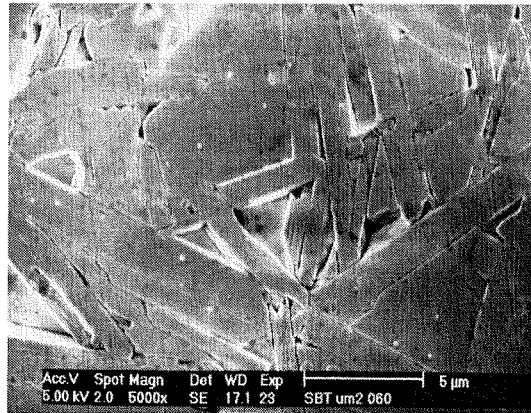


Figure 3-55: SEM micrograph of large grain SrBIT used for impedance analysis.

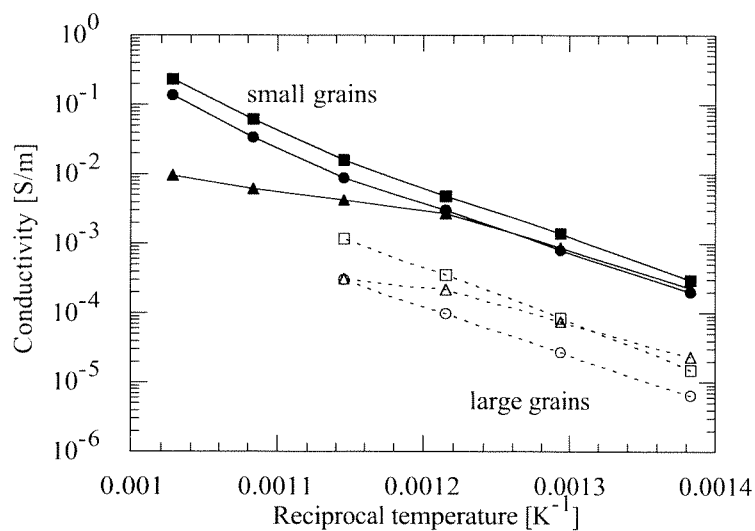


Figure 3-56: three components to the electrical impedance for small grain (filled items) and large grains (empty items) undoped SrBIT. Triangles, circles and squares are first, second and third relaxations respectively.

An increase of the grain size actually decreases the grain boundary contribution to the electrical conductivity since the ratio of the grain to grain boundary increases. This ratio is 3.6 for large grains and 1.1 for small grains at 450°C. As presented in section 3.4.3 for the bricklayer model, the grain boundary conductivity can be calculated using the following expression:

$$\sigma_{gb} = \frac{x_{gb}}{3} \frac{l}{R A} \quad \text{Equation 3-40}$$

where x_{gb} is the volume fraction of grain boundaries, R the associated calculated resistance and t and A the macroscopic dimensions of the sample (thickness and area). For larger grains, the volume fraction of the boundaries decreases, since x_{gb} can be calculated with:

$$x_{gb} = \frac{2d}{D} \quad \text{Equation 3-41}$$

where d is the grain boundary thickness and D the grain size, as D increases, x_{gb} decreases. Thus, it is not surprising that the grain boundary conductivity decreases compared to the grain conductivity in the case of large grain size SrBIT.

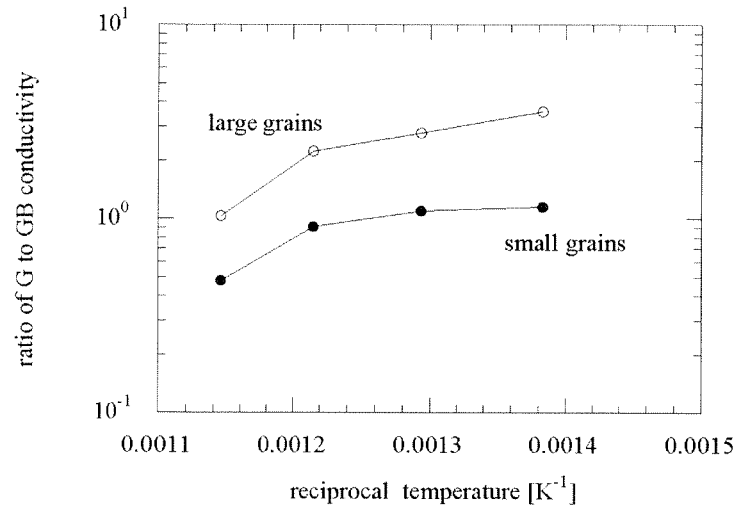


Figure 3-57: grain to grain boundary conductivity versus temperature for both large and small grains undoped SrBIT.

Impedance measurements of small grains SrBIT are consistent with the simulation of the system with three RC elements and with identification of two of these elements with grains and grain boundaries since a consistent behavior has been observed.

The last step of the evaluation of the impedance model is presented in the next section. It consists of impedance transients measurements under changing oxygen partial pressure. These measurements give informations about the dynamic response of the ceramic, it highlights diffusion coefficient differences for grains and grain boundaries.

3.6.8 Impedance transient under changing pO_2

A quite simple way to identify the different components of the impedance model is to submit the oxide to an oxygen partial pressure change. As the oxygen partial pressure and the concentrations of charge carriers are closely related, see Chapter 4, a modification of the oxygen partial pressure changes the electrical conductivity. How fast this change occurs is related to the diffusion coefficient of oxygen in the involved microstructural element. Diffusion along grain boundaries is known to be faster than diffusion inside grains, thus grain boundary conductivity should be modified more rapidly than grain conductivity. This will actually be demonstrated in this section for undoped SrBIT.

The method described in this section is actually a complement to both impedance analysis (this chapter) and low oxygen partial measurement (Chapter 4). Compared to DC conductivity

measurements, the impedance analysis is more sophisticated since it allows the separate observation of the transient behaviors of all components to the impedance.

The transients impedance experiments were carried out as follow: at elevated temperature (650°C), the electric impedance of a bar-shaped ceramic sample is measured first in flowing pure oxygen (at this moment, the oxygen partial pressure is close to one). Then, oxygen is replaced by flowing Ar (150 sccm) and the electric impedance is measured every ten minutes while the oxygen partial pressure is falling, Figure 3-58. The impedance was measured from 50 Hz up to 1 MHz with the smallest available integration time.

The real and imaginary parts of the impedance of 2 mol.% Mn doped SrBIT measured at 650°C is shown in Figure 3-58. The impedance has been recorded every ten minutes after introducing flowing Ar (150 sccm). In these conditions, the oxygen partial pressure drops from 0.2 atm down to about 10^{-5} atm in four hours, Figure 3-59. It is obvious from Figure 3-58 that the low frequency part of the impedance spectrum reacts first to the oxygen partial pressure change. Then, modification of the curve proceeds at higher frequency. The global trend is a decrease of both real and imaginary parts with time, as observed for DC conductivity (see Chapter 4) at high temperature, the conductivity increases when the oxygen partial pressure is decreased.

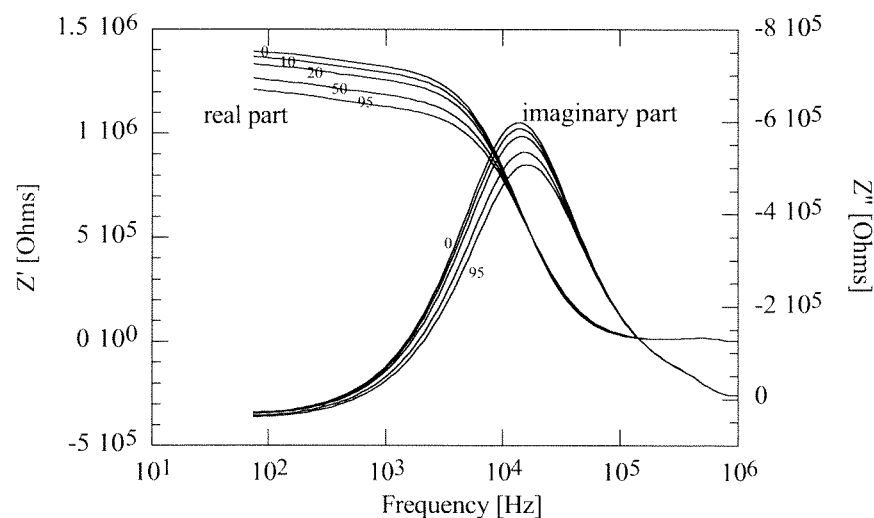


Figure 3-58: real and imaginary part of the impedance versus frequency measured at 650°C under 150 sccm flowing Ar after 10, 20, 50, 95 minutes as indicated on the graph.

The impedance analysis has been conducted the same way as before with three discrete RC components, the results are presented in Figure 3-60 and Figure 3-61. There are two resistances that increase with time (called “ R_1 ” and “ R_2 ”) and one that decreases (“ R_3 ”). The last one (1.3 M Ω at $t=0$) is larger than the other (42 k Ω and 1.6 k Ω at $t=0$ respectively) and thus in the serial model, this resistance controls the overall resistance of the system.

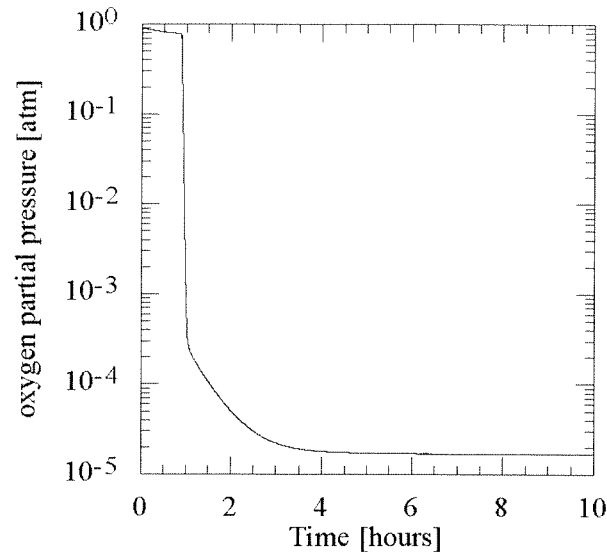


Figure 3-59: oxygen partial pressure transient at 650°C under 150 sccm flowing Ar

The behavior of the first and second contributions is very surprising, since equilibrium DC conductivity measurements always indicate an increase of conductivity as the oxygen partial pressure is decreased. In the frame of the 3-RC model, these shows that the grain boundaries may behave differently compared to the grains. Thus, these measurements would indicate p-type grain boundaries, while grains are n-type.

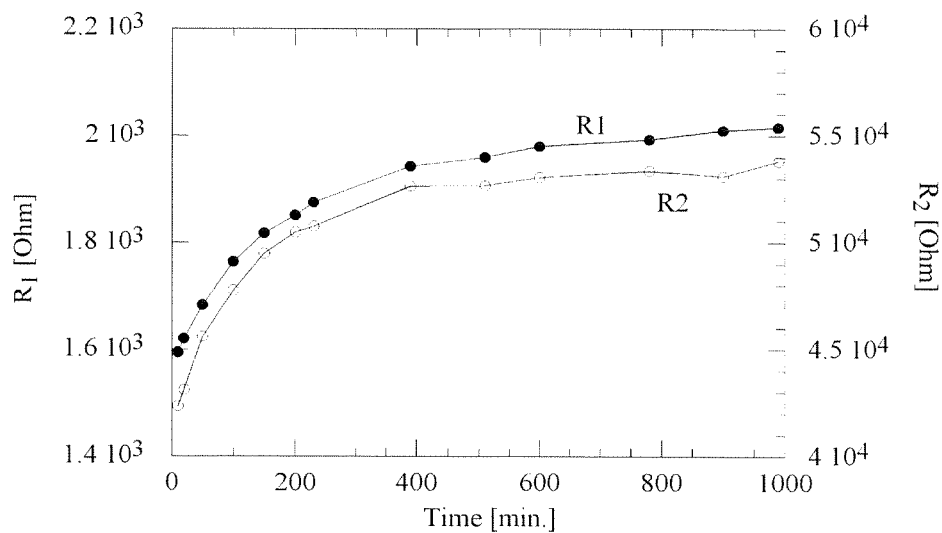


Figure 3-60: first and second calculated resistances using a three RC model versus time for Mn doped SrBIT at 650°C under 150 sccm flowing Ar

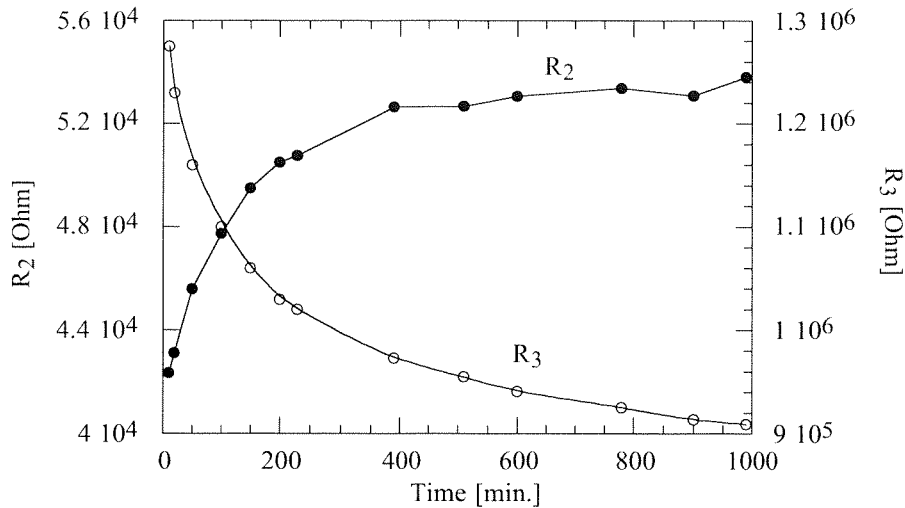


Figure 3-61: second and third calculated resistances using a three RC model versus time for Mn doped SrBIT at 650°C under 150 sccm flowing Ar.

Using the diffusion model described below in Chapter 4, and the normalization equation, Equation 3-42, the diffusion coefficient was calculated for every component, the result is presented in Table 3-10 and in Figure 3-62. In order to apply the diffusion model, data below 100 minutes were not used, as variation of pO_2 is very large in this region and the model assume a step function for pO_2 . The agreement with the model is good, Figure 3-62. In this calculation, the initial resistance was taken as the first measurement and the final one (or infinite) was calculated by the model; a characteristic diffusion length of 0.2 cm corresponding to about half the thickness of a sample was used throughout the calculation. The conductivity value at infinite time can be used for the equilibrium determination of the conductivity at a certain pO_2 value. The measured resistances are normalized with Equation 3-42:

$$R_{\text{normalized}} = \frac{R - R_0}{R_{\infty} - R_0} \quad \text{Equation 3-42}$$

where R_0 is the initial resistance and R_{∞} the equilibrium one.

Table 3-10: result of the calculation of the diffusion coefficients for the impedance transient at 650°C for 2 mol.% Mn doped SrBIT.

Resistance number	Element	Calculated diffusion coefficient [cm ² /s]
1	Electrode	2.8 10 ⁻¹⁰
2	Grain boundary	4.0 10 ⁻¹¹
3	Grain	2.5 10 ⁻¹²

The calculated diffusion coefficients differ by one order of magnitude each. The smallest value (for the third component) is also associated with the resistance decrease, Figure 3-61. If this contribution is identified as the response of grains, then it is reasonable to find that its diffusion

coefficient is the smallest. It is also not surprising to compute a grain boundary diffusion coefficient ($4.0 \cdot 10^{-11} \text{ cm}^2/\text{s}$) larger than the grain one ($2.5 \cdot 10^{-12} \text{ cm}^2/\text{s}$).

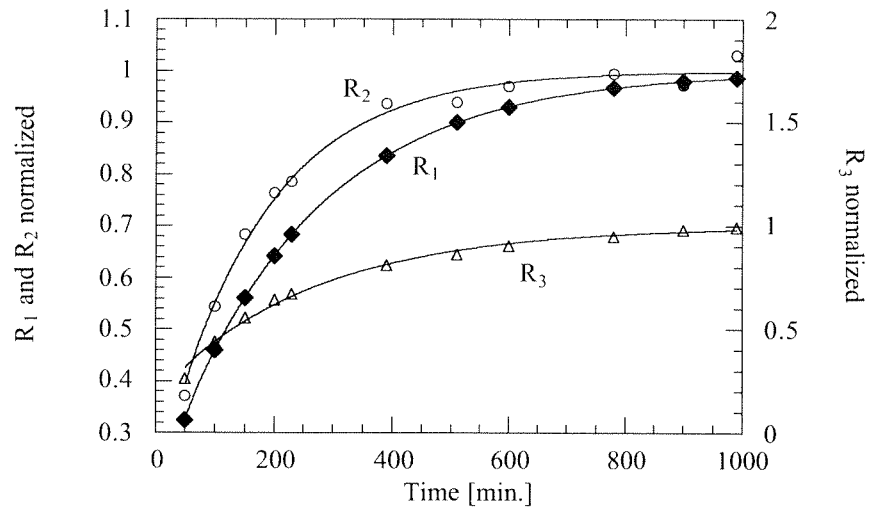


Figure 3-62: normalized resistances (marks) versus time together with the fitted diffusion law (solid lines)

These results indicate that the modelization of the electrical impedance by three separate contributions is consistent with a transient experiment under changing oxygen partial pressure.

3.7 SUMMARY AND CONCLUSION

The charge-discharge method was extensively used to measure the electrical conductivity of SrBIT in the 140-220°C temperature range. "True" DC conductivity was extracted from these measurements by taking the long-term steady state current. The first part of the charging current was investigated with direct charge measurements. At elevated temperature, the complex electrical impedance of SrBIT was simulated with equivalent circuits. Both doping and oxygen partial pressure were used to test the validity of a three RC model.

DC conductivity measurements of SrBIT provided similar results as published in the literature by others groups on related materials. It was found that the typical activation energy between 140°C and 220°C of undoped SrBIT is 1 eV. In a higher temperature range, this energy is larger, AC measurements revealed activation energy for conduction of 1.5 eV in the 450°C-700°C temperature range. As estimated from Näfe's advanced bricklayer model, the activation energy for grain boundary conduction is much lower (≈ 0.1 eV). It follows that in the lower temperature range, electrical conductivity of SrBIT is grain boundary-controlled.

With textured ceramic samples, the anisotropy of the electrical conductivity of SrBIT has been characterized. The activation energy is similar in both directions, but the conductivity is one order of magnitude larger parallel to the defined "ab plane" direction compared to the "c" direction.

With both acceptor (Mn) and donor (Nb) doping, it was demonstrated that conductivity of SrBIT is p-type in the 140-220°C temperature range, since acceptor doping increases it and donor doping decreases it. The modification of compensation mechanism observed in Chapter 4 for Mn doped SrBIT appears in DC measurements as a conductivity decrease for small Mn concentrations.

The impedance measurements performed at high temperature (450-700°C) were evaluated in the complex plane with two kinds of equivalent circuits either multiple Debye-type or single distributed. It was shown that the impedance semicircle of SrBIT could actually be approximated with either three Debye-type relaxations or by the Havriliak-Negami expression. For both models Arrhenius behaviors with activation energies around 1.5 eV and dielectric anomalies near ferroelectric phase transition are verified (except for the third relaxation). Extrapolating the highest relaxation frequency down to 100°C gives a relaxation time of 64 s, consistent with the steady-state current measured by the DC technique. The early part of the charging current is described in a higher frequency range with complex modulus representation.

Using modulus representation and master curve drawing, an extra relaxation was actually observed in the high frequency range (a fourth one in the case of the three RC model or a second one for a single distributed circuit). By comparing relaxation frequencies of undoped, 2 mol.% Mn doped and 4 mol.% Nb doped SrBIT, it can be concluded that this additional relaxation comes from Bismuth oxide layers.

Relationship between grain boundary volume fraction and conductivity was verified by measuring the impedance of large and small grains SrBIT. It was observed that in the case of large grains, the ratio of grain to grain boundary conductivity was higher as predicted by the model. It was also a proof that identifying those two relaxations with grain and grain boundary contribution was correct.

A last attempt to definitely identify grain and grain boundary conductivity was performed with impedance measurement under changing oxygen partial pressure. From the impedance transients, three diffusion coefficients have been calculated. These coefficients were consistent with a faster diffusion along grain boundaries, providing a further proof of the model's validity.

4

CONDUCTIVITY UNDER CONTROLLED OXYGEN PARTIAL PRESSURE

4.1 FOREWORD

In Chapter 3, the effect of temperature, frequency and doping were investigated in details for either the DC or the AC conductivity. However, almost all of these measurements were performed in air and concerning the DC one at rather low temperature. In these conditions, the defect structure of SrBIT (concentration of oxygen and metallic vacancies, oxidation states) was not modified. In particular, in the preceding chapter, the concentration of oxygen vacancies was not modified during measurements. This concentration was determined by either the preparation procedure, since the effective sintering atmosphere is slightly reducing (oxygen ions are recovered on cooling) or by the acceptors content (negative acceptor centers are compensated by positive oxygen vacancies).

As the oxygen activity inside the ceramics is directly related to the oxygen partial pressure in the surrounding atmosphere (providing that diffusion is fast enough), the oxygen partial pressure becomes an additional parameter, which has to be evaluated for a complete description of SrBIT. In fact, both conductivity datas at low oxygen partial pressure and rate of conductivity change as the pressure is decreased are significant. The former for example gives a direct comparison basis to check the effect of doping type and concentration, the latter provides valuable information about the defect structure of the material.

Most of the literature about electrical conductivity under controlled oxygen partial pressure of ferroelectric ceramics is dedicated to BaTiO_3 and SrTiO_3 . A great part of work was made in the late 70's [35,36,84-88] and early 80's [37-39,89-93], however the interest is still strong and many interesting studies have been published in the 90's [75,94-101]. This shows at least two things: first that the interest for such a characterization is strong in the scientific community and second that even after thirty years of careful scientific investigations by several groups for such simple materials (two cations and perovskite structure), there remain a lot of questions to be answered. Considering this, the present work on SrBIT should be read as one of the first attempts to describe the electrical conductivity of one Bismuth Titanate under controlled oxygen partial pressure.

As Bismuth Titanates are made of pseudo-perovskite units too, their behavior may be similar to BaTiO_3 , in another hand the Bismuth oxide layers could also affect this behavior. Those are actually open structures, where oxygen vacancies are much more easily created [78]. In addition, Bismuth Titanates and especially SrBIT are prepared at elevated temperatures, where diffusion is fast enough to modify defect structure of the material. Finally, cation exchange between Sr^{2+} sitting on the A site of the perovskite and Bi^{3+} of the Bismuth oxide layers was proposed recently as a source of intrinsic donors. In conclusion, until the electrical conductivity of SrBIT has been characterized in low oxygen partial pressure, any prediction of its behavior would be very daring.

With all of these open questions, the investigation of the electrical DC conductivity of SrBIT was conducted in the following way. First, the measurement set-up was tested with BaTiO_3 in the oxygen partial pressure range of interest, the result were compared to the literature. The

conductivity of undoped, 2 mol.% Mn doped and 4 mol.% Nb doped SrBIT was measured in the 1 down to 10^{-5} atm pO_2 range from 700°C up to 1000°C. The results were discussed with models (acceptor and donor-controlled conductivity) developed for BaTiO_3 . The conductivity was measured in the full range of pO_2 and the original results were compared with recent reports on electrical conductivity of some Bismuth Titanates. The ionic contribution to the total conductivity was estimated using an experimental method used by Chang [102] for BaTiO_3 characterization. With a rough estimation of the band gap obtained from conductivity measurement of both undoped and Mn doped SrBIT under controlled oxygen partial pressure, a map of the transference number in a band gap-temperature space was built.

4.2 BASICS OF DEFECT CHEMISTRY

4.2.1 Point Defects Considerations

It is not within the scope of this work to give an extensive description of the behavior of ceramic oxides at low oxygen partial pressure, only compounds of interest will be describe in this section to make the comprehension of the results easier and faster. Additional information's can be found in either Kröger's [103] or Tallan's books [104].

Considering a regular and symmetric arrangement of ions building a crystallographic lattice, the first way to create a point defect is to remove one ion and to put it somewhere else either in-between other ions or outside of the lattice. These mechanisms create one interstitial defect and one vacancy respectively, those defects are written M_i or O_i for metallic or oxygen interstitial and V_M or V_O for metallic or oxygen vacancy. The first kind of defects is known as Frenkel disorder and if cationic and anionic vacancies are produced simultaneously, the disorder is called Schottky disorder. Another kind of defects comes from a position exchange between two cations or two anions, these are called substitutional defects such as A_M for the A cation replacing the original M cation. If the cation can be reduced or oxidized to different oxidation states, dismutation defects may also be created such as $M_M^{n\pm}$. Finally considering ionic materials with localized electronic states, it may happen that some electrons, written e' , are delocalized and contribute to the electronic conduction. Similarly, some missing electrons, called holes and written as h' , can be delocalized and move to the valence band.

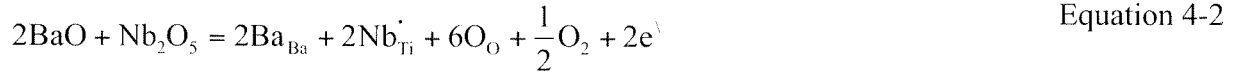
In ionic solids, charges are bound to the crystalline site, when an ion is removed this charge actually remains. For example, sodium chloride is made of Na^+ and Cl^- ; removing Na^+ leaves one extra electron (because Na is ionized into Na^+), which is associated with the sodium vacancy, this is written V_{Na}' . Nevertheless, the remaining charge is not necessarily attached to the vacant site; the separation can be represented by the following ionization equilibrium:



This equation shows that there is a chemical equilibrium between the concentrations of ionized vacancies and neutral one. In this work, oxygen vacancies will be considered as doubly ionized.

Defect chemistry treats the equilibrium concentrations of defects as the temperature or the partial pressure of one constituent are changed. Writing equations for such chemical equilibriums must obey several basic rules [105]: site relation (ratio of anionic to cationic site should be kept identical to the ratio defined by the compound chemical formula), mass balance and electrical neutrality.

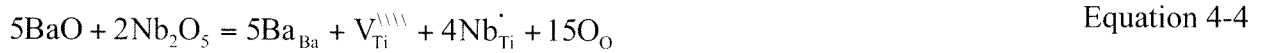
As an example, the incorporation of Nb^{5+} on the Ti^{4+} sites of $BaTiO_3$ may be written in many ways:



for an electronic compensation of the donor defects. However, this is valid for small Nb concentrations, for higher amount of donors other compensation mechanisms should be considered:



In that case, the negatively charged Barium vacancies compensate the positively charged Ti substitution. However, as Titanium vacancies could in principle be created too, a similar equation may be written for Titanium vacancies compensation:



The last possibility is to include oxygen in interstitial sites, this would be written as:



The choice of the appropriate equation can only be performed by a direct evaluation of the creation probability for each induced defect (Ba or Ti vacancy, interstitials ions, oxygen expel). This is probably the key for the interpretation of conductivity measurements. For example, the early work by Daniels [35] excluded the creation of Titanium vacancies and took into account only Barium vacancies. Chan did at first the same assumption in studying donor doped BaTiO₃ [39]. However, in a following publication, the same author interpreted electrical conductivity measurements of highly donor doped BaTiO₃ with Titanium vacancies compensation [91]. The possibility of such a compensation mechanism for donor doped BaTiO₃ is now accepted [3].

As a similar attempt to predict which point defect would be the more favorable in the case of cation substitution in SrTiO₃ by either monovalent, divalent, trivalent and tetravalent oxides, a computer simulation was performed by Akhtar et al. [106]. They calculated that in the cases of either monovalent or divalent oxides, the cation (M⁺ or M²⁺) substitutes Sr²⁺, with oxygen vacancy compensation. For light trivalent oxide substitution (Sc³⁺, V³⁺, Mn³⁺, Fe³⁺), a self-compensation mechanism including simultaneous substitution of both A and B sites of SrTiO₃ is more preferred: creating M_{Sr}[•] and M_{Ti}[\]. This is a different from BaTiO₃ where Mn³⁺ substitute Ti⁴⁺ only [106]. Unfortunately, no similar calculation has been performed for Aurivillius phase. Thus, simultaneous substitution on the A and B sites of the pseudo-perovskite units of SrBIT won't be considered. Finally, for small ionic size tetravalent oxides, like Mn⁴⁺, the substitution in SrTiO₃ is easier as calculated [106] on B site with electron compensation. All of these mechanisms are summarized in Table 4-1.

Table 4-1: summary of substitution sites and compensation mechanisms for SrTiO₃ as calculated by Akhtar et al. [106].

Oxide type	Substitution site...	Compensation
Monovalent	Sr ²⁺	V _O ^{••}
Divalent	Sr ²⁺	V _O ^{••}
Trivalent	Sr ²⁺ + Ti ⁴⁺	Self
Tetravalent	Ti ⁴⁺	e ⁻

In the case of Lanthanum doped Pb(Zr_{0.5}Ti_{0.5})O₃ (PLZT), compensation of donors (La_{Pb}⁺) by metallic vacancies in both A and B sites of the perovskite was demonstrated by Hennings and Härdtl [107]. According to Härdtl [108], the concentration of these vacancies would be reduced by trivalent B site acceptor doping (Mn, Fe and Al).

Since no equivalent investigations are available for Bismuth Titanates, the above considerations about BaTiO₃ and SrTiO₃ will be used as starting points for SrBIT analysis.

4.2.2 Interpretation of Conductivity Measurements

Interpretation of the conductivity measurements in reducing conditions for undoped BaTiO₃ was realized with doubly ionized oxygen vacancies [37,38,90,92,109]. Such a model however assumes some intrinsic source of oxygen vacancies. As presented above, Frenkel and Schottky disorders could be an intrinsic source of oxygen vacancies. Actually oxygen interstitials are very unlikely as are simultaneous creation of Ba and Titanium vacancies. Thus, many authors concluded that impurity centers were actually the only oxygen vacancy source. In addition, as the natural abundance of slightly charged cations of alkali and alkaline earth metals is high, most of the impurity centers act as acceptors or neutral impurities [90]. In conclusion, the four point defects that are significant in undoped BaTiO₃ for a complete description of the electrical conductivity under controlled oxygen partial pressure are free electrons and holes, oxygen vacancies and acceptor centers. Then, the electroneutrality equation of the system is simply:

$$n + [A'] = p + 2[V_O^{\bullet\bullet}] \quad \text{Equation 4-6}$$

Under oxygen deficient atmosphere, oxygen vacancies are created by the reduction equation:



Oxygen vacancies are directly compensated by acceptor centers, simplifying the electroneutrality equation to:

$$[A'] = 2[V_O^{\bullet\bullet}] \quad \text{Equation 4-8}$$

The mass-action constant for reduction associated with Equation 4-7 is:

$$K_R = [V_O^{\bullet\bullet}]n^2p_{O_2}^{\frac{1}{2}} \quad \text{Equation 4-9}$$

with n , the concentration of free electrons and p_{O_2} the oxygen partial pressure of the surrounding atmosphere. Equation 4-9 can be rewritten with Equation 4-8:

$$n = \left(\frac{2K_R}{[A^{\bullet\bullet}]} \right)^{\frac{1}{2}} p_{O_2}^{-\frac{1}{4}} \quad \text{Equation 4-10}$$

The calculation of the electrical conductivity can thus be made with another quite strong assumption concerning the mobility of the charge carriers (electrons in this case). If this mobility is independent of temperature and p_{O_2} (as shown by Fleischer [110]), then the electrical conductivity is directly proportional to the oxygen partial pressure power $-1/4$. This has been verified experimentally many times. The same kind of calculation can be made for both very low oxygen partial pressure and oxygen excess region; this gives a general schematic of the conductivity versus oxygen partial pressure curve.

4.2.2.1 Electron and hole traps

In the case of Alkaline-Earth Titanate, like BaTiO₃, acceptor centers act as deep hole traps and donor centers as shallow electron traps [111]. Thus, it is easy to move free electron into conduction band for n-type alkaline earth Titanates, but difficult to put holes in the valence band. This creates the insulator to semiconductor transition observed in those materials. Nevertheless, either Ba²⁺ or Sr²⁺ do not contribute to the electronic structure, because of their closed-shell inert configuration. On the contrary for Bi³⁺ or Pb²⁺ their 6s² inert pair contributes to the valence band of Bismuth Titanates [112] or Lead Zirconate Titanate (PZT) [111]. For PZT, those levels are shallow hole traps and it was demonstrated that Ti⁴⁺ centers were deep electron traps (1 eV) forming Ti³⁺ centers. Such centers however were not detected neither for BaTiO₃ nor SrTiO₃. Acceptor levels due to impurities forming deep traps are also present in Bismuth or Lead compounds.

Table 4-2: summary of trapping features for alkaline earth and lead compounds

Trapping of ...	SrTiO ₃ , BaTiO ₃	PZT
Electrons	Not observed	Deep Ti ³⁺ (1 eV)
Holes	Deep (acceptor centers)	Deep (acceptor centers) Shallow Pb ³⁺ (0.7 eV)

However, in the p-type region, the appearance of the electrical conductivity versus oxygen partial pressure curve of PbZr_{0.5}Ti_{0.5}O₃ is very similar to BaTiO₃ [111] with a slope close to $+1/4$. In a previous paper from the same author, the possibility of conduction through small polarons was reported. In that case, holes trapped on lead vacancies were thought to be carriers responsible for

conduction. The hole mobility activation energy for PZT is not negligible; several authors measured it around 0.3 eV. This activation energy for SrTiO₃ is zero as given by Cox [113] and 0.15 eV for BaTiO₃.

At much lower oxygen partial pressure, the production of oxygen vacancies, see Figure 4-8, is so high, that acceptor impurities are no longer sufficient to compensate them and free electrons are created. This leads to another slope of the conductivity curve, calculated as follows. The neutrality equation is written as:

$$2[V_O^{\bullet\bullet}] = n \quad \text{Equation 4-11}$$

Then, the concentration of free electrons becomes with the reduction equilibrium, Equation 4-9:

$$n = K_R^{\frac{1}{3}} p_{O_2}^{-\frac{1}{6}} \quad \text{Equation 4-12}$$

With the same assumptions as above concerning the mobility, the equilibrium conductivity is the inversely proportional to the sixth power of the oxygen partial pressure.

This simple theory was presented because the first step in studying the electrical conductivity of SrBIT is to check the presence of either a $\pm 1/4$ or $-1/6$ slope in the log-log representation of the equilibrium conductivity versus oxygen partial pressure. This would be an indication that the same phenomenology as written for BaTiO₃ can be used for SrBIT too.

SrBIT is a ternary oxide and has much more complicated structure than BaTiO₃ or SrTiO₃. Point defects that could be produced in this material are summarized in Table 4-3. As given in this table, Bi³⁺ can either be removed or dismute to other oxidation states, Sr²⁺ can be removed or substitute Bi³⁺ in the Bismuth oxide layer, Titanium vacancies can also be created and finally oxygen vacancies may exist in either the perovskite units or in the Bismuth oxide layer. However, it was shown that oxygen vacancies were predominantly formed in the Bismuth oxide layer [78]. The possibility of interstitial oxygen was rejected for perovskite, but the more open fluorite-coordinated Bismuth oxide layers could allow such interstitial defects.

Table 4-3: summary of point defects in SrBIT.

Ion concerned	Pseudo-perovskite	Bi oxide layer
Bi ³⁺	V _{Bi} , Bi _{Bi} , Bi _{Sr}	V _{Bi} , Bi _{Bi}
Sr ²⁺	V _{Sr}	Sr _{Bi}
Ti ⁴⁺	V _{Ti}	
O ²⁻	V _O	V _O , O _i

The electroneutrality equation for SrBIT can then be written as:

$$V_{Bi}^{\bullet\bullet} + Bi_{Bi}^{\bullet} + V_{Sr}^{\bullet\bullet} + Sr_{Bi}^{\bullet} + V_{Ti}^{\bullet\bullet\bullet} + e^{\bullet} + O_i^{\bullet\bullet} = Bi_{Bi}^{\bullet\bullet} + V_O^{\bullet\bullet} + Bi_{Sr}^{\bullet} + h^{\bullet} \quad \text{Equation 4-13}$$

In addition, as observed in BaTiO₃ acceptor impurities, written A[\] may also be present in SrBIT, they should be added to Table 4-3 and Equation 4-13. In principle, a number of simplified

compensation equations could be written with different defects combinations. Each of these would define a slope for the conductivity curve within a pO_2 range. However, because of the respective energy levels of these defects, some regime may be observed and others not. For example, the pO_2 -independent regime corresponding to the direct compensation of some ionized donors by free electrons could not be seen for very deep donors levels (see Porat and Tuller [114]).

In addition to the investigation of undoped SrBIT, two compositions of doped SrBIT were studied: 2 mol.% Mn doped and 4 mol.% Nb doped. In the first case, Mn probably substitutes Ti on the B sites of the perovskite units as shown for $\text{Bi}_4\text{Ti}_3\text{O}_{12}$ by Kato [48]. It was shown for BaTiO_3 , that Mn's state of oxidation was +2 under moderately reducing conditions [89] and BaTiO_3 sintered in air showed the presence of Mn^{4+} . Finally, those sintered in Ar had Mn^{4+} as well as Mn^{2+} . Under strongly reducing conditions, Mn is expelled from the lattice and this was suggested as the origin of disappearance of any EPR signal. Several authors reported the effects of Mn [49,101] on the electrical conductivity of BaTiO_3 . However, the description slightly differs between the two groups: according to Osawa the sequence of slopes of the log-log representation of the electrical conductivity is $-1/6$ to $-1/4$ to $+1/6$ as the pressure is raised; according to Kim, the equivalent sequence is $-1/6$ to $-1/4$ to $-1/6$ to $+1/6$. In fact, Osawa did not consider the effect of Mn^{4+} state on Ti^{4+} in the n-type region, but according to Kim this introduces a $-1/6$ region.

Donor doping of SrTiO_3 was investigated by Moos [115]. The possibility of a direct compensation of the ionized donors by free electrons leads to a pO_2 independent region. The observed $-1/4$ slope in the slightly reducing conditions is caused in that case by ionic compensation of donors by Strontium vacancies.

4.3 EXPERIMENTAL CONDITIONS

4.3.1 General Presentation

The electrical conductivity was measured from 600°C up to 1000°C in a tube furnace under controlled oxygen partial pressure. The conductivity was measured with a DC four probes technique under constant current; the oxygen partial pressure was measured with a ZrO₂ oxygen probe and the temperature was measured with a thermocouple. The oxygen partial pressure was regulated with different gas mixtures and with a ZrO₂ oxygen pump. A general view of the sample holder, oxygen sensor and thermocouple inside the tube furnace is presented schematically in Figure 4-1. The electrolytic ZrO₂ oxygen pump was placed just beside thermocouple and oxygen probe.

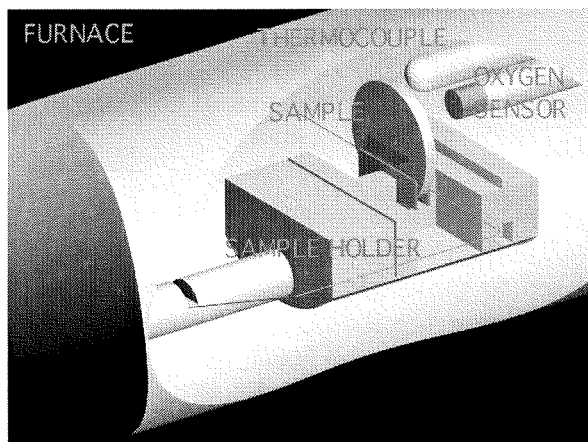


Figure 4-1: general view of the high temperature set-up used for electrical conductivity measurements under oxygen partial pressure. Both discs and bars can be used as samples. Close to the oxygen sensor, one ZrO₂ oxygen electrolytic pump was placed.

4.3.2 Oxygen Partial Pressure Regulation

The oxygen partial pressure was adjusted with two type of gas mixing: Ar and O₂ from 1 atm down to around 10⁻⁵ atm and CO and CO₂ from 10⁻¹⁰ down to 10⁻¹⁵ atm (this range depends on temperature). In the first case, no chemical reaction is used to modify the oxygen activity; the oxygen molecules were only diluted in inert Ar. The lower limit of oxygen partial pressure was defined by gas purity, which was 2 ppm and gas leakage of the system. The two gases were mixed with mass flow controllers at a pressure slightly higher than the ambient (defined by a gas bubbler). Typical flow values of the first pO₂ range were 300 sccm Ar and zero sccm O₂ for the lowest oxygen activity and zero sccm Ar with 10 sccm O₂ for the highest level (about 1 atm).

About one hour delay was necessary to decrease the pressure from 1 atm down to 10⁻⁵ atm above 700°C. No aging of the metallic wires or electrodes was observed with this method. In order to achieve reproducible measurements, the reduction/oxidation path was kept identical for all experiments. The standard measurement procedure was the following:

(1)
15 hours under pure flowing O₂ (10 sccm) and measurement of conductivity.

(2)
Decrease of the oxygen partial pressure down to 10⁻⁵ atm (300 sccm flowing Ar), 10 to 15 hours annealing, and continuous measurement of the conductivity.

(3)
Step by step increase of the pressure (by one order of magnitude), with 5 to 10 hours settling time at each pressure, continuous measurement of the conductivity.

(4)
Check for reversibility, measurement of conductivity under pure flowing O₂.

The effective oxygen partial pressure was measured with a ZrO₂ oxygen gauge consisting of a Zirconia pellet bound to an Alumina tube and covered with porous Platinum ink. Thus, one face of the ZrO₂ cell was exposed to the modified atmosphere (pO₂-in) and the other one to the ambient (pO₂-out=0.21 atm). Measuring the electrical potential drop (E) between the two ZrO₂ pellet's faces gives the oxygen partial pressure inside the furnace, according to:

$$E = \frac{RT}{nF} \ln \left(\frac{p_{O_2}^{\text{in}}}{p_{O_2}^{\text{out}}} \right) \quad \text{Equation 4-14}$$

where R and F are the perfect gas constant (R=8.31 J/molK) and Faraday constant (F=96485 C/mol). In that case n=2 and Equation 4-14 can be rewritten as:

$$p_{O_2}^{\text{out}} = 0.21 \exp \left(-\frac{46.42E}{T} \right) \quad \text{Equation 4-15}$$

According to Fouletier [116], any secondary chemical reactions taking place at the electrode can induce measurement errors. For example, unburned gases, solid particles and metallic dust are slowly oxidized by oxygen. The very local equilibrium pressure at the measuring electrode may be modified by such reactions and the resulting error of measurement can be very large. From the same author it is unadvisable to use a ZrO₂ oxygen probe in carbon monoxide containing atmosphere with Platinum electrodes. As Platinum acts as a catalyst, non-catalytic electrodes should be used [117] for the analysis of the oxygen partial pressure in atmosphere containing CO

or H₂. However, even Gold or Silver still exhibit catalysis of CO oxidation [117]. It was shown that reactions with gas phase CO of either adsorbed molecular oxygen, written O₂^{ad} as described by Equation 4-16 or atomic oxygen, written O^{ad}, as described by Equation 4-17 may decrease the apparent (measured) oxygen activity. For example Haaland [117] reported that in CO gas atmosphere with 4500 ppm O₂, the measured oxygen activity was only 0.1 ppm!



However, these mechanisms are detrimental for elevated CO concentrations, in this work CO content was kept as low as possible and pure CO experiments were mostly avoided. The above oxidation reactions may modify measurements; in addition strong aging of both Platinum electrodes and connecting lines were observed too, Figure 4-2. After long time annealing at elevated temperature (1000°C for 15 hours) of thin sputtered Platinum electrodes, the metal coating is no longer continuous at all. A kind of non-wetting process was observed that caused the complete deterioration of the electrode.

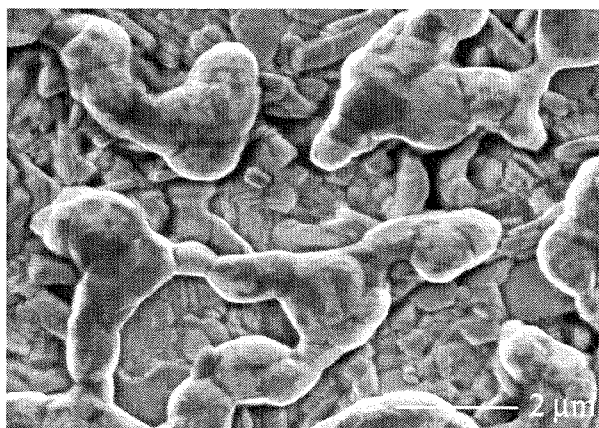


Figure 4-2: thin sputtered Pt electrode after high temperature annealing in CO/CO₂.

With thicker Platinum layers deposited as paint on the ceramic surface, the stability of the coating was considerably improved, Figure 4-3. However, some extra phase were created under CO and CO₂, Figure 4-3, those phases remain unknown as X-rays diffraction analysis was not able to identify them (too small quantities). One possibility would be the formation of PtC. Nevertheless, those phases were removed by subsequent oxygen annealing, Figure 4-3(b).

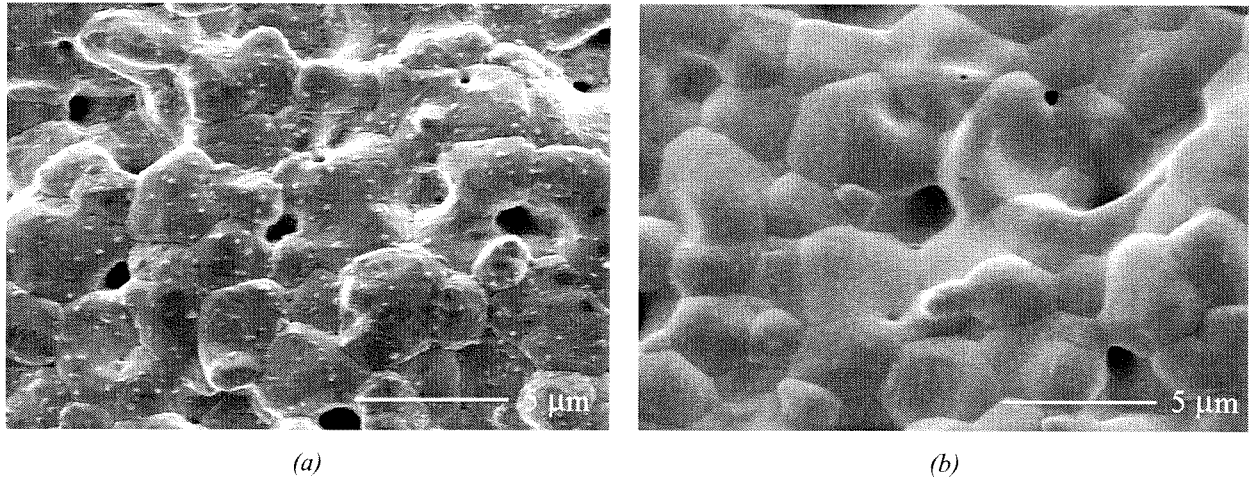


Figure 4-3: thick Platinum coating used as electrode, (a) after high temperature annealing in CO/CO_2 , (b) after oxygen re-oxidation annealing.

The choice of a different electrode was limited by the desired temperature range (up to 1000°C) and oxidation behavior (for the $\text{Ar}-\text{O}_2$ domain). For oxygen poor atmospheres, in CO/CO_2 , copper wires were tested as connecting lines. Their lifetime was much higher than Platinum ones, but the available temperature range was limited (Copper melting point is 1083°C).

The effective oxygen partial pressure established under various O_2 to Ar flows is presented in Figure 4-4. The oxygen activity is directly proportional to the extra oxygen flow down to $2 \cdot 10^{-3}$ O_2/Ar and diverges below.

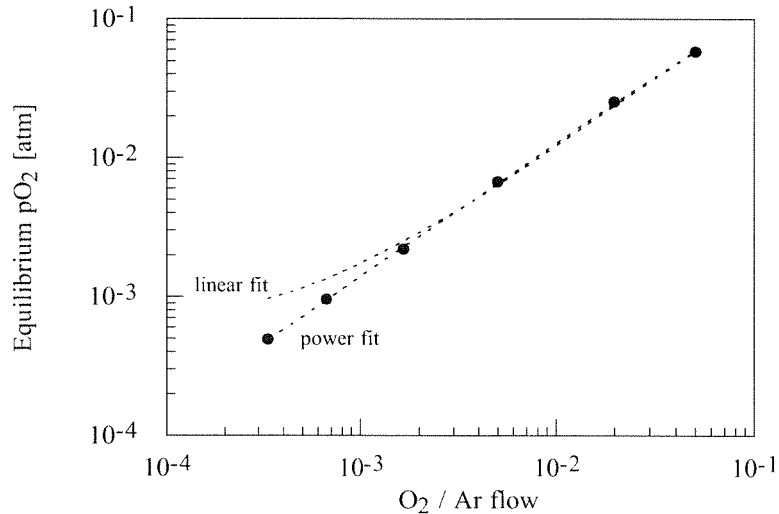


Figure 4-4: equilibrium oxygen partial pressure versus O_2 to Ar flows ratio at 1000°C . The oxygen partial pressure established for pure flowing Ar was $4 \cdot 10^{-5}$ atm in that case.

The second method for oxygen adjustment is the mixture between CO and CO_2 . This not a dilution process but a chemical reaction between three gases, Equation 4-18.



The mass-action equation corresponding to Equation 4-18 leads to a square dependence of the oxygen partial pressure to the ratio of the partial pressures of CO to CO₂. With the assumptions that the partial pressure of CO and CO₂ are proportional to their respective flow (D_{CO} and D_{CO_2}), it follows finally that the oxygen partial pressure has the same dependence towards the gas flows. Thus, the oxygen partial pressure can be written as:

$$p_{\text{O}_2} \propto \left[\frac{D_{\text{CO}}}{D_{\text{CO}_2}} \right]^2 \quad \text{Equation 4-19}$$

This square dependence was actually measured; see solid line in Figure 4-5. Thus, the p_{O_2} range available at 900°C ranges according to Figure 4-5 roughly from 10^{-10} up to 10^{-14} atm with CO and CO₂ and from 1 atm down about 10^{-5} atm with Ar and O₂ (this latter range is independent of temperature). The pressure gap in-between was filled with a ZrO₂ electrolytic pump.

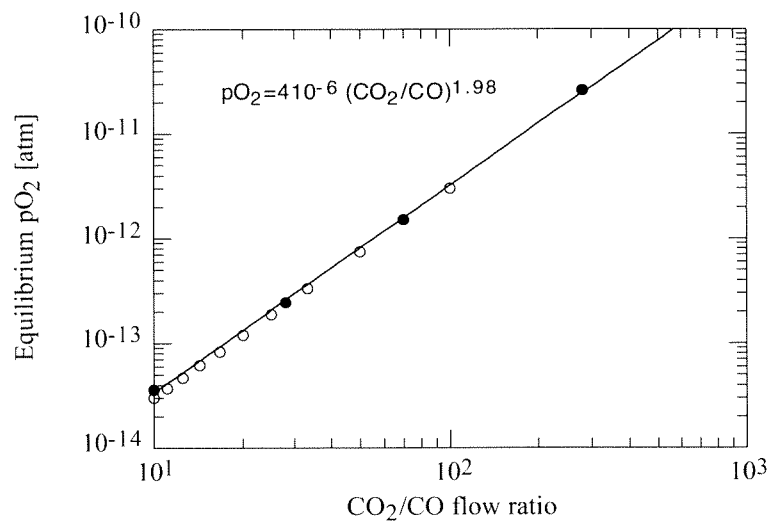


Figure 4-5: equilibrium oxygen partial pressure versus D_{CO} to D_{CO_2} flows ratio. Filled circles are measurements at 900°C and open circles are thermodynamical calculation at 1200 K.

The ZrO₂ pump was made with a cubic stabilized ZrO₂ tube closed at one end. Both inner and outer surfaces were covered with porous Pt coating. The outer surface of the tube was placed inside the furnace and the inner surface was let in contact with the ambient atmosphere. With a DC current source, a constant current was applied to the ZrO₂ tube electrodes. The polarity of the external voltage was either positive or negative. For a positive voltage, the oxygen partial pressure could be increased compared to the equilibrium and it could be decreased for a negative one, Figure 4-6.

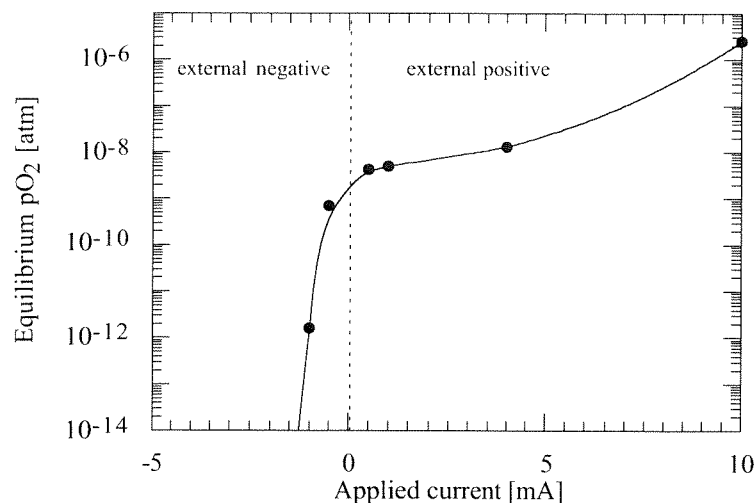


Figure 4-6: equilibrium oxygen partial pressure versus applied DC current at 800°C with $\text{CO}/\text{CO}_2=0.1/100$.

4.3.3 Conductivity Measurement

The electrical conductivity has been measured using HP34401 Multimeter from Hewlett-Packard in the four wires resistance measurement mode. In this mode, the resistance of the sample given by the equipment is calculated under a DC current. The value of this current depends on the chosen current range. It is comprised between 1 mA (100 Ω range) and 500 nA (100 M Ω range). With this method, the electrical resistances of the connecting wires (as long as 50 cm) can be neglected.

Ceramics samples were cut in bar shape. This geometry is usually preferred for equilibrium conductivity measurements. The advantages of this shape is that the exposed area to volume ratio, Table 4-4, is much higher compared to a disc sample, as usually $d \gg a$. Thus, time needed to reach equilibrium is much lower with a bar.

Table 4-4: exposed area to volume ratio for a bar and disc.

Bar (length L, thickness a)	Disc (diameter d, thickness t,)
$\frac{A^{\text{exposed}}}{V} = 4 \frac{1}{a}$	$\frac{A^{\text{exposed}}}{V} = 4 \frac{1}{d}$

4.3.4 Data Processing

4.3.4.1 Conductivity transients

In order to evaluate the real equilibrium (steady-state value) conductivity established after an oxygen partial pressure change, a simple diffusion model was used. This model developed by

Wernicke [87] for BaTiO₃ allows the calculation of both equilibrium conductivity (written σ_∞) and diffusion coefficient (D). The expression for the normalized conductivity is:

$$\frac{\bar{\sigma} - \sigma_0}{\sigma_\infty - \sigma_0} = 1 - \sum_n \frac{8}{\pi^2(2n+1)^2} \exp\left[-\pi^2(2n+1)^2 \frac{Dt}{h^2}\right] \quad \text{Equation 4-20}$$

This equation is actually a solution of Fick's diffusion law for a flat plane of thickness h . In Equation 4-20; t is time. The conductivity is written as a mean value over the entire sample volume, since surface and core are not reduced/oxidized at the same rate. The measured transient conductivities were fitted by Equation 4-20 using a generalized least square method, for given initial conductivity σ_0 and diffusion length, h .

$$\Delta X = (A^T A)^{-1} A^T Y \quad \text{Equation 4-21}$$

Where ΔX is the vector of corrections to the initial conditions, Y is the vector of differences between the measured and calculated conductivity values and A is the matrix of partial derivatives calculated for the initial conditions. In general, five runs were sufficient to find converging values.

However, the establishment of stable oxygen partial can be quite long. Because the diffusion model assumes an instantaneous change of pO_2 , diffusion coefficients calculated with Equation 4-20 can only be used for physical interpretation, providing that the oxygen partial pressure change is much faster than the electrical conductivity change.

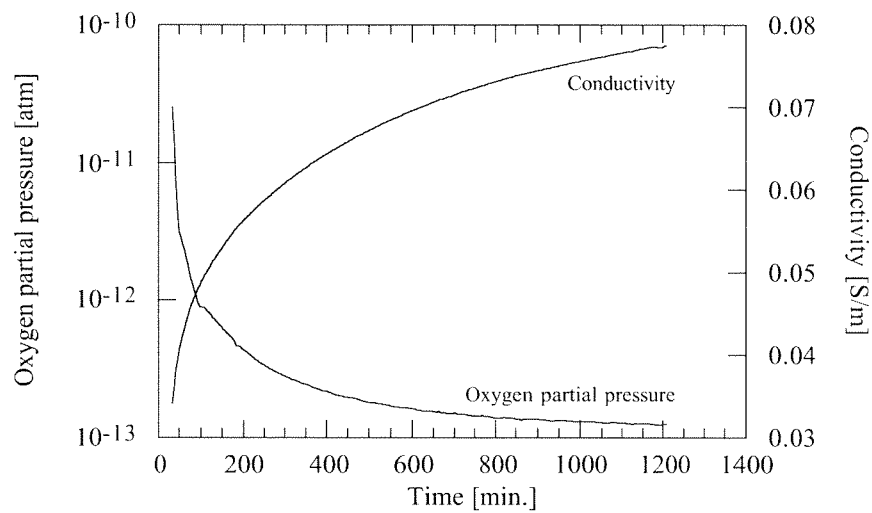


Figure 4-7: oxygen partial pressure and conductivity transients at 800°C.

4.3.4.2 Ionic Conductivity Calculation

An alternative method to EMF measurements to calculate the ionic conductivity contribution is to use conductivity measurements under controlled oxygen partial pressure as proposed by Chang [118]. For BaTiO₃, this is achieved with the assumption that close to the conductivity minimum (in the conductivity versus oxygen partial pressure curve), the conductivity can be written as:

$$\sigma_T = \sigma_i + \sigma_n^0 p_{O_2}^{-\frac{1}{4}} \quad \text{Equation 4-22}$$

In this equation, σ_T is the total conductivity, σ_i the ionic conductivity and σ_n^0 is the electronic contribution at $p_{O_2}=1$ atm. As shown in section 4.4.2 that for SrBIT the electrical conductivity follows a power law with $n=-0.25$ in the 10^{-5} -1 atm p_{O_2} range, Equation 4-22 can be used to calculate the ionic conductivity of SrBIT. This can be done with the assumption of p_{O_2} -independent ionic conductivity as given by the acceptor-controlled model, Equation 4-24. However, because the conductivity minimum was never clearly observed, the extrapolation of conductivity with Equation 4-22 is still a strong assumption. It may exist an extra regime with a different compensation mechanism between the conductivity minimum and the acceptor-controlled region. It should also be noted that in the lowest measurement temperatures (700 and 800°C), the actual conductivity slopes are not very close to -0.25, Equation 4-9. If this could be a proof of the vicinity of the minimum, it also decreases the accuracy of the calculation. Those remarks are very important for a good interpretation of the results, especially for the calculated transference numbers, Equation 4-22.

4.4 ELECTRICAL CONDUCTIVITY OF SRBIT UNDER CONTROLLED OXYGEN PARTIAL PRESSURE

4.4.1 BaTiO₃ used as a reference material

Since the experimental set-up for conductivity measurements under controlled oxygen partial pressure was a home made, a serious authentication procedure had to be undertaken. This was accomplished through measurement of the conductivity of undoped BaTiO₃ in the different oxygen partial pressure ranges. At first, the electrical conductivity was measured from 700°C up to 1000°C in flowing Ar and O₂ gas mixtures (10⁻⁵ - 1 atm pO₂), Figure 4-8. In every measured temperature, the conductivity decreases as the oxygen partial pressure decreases. This is representative of the oxygen excess region, where according to Chan [37], molecular gaseous oxygen is dissociated and fills the oxygen vacancies. This is expressed by the oxidation reaction:



This equation implies the presence of "extrinsic" oxygen vacancies previously created to compensate for the natural acceptor impurities. According to the same author, the possibilities of the introduction of oxygen excess either on interstitial sites or on true anionic sites compensated by Ba and Titanium vacancies were not realistic. Assuming that only a small fraction of vacancies are actually filled by oxygen, the hole concentration can be neglected compared to the oxygen vacancies one and the electroneutrality equation becomes with the acceptor impurities concentration [A']:

$$2[V_o^{\cdot\cdot}] = [A'] \quad \text{Equation 4-24}$$

And finally, the hole concentration (p) can be written as:

$$p \propto p_{O_2}^{+\frac{1}{4}} \quad \text{Equation 4-25}$$

If the hole mobility is independent of oxygen partial pressure, the slope of the electrical conductivity versus oxygen partial pressure should be +0.25 in the log-log representation. As shown in Figure 4-8, the measured slope corresponds to the predicted value. In addition, our results were directly compared to the literature [37], open circles in Figure 4-8 are Chan's [37] measurement of undoped BaTiO₃ and filled circles are conductivity measurements made with our new experimental setup. A very good agreement between the two sets of data is obvious. At 1000°C, the transition to the oxygen deficient region (increasing conductivity as the oxygen

activity is reduced) was also observed. The conductivity minimum reported by Chan was around 10⁻⁴ atm as we measured.

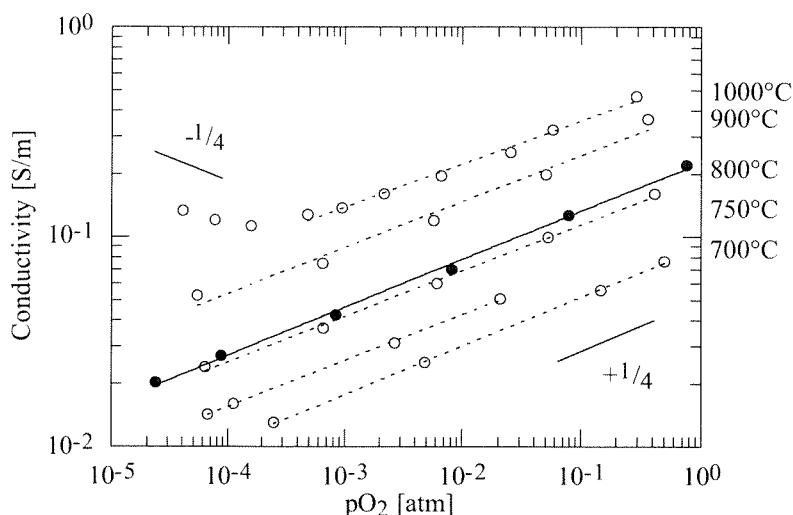


Figure 4-8: electrical conductivity of BaTiO₃ at high temperature under controlled oxygen partial pressure (Ar-O₂ range). Filled circles are measurements and open circles are taken from literature [37].

The complete expression for the electrical conductivity includes the hole mobility μ_p , the acceptor impurities concentration $[A']$, the temperature-independent mass action constant K'_p and the enthalpy of Equation 4-23, ΔH_p .

$$\sigma = \mu_h e \left(\frac{[A']}{2} K'_p \right)^{\frac{1}{2}} \exp\left(-\frac{\Delta H_p}{2k_B T}\right) p_{O_2}^{+\frac{1}{4}} \quad \text{Equation 4-26}$$

If one assumes a temperature-independent mobility, the slope of the Arrhenius plot is half of ΔH_p . Our measurements indicate values of ΔH_p comprised between 1.5 eV (10⁻¹ atm pO₂) and 1.6 eV (10⁻⁵ atm pO₂). However, Chan [37] reported 0.92 eV for the activation energies in the p-type region, which is about half what we measured. As our conductivity results are very close to Chan's measurements, Figure 4-8, the reason for this difference could be a confusion between ΔH_p and E_G that is the actual activation energy for conduction corresponding to $\Delta H_p/2$.

If the electroneutrality equation is written to take into account both electrons and acceptors compensation as Equation 4-27:

$$2[V_O^{\cdot\cdot}] = [A'] + n \quad \text{Equation 4-27}$$

Usually, the electron concentration n can be neglected compared to the acceptor impurity content. However, writing the electroneutrality equation like this allows the separate calculation of the mass-action constant for reduction (K_R) and $[A']$. Equation 4-29 implies the simultaneous

compensation of oxygen vacancies by acceptors and electrons, since the electroneutrality equation is written as Equation 4-27. Usually in the modeling, the two regimes are isolated, leading to two distinct exponent values of $-1/4$ and $-1/6$, when $[V_{O^{\bullet\bullet}}] \gg n$ or $[V_{O^{\bullet\bullet}}] \ll n$ respectively. As shown in Figure 4-9 and further in Figure 4-14, the second regime ($m=-1/6$) was not observed neither in the high oxygen partial pressure range (10^{-5} up to 1 atm) nor in the low (down to 10^{-13} atm). The mass-action constant for reduction becomes Equation 4-28:

$$K_R = \left([A'] + n \right) n^2 p_{O_2}^{\frac{1}{2}} \quad \text{Equation 4-28}$$

It can be rewritten as Equation 4-30:

$$p_{O_2} = \left[\frac{2(\mu_e e)^3 K_R}{\sigma^2 (\sigma + A' \mu_e e)} \right]^2 \quad \text{Equation 4-29}$$

According to the acceptor-controlled model, fitting the oxygen partial pressure versus conductivity data's with Equation 4-29 with the appropriate electron mobility should give the net acceptor impurities concentration $[A']$ and the temperature dependent mass-action constant K_R . As calculated by Chan for $BaTiO_3$, a typical value for the acceptor concentration is 50 ppm. This concentration was slightly temperature dependent; the author explained this as an effect of some defect association; ionization of the impurity centers can also account for the observed change in $[A']$. This acceptor-controlled model will be applied to SrBIT as a first description of the defect structure of this material.

4.4.2 DC Electrical conductivity of SrBIT in Ar-O₂

4.4.2.1 Undoped SrBIT

The electrical conductivity of undoped SrBIT has been measured as a function of the oxygen partial pressure, at first in the Ar-O₂ range ($10^{-5} - 1$ atm) at elevated temperature (700°C-900°C), Figure 4-9. In this p_{O_2} range, the electrical conductivity of SrBIT increases as the oxygen activity is decreased. This is opposite to measured $BaTiO_3$ behavior, Figure 4-8; it is an indication of an oxygen deficient regime, with n-type conductivity. Despite careful investigations of the upper level of oxygen (0.1 – 1 atm), the occurrence of a conductivity minimum cannot be reported. This may also be due to a poor quality of the ZrO₂ gauge oxygen concentration measurement in this pressure range.

In the log-log scale representation, the slope of the curve gets closer and closer to -0.25 as the temperature is raised. This experimental fact would suggest a first hypothesis on the actual compensation mechanism. This mechanism would be the compensation of some natural acceptor impurities (singly ionized) by oxygen vacancies (doubly ionized) [37,38,90,109,119]; this was already presented in section 4.2.2. According to this model, the expression for the electrical

conductivity is Equation 4-30 with the electroneutrality equation written as Equation 4-24. This equation predicts a -0.25 slope, as actually measured.

$$\sigma = \mu_e e \left(\frac{2K_R}{[A']} \right)^{\frac{1}{2}} pO_2^{-\frac{1}{4}} \quad \text{Equation 4-30}$$

where μ_e is the electron mobility and e is the elementary charge $e=1.602 \cdot 10^{-19}$ C. It is important to note that the assumption of acceptors-controlled conductivity is not the only solution to interpret our results. As shown below in section 4.4.3, some donor-doped features (electronic conductivity independent of oxygen partial pressure) would suggest to modelize SrBIT with some "intrinsic" donors concentration that also provides a $-1/4$ slope in the highest pO_2 range.

At 700°C , the slope is smaller, it is only about -0.16 . Several reasons could account for the occurrence of such a lower slope value. It could be the indication of an additional compensation mechanism, it could be related to the vicinity of the conductivity minimum or it may be caused by poor measurement quality in the lower temperature range (both oxygen partial pressure and conductivity measurement), because of small diffusion coefficients. The reduction regime (electronic compensation of oxygen vacancies), below the acceptor controlled region would provide a -0.16 slope in log-log scales. However if this compensation condition occurred at 700°C in this pO_2 range, it should be seen at higher temperature too. It is not the case, since the slope is -0.25 at 900°C . Another compensation could nevertheless be present above the acceptor-controlled regime, just below conductivity minimum. For example, divalent Bismuth cations on trivalent Bismuth sites (in the pseudo-perovskite sub-unit or in the Bismuth oxide layers) would provide a -0.16 slope. Oxygen dependent cation place exchange between Strontium in the pseudo-perovskite sub-units (Sr'_{Bi}) and fluorite-coordinated Bismuth oxide layers would lead to the same slope too.

Electrical conductivity measurements of BaTiO_3 have shown, Figure 4-8 and [37], a rapid transition between deficient and excess regions, with a sharp conductivity minimum, even at 750°C , [37]. If the 700°C measurement of SrBIT corresponded to the same transition, it would be very wide, extending on three to four orders of magnitude. Finally, measurement accuracy problem is rejected in this pO_2 range, since measured oxygen activity corresponded to dilution ratios at every temperature, Figure 4-4. Electrical conductivity transients were also well defined for an accurate determination of equilibrium conductivities. In conclusion, the -0.16 slope observed at 700°C for undoped SrBIT could be caused by a different compensation mechanism due to an "intrinsic" kind of disorder, such as dismutation of Bismuth or cation place exchange between Strontium in the perovskite and Bismuth in the Bismuth oxide layers.

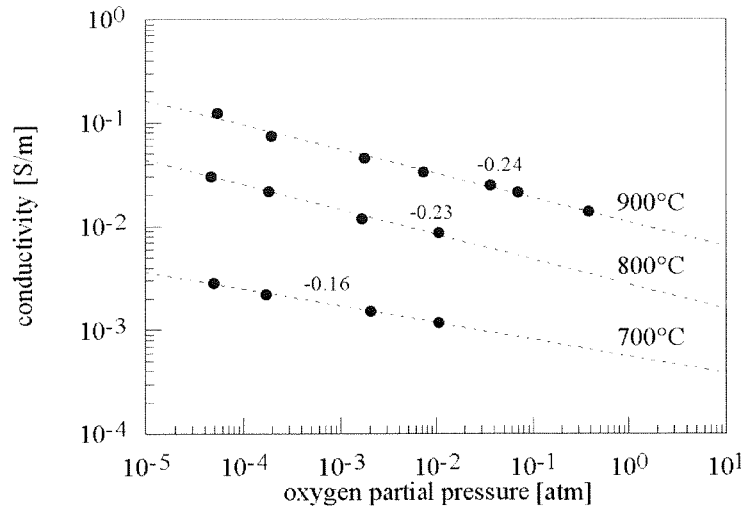


Figure 4-9: electrical conductivity versus oxygen partial pressure for undoped SrBIT.

With the point defect model, it is possible to estimate the net acceptor impurities content, as already discussed above for BaTiO₃. This is realized through curve fitting of the oxygen partial pressure versus conductivity using Equation 4-29, as shown in Figure 4-10. The calculated acceptor content for undoped SrBIT is 700 ppm assuming a hypothetical electron mobility of 0.1 cm²/Vs for SrBIT. The amount of acceptor is actually 70 10¹⁵ cm⁻³ and since molecular density of SrBIT is 9 10¹⁹ molecule per cm³, its concentration in SrBIT is 700 ppm.

This calculated natural acceptors impurity content can be evaluated with donor doping experiments already presented in Chapter 3. In the low temperature range (120-220°C) conductivity measurements after reducing annealing, indicate a transition from p-type to n-type by Niobium doping, Figure 3-22. This was demonstrated by the fact that conductivity increases after reducing annealing above 4 mol.% Niobium. Moreover, the occurrence of such a transition is a good indication of the actual existence of a conductivity minimum that is not observed at high temperature. Compared to the acceptor impurities content (700 ppm) calculated here, the Niobium concentration that compensates them is much larger (4 mol.%). This may be an indication that the acceptor-controlled model is actually not valid for a consistent description of SrBIT, another model based on natural donor-excess will be presented below in section 4.4.3.

With Equation 4-29, the mass-action constant for reduction can be calculated at every temperature using a hypothetical electron mobility of 0.1 cm²/Vs. Thus, the enthalpy corresponding to the reduction equation can be calculated. It was found that this energy was 2.3 eV, a lower energy compared to BaTiO₃'s, which was reported as 5.9 eV by Chan [37] and also lower to SrTiO₃'s, that was reported as 6.1 eV by Moos [120].

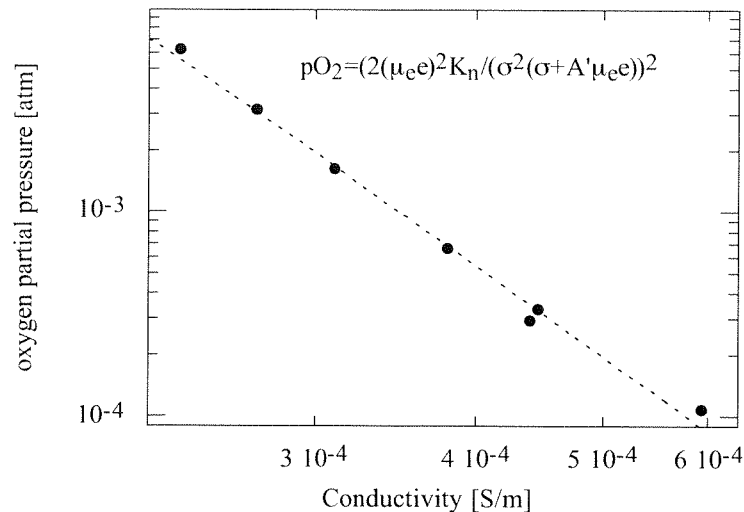


Figure 4-10: curve fitting of the electrical conductivity measurements to calculate the acceptor impurity concentration with Equation 4-29.

Electrical conductivity of undoped SrBIT in the 10^{-5} –1 atm pO_2 range behaves quite similarly to BaTiO₃'s n-type regime (below 10^{-5} atm at 1000°C), for this reason, the same point defect model was used to describe both of them. However, the model predicts in case of acceptor doping that the p-type region should be extended to much lower pO_2 range, shifting the conductivity minimum [38,92]. This was not clearly established for SrBIT. Nevertheless, for a complete agreement of the model, there should exist a slope change (to $-1/6$ according to Equation 4-12) in SrBIT at lower oxygen partial pressures, when free electrons are much numerous than acceptor centers; as presented below, the measured behavior of SrBIT is quite different.

Acceptor doping has been evaluated with some Mn substitution on the Ti⁴⁺ site of the perovskite sub-unit; the composition used for this purpose was SrBi₄Ti_{3.98}Mn_{0.02}O₁₅. As Mn oxidation states in BaTiO₃ are +2, +3 and +4 depending on the oxygen partial pressure [121], it likely acts as an acceptor on the Titanium sub-lattice. Manganese is also known to reduce the conductivity increase of BaTiO₃ due to reduction [49,101,121,122]. Detailed analysis of acceptor doping is presented in the next section.

4.4.2.2 Manganese doping outcome

In this section, the electrical conductivity of acceptor doped SrBIT (with 2 mol.% Mn) will be described in details. Large behavior difference will be demonstrated and interpreted with the aid of a point defect model reported by Kim [101] for Mn doped BaTiO₃. With the assumptions that the equilibrium reduction of Mn⁴⁺ into Mn³⁺ in SrBIT is identical for SrBIT and BaTiO₃ and that the electron mobility is about 0.1 cm²/Vs, the equilibrium constants for both oxygen vacancies creation (K_R) and for intrinsic ionization of electronic carriers across the band gap (K_i) have been calculated at several temperatures. Fitting those mass-action constants with Arrhénus expressions conducted to the determination of the activation energy for reduction and the energy of the band gap, E_g .

The effect of Mn doping at 800°C is obvious from Figure 4-11, at 10^{-5} atm pO_2 the electrical conductivity of Mn doped SrBIT is about half-smaller than undoped SrBIT. The slope of conductivity is much smaller, it is only -0.15 compared to the -0.25 value of undoped SrBIT. This change is highly significant and its interpretation requires the use of a different point defect model. Conductivity minimum is not observed in the reliable pressure range (up to 10^{-1} atm) that is no p-type region (decrease of conductivity as the pressure is reduced) is observed. A shift of this minimum could however be expected for acceptor doped material [38].

Less reliable measurements in the high-pressure range (close to oxygen pure atmosphere) would indicate the increase of electrical conductivity by Mn doping in this pressure range. Such an increase of the electrical conductivity near the conductivity minimum has been reported for Calcium doped BaTiO₃ [92]. This would show that Manganese doping in SrBIT is coherent with reported behavior of acceptor doped BaTiO₃ and that a conductivity minimum for SrBIT could actually be present at high temperature and elevated oxygen partial pressure

Stabilization of the electrical conductivity, which is of great interest for applications, is actually known in the case of BaTiO₃ as reported by Desu for example [122]. However, a good description of the compensation mechanisms in the case of Mn doped BaTiO₃ was only recently brought by Kim [101]. The point defect model developed by Kim will be presented below in details as further characterization of SrBIT was made with the aid of this model, Table 4-5 and Table 4-6.

The starting point of the model is the equilibrium between Mn^{3+} and Mn^{4+} that can be written as:



The mass action constant K_A corresponding to Equation 4-31 is:

$$K_A = \frac{[Mn_{Ti}^{\backslash}]p}{[Mn_{Ti}^x]} \quad \text{Equation 4-32}$$

As the total amount of Mn, written as $[Mn]_T$ is kept constant Equation 4-32 can be rewritten as:

$$[Mn_{Ti}^{\backslash}] = \frac{K_A [Mn]_T}{p + K_A} \quad \text{Equation 4-33}$$

At low oxygen partial pressure, the favored oxidation state of Mn is +3 and +4 at higher oxygen activity. If $[Mn_{Ti}^x] \gg [Mn_{Ti}^{\backslash}]$ then $p \gg K_A$, according to Equation 4-32. In addition, with the intrinsic mass-action constant K_i , the concentration of singly ionized Manganese defects can be written:

$$[\text{Mn}_{\text{Ti}}^{\cdot}] = \frac{nK_A [\text{Mn}]_{\text{I}}}{K_i} \quad \text{Equation 4-34}$$

And finally with the reduction equation, Equation 4-9, the equilibrium concentration of free electrons is given by:

$$n = \left(\frac{2K_i K_R}{K_A} \right)^{\frac{1}{3}} ([\text{Mn}]_{\text{I}})^{-\frac{1}{3}} p_{\text{O}_2}^{-\frac{1}{6}} \quad \text{Equation 4-35}$$

providing that the electroneutrality equation can be written as:

$$[\text{Mn}_{\text{Ti}}^{\cdot}] = 2[V_{\text{O}}^{\cdot}] \quad \text{Equation 4-36}$$

Equation 4-35 predicts a $-1/6$ slope in log-log scales for the electrical conductivity versus oxygen partial pressure curve, which has been actually measured at 800°C and 900°C for 2 mol.% Mn doped SrBIT, Figure 4-12. At lower oxygen activities, Manganese defect are fully ionized into Mn^{3+} , thus $p \ll K_A$ and the carrier concentration is:

$$n = (2K_R)^{\frac{1}{3}} ([\text{Mn}]_{\text{I}})^{-\frac{1}{3}} p_{\text{O}_2}^{-\frac{1}{4}} \quad \text{Equation 4-37}$$

However, this compensation was not observed in the 10^{-5} -1 atm p_{O_2} range. As the $-1/6$ region observed in BaTiO_3 by Kim [101] was quite narrow, finding the $-1/4$ regime at lower oxygen partial pressure seems unlikely. The absence of this region may indicate different compensation mechanisms that would extend the $-1/6$ regime. It may also show that in SrBIT the reduction of Mn^{4+} into Mn^{3+} occurs on a wider p_{O_2} -range than in BaTiO_3 . However, for calculations it will be assumed that the thermodynamics of the reduction of Mn^{4+} into Mn^{3+} is identical in SrBIT and BaTiO_3 .

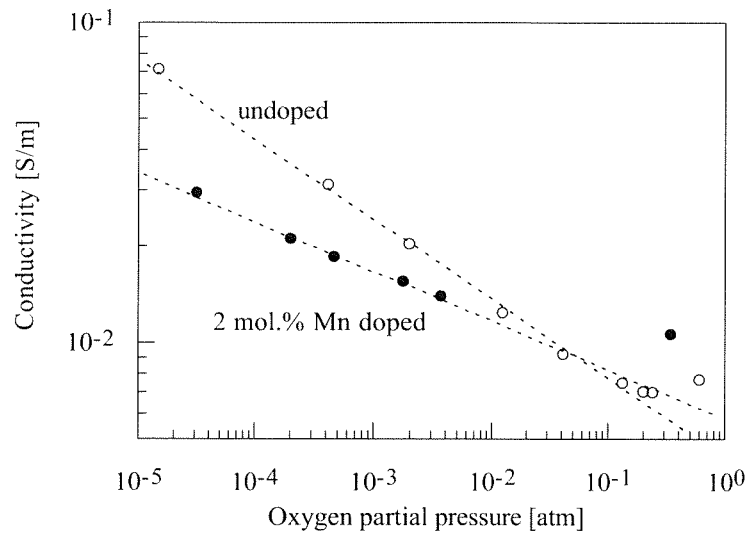


Figure 4-11: electrical conductivity versus oxygen partial pressure for undoped and 2 mol.% Mn doped SrBIT at 800°C.

Assuming that the enthalpy for reduction is modified by Mn doping and taking as before a hypothetical mobility of $0.1 \text{ cm}^2/\text{Vs}$, the mass-action constant K_i can be calculated with the appropriate expression for K_A . In a first approximation, the mass-action constant for Mn^{4+} ionization in BaTiO_3 will be taken here:

$$K_A = 3.2210^{22} \exp\left(-\frac{19618}{T}\right) \quad \text{Equation 4-38}$$

Thus, with Equation 4-35, K_i can be calculated with K_R 's values obtained above, the activation energy for K_i is actually the band gap, since:

$$K_i = N_c N_v \exp\left(-\frac{E_g}{k_B T}\right) \quad \text{Equation 4-39}$$

The calculated values extracted from conductivity measurements at 700°C, 800°C and 900°C for both undoped and 2 mol.% Mn doped are listed in Table 4-5. The Manganese content used for these calculations was $60 \cdot 10^{15} \text{ cm}^{-3}$. The enthalpy for ionized oxygen vacancies creation and band gap energy were calculated with exponential curve fittings (Arrhénus plots) of K_R 's and K_i 's values respectively. The results of these approximations are given in Table 4-5 and Table 4-6.

Table 4-5: estimation of mass-action constants for reduction (K_R) and for intrinsic carriers ionization (K_i) at several temperatures calculated using both undoped and Mn doped SrBIT. The equilibrium constant (K_A) for Mn^{4+} ionization is calculated using Equation 4-38 from [101].

Temperature [°C]	K_A [cm ⁻³]	K_R [cm ⁻⁹]	K_i [cm ⁻⁶]
700	$5.5 \cdot 10^{13}$	$5.6 \cdot 10^{45}$	$2.4 \cdot 10^{32}$
800	$3.7 \cdot 10^{14}$	$1.8 \cdot 10^{46}$	$3.2 \cdot 10^{34}$
900	$1.7 \cdot 10^{15}$	$7.3 \cdot 10^{47}$	$4.1 \cdot 10^{35}$

Table 4-6: mass-action constants for reduction (K_R) and intrinsic carrier ionization (K_i).

Mass-action constant	K_R	K_i
Pre-exponential factor	$5 \cdot 10^{57}$	$4 \cdot 10^{51}$
Energy	2.3 eV	3.5 eV

As indicated in Figure 4-12, at 700°C the slope of the curve ($m=0.09$) is different from the “ideal” value ($-1/6 = 0.16$). Despite of this, these measurements were used to estimate the mass-action constants. The much lower value of the slope can be explained in several ways. At first, the eventual conductivity minimum could stand inside the considered pO₂ range or be much closer to it compared to undoped material. A second explanation would be that due to some ionic charge transport, the total conductivity becomes either pO₂-independent or much less dependent to the oxygen activity. As demonstrated below, Manganese doping increases the transference number of SrBIT, thus some ionic conductivity tracks would not be so surprising.

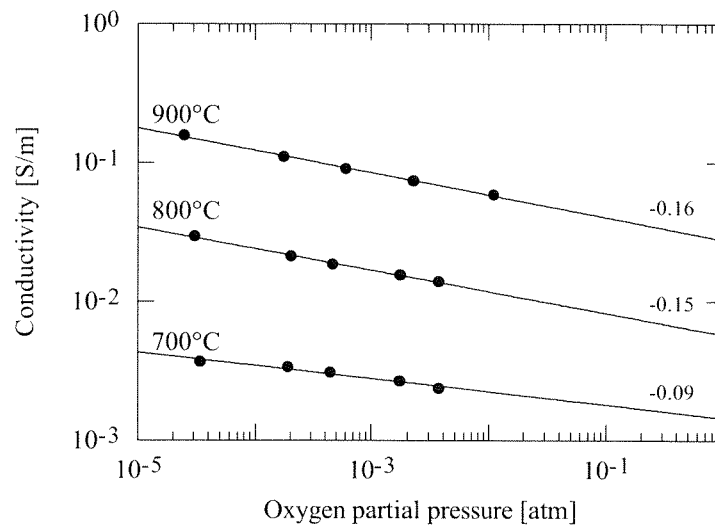


Figure 4-12: electrical conductivity versus oxygen partial pressure at different temperatures for 2 mol.% Mn doped SrBIT.

Two of the expected effects of Manganese doping on the electrical conductivity of SrBIT were actually observed: decrease of the conductivity in the n-type region, since Mn^{3+} acts as an

acceptor on Ti^{4+} sites and transition of the slope from $-1/4$ for the pure material to $-1/6$ for Mn doped SrBIT. However, it was also predicted that the conductivity minimum separating n-type and p-type regions was shifted to lower $p\text{O}_2$ values through acceptor doping. This was not observed, because of either experimental problems (low sensitivity of the ZrO_2 gauge in the high $p\text{O}_2$ range), or insufficient amount of doping.

The characterization of the electrical conductivity of undoped and acceptor doped SrBIT in the 10^{-5} -1 atm $p\text{O}_2$ range show that point defect models elaborated mainly for BaTiO_3 could be used successfully. In addition, using several more or less strong assumptions, such as hypothetical electron mobility close to $0.1 \text{ cm}^2/\text{s}$, several important characteristic parameters (band gap, enthalpy for reduction, activation energy for ionic conduction) have been estimated. At the end, a first detailed description of the electrical conductivity of SrBIT at elevated temperature was proposed.

The change in conductivity magnitude at low temperature by donor doping was already described in Chapter 3; the interest of the next section is actually to find out any behavior change due to Niobium doping using controlled oxygen partial pressure measurements. Predictions of the effect of donor doping on the electrical behavior of SrBIT at low oxygen partial pressure will be mainly conducted by referring earlier work on BaTiO_3 .

4.4.2.3 Donor doping effect

Donor doping was studied using Nb^{5+} substitution of Ti^{4+} . On the contrary to Manganese doping, no valence state change can be expected for Niobium. As discussed above, conductivity measurements of both undoped and acceptor doped SrBIT can be interpreted with acceptor impurities compensated by oxygen vacancies. Adding positively charged donor defects would thus first balance the existing "intrinsic" acceptors acting in an opposite way to acceptor doping. However, when all acceptors are compensated, different compensation mechanisms have to be considered.

The electroneutrality equation is written as Equation 4-40 with the assumption of Bismuth vacancies as negative ionic defects to compensate positive donors.

$$\left[\text{Nb}_{\text{Ti}}^{\cdot}\right] + 2\left[\text{V}_{\text{O}}^{\cdot\cdot}\right] + p = 3\left[\text{V}_{\text{Bi}}^{\cdot\cdot\cdot}\right] + \left[\text{A}'\right] + n \quad \text{Equation 4-40}$$

This equation can be simplified if there are much more donors than oxygen vacancies and providing that acceptors are fully compensated by donors. In the n-type regime, holes can be omitted. Thus Equation 4-40 can be rewritten as:

$$\left[\text{Nb}_{\text{Ti}}^{\cdot}\right] = 3\left[\text{V}_{\text{Bi}}^{\cdot\cdot\cdot}\right] + n \quad \text{Equation 4-41}$$

If the oxygen partial pressure is not too low, the electron concentration can be neglected compared to Bismuth vacancies and the concentration of oxygen vacancies can be calculated as Schottky disorder:

$$\left[V_{Bi}^{\cdot\cdot\cdot} \right] \left[V_{Ti}^{\cdot\cdot\cdot} \right] \left[V_O^{\cdot\cdot} \right] = K_s \quad \text{Equation 4-42}$$

With the reduction equation, the concentration of electron can be written as:

$$n = \left(\frac{K_R}{2K_S} \right)^{\frac{1}{2}} \left[V_{Bi}^{\cdot\cdot\cdot} \right]^{\frac{1}{2}} \left[V_{Ti}^{\cdot\cdot\cdot} \right]^{\frac{1}{2}} p_{O_2}^{-\frac{1}{4}} \quad \text{Equation 4-43}$$

This equation predicts the same slope as the acceptor model presented in section 4.4.2.1. However, the interesting feature of this model is that at lower oxygen partial pressure, electrons would compensate donors. In this situation, electron concentration would be determined by donors concentration and be independent of the oxygen partial pressure. At much lower p_{O_2} , the reduction is so strong that there are much more free electrons provided by oxygen vacancy creation. In this range, the carrier concentration should again be p_{O_2} -dependent (slope equal to $-1/6$). These three stages have been measured for Niobium doped BaTiO₃ by Chan [91].

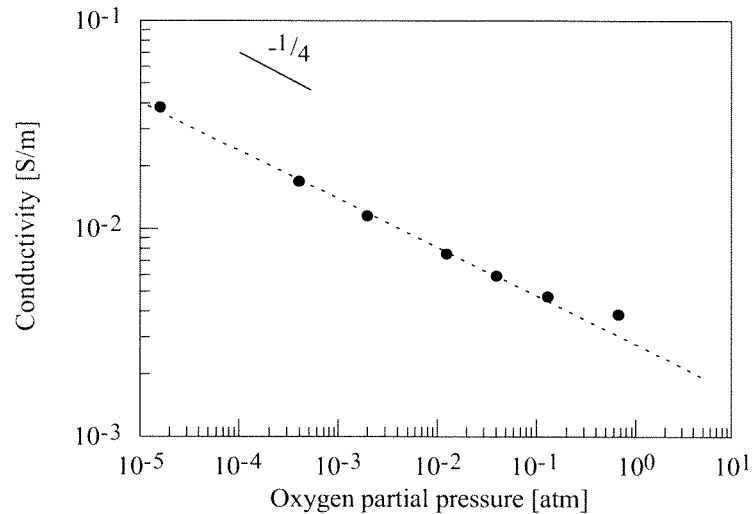


Figure 4-13: electrical conductivity versus oxygen partial pressure for undoped SrBIT at 770°C and 4 mol.% Niobium doped SrBIT at 740°C.

As presented in Figure 4-13, the conductivity slope is close to $-1/4$ what agrees with predictions of the defect model given in the preceding paragraph. However, no p_{O_2} -independent region is observed in the 10^{-5} -1 atm range.

The next question to be answered concerning the electrical conductivity of SrBIT is about its behavior at very low oxygen partial pressure. In this p_{O_2} range for BaTiO₃, the reduction reaction creates so many oxygen vacancies that there are much more compensating electrons than the total amount of ionized acceptors. As a consequence, the slope of the conductivity curve changes from $-1/4$ to $-1/6$. The next section will be devoted to the investigation of the electrical conductivity of undoped SrBIT in a much lower p_{O_2} range (down to 10^{-13} atm).

4.4.3 DC Electrical conductivity of SrBIT in full pO_2 range

The electrical conductivity of SrBIT has been measured at 700 and 900°C down to 10^{-13} atm pO_2 , Equation 4-15. As first results were quite surprising (large conductivity jump and pO_2 -independent values), most efforts were put to obtain reproducible measurements in a continuous range of pO_2 from 1 atm down to 10^{-13} atm.

The oxygen partial pressure was adjusted with two systems: CO/CO₂ mixtures and with a ZrO₂ electrolytic pump. A quite good agreement between the three different pO_2 ranges is easily viewed in Figure 4-14. The ZrO₂ pump efficiency was unfortunately not good at 700°C, and then only a single intermediate oxygen partial pressure could be established.

According to Figure 4-14, the electrical conductivity of undoped SrBIT can be summarized as follow: 1) from 1 atm down to 10^{-5} atm, the conductivity increases as $pO_2^{-0.25}$; 2) 10^{-5} atm down to 10^{-10} atm, the conductivity increases much faster; 3) below 10^{-10} atm, the electrical conductivity reaches a regime much less pO_2 -dependent. Thus, the transition towards the reduction regime ($pO_2^{-1/6}$) does not happen in undoped SrBIT in the investigated pO_2 range. On the contrary, the 900°C measurements would indicate that the $pO_2^{-1/4}$ region is extended to lower pO_2 .

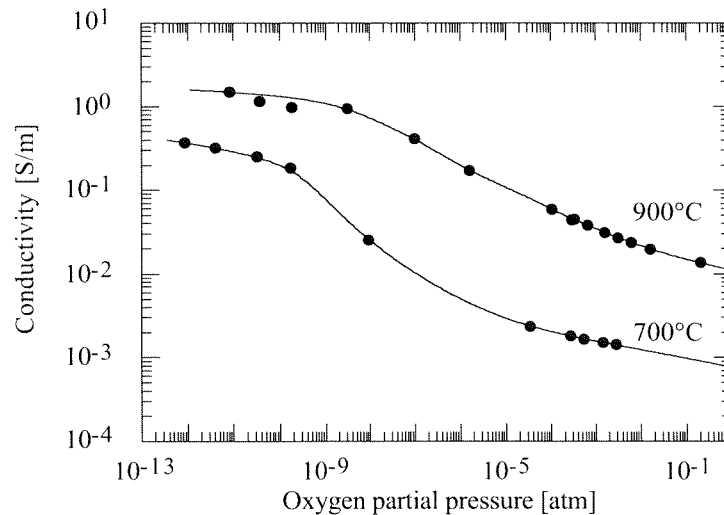


Figure 4-14: electrical conductivity versus oxygen partial pressure for undoped SrBIT in the full pO_2 range at 700 and 900°C.

Conductivity measurements of SrBIT can be directly compared to published results by Palenduz and Smyth [40] of electrical conductivity under controlled oxygen partial pressure for two Aurivillius phases: SrBi₂Ta₂O₉ (written SBT) and SrBi₂Nb₂O₉ (written SBN). Some of these measurements (undoped and acceptor doped SBN) are presented for comparison in Figure 4-15. From Figure 4-14 and Figure 4-15, several common features for SrBIT and SBN behavior are

quite obvious. In the highest pO_2 range, conductivity is proportional to $\text{pO}_2^{-1/4}$, that could be interpreted either as acceptor-controlled regime (see section 4.4.2.1) or as donor-controlled regime (see section 4.4.2.3). Below this region, for SrBIT and SBN, there is a large pO_2 -independent regime. This is the more important feature of these conductivity measurements under controlled oxygen partial pressure. This would support the assumption of donor-controlled conductivity. As already discussed in section 4.4.2.3, in the case of donor doping, either by true doping or due to a natural donor-excess content, when donors are compensated by electrons, conductivity becomes pO_2 -independent. Since the $\text{pO}_2^{-1/4}$ trend can be interpreted with the same model, there are two strong indications in favor of the donor-controlled model.

Palenduz did not explain the conductivity "jump" present in the very low oxygen partial pressure range. However as some reversibility problems related to material deterioration were reported in this region, no comments were made on it [40]. The reduction regime ($\text{pO}_2^{-1/6}$) was not observed neither for SrBIT in our work nor for SBN in Palenduz's measurements.

As acceptor doped $\text{SrBi}_2\text{Nb}_2\text{O}_9$ has a similar behavior to undoped $\text{SrBi}_2\text{Ta}_2\text{O}_9$ and since donor doped $\text{SrBi}_2\text{Ta}_2\text{O}_9$ behaves in the same way as undoped $\text{SrBi}_2\text{Nb}_2\text{O}_9$, the authors [40] concluded that $\text{SrBi}_2\text{Nb}_2\text{O}_9$ was "intrinsically" donor doped.

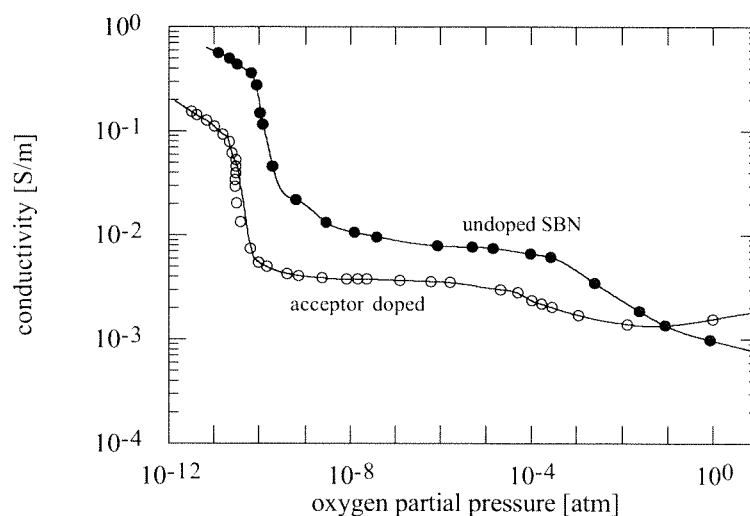


Figure 4-15: electrical conductivity of undoped and acceptor doped (Ti^{4+}) $\text{SrBi}_2\text{Ta}_2\text{O}_9$ at 700°C by Palenduz [40].

The authors of Figure 4-15's work proposed that some cation place exchange between the perovskite units (Sr^{2+}) and the Bismuth oxide layer (Bi^{3+}) could induce two different conduction mechanisms. In the Bismuth oxide layers the substituted Sr^{2+} ions would be compensated by oxygen vacancies (as demonstrated for $\text{Bi}_4\text{Ti}_3\text{O}_{12}$ [78], oxygen vacancies are preferentially situated in the vicinity of Bi ions in the Bismuth oxide layer). On the other hand, electrons would compensate the Bi^{3+} ions sitting on the Sr^{2+} place. Ionic conduction would result from oxygen vacancy creation inside the Bismuth oxide layers and electronic conduction would result from Bi^{3+} and Sr^{2+} exchange in the perovskite. The layer that makes the larger contribution to the total conductivity would then dominate the electrical conductivity. In particular, deep or shallow electron traps are the key parameter for the selected conduction mechanism. For $\text{SrBi}_2\text{Ta}_2\text{O}_9$, the observed large ionic conductivity [40] would be caused by deep electron traps, while the typically

donor-doped electronic conduction of $\text{SrBi}_2\text{Nb}_2\text{O}_9$ would be due to shallow electron traps. This would correspond to undoped SrBIT case, consistent with a small band gap (estimated at 3.5 eV).

The model presented by Palenduz and Smyth will be used for undoped SrBIT in the high oxygen partial pressure range (10^{-5} -1 atm) in the next section to calculate the net donor-excess content.

4.4.3.1 Evaluation of “intrinsic” donor-excess

If some Bi^{3+} from the Bismuth oxide layers and some Sr^{2+} in the perovskite sub-unit exchange their position, then considering separately the two structural elements (without direct compensation of them), Bismuth localized on Strontium site acts as a donor. Those Bismuth defects could in principle be compensated by either electrons or metallic vacancies. Vacancies could be either Strontium, Bismuth or Titanium vacancies. Strontium or Titanium vacancies would create either SrO or TiO_2 second phase expell on the grain boundaries. Such second phase was not observed and since volatility of Bismuth oxide is quite elevated, only Bismuth vacancies will be considered here. The electroneutrality equation becomes:

$$[\text{Bi}_{\text{Sr}}^{\cdot}] = 3[\text{V}_{\text{Bi}}^{\text{'''}}] + n \quad \text{Equation 4-44}$$

Using a Schottky equation for Bismuth, Titanium and oxygen vacancies, we can write:

$$[\text{V}_{\text{Bi}}^{\text{'''}}][\text{V}_{\text{Ti}}^{\text{'''}}][\text{V}_{\text{O}}^{\cdot}] = K_S \quad \text{Equation 4-45}$$

where K_S would be a mass-action constant for this intrinsic disorder. With the reduction equation, it follows that:

$$p_{\text{O}_2}^{+1/2} = \frac{1}{3} \left(\frac{K_R}{K_S} \right) [\text{V}_{\text{Ti}}^{\text{'''}}] \frac{([\text{Bi}_{\text{Sr}}^{\cdot}] - n)}{n^2} \quad \text{Equation 4-46}$$

Thus, fitting conductivity measurements of undoped SrBIT with this equation provides the concentration of “intrinsic” donor-excess, that are trivalent Bismuth cations lying on divalent Strontium sites. The ratio of the mas-action constants K_R to K_S times the Titanium vacancy concentration can be computed too. On the contrary to the acceptor-controlled model, in this case separate determination of K_R is not possible. It was experimentally easier to use carrier concentration instead of conductivity to fit the measurements, therefore conductivity has been replaced by carrier concentration in Figure 4-16.

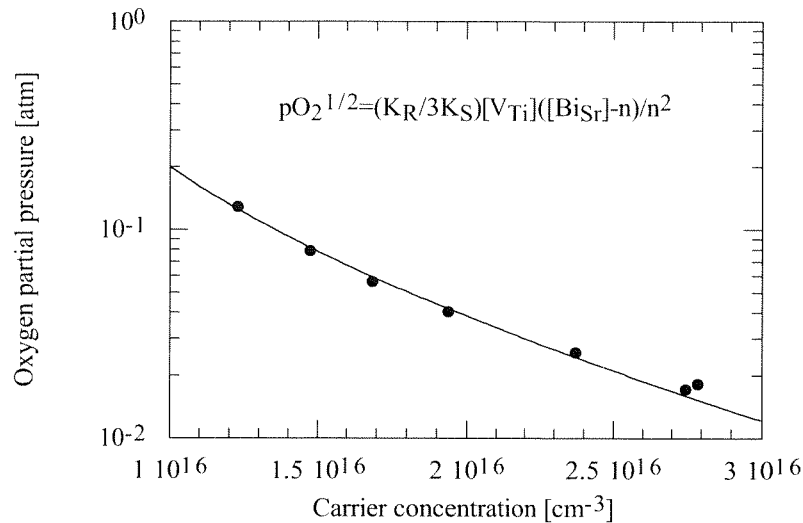


Figure 4-16: oxygen partial pressure versus carrier concentration from conductivity measurements of undoped SrBIT at 900°C in the 10^{-5} -1 atm range.

Calculated amount of donor-excess are given in Figure 4-17 versus reciprocal temperature. It is interesting to note that the calculated value ($60 \times 10^{15} \text{ cm}^{-3}$ at 900°C) is similar to the acceptor content calculated previously in section 4.4.2.1 with the acceptor-controlled model ($70 \times 10^{15} \text{ cm}^{-3}$).

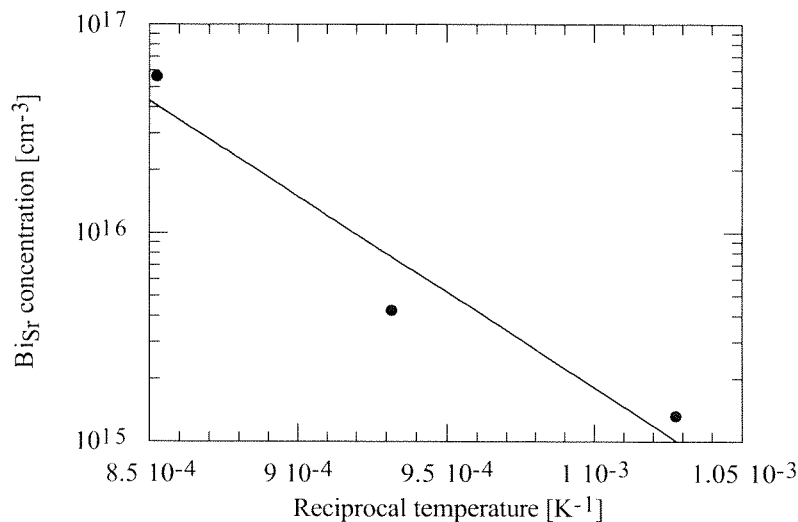


Figure 4-17: donor-excess identified as misplaced trivalent Bismuth versus reciprocal temperature for undoped SrBIT calculated using Equation 4-46.

The point defect model implies some ionic conductivity too, possibly caused by oxygen vacancies created in the Bismuth oxide layers through Sr^{2+} substitution. Evaluation of the transference number as shown in the next section will demonstrate that conductivity includes ionic and electronic charge transport. As the right nature of the oxygen vacancies source will remain undetermined (acceptor impurities or cation place exchange), only clear evidence of ionic conduction will be given.

4.4.4 Ionic conductivity calculation

The ionic conductivity of undoped and 2 mol.% Mn doped SrBIT has been evaluated at high temperature using conductivity measurements under controlled oxygen partial pressure. Details of the calculation procedure were given above in

Data Processing section. The representation of the electrical conductivity versus $pO_2^{-1/4}$ or $pO_2^{-1/6}$ is presented in Figure 4-18 for undoped SrBIT and in Figure 4-19 for 2 mol.% Mn doped SrBIT.

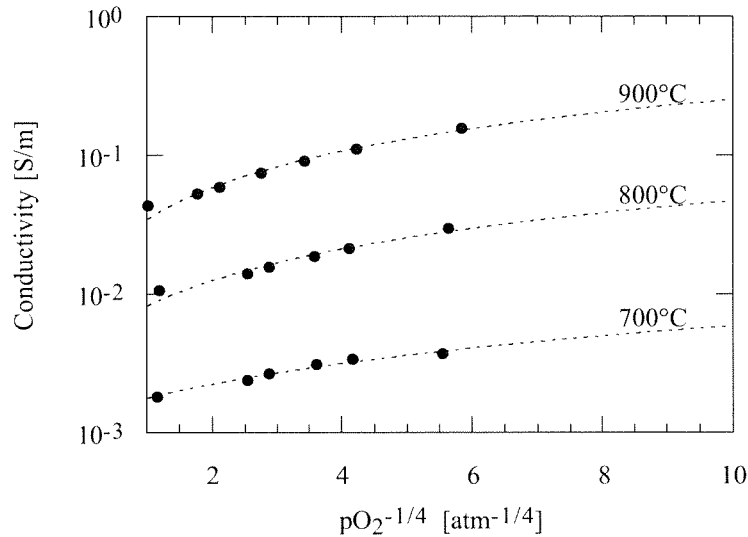


Figure 4-18: conductivity versus $pO_2^{-1/4}$ for ionic conductivity estimation for undoped SrBIT.

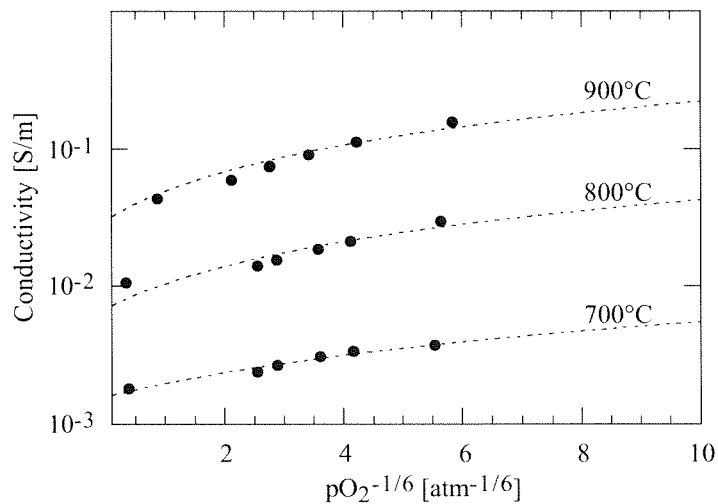


Figure 4-19: conductivity versus $pO_2^{-1/6}$ for ionic conductivity estimation for 2 mol.% Mn doped SrBIT.

The ionic conductivity is presented in Figure 4-20 in an Arrhenius plot. The activation energies are 1.44 eV for undoped SrBIT and 1.45 eV for Mn doped SrBIT; that indicates a conservation of the physical origin for ionic transport after acceptor doping.

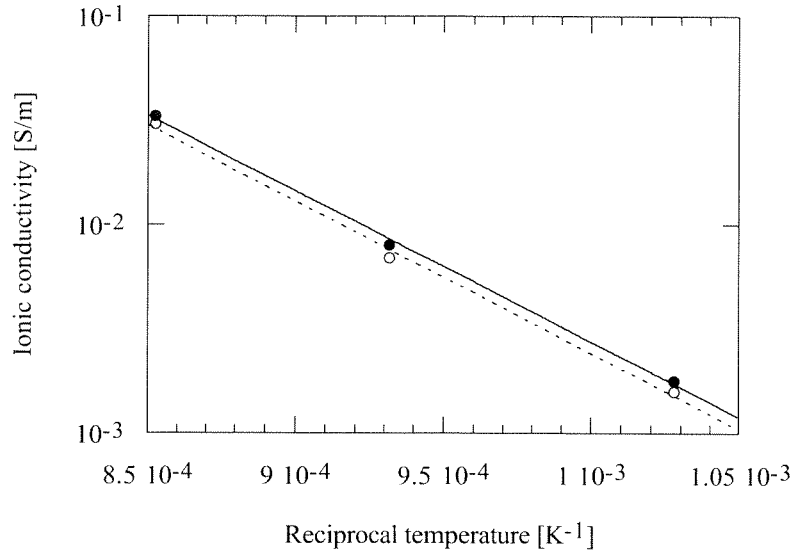


Figure 4-20: calculated ionic conductivity versus reciprocal temperature for undoped SrBIT (open circles) and Mn doped (filled circles) SrBIT.

According to Tuller [123], transference number (t_i), temperature (T) and the smallest band gap consistent with the existence of an electrolytic domain (E_g) are related through the expression:

$$E_g = 2k_B T \left[\ln \frac{t_i}{1-t_i} + \ln \left(\frac{A}{B} \right) \right] + 2E_m \quad \text{Equation 4-47}$$

Where $A(T)$ and $B(T)$ are the temperature dependent pre-exponential factors for the intrinsic electronic and ionic conductivities, E_m is the activation energy for the ionic conductivity. This equation means that the transference number for a given band gap energy depends on temperature. As the temperature is raised transition from purely electronic to mixed conductivity is possible. The pre-exponential factors have been calculated in the highest pO₂ range for the “intrinsic” conductivity and in the full 10⁻⁵ – 1 atm range for the ionic conductivity using the following expressions according to [123]:

$$\sigma_{\text{elect}} = A' T^{\frac{3}{2}} \exp \left(-\frac{E_g}{2k_B T} \right) \quad \text{Equation 4-48}$$

$$\sigma_{\text{ionic}} = B'T^{-1} \exp\left(-\frac{E_m}{k_B T}\right)$$

Equation 4-49

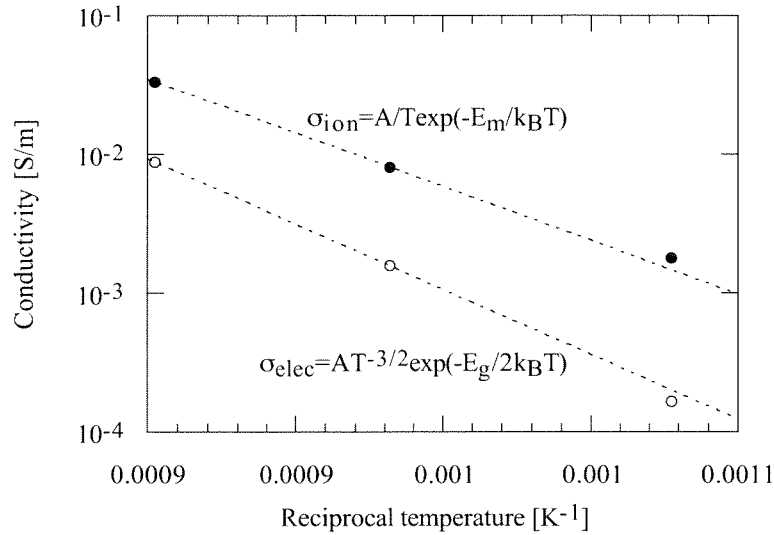


Figure 4-21: electronic (open circles) and ionic conductivities (filled circles) as calculated with Equation 4-22 for undoped SrBIT.

The calculated parameters corresponding to Equation 4-48 and Equation 4-49 are listed in Table 4-7. Result of these calculations is a transference number map presented in a band gap-temperature space, Figure 4-22. In this map, the dotted area represents the conditions (temperature-band gap) satisfying transference number comprised between 0.001 (purely electronic) and 0.999 (entirely ionic), corresponding to mixed conduction. Depending on the band gap value, either transition from ionic to electronic (for large band gap) or from electronic to mixed are possible. For example, in the case of MgO, because of a large band gap (about 7.0 eV [123]), the conduction is strictly ionic up to 1300°C and slightly electronic above (t_i still greater than 0.5). As the band gap value of SrBIT should be around 3.5 eV (as determined with our conductivity measurements), conductivity is always mixed according to Figure 4-22. Alternatively, it turns out that the predicted transference number of undoped SrBIT at 800°C would be 1, satisfying Equation 4-47. The actual transference number measured for undoped SrBIT at 800°C was 0.8, quite close to the expected value. The measured transference number decreases as temperature increases, as actually predicted by Equation 4-47 with our parameters. Thus, it appears that the electrical conductivity of undoped SrBIT is very likely shared between ionic and electronic charge transport.

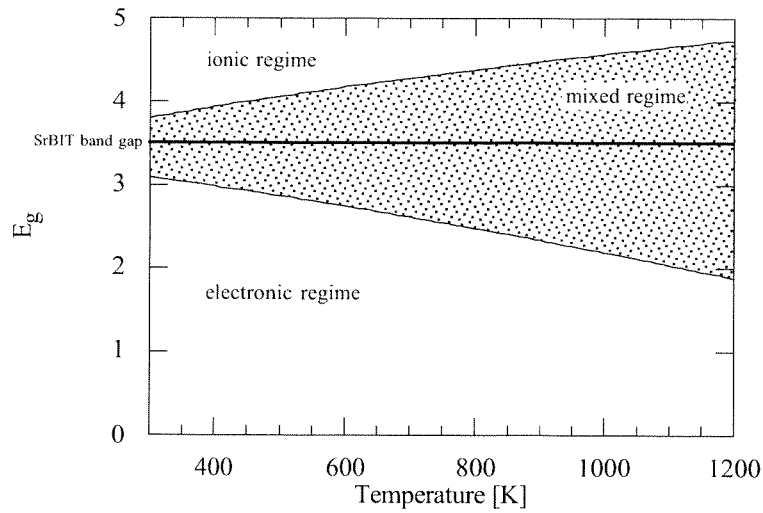


Figure 4-22: transference number map in the band gap-temperature space for undoped SrBIT calculated with Equation 4-47.

The right nature of the mobile ionic species cannot be determined yet with the available data's. However, typical ionic jump relaxations through oxygen vacancies have already been shown for $\text{Bi}_4\text{Ti}_3\text{O}_{12}$ [11]. Thus, attributing the ionic contribution to oxygen migration in the anionic sub lattice seems to be reasonable. In addition, it is interesting to note that Kilner [124] proposed Bismuth oxide in the δ phase as an oxygen ion conductor. The open fluorite structure of this material contains 25% of anionic vacant sites and do not need any doping to promote vacancies. Bi cations of the intermediate Bismuth oxide layers of Aurivillius phases have also a tetragonal coordination in a fluorite-like structure; therefore the plausibility of some ionic conductivity in Aurivillius phases is reinforced.

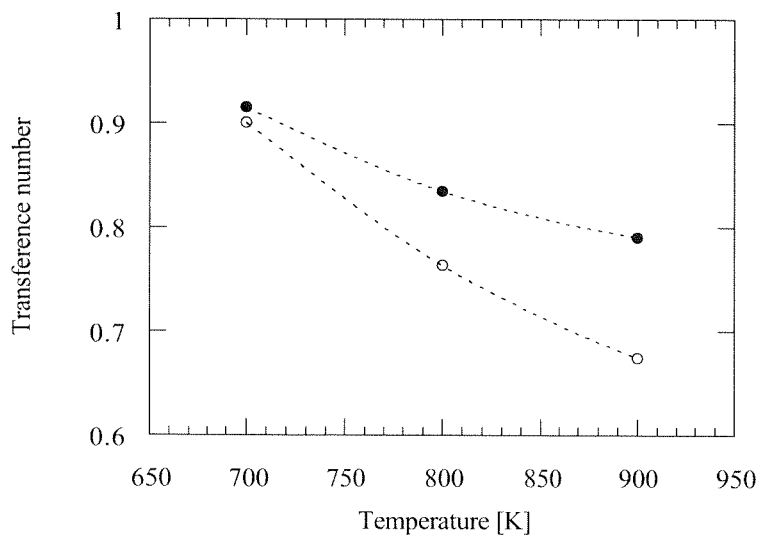


Figure 4-23: transference numbers calculated from ionic and electronic conductivity calculations for undoped SrBIT (filled circles) and 2 mol.% Mn doped SrBIT.

Table 4-7: calculated parameters corresponding to Equation 4-48 and Equation 4-49.

Parameter	Electronic conduction	Ionic conduction
Pre-exp. factor (T-indep.)	5.6	$3.8 \cdot 10^8$
Energy	1.72 eV	1.62 eV

4.5 SUMMARY AND CONCLUSION

DC electrical conductivity of SrBIT has been investigated at high temperature (700-900°C) under controlled oxygen partial pressure. According to the experimental set-up, measurements were performed in three distinct oxygen partial pressure ranges. In mixtures of Argon and Oxygen from 1 atm down to 10^{-5} atm, in carbon monoxide and carbon dioxide from about 10^{-10} down to 10^{-15} atm and with an electrochemical oxygen pump made of ZrO_2 from 10^{-5} atm down to 10^{-10} atm. Comparison between predicted and measured oxygen partial pressures showed that the atmosphere was properly defined.

In order to definitely validate the system, the electrical conductivity of BaTiO_3 was measured as a function of the oxygen partial pressure; the results were successfully compared to the literature. Both excellent qualitative and quantitative agreements in the p-type regime of BaTiO_3 were found.

In the 10^{-5} -1 atm range, it was shown that the electrical conductivity of undoped SrBIT follows a $\text{pO}_2^{-1/4}$ law. At first, results were evaluated with an acceptor-controlled model. This model allowed the determination of the net acceptor content (700 ppm) that should compensate doubly ionized oxygen vacancies in SrBIT. In addition, the mass-action constant for reduction (K_R) was determined at different temperatures.

The conductivity of 2 mol.% Mn doped SrBIT (acceptor doped) measured from 10^{-5} up to 1 atm revealed a quite different behavior. For this composition, it was established that the $\text{pO}_2^{-1/4}$ law was replaced by $\text{pO}_2^{-1/6}$ one. The acceptor-controlled model was adjusted to account for this different exponent by considering the ionization equilibrium of Mn^{4+} into Mn^{3+} . With the modified model, the mass-action constant for intrinsic carriers (K_i) and its activation energy, which is actually the band gap (E_g) have been estimated. Thus, the band gap of SrBIT was estimated for the first time at 3.7 eV.

Both undoped and Mn doped SrBIT were modeled with the acceptor-controlled model. This means that considered defects were oxygen vacancies, singly ionized acceptors, Manganese sitting on Titanium site, free electrons and holes. Yet, for donor doped SrBIT, metallic vacancies were included in the model to compensate for the positive donors (Niobium on Titanium site).

In the case of 4 mol.% Nb doped SrBIT (donor doped), it was demonstrated that the conductivity follows a $\text{pO}_2^{-1/4}$ law, similar to both undoped and acceptor doped SrBIT. This behavior was explained with a donor-controlled model based on donor centers compensated by metallic vacancies. Due to elevated Bismuth volatility, Bismuth vacancies were preferred to Strontium and Titanium vacancies in the model.

Evidence of pO_2 -independent conductivity in the very low pressure range was established for undoped SrBIT at 700, 800 and 900°C. A donor-controlled model built from the assumption of "intrinsic" donors within SrBIT was presented. According to the literature, cation place exchange

between Sr^{2+} in the perovskite and Bi^{3+} in the Bismuth oxide layers would provide donors in the perovskite.

The ultimate choice of the right model either acceptor-controlled or donor-controlled could not be decided based on presented data. The cation place exchange is probably pressure dependent, as it is a way to balance oxygen vacancies created in the layers. Thus, in the high pressure range (Ar-O_2), necessary acceptor impurities may be more abundant than “intrinsic” donors. In this situation, acceptor-controlled model would be true. On the contrary, in the low oxygen partial pressure range, “intrinsic” donors would be dominant over acceptors. This is the reason why the acceptor-controlled model cannot be rejected even if the $p\text{O}_2$ -independent regime is due to a net excess of donor centers. Consequently, band gap (3.7 eV) and mass-action constants (K_R and K_i) determined in this chapter can still be considered.

The ionic conductivity was evaluated from total conductivity measurements using the acceptor-controlled model. Actually, under acceptor compensation, the oxygen vacancy concentration is fixed, thus the ionic conductivity is $p\text{O}_2$ -independent as long as the acceptor-controlled regime applies. The activation energy for ionic conductivity was found to be 1.5 eV for both undoped and 2 mol.% Mn doped SrBIT. This provides another explanation for the curve bending observed for total DC conductivity in air (see Chapter 3). At low temperature (140-220°C), the activation energy for conduction is 1 eV for SrBIT; but at elevated temperature, it is 1.5 eV. Thus, a transition from electronic to ionic conductivity would be another way to interpret the observed bending of the conductivity curve in the Arrhenius plot.

A transference number map in the temperature-band gap space has been proposed, which allows estimation of ionic conduction at every temperature. With the previously determined band gap of SrBIT (3.7 eV), a mixed conduction regime has been predicted in a large temperature range (above 300 K). At 800°C, the measured transference number was 0.8, while using the transference map, it should be close to one. Thus, the validity of our estimation of the ionic conductivity has been demonstrated.

5

PIEZOELECTRIC PROPERTIES

5.1 FOREWORD

The last chapter of this work is dedicated to piezoelectricity, the most interesting property of SrBIT. This unique feature of transforming elastic energy into electric energy will be described under standard simple conditions, with the longitudinal piezoelectric coefficient d_{33} . At first, it will be shown that at room temperature, the piezoelectric coefficient of undoped SrBIT remains stable over a large stress and frequency range, as already demonstrated by Damjanovic [125]. Second, release of non-linear behavior above a threshold elastic field will be demonstrated with high temperature piezoelectric measurements. The measured properties will be discussed using both widely used ferroelectric domain walls motion theory and recently published phenomenological models. Third, the piezoelectric relaxation encountered in some SrBIT samples will be analyzed with the help of experimental and theoretical composite-based models. These models will demonstrate that in the case of a multiphase system, differences in piezoelectric coefficient, permittivity and conductivity could lead to either a positive or a negative piezoelectric relaxation. Simultaneous occurrence of a positive and a negative relaxation will be presented with a piezoelectric composite made of ab and c oriented SrBIT samples.

5.2 PIEZOELECTRICITY BASICS

If a mechanical stress is applied to some non-centrosymmetric materials (crystals, ceramics, and polymers), they develop an electric moment whose magnitude is proportional to the applied stress. This is known as the direct piezoelectric effect expressed by the following relation:

$$Q = d X \quad \text{Equation 5-1}$$

Where Q is the charge per unit area and X is the applied stress. For any anisotropic material, directions of measurement and applied force should be taken into account also; therefore Equation 5-1 has to be rewritten as tensors:

$$Q_i = d_{ijk} \sigma_{jk} \quad \text{Equation 5-2}$$

In that case, the piezoelectric coefficient is a third rank tensor; the matrix notation can be used to reduce the number of tensor coefficients to two, because stress and strain tensors are symmetric. Alternatively, under electrical field (E_k), a piezoelectric material undergoes a deformation (ϵ_{ij}); this is the converse effect:

$$\epsilon_{ij} = d_{ijk} E_k \quad \text{Equation 5-3}$$

Both direct and converse piezoelectric coefficients are actually identical. As poled ceramics get cylindrical symmetry, three independent piezoelectric coefficients are sufficient to describe the piezoelectric effect in any measurement direction [126]. Those coefficients are called longitudinal, transverse and shear piezoelectric coefficients, written as d_{33} , d_{31} and d_{15} respectively. Throughout this work only d_{33} has been characterized. Under an oscillating elastic field, the piezoelectric coefficient can be expressed in complex notations as follows:

$$d_{33}^* = d'_{33} + id''_{33} \quad \text{Equation 5-4}$$

Then, the piezoelectric loss (written δ_p) may be defined as:

$$\text{Tan}(\delta_p) = \frac{d''_{33}}{d'_{33}} \quad \text{Equation 5-5}$$

which is also the phase angle between the applied stress and the measured charge signals.

Direct coupling between external elastic or electric fields with internal polarization or strain has been called the intrinsic piezoelectric effect [127]. However, application of an external electric/elastic field to ferroelectrics induces others effects. The most important one is the movement of ferroelectric domain walls. Ferroelectric domain walls are boundaries between crystalline regions with common polarization direction. In the simplest configuration, the

polarization vectors of two adjacent domains are anti-parallel (180° domain wall). Nevertheless, depending on the crystallographic symmetry of the material, extra polarization vector configurations may also exist. After poling some residual non- 180° domain walls in poled ceramics may move under external elastic or electric field and contribute to the piezoelectric effect. This is well known for BaTiO_3 and PZT.

As stated by Reaney and Damjanovic [24], in the case of SrBIT, polarization and strain are not coupled in the same way as in BaTiO_3 or PZT. The splitting of the ferroelastic and ferroelectric phase transitions highlighted this. It is believed [24] that unique room temperature piezoelectric properties of SrBIT are related to this splitting.

Piezoelectric ceramics are used in the poled state, with switched domains. However, small vibrations of domain walls under sub-coercive fields are still allowed as described by Damjanovic in his review on piezoelectric properties of ferroelectrics [128]. If these displacements become partly irreversible, they introduce non-linear field and frequency response of d_{33} . Irreversibility can be caused by the interaction of domain walls with any kind of defects. Energy dissipation resulting from this process creates also a piezoelectric hysteresis.

5.3 EXPERIMENTAL

5.3.1 Poling Procedure

The poling process had to be carried at quite high temperature (above 200°C) because of a very high coercive field at room temperature. At higher temperature, the coercive field of undoped SrBIT was smaller (about 50 kV/cm) allowing poling to saturation. The high voltage was slowly applied (about 1 kV/min.) to SrBIT sample in a silicon oil bath under controlled temperature. Actually, breakdown occurs quite often above 50 kV/cm for 1-2 mm thick samples. After poling, cooling of poled material was performed in air without field. Samples used for piezoelectric characterization were discs of about 8 mm in diameter and 1-2 mm thick.

Ferroelectric hysteresis was measured at high temperature (200°C) using a Sawyer and Tower based circuit, Figure 5-1. The coercive field measured at this temperature was 40 kV/cm. Measurement of the hysteresis at room temperature was not possible due to very large coercive field.

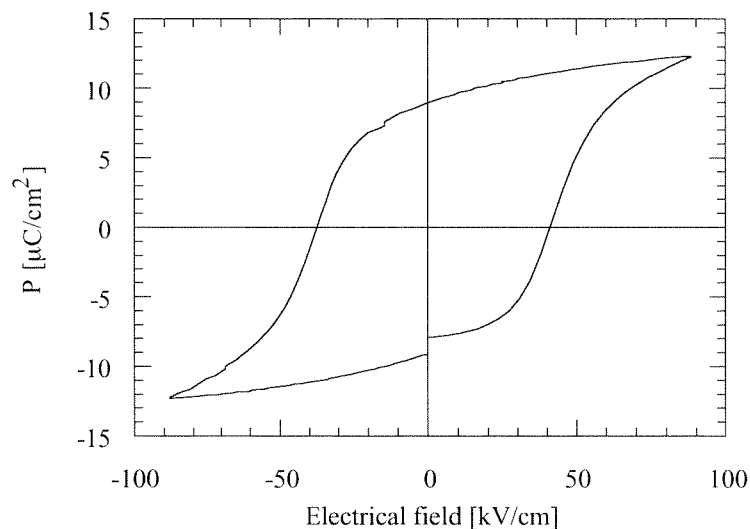


Figure 5-1: ferroelectric hysteresis for undoped SrBIT measured at 200°C.

5.3.2 Measurement Set-up

The longitudinal piezoelectric constant d_{33} was measured using the direct piezoelectric effect. With a multilayer actuator a longitudinal force was applied to a disc-shaped sample and the induced piezoelectric charges were converted into voltage with a charge amplifier. The actual applied force was measured with a precision quartz transducer whose charges were also

transformed into voltage with another charge amplifier. The experimental setup is schematically presented in Figure 5-2. The actuator was driven with a sinusoidal voltage, therefore both amplitude and loss of the piezoelectric coefficient could be measured as a function of frequency (20 mHz to 100 Hz) and amplitude of the applied force. The AC stress range depends on sample diameter, typically for 8 mm in diameter samples; the upper limit of applied stress was 10 MPa. However, for high field investigation much smaller samples were used allowing applied stress as high as 70 MPa. In addition a large DC component (1 kN) was added to the elastic field to ensure good mechanical and electrical contacts. For small samples, as DC components had to be decreased to keep stress constant, the AC force range available from the multilayer actuator was smaller. This is why a large sample area decrease does not lead to a similar large AC stress increase.

The piezoelectric coefficient was calculated from the charge amplifiers recorded signals (force and charge) as the ratio of the two amplitudes; the piezoelectric loss was identified with the phase angle between force and charge. A one-hour delay under maximum AC field and frequency was used before each piezoelectric measurement. In addition, a one minute stabilization time before any measurement during either field or frequency sweep (linear and logarithmic respectively) was used. A heating system was mounted around the piezoelectric equipment to change temperature up to 200°C.

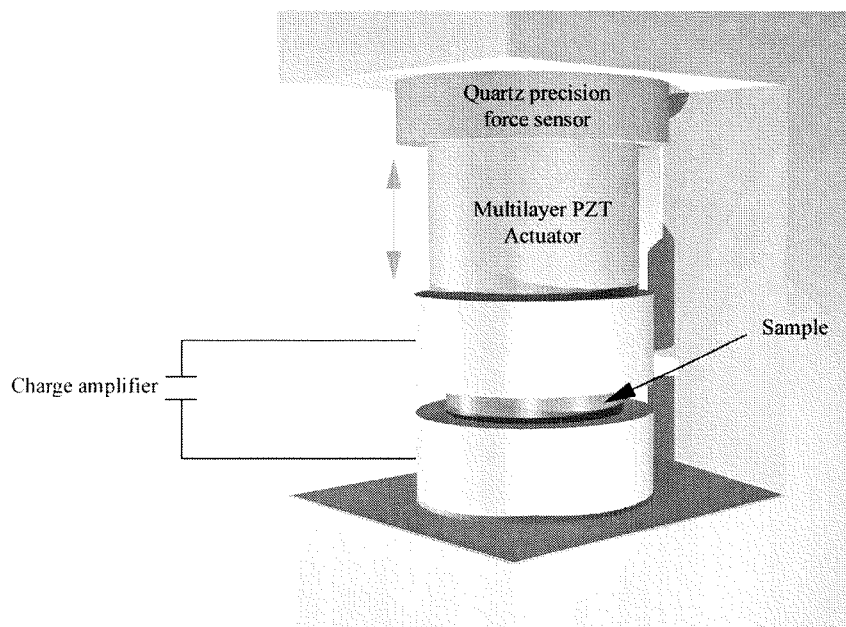


Figure 5-2: schematic representation of the experimental set-up used for piezoelectric characterization of SrBIT.

5.4 PIEZOELECTRIC PROPERTIES OF SRBIT

5.4.1 General Behavior

The piezoelectric effect, represented by stress induced polarization (identical to charge density), of undoped SrBIT at room temperature under low field is presented in Figure 5-3. From this figure, the hysteresis-free behavior of SrBIT is obvious. These remarkable properties were already reported by Damjanovic [125,129]. The piezoelectric coefficient value corresponding to Figure 5-3 is 11 pC/N. Compared to other ferroelectric compounds, this sensitivity value is quite small. Jaffe reported 191 pC/N for BaTiO₃ ceramic and 223 pC/N for PbZr_{0.52}Ti_{0.48}O₃. Nevertheless, this value agrees with reported properties for four-layers Bismuth Titanates [130]. Loss-free behavior in these experimental conditions indicates also the absence of any energy dissipating mechanism, such as irreversible movement of ferroelectric domain walls. This is further demonstrated by the AC field and frequency independence of d_{33} , Figure 5-4, Figure 5-5.

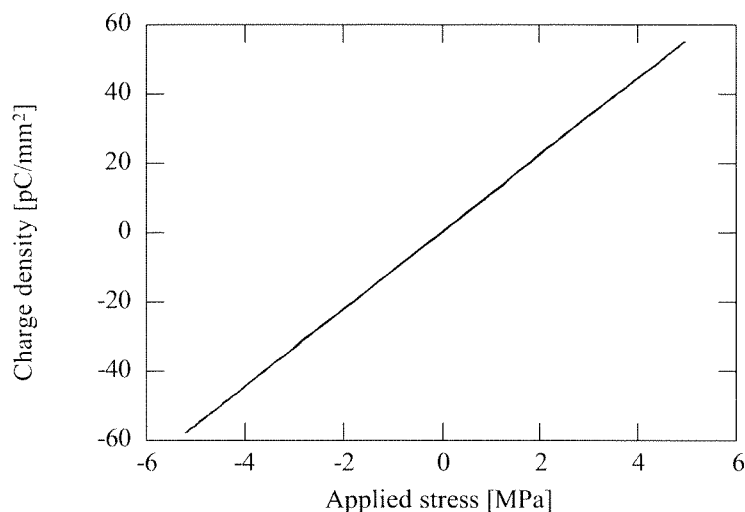


Figure 5-3: collected charge versus applied force for undoped SrBIT at room temperature.

Piezoelectric coefficient versus maximum applied AC stress measured at room temperature for undoped SrBIT is presented in Figure 5-4. Coefficient drift observed for many ferroelectrics [128] do not occur for SrBIT, piezoelectric sensitivity remains almost constant up to 10 MPa at room temperature.

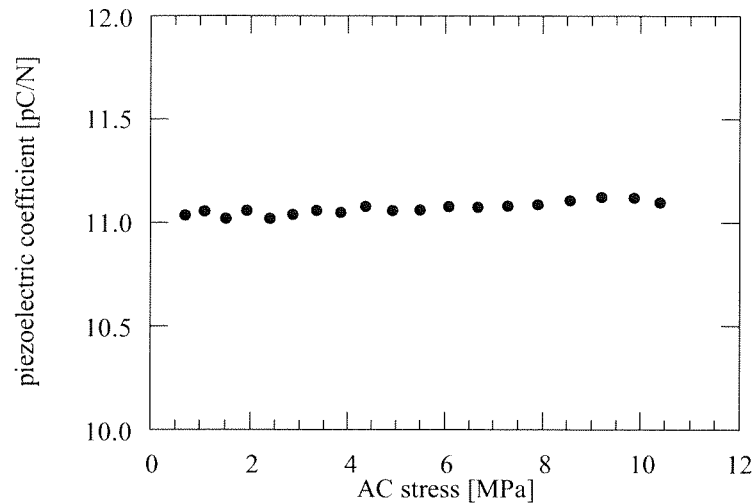


Figure 5-4: longitudinal piezoelectric coefficient versus amplitude of the applied AC stress at room temperature for undoped SrBIT.

Piezoelectric coefficient in the frequency domain is presented in Figure 5-5 for undoped SrBIT at room temperature. Similarly to AC stress response, no strong sensitivity deterioration occurs in the available frequency window. For many ferroelectrics, a logarithmic dependence of d_{33} towards frequency is observed [129]. This behavior, which comes from dispersion of domain walls vibrations, is not seen in SrBIT.

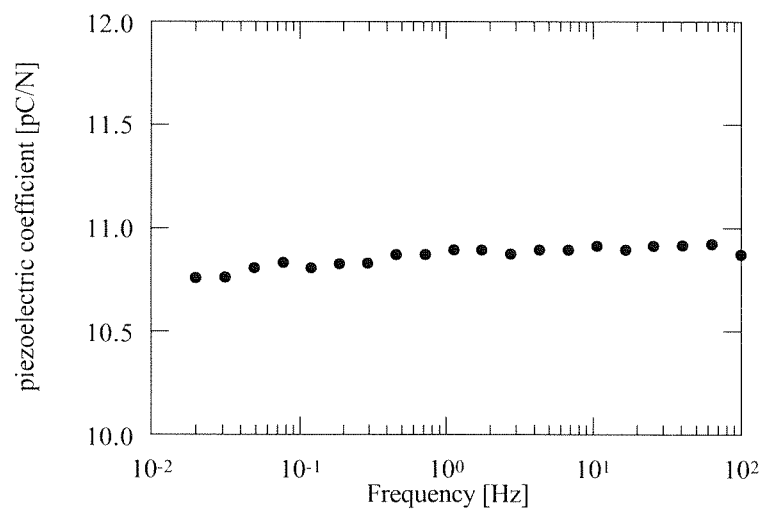


Figure 5-5: longitudinal piezoelectric coefficient versus frequency at room temperature for undoped SrBIT under 9 MPa AC stress.

Recent description of piezoelectric measurements of Lead Titanate Zirconate ceramics with early empirical model developed by Rayleigh [131] for magnetism [125,128,129,132] brought new tools for qualitative interpretation of the observed behaviors. According to this description, the

field-independent (originating from the lattice and reversible domain walls vibrations) and non-linear (due to irreversible domain walls movements) contributions to d_{33} are separated into two components, Equation 5-6:

$$d_{33} = d_{\text{init}} + \alpha X \quad \text{Equation 5-6}$$

where X is the applied stress and, d_{init} the initial piezoelectric coefficient depending on the poling procedure; the irreversible contributions to the piezoelectric constant are expressed by the coefficient α . Their relative contribution to d_{33} is calculated with the ratio $\alpha X / (d_{\text{init}} + \alpha X)$. For Niobium doped Lead Zirconate Titanate, this ratio is equal to 20%, indicating a large contribution of irreversible domain walls movements [128]. According to Figure 5-4, the Rayleigh parameter of undoped SrBIT at room temperature is very small, it is actually close to zero ($\alpha=0.008$).

The remarkable piezoelectric stability of undoped SrBIT was already discussed from a crystallographic point of view by Reaney and Damjanovic [24]. High temperature transmission electron microscopy observations showed [24] that on cooling ferroelectric and ferroelastic phase transitions were split into two distinct transitions. The high temperature parent phase of SrBIT is tetragonal and paraelectric, as the temperature is decreased at 680°C, the crystallographic cell becomes orthorhombic (slight distortion). However, this latter phase remains paraelectric. Finally, ferroelectric phase transition occurs at 530°C in the orthorhombic phase. As this latter transformation is from orthorhombic to orthorhombic only 180° ferroelectric domains are created inside early-formed ferroelastic domains. Thus, non-180° domains correspond to ferroelastic one, as depicted in left part of Figure 5-6. According to Reaney [24], non-180° ferroelectric domain walls in SrBIT should be sitting at bottom of deep energy potential wells, preventing any irreversible movements. On the contrary, reversible displacement would still be allowed and contribute to piezoelectric response.

Decoupling of polarization and cell strain is schematically presented in Figure 5-6. In this figure, single arrow represent 180° ferroelectric domain walls and ferroelastic domains correspond to rectangles. In BaTiO₃ and in PZT, there are two types of domain walls that are created at the ferroelectric-ferroelastic phase transition. In SrBIT, the appearance of the two types of domain walls is not simultaneous and such domain walls are believed to be less mobile.

The piezoelectric charge density versus applied stress for SrBIT at 150°C under 60 MPa AC stress oscillating at 1 Hz is presented in Figure 5-8. Compared to Figure 5-3, there is a slight hysteresis that is also different from the relaxation behavior depicted in the next section, Figure 5-11. According to piezoelectric theory developed for other ferroelectrics, when irreversible movements of ferroelectric domain walls contribute to piezoelectric coefficient, hysteresis should be measured in the charge-versus-force plot. This is representative of energy consuming interfaces motion.

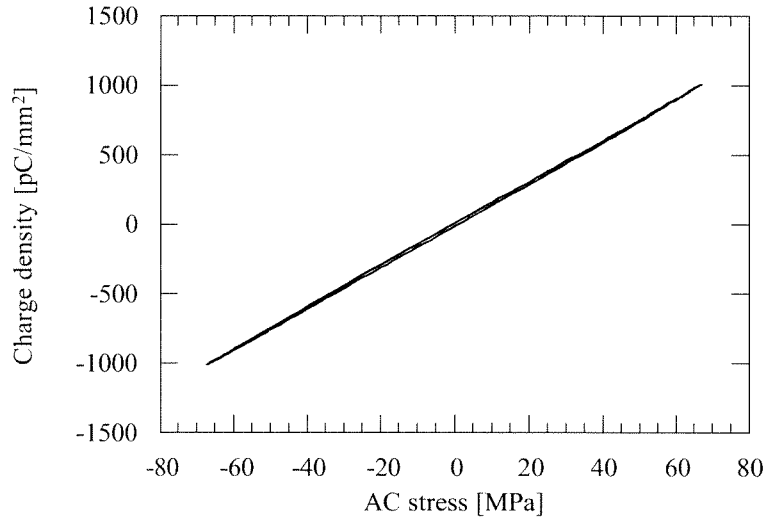


Figure 5-8: piezoelectric hysteresis for undoped SrBIT at 1 Hz measured at 150°C

As frequency is increased, the stress dependence of the piezoelectric coefficient of undoped SrBIT disappears, as shown in Figure 5-9 at 10 Hz. This is consistent with behavior observed in PZT where Rayleigh-type behavior is accompanied with frequency dispersion [128].

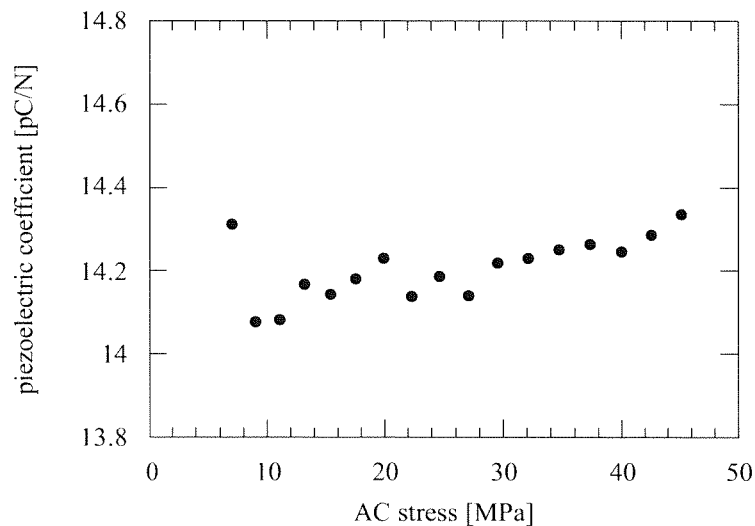


Figure 5-9: piezoelectric coefficient versus AC stress for undoped SrBIT at 10 Hz measured at 150°C.

As the frequency dispersion of domain walls vibration is temperature dependent, at 200°C it is possible to see the onset of the non-linear regime at 10 Hz, Figure 5-10. At this temperature, the threshold field is only 36 MPa indicating that it is thermally activated. Small depolarization around 200°C is also observed in Figure 5-10 compared to Figure 5-9. Due to large charge drift (because of electrical conductivity), measurements performed at 1 Hz and 200°C are not reliable, and they are not presented here.

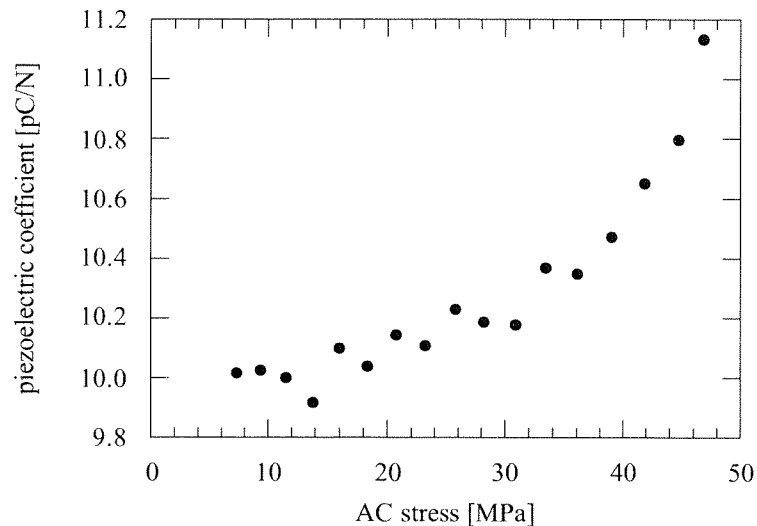


Figure 5-10: piezoelectric coefficient versus AC stress of undoped SrBIT at 10 Hz measured at 200°C.

The complete absence of non-180° ferroelectric domain walls in SrBIT was one assumption to account for the extremely stable piezoelectric properties of this material. In return, high temperature piezoelectric measurements have shown the occurrence of a stress dependent piezoelectric coefficient. It is believed that unlocking of non-180° ferroelectric domain walls above a temperature-dependent threshold field creates such dependence. As both elevated temperature and elastic field were applied in order to detect the stress dependence, ferroelectric domains should be sitting in very deep potential wells. This is consistent with the model of Reaney and Damjanovic [24].

A third piezoelectric behavior was observed in SrBIT, it is a piezoelectric relaxation whose features are different from the above-described non-linear behavior. It was mostly observed for 2 mol.% Mn doped SrBIT, but some results indicate its occurrence in pure SrBIT. However, only clear results obtained with Mn doped SrBIT will be presented here in the next section, as the aim of this paragraph is only a phenomenological description of the observed relaxation. A very simple model will be developed that is sufficient to qualitatively explain the observed responses.

5.4.3 Piezoelectric Relaxation

This paragraph is dedicated to the frequency response of 2 mol.% Mn doped SrBIT mainly at room temperature. These experimental conditions provide a third kind of piezoelectric behavior of SrBIT. It is a frequency dispersion, Figure 5-12, that is very different from the one measured for other ferroelectrics in the case of irreversible domain walls motion [129]. In addition, for the

same nominal composition, it could be positive, negative or absent. Such a variety of behaviors should obviously be related to the extremely small processing window that was described in Chapter 2. Actually, with a simple model, it can be shown that imperfect microstructure (multiphase) can lead to the occurrence of either a positive or a negative piezoelectric relaxation.

Deterioration of piezoelectric stability is easily observed in a charge versus force measurement, Figure 5-11. Loss-free loop of undoped SrBIT is replaced by a significant hysteresis at low frequency in the case of 2 mol.% Mn doped SrBIT. However, no field dependence was brought by Manganese doping, Figure 5-14.

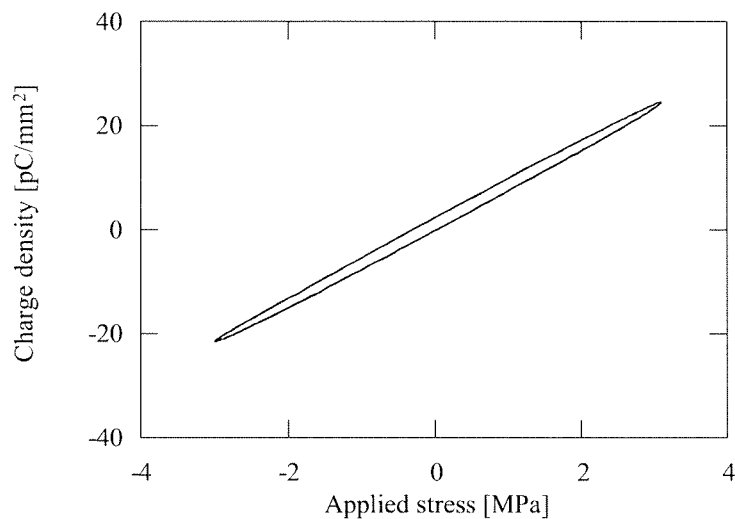


Figure 5-11: collected charge versus applied force for 2 mol.% Mn doped SrBIT at 490 MHz at room temperature.

In the frequency domain, a much more spectacular change was observed, Figure 5-12. A typical Debye-like relaxation is clearly seen in the measured frequency range on both piezoelectric coefficient and loss. The highest deviation is 28% at 20 mHz compared to initial 100 Hz value. In that case, it is a relaxational process, since loss is positive and piezoelectric coefficient increases. However, for the same nominal composition (2 mol.% Mn), a retarded process can be observed too, Figure 5-13. In this situation, loss is negative and piezoelectric coefficient decreases as frequency is decreased.

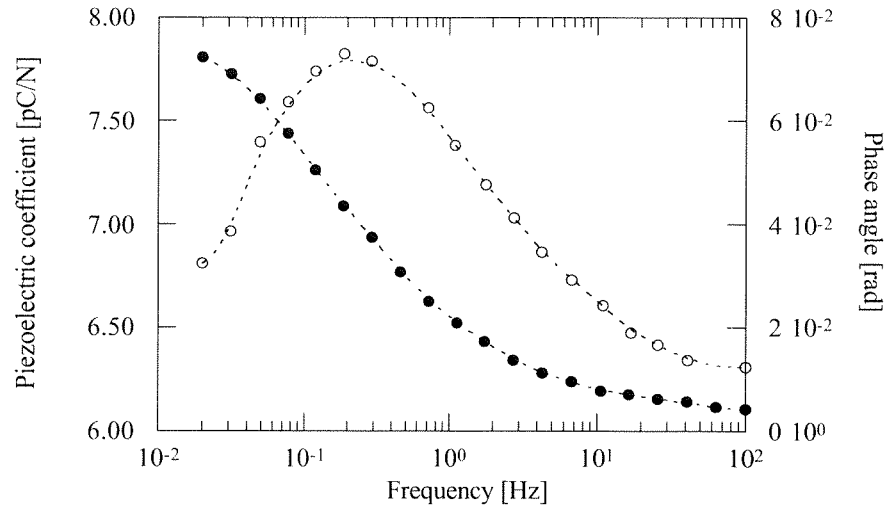


Figure 5-12: piezoelectric coefficient (filled circles) and phase angle (open circles) for 2 mol.% Mn doped SrBIT versus frequency measured at room temperature.

Calculated complex piezoelectric coefficients from Figure 5-12 and Figure 5-13 can also be represented in the complex plane. This is the usual way to identify relaxational and retarded mechanisms.

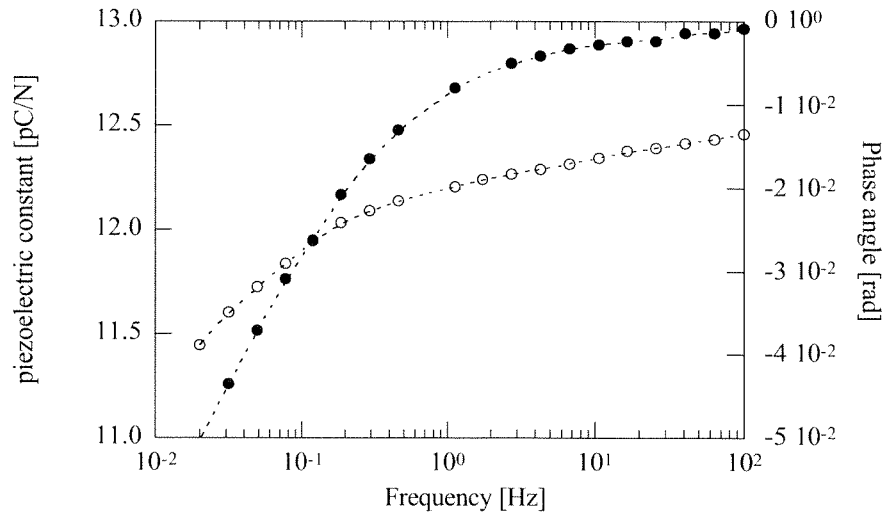


Figure 5-13: piezoelectric coefficient (filled circles) and phase angle (open circles) for 2 mol.% Mn doped SrBIT versus frequency measured at room temperature.

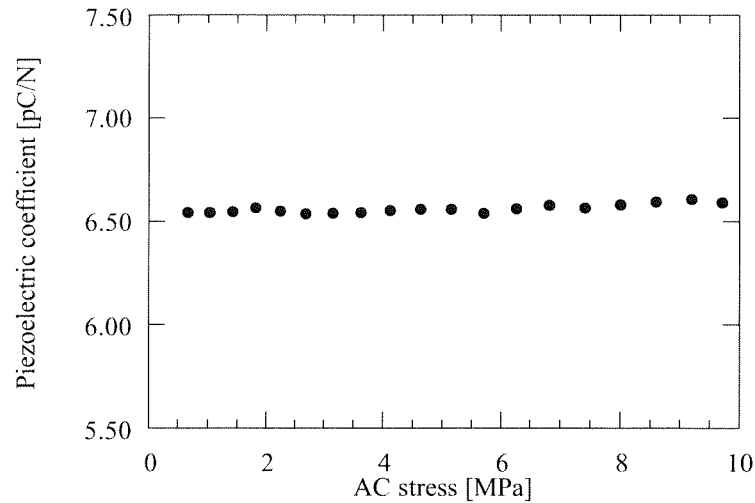


Figure 5-14: piezoelectric coefficient versus AC stress for 2 mol.% Mn doped SrBIT measured at room temperature with 1 Hz AC signal.

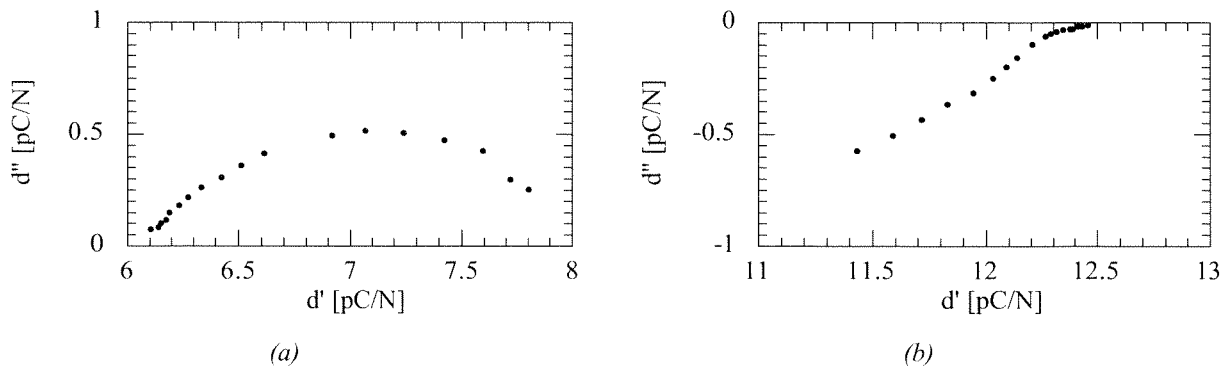


Figure 5-15: complex plane representation of piezoelectric coefficient for 2 mol.% Mn doped SrBIT.

Negative loss values may seem unrealistic, however since piezoelectric loss involves three kind of loss (mechanical, electrical and electromechanical), summation of the different components can lead to negative values. In addition, theoretical considerations by Hamano [133] have shown that thermodynamics allows retarded piezoelectric process.

The observed relaxations are temperature sensitive, Figure 5-16, which agrees with Debye-like relaxations.

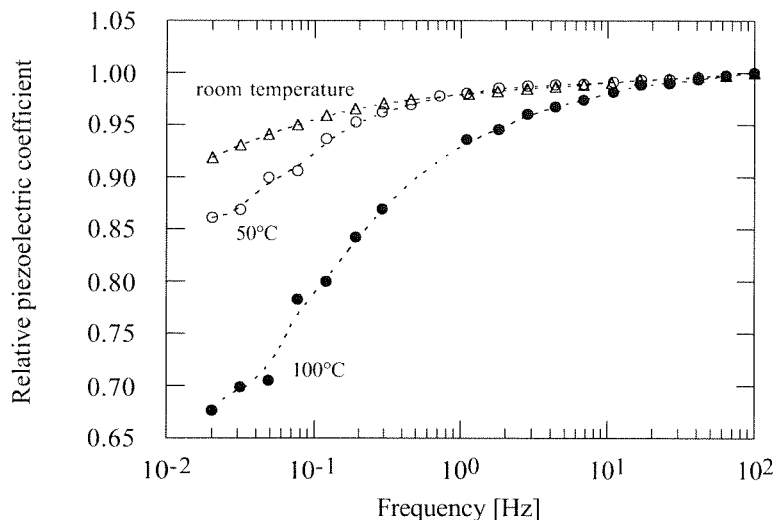


Figure 5-16: relative piezoelectric coefficient versus frequency for 2 mol.% Mn doped SrBIT at room temperature (triangles), 50°C (open circles) and 100°C (filled circles).

Relaxation of the piezoelectric coefficient leading to much smaller values at high frequency may be understood using common ferroelectric domain walls phenomenology. In that case, because of relaxed walls, the extrinsic component to piezoelectricity is strongly decreased. However, it is much more difficult to interpret an increase of the piezoelectric constant with frequency. Nevertheless, direct optical observation of domain walls oscillation of Gadolinium Molybdate single crystals by Tikhomirov [134] indicated that below 3 Hz, domain wall amplitude increases with frequency. The explanation for this behavior is that at low frequency, the electrical conductivity would balance the field in two adjacent domains [59]. However, Tikhomirov [134] and Fousek's [59] work were performed on single crystals, but for ceramics, the effect of microstructure has also to be taken into account. Chapter 3 was partly dedicated to the investigation of microstructure influence on either DC or AC conductivity, in the next section; it will be demonstrated that SrBIT piezoelectric properties could also be related to microstructure.

5.4.4 Modelization of the Piezoelectric Relaxation

In this section, a simple model will provide a physical justification to the piezoelectric relaxations observed in SrBIT. The approach chosen for this purpose is the building of a piezoelectric composite with two piezoelectric materials. As many authors reported the properties of piezoelectric-epoxy composites [135-139], equivalent treatment for piezoelectric-piezoelectric solid-state composites are lacking. The main hypothesis of the following analysis will be that SrBIT piezoelectric properties reflect the interactions between different phases within the material. Such interaction could be for example, Maxwell-Wagner polarization between two phases.

The composite that was chosen for our model is a serial building of two piezoelectric phases, Figure 5-17. Each of the constituting materials has its own piezoelectric coefficient, permittivity and conductivity.

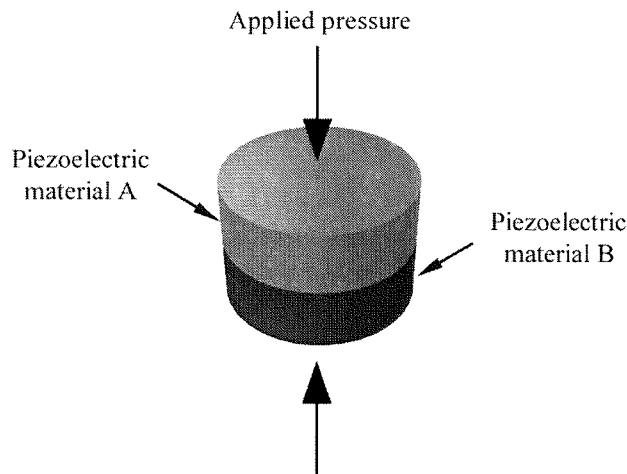


Figure 5-17: piezoelectric composite made of two piezoelectric materials used for modelization of the relaxation

According to Newnham [140], the longitudinal piezoelectric coefficient for a lamellar composite is given by Equation 5-7:

$$\bar{d} = \frac{d_1 \epsilon_2 V + d_2 \epsilon_1 (1 - V)}{\epsilon_2 V + \epsilon_1 (1 - V)} \quad \text{Equation 5-7}$$

In this equation, subscripts refer to each phase and volume fraction of the first phase is written V . If the complex permittivity is taken in the complex form as Equation 5-8:

$$\epsilon^* = \epsilon' - i\epsilon'' \quad \text{Equation 5-8}$$

Then, the global piezoelectric coefficient becomes Equation 5-9:

$$\bar{d} = \frac{d_1 (\epsilon_2' - i\epsilon_2'') V + d_2 (\epsilon_1' - i\epsilon_1'') (1 - V)}{(\epsilon_2' - i\epsilon_2'') V + (\epsilon_1' - i\epsilon_1'') (1 - V)} \quad \text{Equation 5-9}$$

In the next section, Equation 5-7 will be verified with piezoelectric measurements of the composite. In addition, these measurements will show that depending on measurement temperature, either a positive or a negative relaxation is observed.

5.4.5 Experimental Verification of the Model

Equation 5-7, [140], has been tested with a two-phase composite made of two ceramic discs of two different piezoelectric materials put in series. The two materials, prepared in the Ceramics Laboratory, were selected to have very different permittivities and piezoelectric coefficients. These materials were two solid solutions: one of $\text{Bi}_4\text{Ti}_3\text{O}_{12}$ (88%) and $\text{Bi}_3\text{TiNbO}_9$ (12%) and

another of $\text{Bi}_3\text{TiNbO}_9$ (99%) and BiWO_6 (1 %). In the following discussion, the first solid solution will be called BITO12-BITO9 and the second one BITO9-BW.

Equation 5-7 was applied to the composite considering first only the real part of the piezoelectric coefficient of the constituting materials. The complex permittivity versus frequency is given in Figure 5-18 for BITO12-BITO9 (circles) and BITO9-BW (diamond-shaped) at room temperature and in Figure 5-19 at 150°C . A plot of ϵ'' versus $1/f$ would show for both compositions and temperatures that conductivity is not the major contribution to dielectric loss for these materials at these temperatures. In addition, at 150°C , both real and imaginary components of BITO12-BITO9 exhibit a dielectric relaxation in the low frequency range (below 1 Hz).

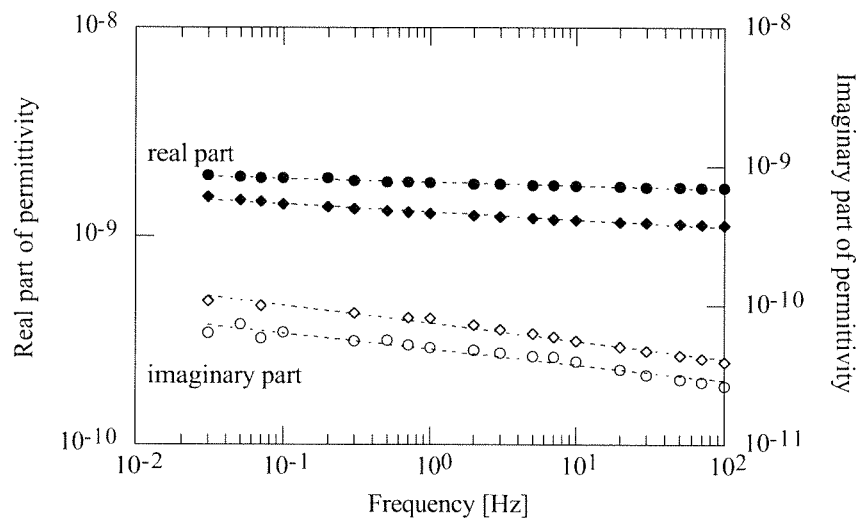


Figure 5-18: measured complex permittivity versus frequency for BITO12-BITO9 (circles) and BITO9-BW (diamond-shaped) at room temperature.

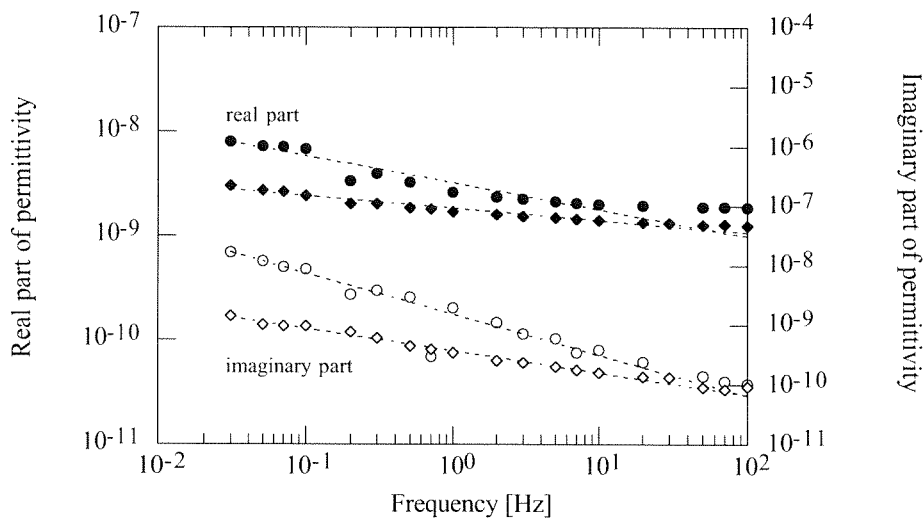


Figure 5-19: measured complex permittivity versus frequency for BITO12-BITO9 (circles) and BITO9-BW (diamond-shaped) at 150°C .

In Equation 5-7, in order to simplify Equation 5-7 only the modulus of the complex piezoelectric coefficient of each material was used to calculate the piezoelectric coefficient of the composite. These coefficients are given in Figure 5-20 and Figure 5-21 at room temperature and 150°C respectively. According to these figures, the piezoelectric coefficient of BITO12-BITO9 was about four times larger than BITO9-BW's. The coefficients are almost frequency independent at room temperature for both materials and there is a slight frequency dependence of the coefficient in the case of BITO9-BW at 150°C.

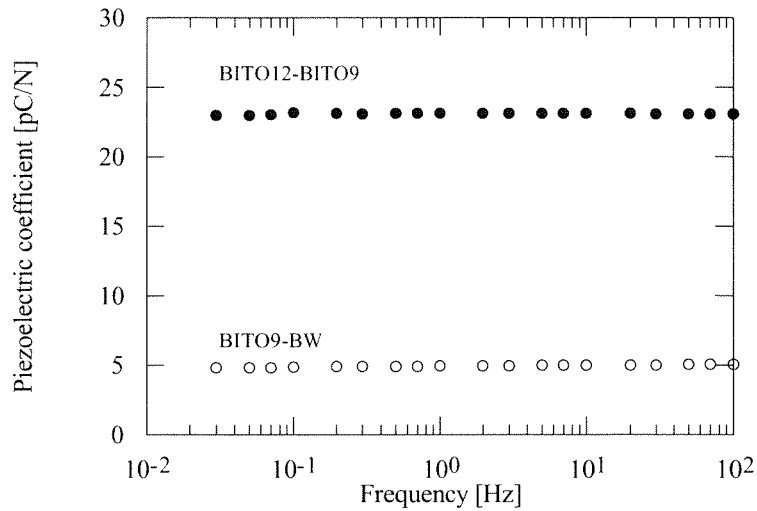


Figure 5-20: piezoelectric coefficient versus frequency for BITO12-BITO9 (filled circles) and BITO9-BW (open circles) at room temperature.

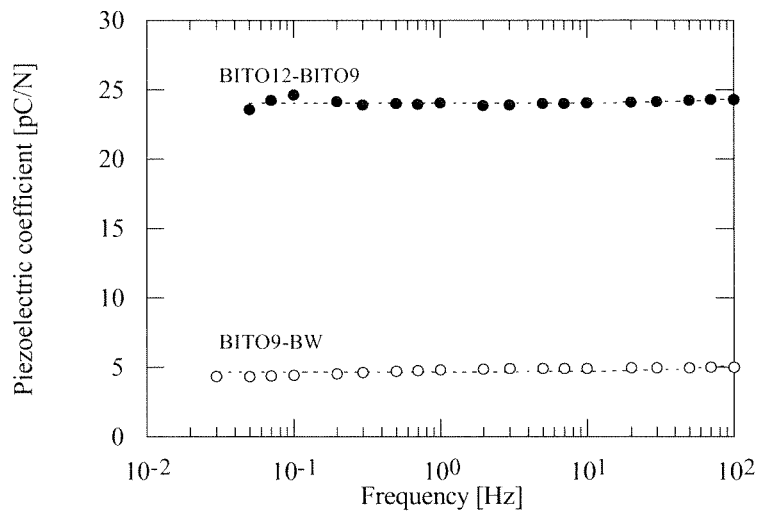


Figure 5-21: piezoelectric coefficient versus frequency for BITO12-BITO9 (filled circles) and BITO9-BW (open circles) at 150°C.

The complex piezoelectric coefficient of the composite was calculated using Equation 5-7 and is expressed as Equation 5-10 and Equation 5-11. In these equations subscript "1" referred to

BITO12-BITO9 and subscript “2” to BITO9-BW. It is taken that volume fraction of the two components are the same.

$$d' = \frac{(d_1 \epsilon_2' + d_2 \epsilon_1')(\epsilon_1' + \epsilon_2') + (d_1 \epsilon_2'' + d_2 \epsilon_1'')(\epsilon_1'' + \epsilon_2'')}{(\epsilon_1' + \epsilon_2')^2 + (\epsilon_1'' + \epsilon_2'')^2} \quad \text{Equation 5-10}$$

$$d'' = \frac{(d_1 \epsilon_2' + d_2 \epsilon_1')(\epsilon_1'' + \epsilon_2'') - (d_1 \epsilon_2'' + d_2 \epsilon_1'')(\epsilon_1' + \epsilon_2')}{(\epsilon_1' + \epsilon_2')^2 + (\epsilon_1'' + \epsilon_2'')^2} \quad \text{Equation 5-11}$$

Measured complex piezoelectric coefficient for the composite is given in Figure 5-22 at room temperature and Figure 5-23 at 150°C. In Figure 5-22, the piezoelectric coefficient (both real and imaginary parts) of the composite slightly decreases as frequency increases. Such behavior is quite peculiar compared to isolated ones; it shows in concrete terms model's predictions: when two piezoelectric materials are brought together, their interaction could produce an entirely new behavior. In particular, in the case of BITO12-BITO9 and BITO9-BW composite, the interaction creates a piezoelectric relaxation causing a 10% decrease of d_{33}' from 20 mHz up to 100 Hz.

At room temperature, qualitative agreement between measurement and calculation is seen, Figure 5-22. The model actually properly predicts the increasing trends of both real and imaginary components. Poor temperature definition at room temperature (no temperature regulation system) could explain the observed quantitative misfit.

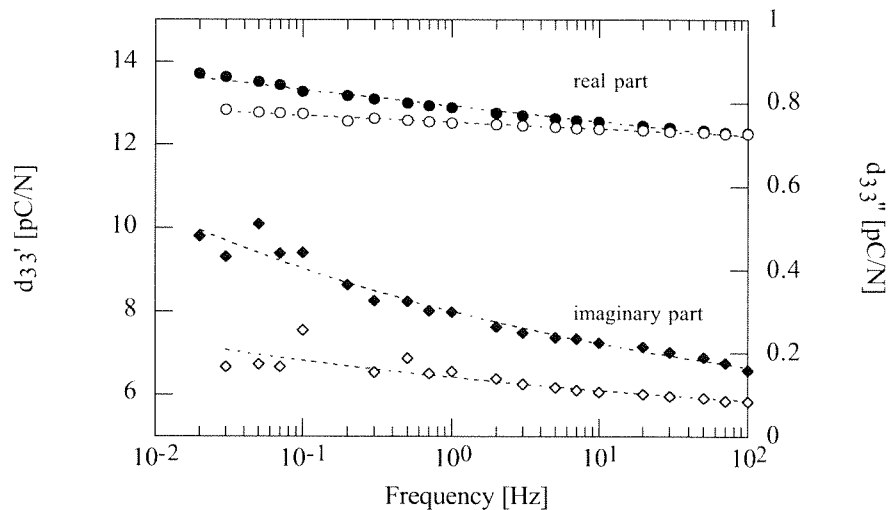


Figure 5-22: measured (filled items) and calculated (open items) complex piezoelectric coefficient versus frequency for a composite made of BITO12-BITO9 and BITO9-BW samples at room temperature.

At 150°C, Figure 5-23, the piezoelectric coefficient decreases as much as 50 % from 20 mHz down to 100 Hz. The imaginary part of the composite's piezoelectric coefficient is negative at 150°C as already seen in Figure 5-13 for 2 mol.% Mn doped SrBIT. Those features are actually consistent with a retardation process as described above. At this temperature, there is a very good

qualitative and quantitative agreement between measurements and calculations, Figure 5-23. Thus, the theoretical model is able to predict both kinds of relaxations.

Figure 5-22 and Figure 5-23 show that depending on respective physical properties that are temperature dependent, the piezoelectric coefficient of a two phases ceramic composites can have two opposite behaviors: either a “positive”, Figure 5-22, or a “negative” relaxation, Figure 5-23. As a consequence, it gives a definitive phenomenological justification to the results of Figure 5-12 and Figure 5-13 for Mn doped SrBIT. Depending on the respective values of piezoelectric coefficient, permittivity and conductivity of each phase, either “positive” or “negative” relaxation occurs.

Identifying SrBIT with a piezoelectric composite requires finding at least two different phases within the material. No such second phase was ever detected in SrBIT (SBTO18 content described in Chapter 2 is never comparable to SrBIT). On the opposite, anisotropic properties could create within SrBIT microstructure a two-phase composite. Considering any direction measurement, the (001) direction of every grain is more or less favorably oriented. Taking grains whose (001) direction makes an angle larger than $\pi/2$ with measurement direction as one phase and the others as a second phase actually define a piezoelectric composite.

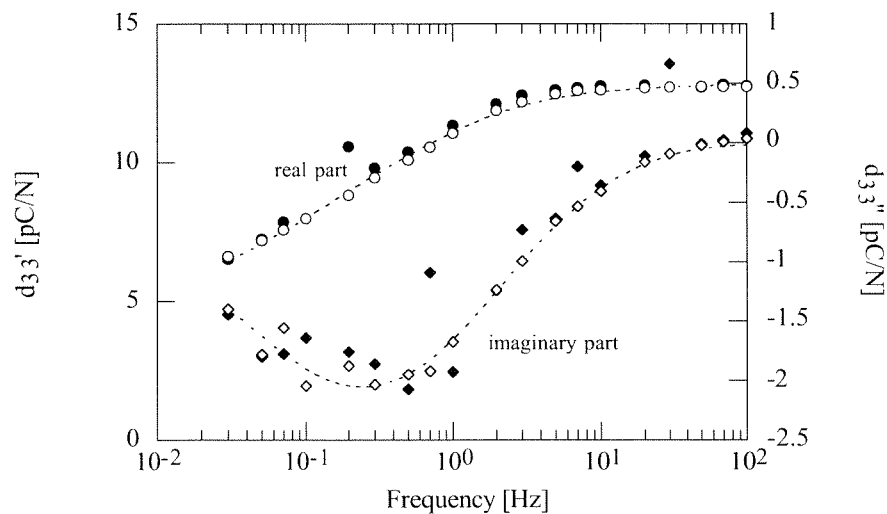


Figure 5-23: measured (filled items) and calculated (open items) complex piezoelectric coefficient versus frequency for a composite made of BITO12-BITO9 and BITO9-BW samples at 150°C.

5.4.6 Numeric Simulation of Equation 5-7

Evaluation of Equation 5-9 reveals that depending on either piezoelectric coefficient or dielectric permittivity values, there could exist a relaxation or a retardation process, Figure 5-24, Figure 5-25, Figure 5-27. Equation 5-9 was evaluated from 10^{-3} up to 10^2 Hz with either d_1 , Figure 5-24 and Figure 5-25, or ϵ_1 , Figure 5-27, as the second variable. For the simulation, the imaginary part of permittivity was written as:

$$\varepsilon'' = \frac{\sigma}{\omega}$$

Equation 5-12

With the electrical conductivity σ . The volume fraction was 0.5 in all cases.

The effect of the piezoelectric coefficient of the first phase (d_1) on the global piezoelectric coefficient is presented in Figure 5-24 for the real part and in Figure 5-25 for the imaginary one. As d_2 was 10 pC/N, d_1 was varied from 0 to 20 pC/N. The piezoelectric coefficient is relaxed for large d_1 values, but it increases for low d_1 . In the latter case, the associated imaginary part becomes negative. When $\varepsilon_1 > \varepsilon_2$ as in Figure 5-24, the low frequency coefficient is mainly controlled by phase "1", while the high frequency value is given by phase "2".

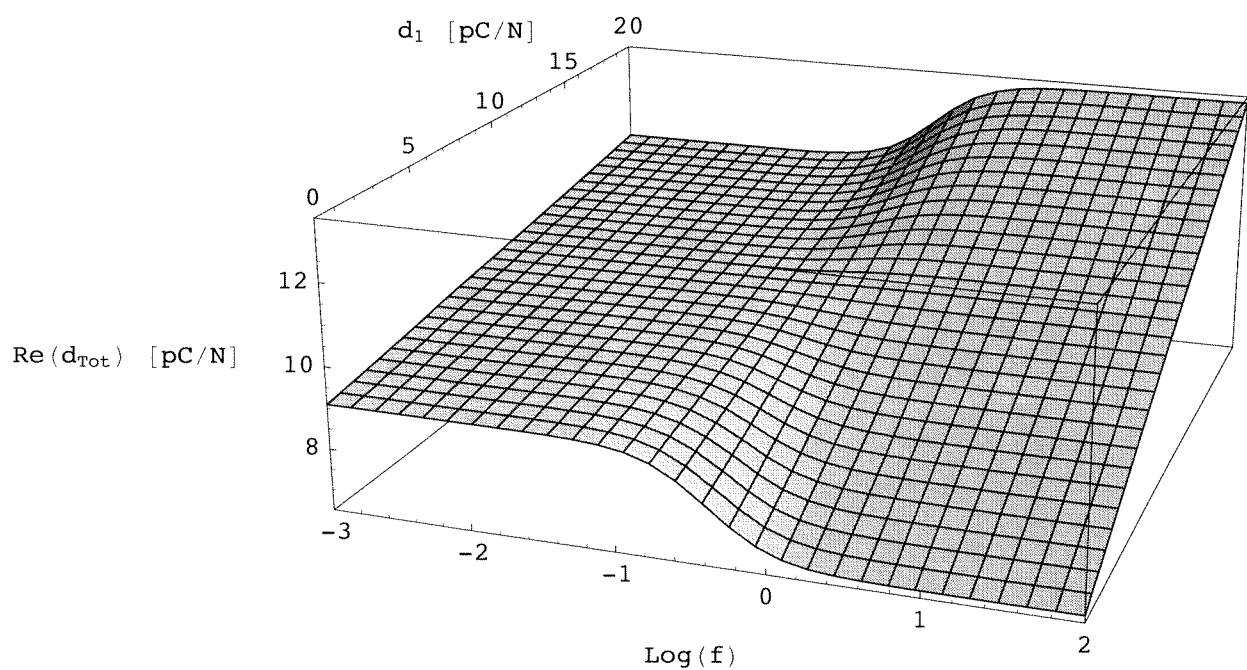


Figure 5-24: calculated real part of the piezoelectric coefficient versus frequency and piezoelectric coefficient of the first material (d_1) calculated with Equation 5-9. Others parameters are $d_2=10$ pC/N, $\varepsilon_1=200$, $\varepsilon_2=100$, $\sigma_1=10^{-9}$ S/m, $\sigma_2=10^{-10}$ S/m, $V=0.5$.

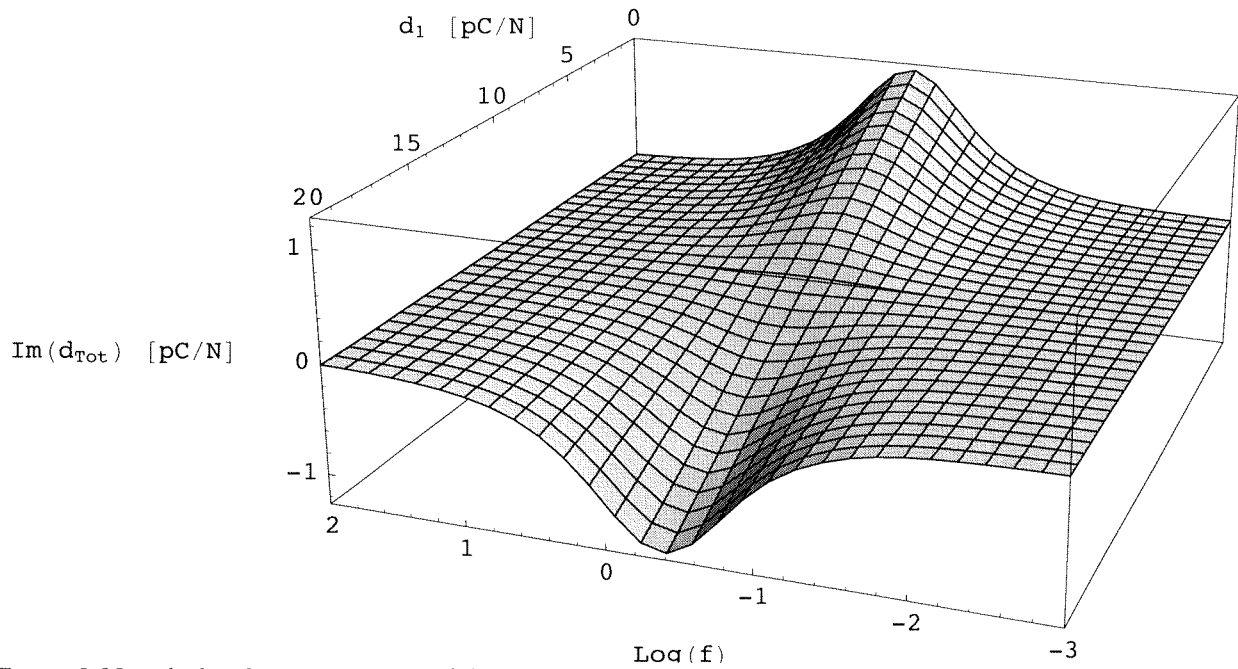


Figure 5-25: calculated imaginary part of the piezoelectric coefficient versus frequency and piezoelectric coefficient of the first material (ϵ_1) calculated with Equation 5-9. Others parameters are $d_2=10$ pC/N, $\epsilon_1=200$, $\epsilon_2=100$, $\sigma_1=10^{-9}$ S/m, $\sigma_2=10^{-10}$ S/m, $V=0.5$.

A similar transition is observed when the dielectric permittivity of the first phase is changed, Figure 5-27. If the permittivity of the second phase is fixed to 200 and $d_1 > d_2$, the relaxation transforms into a retard as the permittivity of the first phase increases.

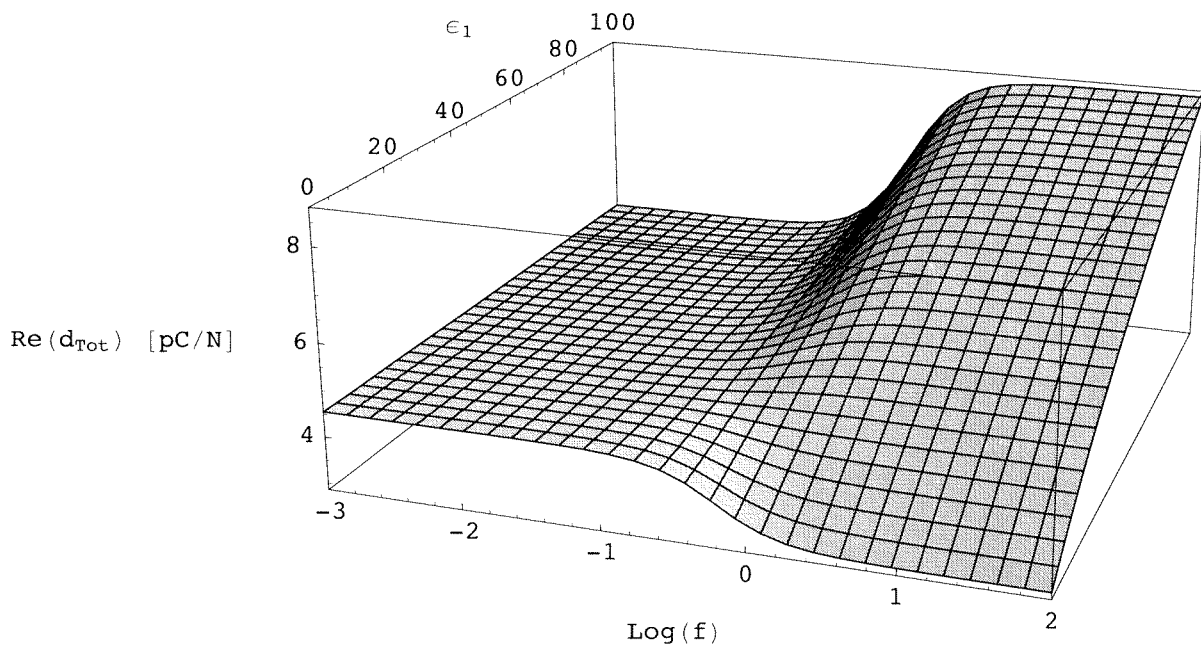


Figure 5-26: calculated real part of the piezoelectric coefficient versus frequency and permittivity of the first material (ϵ_1) calculated with Equation 5-9. Others parameters are $d_1=3$ pC/N, $d_2=20$ pC/N, $\epsilon_2=200$, $\sigma_1=10^{-10}$ S/m, $\sigma_2=10^{-9}$ S/m, $V=0.5$.

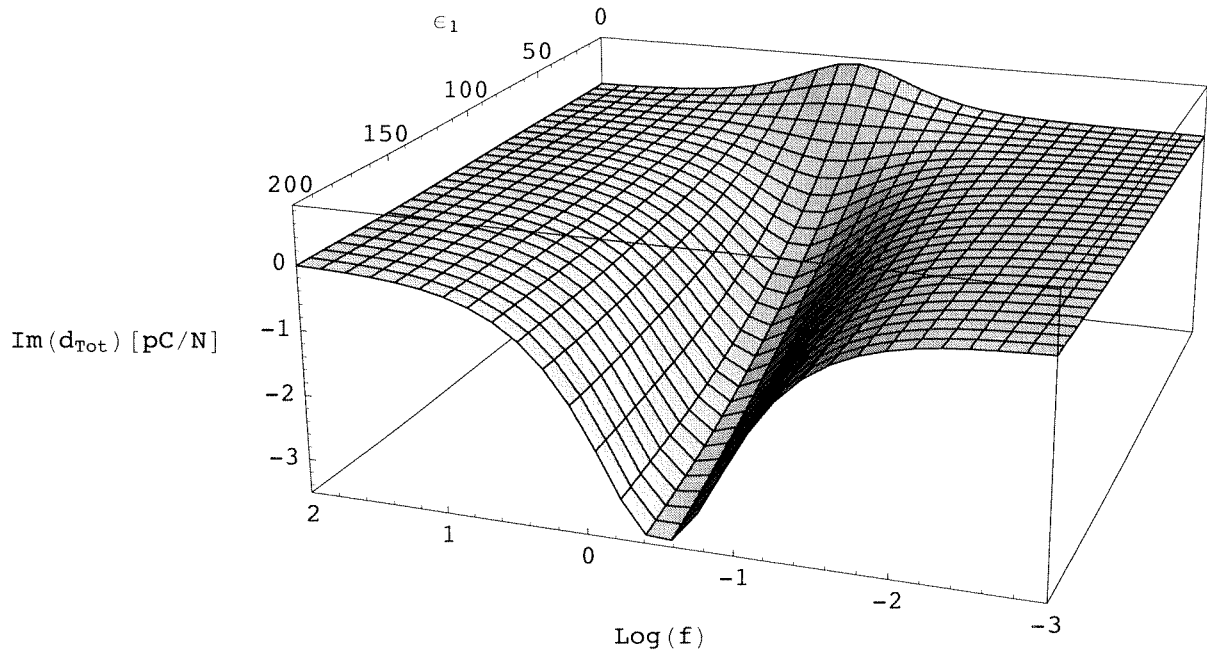


Figure 5-27: calculated imaginary part of the piezoelectric coefficient versus frequency and permittivity of the first material (ϵ_1) calculated with Equation 5-9. Others parameters are $d_1=3$ pC/N, $d_2=20$ pC/N, $\epsilon_2=200$, $\sigma_1=10^{-10}$ S/m, $\sigma_2=10^{-9}$ S/m, $V=0.5$.

It is interesting to note that the high frequency coefficient becomes strongly dependent towards ϵ_1 or d_1 while the low frequency part is either permittivity or piezoelectric coefficient independent.

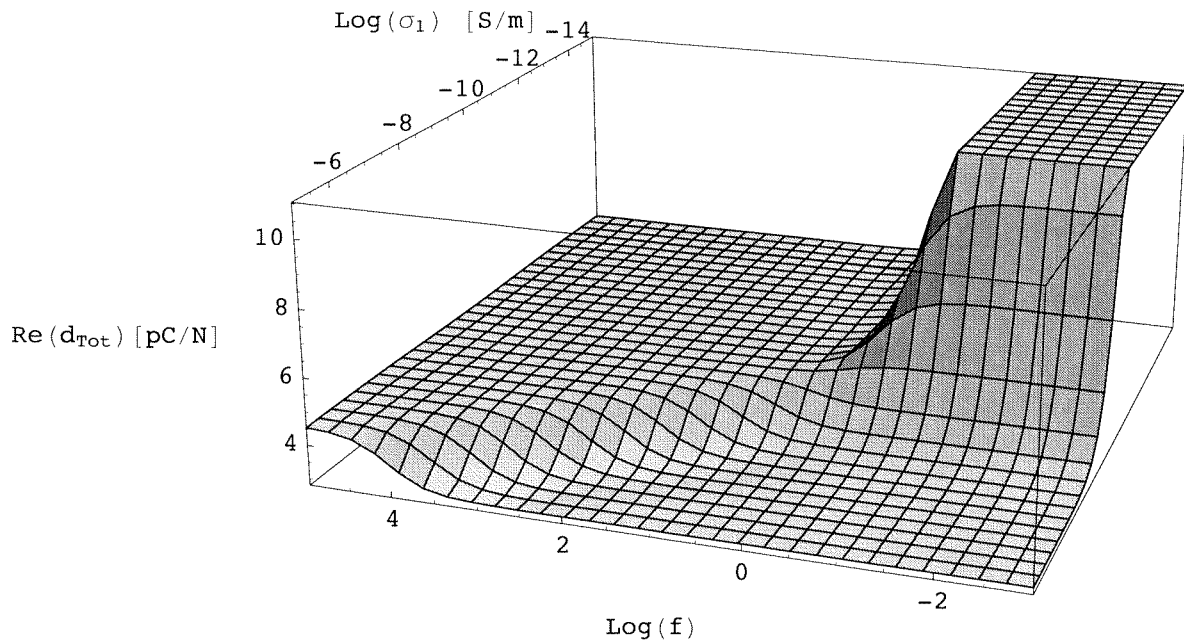


Figure 5-28: calculated real part of the piezoelectric coefficient versus frequency and conductivity of the first material (d_1) calculated with Equation 5-9. Others parameters are $d_1=20$ pC/N, $d_2=3$, $\epsilon_1=100$, $\epsilon_2=10$, $\sigma_2=10^{-10}$ S/m, $V=0.5$.

According to Figure 5-28, a similar transition from a positive to a negative relaxation is caused by an increase of the conductivity of one phase. But in this case, the relaxation frequency increases with the conductivity of phase “1”. The electrical conductivity was included in the model as a $1/\omega$ contribution to the imaginary part of permittivity. This is the simplest way to express the influence of conductivity on the dielectric permittivity. However, as discussed in Chapter 3, either non-Debye or multiple relaxations may exist. In these cases, the contribution of conductivity becomes much more complicated and cannot be summarized by a $1/\omega$ law. This was actually demonstrated with the experimental model by a poor agreement between measurement and calculation when ϵ'' was replaced by σ/ω .

Electrical conductivity is however the key parameter for the occurrence of piezoelectric relaxations, since for non-conducting piezoelectrics (i.e. $\epsilon''=0$), there are no relaxations, Figure 5-29 and imaginary part of piezoelectric constant is zero. Thus, because of conductivity in two-phase piezoelectric composite, there are either positive or negative relaxations.

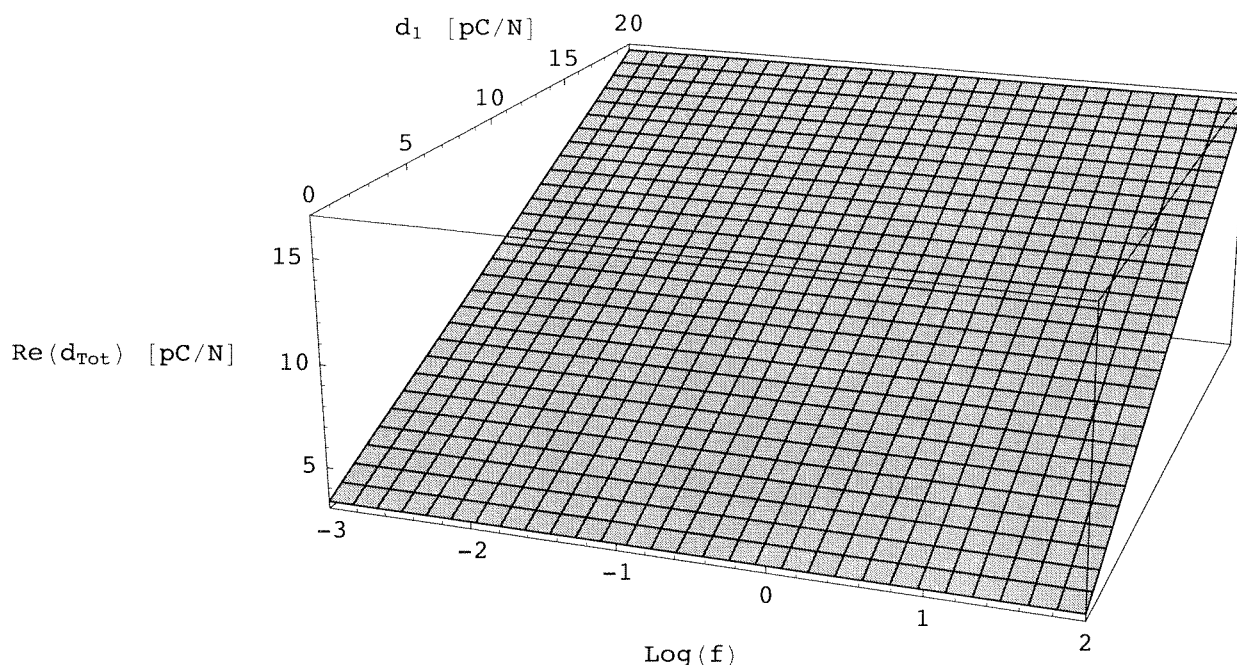


Figure 5-29: real part of the piezoelectric coefficient versus frequency and piezoelectric coefficient of the first material in the case of non-conducting materials ($\sigma_1 = \sigma_2 = 0$) and $\epsilon_1 = 100$, $\epsilon_2 = 200$, $d_2 = 10$.

Concerning volume fraction influence, no interesting effect is seen, for this reason its plot is not presented here.

The very simple model presented in this section is obviously not sufficient for a complete description of the piezoelectric properties of SrBIT, since ceramics are not made of two distinct homogeneous phases. However it allowed the prediction of both relaxation and retard process, that were actually measured in SrBIT. Finding a cause for either piezoelectric coefficient or dielectric permittivity difference in SrBIT is not difficult. The strong anisotropy of the material creates large differences in both piezoelectric coefficient and dielectric permittivity at high temperature. The dielectric permittivity and piezoelectric coefficient are larger in the ab plane direction than in the c direction and the electrical conductivity is also higher in the ab plane direction than in the c direction. For an “ideal” ceramics made of random oriented grains, those differences disappear on a global scale. However, for poled ceramics, anisotropy may be exacerbated. In a simplified point of view, for such materials, there exist two kinds of polarization directions: either close to the field or far from it. This creates two “phases”, one with a large contributing polarization (large permittivity and piezoelectric coefficient) and another one without any polarization contribution (very small permittivity and piezoelectric coefficient). In addition, the electrical conductivity of the first one would be larger than the second one. This is only possible for highly anisotropic materials where one direction does not contain polarization *at all*. It cannot happen in PZT.

To illustrate the relation between anisotropy and piezoelectric relaxation, the piezoelectric coefficient *calculated* at 195°C for a two-phase composite made of ab and c oriented SrBIT samples put in serie is presented in Figure 5-30. The calculation was made after separate measurement of permittivity and piezoelectric coefficient of each phase. Figure 5-30 definitely

demonstrates the possibility of a piezoelectric relaxation within anisotropic material such as SrBIT. Permittivities and piezoelectric coefficient are different along the two directions as discussed many times in this thesis and due to conductivity, their electromechanical coupling creates a negative piezoelectric relaxation.

Figure 5-30 is the last figure of this thesis but it is also a remarkable summary of the whole work realized with SrBIT: it includes its anisotropy, conductivity and piezoelectric properties. As a matter of fact, the composite model was developed because SrBIT is made of colonies (described in Chapter 2) and the piezoelectric relaxation exists because of SrBIT anisotropy (extensively discussed in Chapter 3) and conductivity (Chapter 3 and 4). Thus, Figure 5-30 really expresses microstructure, conductivity and piezoelectricity in SrBIT that were actually the subject of this thesis.

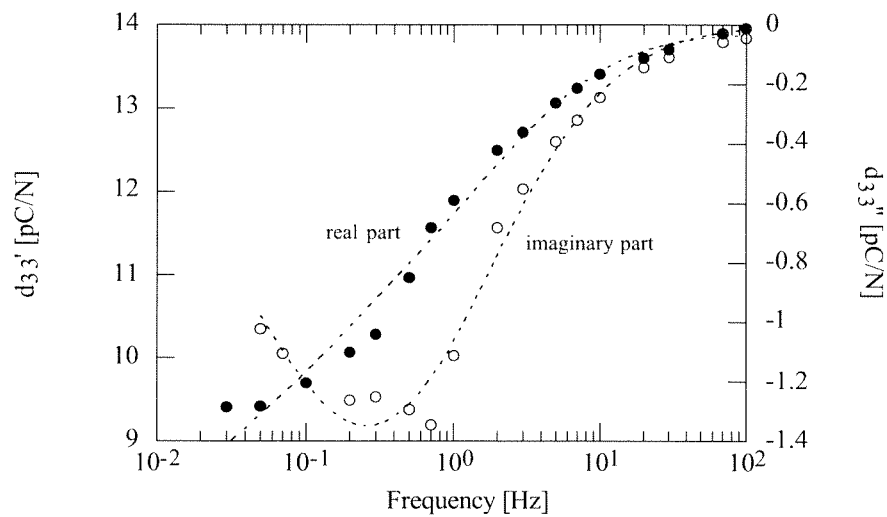


Figure 5-30: calculation of the complex piezoelectric coefficient of a two-phase composite made of *ab* and *c* oriented *c* samples put in series at 195°C.

Presence of an extra phase at grain boundaries may be another origin for the building of a two-phase material. Either Bi_2O_3 segregation or SrBIT decomposition at firing temperature may create such additional phase.

Measurement of piezoelectric coefficient for Bi_2O_3 excess (3 and 5 wt.% excess and 5 wt.% deficient) containing SrBIT were performed at room temperature, they did not reveal any piezoelectric relaxation or retard. Similar measurements were made at high temperature, however in these conditions due to strong charge drift measurement quality was quite low. Finally, no clear evidence of a second phase (coming from decomposed SrBIT) causing a piezoelectric relaxation was seen.

5.5 SUMMARY AND CONCLUSION

The longitudinal piezoelectric coefficient of undoped and 2 mol.% Mn SrBIT has been investigated as a function of AC field amplitude, frequency and temperature using piezoelectric direct effect. Both experimental and theoretical modeling was used to investigate the Debye-type piezoelectric relaxation observed specially for 2 mol.% Mn doped SrBIT. The experimental model was a two-phase piezoelectric composite, whose component materials had different properties (piezoelectric coefficients, permittivity and conductivity). This experimental model was also simulated using a simple theoretical model for piezoelectric composites.

Extremely stable piezoelectric properties have been observed at room temperature under small elastic field. No dependence towards either field or frequency was seen as already reported in the literature. Consequently no charge hysteresis was measured during elastic field cycling. However, at much higher field and temperature, triggering of a nonlinear behavior was noticed for undoped SrBIT. At 150°C under at 1 Hz, above a threshold field, it was shown that the piezoelectric coefficient of undoped SrBIT becomes field-dependent. In the measured non-linear regime, the piezoelectric coefficient was directly proportional to the field. Such behavior has been encountered many times for other ferroelectrics. It can be concluded that clamped non-180° domain walls of SrBIT are thermally and field activated. It also proves the actual existence of piezoelectrically active ferroelectric domain walls.

A Debye-type piezoelectric relaxation either positive or negative without any field dependence was measured for 2 mol.% Mn doped at room temperature. Real and imaginary parts of the piezoelectric coefficient were consistent with either a relaxation or a retard process. Temperature dependence of the relaxation was demonstrated by piezoelectric measurements at room temperature, 50 and 100°C. As a starting point to understand the physical process involved in the piezoelectric relaxation, piezoelectric measurements have been performed with a ceramic composite.

It was possible to regenerate the piezoelectric relaxation with a two-phase composite. Depending on temperature either a positive or a negative relaxation was observed. Thus, it was experimentally demonstrated that direct electromechanical coupling between two relaxation-free materials could produce a strong piezoelectric relaxation.

As a complement to the experimental model, the piezoelectric response of the composite has been calculated using a model. The validity of the model has been demonstrated by the excellent agreement between measurements and calculation at 150°C. With the theoretical model, the influence of piezoelectric coefficient, permittivity and conductivity of one phase on composite's response was clearly established.

6

CONCLUSION

6.1 SUMMARY AND CONCLUSION

6.1.1 Material Processing

A reproducible processing route has been developed for $\text{SrBi}_4\text{Ti}_4\text{O}_{15}$ bulk ceramics using solid-state calcination and natural sintering. Formation of intermediate crystalline phases during calcination step has been established and those phases were identified as SrO-Bi₂O₃ solid solution, Bi₁₂TiO₂₀, Bi₄Ti₃O₁₂ and SrTiO₃. It was shown that complete conversion of the intermediate phases into SrBIT occurs only at very high temperature.

Two densification mechanisms have been highlighted for SrBIT natural sintering. It was established that re-arrangement of particle agglomerates was the first densification stage. The second mechanism, which is liquid-phase-assisted sintering, was demonstrated by cycling dilatometry experiments. Incongruent melting was proposed as the source of liquid phase as some traces of $\text{Sr}_2\text{Bi}_4\text{Ti}_5\text{O}_{18}$ were detected by X-ray diffraction in selected sintered samples.

No grain coarsening due to long time sintering, acceptor or donor doping was observed in optimized sintering conditions, demonstrating the low mobility of SrBIT grain boundaries. However, probably due to partial melting, large grain SrBIT was produced 10°C above the temperature optimum.

Actual incorporation of Manganese cations on the Titanium sites for 2 mol.% Mn doped SrBIT was demonstrated by the progressive deformation of the crystallographic cell of SrBIT.

6.1.2 DC and AC Conductivity

The DC electrical conductivity of undoped, Mn and Nb doped SrBIT has been studied with the charge-discharge method. Activation energy of 1 eV in the 140-220°C temperature range was found and significant curve bending in the Arrhenius plot was explained by grain boundary influence, small polarons conduction or transition from ionic to electronic conduction.

The anisotropy of SrBIT has been established with textured materials. It was verified that the electrical DC conductivity along the c direction (or 004 texture axis) was about one order of magnitude smaller compared to its perpendicular direction value (ab plane direction).

With the conductivity of both acceptor and donor doped SrBIT, a strong indication was found for p-type conductivity up to 220°C. This result should however be confirmed with thermopower or Hall coefficient measurement in order to definitely demonstrate it. This temperature range was unfortunately too low for any investigation under controlled oxygen partial pressure due to extremely small diffusion coefficients.

Charging current was evaluated at room temperature down to $1\mu\text{s}$ using measurement of the electrical charge. Due to either incomplete resolution of a Debye-type relaxation or non-Debye relaxation, study of the immediate polarization with the DC method was not possible.

The impedance analysis was mostly performed at elevated temperature (450-700°C), where the measuring frequency window (20 Hz-1 MHz) matches the best SrBIT's relaxation frequency range (complete definition of the impedance arc). Several kinds of equivalent circuits were tested as according to the literature either discrete multi-component Debye-type or distributed models could be employed to simulate Bismuth Titanate's impedance. The best measurement approximation was actually found with a single Havriliak-Negami distributed circuit as already shown for others Bismuth Titanates, but unusual values of best-fit parameters (α , β) lead to the consideration of other circuits. In addition, as distributed models are mostly used to describe dielectric behavior of glassy systems, physical justification for its use in SrBIT was not obvious. Since the Havriliak-Negami model is an empirical law, whose parameters are not directly related to any physical properties, it was not as suitable tool for a detailed analysis of the impedance. It was however sufficient for the calculation of the overall conductivity (low frequency one), permittivity and relaxation frequency. It was found that for undoped SrBIT in the 450-700°C temperature range, the activation energy for conduction was 1.5 eV. Compared to the low temperature value (1 eV), this was interpreted the same way as the curve bending observed with the DC method: by grain boundary influence.

As an attempt to discriminate between grain, grain boundary and electrode influences on the total impedance of SrBIT, an equivalent circuit made of three RC elements was tested with three different parameters: temperature, grain size and oxygen partial pressure. It was found that this circuit could satisfactorily simulate the experimental impedance arc. This simulation provided three sets of relaxation parameters (resistance, capacity and characteristic frequency) that were sorted according to their characteristic frequency. It was shown that two of the components (with the two highest frequencies) exhibited a ferroelectric anomaly near the ferroelectric phase transition of SrBIT (540°C). Identification of the second relaxation with grain boundaries was confirmed by impedance measurement of large grain SrBIT as the ratio of grain-to-grain boundary increased for large grain material. Diffusion coefficient calculation with impedance transient measurements gave another indication for grain and grain boundary relaxation identification. The diffusion coefficient calculated for grain boundaries was as expected actually much higher than the grain one.

With the impedance analysis performed with a three RC model, it was concluded that discrimination of grain, grain boundary and electrode separate contribution to the impedance of SrBIT is possible. Compared to low temperature measurements, this allowed us to interpret the second part of the charging current (above one second).

As reported for other Bismuth Titanates, a high frequency relaxation was highlighted for SrBIT with the evaluation of the electrical modulus instead of the impedance. By either building master curves or approximating the high frequency "tail" of the modulus arc, it was shown that at much higher frequency than the main relaxation, an extra contribution to the impedance could be determined. According to the literature and by comparing the characteristic frequencies, this

additional relaxation could be identified with Bismuth oxide layers within SrBIT crystallographic cell. The immediate polarization measured with the DC technique may actually be the dielectric polarization inside Bismuth oxide layers. However, this would imply very low activation energy, since the characteristic frequency at 500°C is in the Megahertz range and the immediate polarization at room temperature is saturated below 1 microsecond.

6.1.3 Conductivity under Controlled Oxygen Partial Pressure

The experimental set-up has been validated with conductivity measurements of BaTiO₃ and comparison with published data. Both qualitative (p-type conductivity) and quantitative agreements were found in the 10⁻⁵-1 atm pressure range.

DC conductivity of undoped, 2 mol.% Mn and 4 mol.% Nb doped SrBIT was measured in the same pressure range. It was found in these conditions that the electrical conductivity of undoped SrBIT increases as the oxygen partial pressure was decreased. This is representative of n-type conductivity up to standard pressure (0.2 atm pO₂), while low temperature measurements indicated p-type conductivity. This transition has been explained with the shift of the conductivity minimum as temperature increases. At elevated temperature, the p-type region was even not visible any more. Above 700°C, the electrical conductivity of undoped SrBIT follows a pO₂^{-1/4} law. This behavior was interpreted with the aid of an acceptor-based model developed for BaTiO₃. With this model, it is believed that some singly ionized acceptor centers (present as impurities within the undoped material) compensate the oxygen vacancies. Thanks to this model, the mass-action constant for reduction and the net acceptor-excess concentration were calculated.

For 2 mol.% Manganese doped SrBIT, it was shown that conductivity is still p-type, but with a smaller exponent. In this case, the electrical conductivity follows a pO₂^{-1/6} law. According to the literature, taking into account the reduction equilibrium of Mn⁴⁺ into Mn³⁺, the acceptor-controlled model was modified to provide the required pO₂^{-1/6} dependence. With these experiments, the mass-action constant for intrinsic carriers ionization (free electrons and holes) and its activation energy, which is the band gap energy, were calculated. With some restrictions from experimental precision, the band gap energy of SrBIT was estimated for the first time as 3.7 eV.

In the case of 4 mol.% Nb doped SrBIT, the conductivity is still n-type with a pO₂^{-1/4} dependence. However for donor doped SrBIT, this was interpreted with the formation of Bismuth vacancies as a way to compensate the positive donors. Loss of Bismuth was actually the more likely to consider due to the natural elevated volatility of Bismuth Oxide. However, no weight loss was observed for sintered SrBIT after long time annealing at elevated temperature. That is, Bismuth loss occurs on calcination and sintering. However, this donor-controlled model predicts a pO₂-independent regime, when free electron concentration is determined by donor concentration; this regime was not observed in the 10⁻⁵-1 atm pressure range for 4 mol.% Nb doped SrBIT.

At much lower oxygen partial pressure, instead of a pO₂^{-1/6} trend, it was shown that the electrical conductivity of undoped SrBIT becomes pO₂-independent. With the assumption of intrinsic donors, this behavior was explained with the donor-controlled model used for Nb doped SrBIT.

As proposed in the literature, cation place exchange between Sr^{2+} lying in the perovskite with Bi^{3+} in the Bismuth oxide layers was assumed as an intrinsic source of donors providing that no direct compensation between the exchanged cations occurs.

We proposed that both models (acceptor and donor controlled) could simultaneously exist within SrBIT. Complete compensation of acceptor impurities by cation exchange without structural changes seems unreasonable. In addition, cation place exchange is probably $p\text{O}_2$ -dependent, as Sr^{2+} sitting on Bi^{3+} site in the Bismuth oxide layer would be compensated by oxygen vacancies. Thus the electro-neutrality equation could be written as acceptor-controlled in a high oxygen partial pressure range and as donor-controlled in the low-pressure range. No definite proofs of this mechanism were found during this work, however it shows that the acceptor-controlled model and the estimated band gap energy cannot simply be rejected because the donor-controlled model predicts both $p\text{O}_2^{-1/4}$ and $p\text{O}_2$ -independent regimes.

As the acceptor-controlled model assumes that the oxygen vacancy concentration is fixed by the acceptor impurity content, the ionic conductivity should be $p\text{O}_2$ -independent as long as the reduction equation does not create too much "intrinsic" oxygen vacancies. With this last assumption the ionic conductivity of SrBIT has been calculated. It was found that the ionic contribution to conductivity was very large for both undoped and 2 mol.% Mn doped SrBIT. For example, at 800°C , the transference number of SrBIT was estimated as 0.8. This demonstrated that SrBIT electrical conductivity at high temperature is mostly ionic in nature. From separate evaluation of ionic and electronic conductivities with generalized Arrhenius expressions, a transference map was built in the temperature-band gap space. This map predicts mixed conductivity of SrBIT in a wide temperature window. For example, from the model, the transference number of SrBIT at 800°C should be very close to one.

6.1.4 Piezoelectric Properties

The longitudinal piezoelectric coefficient of undoped and 2 mol.% Mn doped SrBIT has been measured in dynamic conditions as a function of elastic field amplitude, frequency and temperature. At room temperature, the absence of any dependence of the piezoelectric coefficient towards either field or frequency that has been already reported in the literature was confirmed in this work. This was interpreted as the absence of any contribution from the ferroelectric domain walls to the measured piezoelectric coefficient. The two assumptions formulated by Reaney and Damjanovic were that either non- 180° are strongly locked in deep potential wells or there are no piezoelectrically active domains in SrBIT. Our piezoelectric measurements at 150°C under higher field have demonstrated the first assumption, since thermal activation and high fields lead to non-linear piezoelectric regime was observed for SrBIT. It was demonstrated that in these conditions the hysteresis-free behavior measured under low field is replaced by a non-linear hysteresis.

For 2 mol.% Mn doped SrBIT, both positive and negative piezoelectric relaxations have been described at room temperature under low elastic field. The absence of any field dependence indicated that these mechanisms were quite different from non-linear effects induced by ferroelectric domain wall movements. A phenomenological justification for the relaxations was given with the measurement of the piezoelectric coefficient of a two-phase composite. The

composite was made of two Bismuth Titanates, the first one was a solid solution between $\text{Bi}_4\text{Ti}_3\text{O}_{12}$ (88%) and $\text{Bi}_3\text{TiNbO}_9$ (12%) and the second was a mixture of $\text{Bi}_3\text{TiNbO}_9$ (99%) and BiWO_6 (1%). This composite exhibited either a positive or a negative relaxation depending on measurement temperature and frequency. This experimentally demonstrated the possibility of both kinds of relaxations.

With composite model for the piezoelectric coefficient, the piezoelectric relaxations of our two-phase composite could be accurately predicted with separate measurements of the piezoelectric coefficients and permittivities of each phase. This gave a definite validation to the theoretical model. It was then presented how a change in either piezoelectric coefficient or permittivity of one phase could transform a positive relaxation into a negative one and vice versa.

6.2 FUTURE WORK AND OUTLOOK

As already mentioned in the conclusion of Chapter 2, different routes for SrBIT powder production could be explored as the dissolution-precipitation method. With the aid of surface energy modification, this might allow processing of isotropic SrBIT particles. It would then be interesting to compare properties (e.g. piezoelectric dispersion) of equiaxed grain microstructure with the results presented in this thesis for plate-like grains. Some unsuccessful attempts (not reported) to prepare SrBIT single crystals were made with the flux method. Better results might be achieved with either solid-state reaction, high pressure, hydrothermal or gel methods. However, in order to have a better control of the crystallization, a better knowledge of the phase diagram of SrO-Bi₂O₃-TiO₂ is required. Measurements of single crystal properties would bring additional valuable informations about Bismuth oxide and pseudo-perovskite units respective impedance. Low temperature conductivity measurements of SrBIT could be very interesting as the observed curve bending in the Arrhenius plot would be exacerbated. Such experiments could help to definitely identify polaron or grain boundary conductivity. It would also make easier the approximation of the measurements with Nafe's model. Conductivity measurements under very low oxygen partial pressure of other Aurivillius phases may reinforce the intrinsic donor-controlled model. Using Al³⁺ as an acceptor may help detecting the conductivity minimum, as no reduction/oxidation of the cation is expected for Al³⁺. The sharp conductivity observed for SBN by Palenduz was observed in some cases for SrBIT too, it is worth making more experimental work in this extreme region, as no interpretation for it is available yet. Low temperature defect chemistry should be considered also in order to properly interpret low temperature DC conductivity measurements of both donor and acceptor doped SrBIT.

In the frame of the description of piezoelectricity in ferroelectrics by Rayleigh-law, the investigation of SrBIT piezoelectric properties at elevated temperature under high field has to be continued. SrBIT behavior actually provides valuable informations about non-180° ferroelectric domain walls sitting in very deep potential wells. The simple two-phase piezoelectric model developed to account for the observed relaxations could be modified in order to simulate the effect of microstructure (colonies) on the piezoelectric response. More sophisticated microstructure models such the one used by Pitchumani [141] for his theoretical model for the anisotropic conductivity of two-phase composites could be selected as a starting point for a better description of the microstructure of SrBIT.

This work presented advantages and limitations of SrBIT for high temperature piezoelectric applications. In order to push further the upper temperature limit, other materials may be considered. These are for example non-ferroelectric materials that remove problems related to ferroelectric phase transition, non-linear piezoelectric properties and conductivity. Such materials could be AlN thin films [142] or Languasite (La₃Ga₅SiO₁₄) single crystals [143]. AlN thin films have another advantage since they should be insensitive to the oxygen partial pressure. However, investigation of Bismuth Titanate solid solutions may also bring interesting new materials for high temperature piezoelectric applications.

BIBLIOGRAPHY

- [1] M. V. Gandhi and B. S. Thompson, *Smart Materials and Structures*, Chapman & Hall, London, 1992.
- [2] P. T. Moseley and A. J. Crocker, *Sensor Materials*, Institute of Physics Publishing, Bristol, 1996.
- [3] A. J. Moulson and J. M. Herbert, *Electroceramics*, Chapman and Hall, Cambridge, 1990.
- [4] M. H. Westbrook and J. D. Turner, *Automotive Sensors*, Institute of Physics Publishing, Bristol, 1994.
- [5] W. P. Kistler, Patent (Switzerland, 1950).
- [6] C. M. Anastasia and G. W. Pestana, A Cylinder Pressure Sensor for Closed Loop Engine Control, *Society of Automotive Engineers*, 1987.
- [7] K. W. Randall and J. D. Powell, A Cylinder Pressure Sensor for Spark Advance Control and Knock Detection, *Society for Automotive Engineers*, 1979, **May**, pp. 63-65.
- [8] R. Mock and H. Meixner, A Miniaturized High-Temperature Pressure Sensor for the Combustion Chamber of a Spark-Ignition Engine, *Sensors and Actuators A*, 1991, **25-27**, pp. 103-106.
- [9] Landolt-Boernstein, *Numerical Data and Functional Relationships in Science and Technology*, Springer, Berlin, 1961.
- [10] L. A. Reznichenko, O. N. Razumovskaya, L. A. Shilkina, and N. V. Dergunova, Correlating the Curie Temperature of Mixed Bismuth Oxides to the Crystalchemical Parameters of Constituent Ions, *Inorganic Materials*, 1996, **32** (4), pp. 423-429.
- [11] H. S. Shulman, *Piezoelectric Bismuth Titanate Ceramics for High Temperature Applications*, EPFL, 1997.
- [12] D. Damjanovic, M. Demartin, H. S. Shulman, and N. Setter, Instabilities in Piezoelectric Properties of Ceramic Sensors and Actuators under Extreme Conditions, The Eighth International Conference on Solid-State Sensors and Actuators and Eurosensors IX, Stockholm, 1995.
- [13] B. Aurivillius, Mixed Bismuth Oxides with Layer Lattices I. The Structure type of $\text{CaNb}_2\text{Bi}_2\text{O}_9$, *Arkiv för Kemi*, 1949, **54** (1), pp. 463-480.
- [14] B. Aurivillius, Mixed Bismuth Oxide with Layer Lattices. II. Structure of $\text{Bi}_4\text{Ti}_3\text{O}_{12}$, *Arkiv för Kemi*, 1949, **1** (58), pp. 499-512.
- [15] B. Aurivillius, Mixed Oxides with Layer Lattices. III. Structure of $\text{BaBi}_4\text{Ti}_4\text{O}_{15}$, *Arkiv för Kemi*, 1949, **2** (37), pp. 519-527.
- [16] E. C. Subbarao, A Family of Ferroelectric Bismuth Compounds, *Journal of Physics and Chemistry of Solids*, 1962, **23**, pp. 665-676.
- [17] R. E. Newnham, R. W. Wolfe, and J. F. Dorrian, Structural Basis of Ferroelectricity in the Bismuth Titanate Family, *Material Research Society Bulletin*, 1971, **6**, pp. 1029-40.
- [18] R. A. Armstrong and R. E. Newnham, Bismuth Titanate Solid Solutions, *Materials Research Bulletin*, 1972, **7** (10), pp. 1025-1034.

- [19] I. M. Reaney, M. Roulin, H. S. Shulman, and D. Damjanovic, Characterisation of the Perovskite-Layer Structure, $\text{SrBi}_8\text{Ti}_7\text{O}_{27}$, Fourth International Conference on Electronic Ceramics & Applications, Electroceramics IV, Aachen, 1994.
- [20] C. L. Guo and Y. Q. Wu., *Acta Physica Sinica*, 1980, **29**, pp. 1491.
- [21] I. M. Reaney, M. Roulin, H. S. Shulman, and N. Setter, In Situ Observations of Octahedral Tilt Transitions in Strontium Bismuth Titanates Layered Perovskites, *Ferroelectrics*, 1995, **165**, pp. 295.
- [22] A. D. Rae, J. G. Thompson, R. L. Whitters, and A. C. Willis., *Acta Cryst. B*, 1990, **46**, pp. 474.
- [23] J. F. Dorrian, R. E. Newnham, and D. K. Smith, Crystal Structure of $\text{Bi}_4\text{Ti}_3\text{O}_{12}$, *Ferroelectrics*, 1971, **3**, pp. 17-27.
- [24] I. M. Reaney and D. Damjanovic, Crystal Structure and Domain-Wall Contributions to the Piezoelectric Properties of Strontium Bismuth Titanate Ceramics, *Journal of Applied Physics*, 1996, **80** (7), pp. 4223-4225.
- [25] A. R. James, G. S. Kumar, T. Bhimasankaram, and S. V. Suryanarayana, Studies on electrical Conduction in $\text{Bi}_4\text{SrTi}_4\text{O}_{15}$, *Bulletin of Materials Science*, 1994, **17** (6), pp. 951-958.
- [26] A. R. James, G. S. Kumar, S. V. Suryanarayana, and T. Bhimasankaram, Impedance Spectroscopic Studies in $\text{SrBi}_5\text{FeTi}_4\text{O}_{18}$, *Ferroelectrics*, 1996, **189**, pp. 81-90.
- [27] A. R. James and T. Bhimasankaram, Electrical and Magnetic Studies on $\text{SrBi}_5\text{FeTi}_4\text{O}_{18}$, *Modern Physics Letters B*, 1998, **12** (19), pp. 785-795.
- [28] A. R. James, S. Balaji, and S. B. Krupanidhi, Impedance-Fatigue Correlated Studies on $\text{SrBi}_2\text{Ta}_2\text{O}_9$, *Materials Science Engineering*, 1999, **B64**, pp. 149-156.
- [29] K. Srinivas and A. R. James, Dielectric Characterization of Polycrystalline $\text{Sr}_2\text{Bi}_4\text{Ti}_5\text{O}_{18}$, *Journal of Applied Physics*, 1999, **86** (7), pp. 3885-3889.
- [30] A. Huanosta, O. Alvarez-Fregoso, E. Amano, C. Tabares-Munoz, M. E. Mendoza-Alvarez, and J. G. Mendoza-Alvarez, AC Impedance Analysis on Crystalline Layered and Polycrystalline Bismuth Titanate, *Journal of Applied Physics*, 1991, **69** (1), pp. 404-408.
- [31] S.-K. Kim, M. Miyayama, and H. Yanagida, Complex Impedance and Modulus Analysis on Electrical Anisotropy of Layer-Structured $\text{BaBi}_4\text{Ti}_4\text{O}_{15}$ Single Crystal in Paraelectric Phase, *Journal of the Ceramic Society of Japan*, 1995, **103** (3), pp. 320-323.
- [32] T.-C. Chen, C.-L. Thio, and S. B. Desu, Impedance Spectroscopy of $\text{SrBi}_2\text{Ta}_2\text{O}_9$ and $\text{SrBi}_2\text{Nb}_2\text{O}_9$ Ceramics Correlation with Fatigue Behavior, *Journal of Material Research*, 1997, **12** (10), pp. 2628-2635.
- [33] I.-S. Yi and M. Miyayama, Electrical Anisotropies in Layer-Structured Lead Bismuth Titanate Single Crystals, *Materials Research Bulletin*, 1996, **32** (10), pp. 1349-1357.
- [34] P. S. R. Sastry, T. Bhimasankaram, G. S. Kumar, and G. Prasad, Impedance Analysis of Layer Structured NBT-CBT Mixed Ceramics, *Modern Physics Letters B*, 1998, **12** (11), pp. 433-441.
- [35] J. Daniels and K. H. Härdtl, Part I. Electrical Conductivity at High Temperature of Donor-Doped Barium Titanate Ceramics, *Philips Research Reports*, 1976, **31** (6), pp. 489-504.
- [36] J. Daniels, Part II. Defect Equilibria in Acceptor-Doped Barium Titanate, *Philips Research Reports*, 1976, **31** (6), pp. 505-15.
- [37] N.-H. Chan, R. K. Sharma, and D. M. Smyth, Nonstoichiometry in Undoped BaTiO_3 , *Journal of the American Ceramic Society*, 1981, **64** (9), pp. 556-562.

- [38] N.-H. Chan, R. K. Sharma, and D. M. Smyth, Nonstoichiometry in Acceptor-Doped BaTiO₃, *Journal of the American Ceramic Society*, 1982, **65** (3), pp. 167-70.
- [39] N. H. Chan and D. M. Smyth, Defect Chemistry of Donor-Doped BaTiO₃, *Journal of the American Ceramic Society*, 1984, **67** (4), pp. 285-8.
- [40] C. A. Palanduz and D. M. Smyth, The Effect of Cation Place Exchange on the Electrical Conductivity of SrBi₂M₂O₉ (M=Ta, Nb), *Journal of the European Ceramic Society*, 1998, **19** (6-7), pp. 731-735.
- [41] E. C. Subbarao, Ferroelectricity in Mixed Bismuth Oxides with Layer-Type Structure, *Journal of Chemistry and Physics. Letters to the Editor*, 1960, **34**, pp. 695-696.
- [42] J. H. Cho, G. W. Lee, S. J. Kim, and Y. S. Yang, Dielectric Properties of SrBi₄Ti₄O₁₅ Glass, *Journal of the Korean Physical Society*, 1998, **32** (S343-345), pp.
- [43] K. Yamamuro, M. Tachiki, and T. Kobayashi, Pt/SrBi₄Ti₄O₁₅/Si-MOS System : Preliminary Study Employing an Inverted MOS Configuration, *Material Science and Engineering*, 1996, **B41**, pp. 174-177.
- [44] L. Nibou, A. Aftati, M. E. Farissi, and J.-P. Mercurio, Chemical Fabrication SrBi₄Ti₄O₁₅ Thin Films, *Journal of the European Ceramic Society*, 1999, **19** (6-7), pp. 1383-1386.
- [45] M. V. Gelfuso, D. Thomazini, and J. A. Eiras, Synthesis and Structural, Ferroelectric, and Piezoelectric Properties of SrBi₄Ti₄O₁₅, *Journal of the American Ceramic Society*, 1999, **82** (9), pp. 2368-2372.
- [46] Powder Diffraction File, edited by I. C. f. D. Data, Newtown Square, USA, 1998.
- [47] Phase Diagrams for Ceramist, edited by E. M. Levin, C. R. Robbins, and H. F. McMurdie, 1964.
- [48] T. Kato, ESR Spectrum and Thermal Expansion of Grain Oriented Bi₄Ti₃O₁₂ Ceramics, *Japanese Journal of Applied Physics*, 1983, **22**, pp. 47-49.
- [49] S.-I. Osawa, A. Furuzawa, and N. Fujikawa, Effect of the Manganese Valence State on the Electrical Conductivity of Barium Titanate, *Journal of the American Ceramic Society*, 1993, **76** (5), pp. 1191-1194.
- [50] T. Takenaka and K. Sakata, Grain Orientation and Electrical Properties of Hot-Forged Bi₄Ti₃O₁₂ Ceramics, *Japanese Journal of Applied Physics*, 1980, **19** (1), pp. 31-9.
- [51] T. Takenaka and K. Sakata, Electrical Properties of Grain-Oriented Ferroelectric Ceramics in some Lanthanum Modified Layer-Structure Oxides, *Ferroelectrics*, 1981, **38**, pp. 769-772.
- [52] T. Takenaka and K. Sakata, Pyroelectric Properties of Grain-Oriented Bismuth Layer-Structured Ferroelectric Ceramics, *Japanese Journal of Applied Physics*, 1983, **22**, pp. 53-56.
- [53] T. Takenaka, K. Sakata, and K. Toda, Surface Acoustic Wave Characteristics of Grain-Oriented Bismuth Layer-Structured Ferroelectric Ceramics, 4th Symposium on Ultrasonics Electronics, Tokyo, 1983, *Japanese Journal of Applied Physics*, pp. 153-155.
- [54] T. Takenaka and K. Sakata, Grain Orientation Effects on Electrical Properties of Bismuth Layer-Structured Ferroelectric Pb_(1-x)(NaCe)_{x/2}Bi₄Ti₄O₁₅ solid solution, *Journal of Applied Physics*, 1984, **55** (4), pp. 1092-1099.
- [55] T. Takenaka, K. Sakata, and K. Toda, Piezoelectric Properties of Bismuth Layer-Structured Ferroelectric Na_{0.5}Bi_{4.5}Ti₄O₁₅ Ceramic, Sixth International Meeting on Ferroelectricity, Kobe, 1985, *Japanese Journal of Applied Physics*, pp. 730-732.
- [56] T. Takenaka and K. Sakata, Compositions and Electrical Properties of Complex Bismuth Layer-Structured Ferroelectric Ceramics, Fifth Meeting on Ferroelectric Materials and Their Applications, Kyoto, 1985, *Japanese Journal of Applied Physics*, pp. 117-119.

- [57] T. Takenaka and K. Sakata, Grain-Oriented and Mn-Doped $(\text{NaBi})_{(1-x)/2}\text{Ca}_x\text{Bi}_4\text{Ti}_4\text{O}_{15}$ Ceramics for Piezo- and Pyrosensor Materials, *Sensors and Materials*, 1988, **1**, pp. 35-46.
- [58] T. Takenaka, A. S. Bhalla, and L. E. Cross, Dielectric, Piezoelectric and Pyroelectric Properties of Lead Zirconate-Lead Zinc Niobate Ceramics, *Journal of the American Ceramic Society*, 1989, **72** (6), pp. 1016-1023.
- [59] J. Fousek and B. Brezina, Relaxation of 90° Domain Walls of BaTiO_3 and Their Equation of Motion, *Journal of the Physical Society of Japan*, 1964, **19** (6), pp. 830-838.
- [60] O. A. Tikhomirov, Vibrations of Domain Walls in AC Field and the Low Frequency Permittivity of Ferroelectrics, *Ferroelectrics*, 1997, **190**, pp. 37-42.
- [61] A. K. Jonsher, Dielectric Relaxation in Solids, *Journal of Physics D*, 1999, **32**, pp. 57-70.
- [62] J. R. Macdonald, Impedance Analysis, Emphasizing Solid Materials and Systems, Vol. 1, John Wiley & Sons, Inc., New York, 1987.
- [63] A. K. Jonsher, Dielectric Relaxations in Solids, Chelsea Dielectrics Press Ltd, London, 1983.
- [64] R. Waser, Bulk Conductivity and Defect Chemistry of Acceptor-Doped Strontium Titanate in the Quenched State, *Journal of the American Ceramic Society*, 1991, **74** (8), pp. 1934-1940.
- [65] R. Waser and M. Klee, in *Integrated Ferroelectrics; Vol. 2*, Gordon and Breach Science Publishers., 1992, p. 23-40.
- [66] R. Waser, The Role of Grain Boundaries in Conduction and Breakdown of Perovskite-Type Titanates, *Ferroelectrics*, 1992, **133**, pp. 109-114.
- [67] M. Vollmann and R. Waser, Impedance Characterization of Grain Boundary Doped SrTiO_3 , *Electroceramics IV*, Aachen, 1994.
- [68] M. Vollmann and R. Waser, Grain Boundary Defect Chemistry of Acceptor-Doped Titanates: Space Charge Layer Width, *Journal of the American Ceramic Society*, 1994, **77** (1), pp. 235-243.
- [69] M. Vollmann and R. Waser, Grain Boundary Defect Chemistry of Acceptor-Doped Titanates: High field Effects, *Journal of Electroceramics*, 1997, **1** (1), pp. 51-64.
- [70] H. Näfe, Ionic Conductivity of ThO_2 and ZrO_2 Based Electrolytes Between 300 and 2000 K, *Solid State Ionics*, 1984, **13**, pp. 255-263.
- [71] F. Alvarez, A. Alegria, and J. Colmenero, Interconnection between Frequency-Domain Havriliak-Negami and Time-Domain Kohlrausch-Williams-Watts Relaxation functions, *Physical Review B*, 1993, **47** (1), pp. 125-130.
- [72] J. C. Wang and J. B. Bates, Non-Debye Dielectric Response and Distribution of Activation Energies, *Solid State Ionics*, 1992, **50**, pp. 75-86.
- [73] C. Leon, J. Santamaria, M. A. Paris, J. Sanz, J. Ibarra, and A. Varez, Non-Debye Conductivity Relaxation in the Non-Arrhenius $\text{Li}_{0.5}\text{La}_{0.5}\text{TiO}_3$ Fast Ionic Conductor. A Nuclear Magnetic Resonance and Complex Impedance Study, *Journal of Non-Crystalline Solids*, 1998, **235-237**, pp. 753-760.
- [74] H. Q. Fan, L. T. Zhang, L. Y. Zhang, and X. Yao, Non-Debye Relaxation and the Glassy Behavior of Disordered Perovskite Ferroelectrics, *Solid State Communications*, 1999, **111**, pp. 541-546.
- [75] E. Iguchi, N. Kubota, T. Nakamori, N. Yamamoto, and K. J. Lee, Polaronic conduction in n-type BaTiO_3 doped with La_2O_3 or Gd_2O_3 , *Physical Review B*, 1991, **43** (10), pp. 8646-8649.
- [76] P. A. Cox, Transition Metal Oxides: an Introduction to their Electronic Structure and Properties, Vol. 27, Oxford University Press, Oxford, 1995.

- [77] T. P. Myasnikova, S. G. Gakh, and V. N. Shalaev, Studies of Layered Bismuth Titanate by Methods, *Crystallography Reports*, 1998, **43** (3), pp. 463-464.
- [78] C. Jovalekic, M. Pavlovic, P. Osmokrovic, and L. Atanasoska, X-ray Photoelectron Spectroscopy Study of $\text{Bi}_4\text{Ti}_3\text{O}_{12}$ Ferroelectric Ceramics, *Applied Physics Letters*, 1998, **72** (9), pp. 1051-1053.
- [79] K. Sasaki and J. Maier, Low Temperature Defect Chemistry of Oxides, *Journal of the European Ceramic Society*, 1999, **19** (6-7), pp. 741-745.
- [80] A. K. Jonsher, Universal Relaxation Law, Chelsea Dielectrics Press, London, 1996.
- [81] M. Kleitz, H. Bernard, E. Fernandez, and E. Schouler, in *Advances in Ceramics, Science and Technology of Zirconia; Vol. 3*,, 1981.
- [82] S.-K. Kim, M. Miyayama, and H. Yanagida, Electrical Anisotropy of $\text{BaBi}_4\text{Ti}_4\text{O}_{15}$ single Crystal, *Journal of the Ceramic Society of Japan*, 1994, **102** (8), pp. 719-723.
- [83] R. J. Young and P. A. Lovell, Introduction to Polymers, Chapman & Hall, London, 1991.
- [84] H. Ihrig, On the Polaron Nature of the Charge Transport in BaTiO_3 , *Journal Physics C : Solid State Physics*, 1975, **9**, pp. 3469-3474.
- [85] G. V. Bois, N. A. Mikhailova, E. I. Prodastova, and V. A. Yusova, Partial Pressure of Oxygen, and Oxygen Vacancies in BaTiO_3 , *Translated from Izvestiya Akademii Nauk SSSR, Neorganicheskie Materialy*, 1976, **12** (9), pp. 1588-1591.
- [86] D. Hennings, Part III. Thermogravimetric Investigations, *Philips Research Reports*, 1976, **31** (6), pp. 516-25.
- [87] R. Wernicke, Part IV. The Kinetics of Equilibrium Restoration in Barium Titanate Ceramics, *Philips Research Reports*, 1976, **31** (6), pp. 526-43.
- [88] N. G. Eror and D. M. Smyth, Nonstoichiometric Disorder in Single-Crystalline BaTiO_3 , *Journal of Solid State Chemistry*, 1978, **24**, pp. 235-244.
- [89] S. B. Desu and E. C. Subbarao, in *Advances in Ceramics; Vol. 1*, edited by L. M. Levinson and D. C. Hill, The American Ceramic Society, Chicago, 1981, p. 189-206.
- [90] D. M. Smyth, The Role of impurities in Insulating Transition Metal Oxides, *Progress in Solid State Chemistry*, 1984, **15**, pp. 145-71.
- [91] H. M. Chan, M. P. Harmer, and D. M. Smyth, Compensating Defects in Highly Donor-Doped BaTiO_3 , *Journal of the American Ceramic Society*, 1986, **69** (6), pp. 507-10.
- [92] Y. H. Han, J. B. Appleby, and D. M. Smyth, Calcium as an Acceptor Impurity in BaTiO_3 , *Journal of the American Ceramic Society*, 1987, **70** (2), pp. 96-100.
- [93] X. W. Zhang, Y. H. Han, M. Lal, and D. M. Smyth, Defect Chemistry of BaTiO_3 with Additions of CaTiO_3 , *Journal of the American Ceramic Society*, 1987, **70** (2), pp. 100-3.
- [94] V. Bheemineni, E. K. Chang, M. Lal, M. P. Harmer, and D. M. Smyth, Suppression of Acceptor Solubilities in BaTiO_3 Densified in Highly Reducing Atmospheres, *Journal of the American Ceramic Society*, 1994, **77** (12), pp. 3173-3176.
- [95] C. Gillot and J. P. Michenaud, Electrical Conductivity of Similarly Doped BaTiO_3 Single Crystals and Ceramics in the Rhombohedral Phase, *Solid State Communications*, 1994, **90** (1), pp. 23-25.
- [96] W. L. Warren, D. Dimos, and B. A. Tuttle, Electronic and Ionic Trapping at Domain Walls in BaTiO_3 ,, 1994, **77** (10), pp. 2753-57.
- [97] J. Kim, R. Roseman, and R. C. Buchanan, Microstructural Effects on Conductivity in Donor Doped BaTiO_3 , *Ferroelectrics*, 1996, **177** (3-4), pp. 255-271.
- [98] D. Kolar, Phase Equilibria and Dielectric Properties of Rare Earth Containing BaTiO_3 Ceramics, *Solid-State Chemistry of Inorganic Materials*, Boston, 1996, Material Research Society, pp. 425-435.

- [99] A. C. Caballero, J. F. Fernandez, C. Moure, P. Duran, and J. L. G. Fierro, Dopant Distribution and Grain Growth Control in BaTiO₃ Ceramics Doped with ZnO-SiO₂-P₂O₅, *Journal of the European Ceramic Society*, 1997, **17**, pp. 1223-1230.
- [100] A. C. Caballero, J. F. Fernandez, C. Moure, P. Duran, and J. L. G. Fierro, Dopant Distribution and Grain Growth Control in BaTiO₃ Ceramics Doped with ZnO-SiO₂-P₂O₅, *Journal of the European Ceramic Society*, 1997, **17** (10), pp. 1223-1230.
- [101] J.-Y. Kim, C.-R. Song, and H.-I. Yoo, Mn-doped BaTiO₃ : Electrical Transport Properties in Equilibrium State, *Journal of Electroceramics*, 1997, **1** (1), pp. 27-39.
- [102] E. K. Chang, A. Mehta, and D. M. Smyth, Ionic Transport Numbers from Equilibrium Conductivities, Symposium on Electro-Ceramics and Solid-State ionics, Honolulu, Hawaii, 1987, The Electrochemical Society, pp. 35-45.
- [103] F. A. Kröger, Imperfection Chemistry of Crystalline Solids, Vol. 2, North-Holland Publishing Company, 1974.
- [104] Electrical Conductivity in Ceramics and Glass; *Vol. 4*, edited by N. M. Tallan, Marcel Dekker Inc., New York, 1974.
- [105] W. D. Kingery, H. K. Bowen, and D. R. Uhlmann, Introduction to Ceramics, Wiley-Interscience, 1976.
- [106] M. J. Akhtar, Z.-U. Akhtar, R. A. Jackson, and C. R. A. Catlow, Computer Simulation Studies of Strontium Titanate, *Journal of the American Ceramic Society*, 1995, **78** (2), pp. 421-428.
- [107] D. Hennings and K. H. Härdtl, Distribution of Vacancies in Lanthan-Doped Lead Titanate, *Phys. Status Solidi A*, 1970, **3** (2), pp. 465-474.
- [108] K. H. Härdtl, Defect Structure of PLZT Doped with Mn, Fe and Al, *Journal of the American Ceramic Society*, 1981, **64** (5), pp. 283-288.
- [109] D. M. Smyth, The Influence of Defect on the Electrical Properties of Perovskite-Related Materials, *Ferroelectrics*, 1992, **133**, pp. 13.
- [110] M. Fleischer and H. Meixner, Hole Mobility in Acceptor-Doped, Monocrystalline SrTiO₃, *Journal of the American Ceramic Society*, 1992, **75** (6), pp. 1666-1668.
- [111] M. V. Raymond and D. M. Smyth, in *Science and Technology of Electroceramics Thin Films*, edited by O. Auciello and R. Waser, Kluwer Academic Publishers, 1995, p. 315-25.
- [112] N. I. Medvedeva and V. A. Gubanov, Electronic Structure and Properties of Aurivillius Phases, *Journal of Structural Chemistry*, 1996, **37** (3), pp. 409-416.
- [113] P. A. Cox, Transition Metal Oxides, Vol. 27, Oxford University Press, Oxford, 1995.
- [114] O. Porat, Simplified Analytical Treatment of Defect Equilibria : Applications to Oxides with Multivalent Dopants, *Journal of Electroceramics*, 1997, **1** (1), pp. 41-9.
- [115] R. Moos and K. H. Härdtl, Defect Chemistry of Donor-Doped and Undoped Strontium Titanate Ceramics between 1000°C and 1400°C, *Journal of the American Ceramic Society*, 1997, **80** (10), pp. 2549-2562.
- [116] J. Fouletier, Gas Analysis with Potentiometric Sensors. A Review, *Sensors and Actuators*, 1982, **3**, pp. 295-314.
- [117] D. M. Haaland, Noncatalytic Electrodes for Solid-Electrolyte Oxygen Sensors, *Journal of the Electrochemical Society*, 1980, **127**, pp. 796-804.
- [118] E. K. Chang, A. Mehta, and D. M. Smyth, Ionic Transport Numbers from Equilibrium Conductivities, Symposium ElectroCeramics and Solid State ionics, 1988.
- [119] D. M. Smyth, Defect Structure in Perovskite Titanates, *Current Opinion in Solid State & Materials Science*, 1996, **1**, pp. 692-697.

-
- [120] R. Moos, Donatordotierungen im Strontiumtitanat: Elektrische Eigenschaften und modellhafte Beschreibung, Keramikverbundes Karlsruhe-Stuttgart, 1994.
- [121] S. B. Desu and E. C. Subbarao, Effect of Oxidation States of Mn on the Phase Stability of Mn-Doped BaTiO₃, *Ferroelectrics*, 1981, **37** (1-4), pp. 665-668.
- [122] S. B. Desu and E. C. Subbarao, Inhibition of Reduction of BaTiO₃, *Journal of Materials Science Letters*, 1980, **15**, pp. 2113-2115.
- [123] H. L. Tuller, in *Nonstoichiometric Oxides*, edited by O. T. Sørensen, Academic Press Inc., New York, 1981.
- [124] J. A. Kilner and B. C. H. Steele, in *Nonstoichiometric Oxides*, edited by O. T. Sørensen, Academic Press Inc., New York, 1981.
- [125] D. Damjanovic, M. Demartin, H. S. Shulman, M. Testorf, and N. Setter, Instabilities in the Piezoelectric Properties of Ferroelectric Ceramics, *Sensors and Actuators*, 1996, **A53**, pp. 353-360.
- [126] J. F. Nye, Physical Properties of Crystals, Their Representation by Tensors and Matrices, Oxford University Press,, 1990.
- [127] L. E. Cross, in *Ferroelectric Ceramics*, edited by N. Setter and E. L. Colla, Birkhäuser Verlag, Basel, 1993.
- [128] D. Damjanovic, Ferroelectric, Dielectric and Piezoelectric Properties of Ferroelectric Thin Films and Ceramics, *Reports on Progress in Physics*, 1998, **61**, pp. 1267-1324.
- [129] D. Damjanovic and M. Demartin, The Rayleigh Law in Piezoelectric Ceramics, *Journal of Physics D*, 1996, **29** (7), pp. 2057-2060.
- [130] B. Jaffe, W. R. Cook, and H. Jaffe, Piezoelectric Ceramics, Vol. 3, Academic Press Inc., New York, 1971.
- [131] L. Rayleigh, *Philos. Mag.*, 1887, **23**, pp. 225.
- [132] D. Damjanovic and M. Demartin, Contribution of the Irreversible displacement of Domain Walls to the Piezoelectric Effect in Barium Titanate and Lead Zirconate Titanate Ceramics, *Journal of Physics-Condensed Matter*, 1997, **9** (23), pp. 2057-2060.
- [133] K. Hamano and T. Yamaguchi, Piezoelectric Relaxation in Ferroelectrics and Polymers, *Ferroelectrics*, 1982, **42**, pp. 23-33.
- [134] O. A. Tikhomirov and B. S. Red'kin, Direct Optical Investigation of the Domain Wall Oscillations in AC Field, *Ferroelectrics*, 1996, **189**, pp. 73-80.
- [135] T. Furukawa, K. Fujino, and E. Fukada,, *Japanese Journal of Applied Physics*, 1976, **15**, pp. 2119.
- [136] T. Furukawa and E. Fukada, Piezoelectric Relaxation in Composite Epoxy-PZT System Due to Ionic Conduction, *Japanese Journal of Applied Physics*, 1977, **16** (3), pp. 453-458.
- [137] T. Furukawa, K. Ishida, and E. Fukada, Piezoelectric Properties in the Composite Systems of Polymer and PZT Ceramics, *Journal of Applied Physics*, 1979, **50** (7), pp. 4904-4912.
- [138] T. Furukawa and E. Fukada, Piezoelectric Relaxation in Poly(γ -benzyl-glutamate), *Journal of Polymer Science*, 1979, **14**, pp. 1979-2010.
- [139] G. S. Kumar and G. Prasad, Piezoelectric Relaxation in Polymer and Ferroelectric Composites, *Journal of Materials Science*, 1993, **28**, pp. 2545-2550.
- [140] R. E. Newnham, D. P. Skinner, and L. E. Cross, Connectivity and Piezoelectric-Piezoelectric Composites, *Materials Research Bulletin*, 1978, **13**, pp. 525-536.

- [141] R. Pitchumani, P. K. Liaw, S. C. Yao, D. K. Hsu, and H. Jeong, Theoretical Models for the Anisotropic Conductivities of Two-Phase and Three-Phase Metal-Matrix Composites, *Acta Metall. Mater.*, 1995, **43** (8), pp. 3045-3049.
- [142] M.-A. Dubois and P. Muralt, Properties of Aluminium Nitride Thin Films for Piezoelectric Transducers and Microwave Filter Applications, *Applied Physics Letters*, 1999, **74** (20), pp. 3032-3034.
- [143] D. Damjanovic, Materials for High Temperature Piezoelectric Transducers, *Current Opinion in Solid State & Materials Science*, 1998, **3** (5), pp. 469-473.

FIGURE CAPTION

- Figure 1-1: crystal structure of $\text{BaBi}_4\text{Ti}_4\text{O}_{15}$ high temperature tetragonal phase..... 17
- Figure 2-1: schematic view of the ceramic stack used for dilatometry. The SrBIT sample is placed between two buffering sintered SrBIT discs and two insulating SrTiO_3 discs. The measuring and reference Alumina probes are also shown..... 25
- Figure 2-2: Bismuth oxide used for SrBIT preparation..... 27
- Figure 2-3: Titanium oxide used for SrBIT preparation..... 27
- Figure 2-4: Strontium carbonate used for SrBIT preparation..... 28
- Figure 2-5: Temperature profile used for a "one step" SrBIT synthesis from Bi_2O_3 , TiO_2 and SrCO_3 raw powders. 28
- Figure 2-6: Particle size distribution for undoped SrBIT calcined in three steps (950, 1000, 1050°C, 4 hours each) and ball milled for 72 hours in isopropanol..... 29
- Figure 2-7: example of a typical fired microstructure for undoped SrBIT, indicating the possibility of a liquid phase. 29
- Figure 2-8: expansion and expansion rate versus temperature for $\text{SrCO}_3+2\text{Bi}_2\text{O}_3+4\text{TiO}_2$ powder mixture. 34
- Figure 2-9: x-ray diffraction spectrums after calcination of raw materials at elevated temperature: (a) 14-20° region showing an intermediate $\text{Bi}_4\text{Ti}_3\text{O}_{12}$ (BIT phase ((060) line) replaced by the final $\text{SrBi}_4\text{Ti}_4\text{O}_{15}$ (SrBIT) composition ((008) line). (b) 24-29.5° region indicating some solid solution between SrO and Bi_2O_3 ((101), (012) and (104) lines for a $(\text{SrO})_{0.40}-(\text{Bi}_2\text{O}_3)_{0.60}$ solution) that disappears above 800°C and some cubic $\text{Bi}_{12}\text{TiO}_{20}$ intermediate phase ((220) line as indicated and also (310) at 27.7° as for (117) SrBIT line). (c) 33-35° region showing the intermediate cubic SrTiO_3 phase ((110) line) and the solid solution between SrO and Bi_2O_3 ((107) line). Large diffraction peaks close to 33° are not identified for clarity. 35
- Figure 2-10: Temperature profile used for green bodies sintering. The cooling part of the profile was not controlled (free cooling)..... 37
- Figure 2-11: shrinkage and shrinkage rate for undoped SrBIT at 5°C/min..... 38
- Figure 2-12: shrinkage and temperature versus time during the second heating/cooling cycle of dilatometer experiment. 39
- Figure 2-13: X-ray diffraction spectrum of SrBIT sintered at the optimized temperature (gray line) and 10°C above (black line). The shoulder on the left of $\text{SrBi}_4\text{Ti}_4\text{O}_{15}$ diffraction peak is a good indication of $\text{Sr}_2\text{Bi}_4\text{Ti}_5\text{O}_{18}$ formation and incongruent melting of $\text{SrBi}_4\text{Ti}_4\text{O}_{15}$ 39
- Figure 2-14: fracture surface by SEM for SrBIT sintered at 1230°C, 4 minutes with a heating rate of 5°C/min..... 40
- Figure 2-15: fracture surface by SEM for SrBIT sintered at 1270°C, 4 minutes with a heating rate of 5°C/min..... 41
- Figure 2-16: fracture surface by SEM for SrBIT sintered at 1285°C, 4 minutes with a heating rate of 5°C/min..... 41

Figure 2-17: open (filled circles) and closed (open circles) porosities versus sintering temperature for one sintering in air of undoped SrBIT.....	42
Figure 2-18: microstructure of undoped SrBIT fired at 1250°C for 12 minutes. Arrows indicate localized preferential orientations defining grains colonies.	43
Figure 2-19: microstructure of SrBIT sintered 11°C above the usual firing temperature, but still below decomposition temperature, showing grain coarsening.	44
Figure 2-20: cell parameters versus Mn concentration for sintered SrBIT ceramic measured at room temperature.....	46
Figure 2-21: a over b orthorhombicity ratio versus Mn concentration.....	46
Figure 2-22: microstructure of 1.5 mol.% Mn doped SrBIT fired at 1250°C for 12 minutes.....	47
Figure 2-23: microstructure of 4 mol.% Niobium doped SrBIT fired at 1250°C for 12 minutes..	48
Figure 2-24: temperature and uniaxial force profile used for SrBIT hot forging. The pre-firing process was made at 1100°C for one hour without any applied force and the forging process was done at the same temperature but with a 300 N longitudinal applied force for 5 hours.	49
Figure 2-25: hot forging system employed for textured material preparation.....	50
Figure 2-26: comparison between undoped random SrBIT and undoped Mn or Nb doped c oriented hot forged XRD patterns.	51
Figure 3-1: Example of a charge-discharge curve used for DC conductivity measurement. Open circles are charging current and filled circles are discharging current. The two curves can be fitted with a power law ($At^{-n} + B$) with $n \approx 1.2$	61
Figure 3-2: idealized bricklayer microstructure. The grains (cubes of size D) are mono-dispersed one separated by the same length in every direction (grain boundary thickness d).	62
Figure 3-3: electrical equivalent circuit made of two RC elements consisting of one resistor and one capacitor in parallel.....	62
Figure 3-4: Schematic interpretation of the charging current in the frame of the serial model.....	63
Figure 3-5: charging current measured at 120°C for undoped SrBIT using the electrometer with different electrical fields. In this measurement the A/D conversion was made within the electrometer.	65
Figure 3-6: charging current versus time for grounded resistor (1 kΩ) measurement for undoped SrBIT at room temperature.	66
Figure 3-7: charge versus time under 4 V DC voltage for undoped SrBIT at room temperature. Measurement was made in two steps; therefore charge level is different for the measurements.	67
Figure 3-8: current versus time calculated from charge measurement of undoped SrBIT at room temperature.....	67
Figure 3-9: admittance versus frequency for undoped SrBIT at room temperature, 560 and 1000°C.	68
Figure 3-10: Electrical DC conductivity of undoped SrBIT between 180°C and 220°C measured in air after oxygen annealing.....	69
Figure 3-11: charging current for undoped SrBIT at 120°C (sold line) approximated with an exponential (Debye-type relaxation) and stretched exponential.....	71
Figure 3-12: electrical conductivity of undoped random oriented SrBIT (filled circles) versus reciprocal temperature together with Nāfe model (dashed line). Grain and grain boundary conductivities were calculated with parameters obtained from the approximation.....	72

Figure 3-13: electrical conductivity versus temperature of, ab plane and c oriented undoped SrBIT.	75
Figure 3-14: conductivity of undoped SrBIT at high temperature measured in the c direction (filled circles) and in the ab direction (open circles) from low frequency extrapolated AC measurements.....	75
Figure 3-15: electrical conductivity of undoped SrBIT measured in the ab plane direction (open circles) and c direction (filled circles) with DC method (low temperature range) and low frequency extrapolation of AC method (higher temperature range).	76
Figure 3-16: dielectric permittivity calculated from C_p measurements for undoped SrBIT measured in the ab plane direction (filled circles) and c direction (open circles)....	77
Figure 3-17: longitudinal piezoelectric coefficient versus applied stress (AC field) of undoped SrBIT at room temperature at 1Hz in the ab plane and c direction. Poling was performed along measured direction.	77
Figure 3-18: DC conductivity measured at 220°C versus Mn concentration.	78
Figure 3-19: schematic of typical conductivity versus oxygen partial pressure curves for undoped, slightly Mn doped and heavily Mn doped SrBIT as determined in Chapter 4.	79
Figure 3-20: DC electrical conductivity versus reciprocal temperature for 2 mol.% Mn doped SrBIT.	80
Figure 3-21: DC conductivity measured at 220°C (filled circles) versus doping concentration for Nb doped SrBIT in the as sintered state and power law curve fitting (solid line). ..	81
Figure 3-22: DC conductivity for Nb doped SrBIT at 220°C in the as sintered state (filled circles) and after annealing in reducing atmosphere (Ar) for 15 hours at 800°C (open circles).....	82
Figure 3-23: impedance in the complex plane in the case of a depressed semicircle corresponding to a simple R-C circuit made of one resistance R_0 and one capacitance C_0 in parallel.	87
Figure 3-24: illustration of the impedance calculated with the Havriliak-Negami equation with arbitrary parameters.	88
Figure 3-25: impedance in the complex plane of a system consisting of two parallel R-C element in series. This is a simulation calculated with $R_1=R_2=1\text{ M}\Omega$ and $C_1=10\text{ pF}$, $C_2=1\text{ nF}$	89
Figure 3-26: simulated impedance (left) and modulus (right) for a double RC circuit with following parameters: $R_1=1\text{ M}\Omega$, $C_1=10\text{ pF}$, $R_2=20\text{ k}\Omega$ and $C_2=5.7\text{ pF}$ according to Kim's analysis of $\text{BaBi}_4\text{Ti}_4\text{O}_{15}$ [31].	90
Figure 3-27: measured reactance at 600°C (filled circles) and curve fitting (solid and dashed lines) for undoped SrBIT using one, two or three RC- elements as indicated.....	94
Figure 3-28: curve fitting of the impedance results (filled circles) in the complex plane for undoped SrBIT random at 600°C with one, two or three RC components.	95
Figure 3-29: curve fitting of the impedance results (filled circles) in the complex plane for undoped SrBIT random at 600°C with distributed elements.	95
Figure 3-30: associated resistance for single distributed element (Havriliak-Negami) for undoped SrBIT ceramics from 450°C up 650°C.....	97
Figure 3-31: comparison between low temperature DC measurements and high temperature AC calculations for undoped SrBIT ceramics.....	97
Figure 3-32: associated capacity for single Havriliak-Negami element for undoped SrBIT ceramics from 400°C up to 650°C.	98

Figure 3-33: dielectric permittivity as a function of temperature for undoped SrBIT at 1 MHz. This figure can be compared with data in Figure 3-32 determined from Havriliak-Negami equations.	98
Figure 3-34: Havriliak-Negami exponents α (open circles) and β (filled circles) for a single distributed element model for undoped SrBIT from 450°C up to 650°C.....	99
Figure 3-35: calculated resistance associated with each of the three RC components for undoped SrBIT ceramics.....	100
Figure 3-36: calculated capacitance associated with each of the three RC components for undoped SrBIT ceramics.....	101
Figure 3-37: relaxation frequencies versus temperature calculated from fitted R and C values for undoped SrBIT random oriented for three RC components.	102
Figure 3-38: electric modulus for hot forged undoped SrBIT measured in the ab direction at 300°C, 400°C and 500°C.....	103
Figure 3-39: measured (filled circles) and simulated (open circles) impedance (left) and modulus (right) functions for undoped SrBIT in the ab direction at 400°C.	104
Figure 3-40: electrical modulus in the complex plane for undoped SrBIT at 500°C.....	104
Figure 3-41: measured modulus for undoped SrBIT measured in the c direction at 500°C.	105
Figure 3-42: imaginary part of the modulus versus frequency at different temperature for undoped SrBIT ceramic.	106
Figure 3-43: Shift factors measured on the imaginary part of the modulus plot of undoped SrBIT and fitting with a WLF expression (dotted line).	107
Figure 3-44: imaginary part of the impedance (diamond-shaped) and modulus (triangles) versus frequency for undoped SrBIT at 500°C.....	107
Figure 3-45: imaginary part of the modulus versus frequency at different temperature for undoped ab oriented SrBIT ceramic between 200°C and 500°C.	108
Figure 3-46: imaginary part of the modulus versus frequency at different temperature for undoped ab oriented SrBIT ceramic between 500°C and 1000°C.	108
Figure 3-47: Shift factor for the electrical modulus for undoped SrBIT ab oriented.....	109
Figure 3-48: calculated master for undoped SrBIT in the ab direction at 200°C.	109
Figure 3-49: modulus master curves built at 500°C with impedance measurements in the ab direction of hot forged samples between 200°C and 1000°C for undoped (top left), 2 mol.% Mn doped (top right) and 4 mol.% Nb doped (bottom left) SrBIT.	110
Figure 3-50: modulus master curves built at 500°C with impedance measurements in the ab direction of hot forged samples between 200°C and 1000°C for undoped (top left), 2 mol.% Mn doped (top right) and 4 mol.% Nb doped (bottom left) SrBIT.	113
Figure 3-51: electrical impedance in the complex plane (filled circles) of 2 mol.% Mn doped SrBIT at 600°C together with single RC (dotted line), triple RC (solid line) and Havriliak-Negami fittings (dashed line).	114
Figure 3-52: resistance versus temperature for three RC model for Mn doped SrBIT.....	115
Figure 3-53: capacity versus temperature calculated for three RC model for Mn doped SrBIT.	115
Figure 3-54: relaxation frequency versus temperature calculated for three RC model for Mn doped SrBIT.	116
Figure 3-55: SEM micrograph of large grain SrBIT used for impedance analysis.....	117
Figure 3-56: three components to the electrical impedance for small grain (filled items) and large grains (empty items) undoped SrBIT. Triangles, circles and squares are first, second and third relaxations respectively.....	117

- Figure 3-57: grain to grain boundary conductivity versus temperature for both large and small grains undoped SrBIT. 118
- Figure 3-58: real and imaginary part of the impedance versus frequency measured at 650°C under 150 sccm flowing Ar after 10, 20, 50, 95 minutes as indicated on the graph. 119
- Figure 3-59: oxygen partial pressure transient at 650°C under 150 sccm flowing Ar. 120
- Figure 3-60: first and second calculated resistances using a three RC model versus time for Mn doped SrBIT at 650°C under 150sccm flowing Ar. 120
- Figure 3-61: second and third calculated resistances using a three RC model versus time for Mn doped SrBIT at 650°C under 150 sccm flowing Ar. 121
- Figure 3-62: normalized resistances (marks) versus time together with the fitted diffusion law (solid lines). 122
- Figure 4-1: general view of the high temperature set-up used for electrical conductivity measurements under oxygen partial pressure. Both discs and bars can be used as samples. Close to the oxygen sensor, one ZrO₂ oxygen electrolytic pump was placed. 135
- Figure 4-2: thin sputtered Pt electrode after high temperature annealing in CO/CO₂. 137
- Figure 4-3: thick Platinum coating used as electrode, (a) after high temperature annealing in CO/CO₂, (b) after oxygen re-oxidation annealing. 138
- Figure 4-4: equilibrium oxygen partial pressure versus O₂ to Ar flows ratio at 1000°C. The oxygen partial pressure established for pure flowing Ar was $4 \cdot 10^{-5}$ atm in that case. 138
- Figure 4-5: equilibrium oxygen partial pressure versus D_{CO} to D_{CO₂} flows ratio. Filled circles are measurements at 900°C and open circles are thermodynamical calculation at 1200 K. 139
- Figure 4-6: equilibrium oxygen partial pressure versus applied DC current at 800°C with CO/CO₂=0.1/100. 140
- Figure 4-7: oxygen partial pressure and conductivity transients at 800°C. 141
- Figure 4-8: electrical conductivity of BaTiO₃ at high temperature under controlled oxygen partial pressure (Ar-O₂ range). Filled circles are measurements and open circles are taken from literature [37]. 144
- Figure 4-9: electrical conductivity versus oxygen partial pressure for undoped SrBIT. 147
- Figure 4-10: curve fitting of the electrical conductivity measurements to calculate the acceptor impurity concentration with Equation 4-29. 148
- Figure 4-11: electrical conductivity versus oxygen partial pressure for undoped and 2 mol.% Mn doped SrBIT at 800°C. 151
- Figure 4-12: electrical conductivity versus oxygen partial pressure at different temperatures for 2 mol.% Mn doped SrBIT. 152
- Figure 4-13: electrical conductivity versus oxygen partial pressure for undoped SrBIT at 770°C and 4 mol.% Niobium doped SrBIT at 740°C. 154
- Figure 4-14: electrical conductivity versus oxygen partial pressure for undoped SrBIT in the full pO₂ range at 700 and 900°C. 155
- Figure 4-15: electrical conductivity of undoped and acceptor doped (Ti⁴⁺) SrBi₂Ta₂O₉ at 700°C by Palenduz [40]. 156
- Figure 4-16: oxygen partial pressure versus carrier concentration from conductivity measurements of undoped SrBIT at 900°C in the 10⁻⁵-1 atm range. 158

Figure 4-17: donor-excess identified as misplaced trivalent Bismuth versus reciprocal temperature for undoped SrBIT calculated using Equation 4-46.....	158
Figure 4-18: conductivity versus $pO_2^{-1/4}$ for ionic conductivity estimation for undoped SrBIT.	159
Figure 4-19: conductivity versus $pO_2^{-1/6}$ for ionic conductivity estimation for 2 mol.% Mn doped SrBIT.	159
Figure 4-20: calculated ionic conductivity versus reciprocal temperature for undoped SrBIT (open circles) and Mn doped (filled circles) SrBIT.....	160
Figure 4-21: electronic(open circles) and ionic conductivities (filled circles) as calculated with Equation 4-22 for undoped SrBIT.....	161
Figure 4-22: transference number map in the band gap-temperature space for undoped SrBIT calculated with Equation 4-47.....	162
Figure 4-23: transference numbers calculated from ionic and electronic conductivity calculations for undoped SrBIT (filled circles) and 2 mol.% Mn doped SrBIT.	163
Figure 5-1: ferroelectric hysteresis for undoped SrBIT measured at 200°C.	172
Figure 5-2: schematic representation of the experimental set-up used for piezoelectric characterization of SrBIT.....	173
Figure 5-3: collected charge versus applied force for undoped SrBIT at room temperature.	175
Figure 5-4: longitudinal piezoelectric coefficient versus amplitude of the applied AC stress at room temperature for undoped SrBIT.	176
Figure 5-5: longitudinal piezoelectric coefficient versus frequency at room temperature for undoped SrBIT under 9 MPa AC stress.	176
Figure 5-6: Schematic description of ferroelastic and ferroelectric domains formation on cooling SrBIT. Arrows are 180° ferroelectric domain walls.....	178
Figure 5-7: piezoelectric coefficient for undoped SrBIT versus AC stress at 1 Hz measured at 150°C.....	178
Figure 5-8: piezoelectric hysteresis for undoped SrBIT at 1 Hz measured at 150°C	179
Figure 5-9: piezoelectric coefficient versus AC stress for undoped SrBIT at 10 Hz measured at 150°C.....	179
Figure 5-10: piezoelectric coefficient versus AC stress of undoped SrBIT at 10 Hz measured at 200°C.....	180
Figure 5-11: collected charge versus applied force for 2 mol.% Mn doped SrBIT at 490 mHz at room temperature.....	181
Figure 5-12: piezoelectric coefficient (filled circles) and phase angle (open circles) for 2 mol.% Mn doped SrBIT versus frequency measured at room temperature.....	182
Figure 5-13: piezoelectric coefficient (filled circles) and phase angle (open circles) for 2 mol.% Mn doped SrBIT versus frequency measured at room temperature.....	182
Figure 5-14: piezoelectric coefficient versus AC stress for 2 mol.% Mn doped SrBIT measured at room temperature with 1 Hz AC signal.....	183
Figure 5-15: complex plane representation of piezoelectric coefficient for 2 mol.% Mn doped SrBIT.	183
Figure 5-16: relative piezoelectric coefficient versus frequency for 2 mol.% Mn doped SrBIT at room temperature (triangles), 50°C (open circles) and 100°C (filled circles).....	184
Figure 5-17: piezoelectric composite made of two piezoelectric materials used for modelization of the relaxation.....	185
Figure 5-18: measured complex permittivity versus frequency for BITO12-BITO9 (circles) and BITO9-BW (diamond-shaped) at room temperature.....	186

-
- Figure 5-19: measured complex permittivity versus frequency for BITO12-BITO9 (circles) and BITO9-BW (diamond-shaped) at 150°C. 186
- Figure 5-20: piezoelectric coefficient versus frequency for BITO12-BITO9 (filled circles) and BITO9-BW (open circles) at room temperature. 187
- Figure 5-21: piezoelectric coefficient versus frequency for BITO12-BITO9 (filled circles) and BITO9-BW (open circles) at 150°C. 187
- Figure 5-22: measured (filled items) and calculated (open items) complex piezoelectric coefficient versus frequency for a composite made of BITO12-BITO9 and BITO9-BW samples at room temperature. 188
- Figure 5-23: measured (filled items) and calculated (open items) complex piezoelectric coefficient versus frequency for a composite made of BITO12-BITO9 and BITO9-BW samples at 150°C. 189
- Figure 5-24: calculated real part of the piezoelectric coefficient versus frequency and piezoelectric coefficient of the first material (d_1) calculated with Equation 5-9. Others parameters are $d_2=10$ pC/N, $\epsilon_1=200$, $\epsilon_2=100$, $\sigma_1=10^{-9}$ S/m, $\sigma_2=10^{-10}$ S/m, $V=0.5$ 190
- Figure 5-25: calculated imaginary part of the piezoelectric coefficient versus frequency and piezoelectric coefficient of the first material (ϵ_1) calculated with Equation 5-9. Others parameters are $d_2=10$ pC/N, $\epsilon_1=200$, $\epsilon_2=100$, $\sigma_1=10^{-9}$ S/m, $\sigma_2=10^{-10}$ S/m, $V=0.5$ 191
- Figure 5-26: calculated real part of the piezoelectric coefficient versus frequency and permittivity of the first material (ϵ_1) calculated with Equation 5-9. Others parameters are $d_1=3$ pC/N, $d_2=20$ pC/N, $\epsilon_2=200$, $\sigma_1=10^{-10}$ S/m, $\sigma_2=10^{-9}$ S/m, $V=0.5$ 191
- Figure 5-27: calculated imaginary part of the piezoelectric coefficient versus frequency and permittivity of the first material (ϵ_1) calculated with Equation 5-9. Others parameters are $d_1=3$ pC/N, $d_2=20$ pC/N, $\epsilon_2=200$, $\sigma_1=10^{-10}$ S/m, $\sigma_2=10^{-9}$ S/m, $V=0.5$ 192
- Figure 5-28: calculated real part of the piezoelectric coefficient versus frequency and conductivity of the first material (d_1) calculated with Equation 5-9. Others parameters are $d_1=20$ pC/N, $d_2=3$, $\epsilon_1=100$, $\epsilon_2=10$, $\sigma_2=10^{-10}$ S/m, $V=0.5$ 193
- Figure 5-29: real part of the piezoelectric coefficient versus frequency and piezoelectric coefficient of the first material in the case of non-conducting materials ($\sigma_1=\sigma_2=0$) and $\epsilon_1=100$, $\epsilon_2=200$, $d_2=10$ 194
- Figure 5-30: calculation of the complex piezoelectric coefficient of a two-phase composite made of ab and c oriented c samples put in series at 195°C. 195

ACKNOWLEDGEMENTS

I gratefully acknowledge Professor Nava Setter who gave me the opportunity of working in her group and carry out in excellent conditions the research presented in this thesis work.

In particular, I wish to thank my supervisor, Dr. Dragan Damjanovic for his highly professional support during these last five years.

Dr. Marlyse Maeder and Dr. Pedro Duran Martin are also valuable contributors to this thesis work; therefore I would like to warmly thank them too.

I wish to thank Dr. Pedro Moeckli for his constant availability and for his considerable work on SrBIT.

I am indebted to my thesis committee, Professor Wilfried Kurz, Professor Hans-Joerg Mathieu, Dr. Claudio Cavalloni, Dr. Pedro Duran Martin and Dr. Dragan Damjanovic, who kindly agreed to be co-examiners in the jury.

I would like to thank especially Juliette, Alexandra, Marie and Sandrine who shared an office with me and created an enjoyable atmosphere.

Enfin, je remercie mes parents pour leur précieux soutien durant toutes mes années d'études.

CURRICULUM VITAE

Name	Voisard
First Name	Cyril
Date of birth	28 avril 1972
Origin	Fontenais, Canton du Jura
Nationality	Swiss

EDUCATION

1995-2000	PhD in Materials Science, Ceramic Laboratory, Swiss Federal Institute of Technology, Lausanne
1990-1995	Diploma in Materials Science Engineering from Swiss Federal Institute of Technology, Lausanne.
1987-1990	Maturity Diploma Type C, Lycée cantonal de Porrentruy.

LANGUAGES

French	Mother-tongue
English	Speaking and writing fluency
German	Good understanding

